ALLOSTERIC INHIBITION IN PROTEIN KINASES

MOLECULAR MECHANISMS OF ALLOSTERIC INHIBITION IN CYCLIC-NUCLEOTIDE DEPENDENT PROTEIN KINASES

By JUNG AH BYUN, HONOURS B.Sc.

A Thesis Submitted to the School of Graduate Studies in Partial Fulfilment
of the Requirements for the Degree
Doctor of Philosophy

Doctor of Philosophy (2020) **McMaster University**
(Biochemistry) **Hamilton, Ontario**

Thesis Title: Molecular Mechanisms of Allosteric Inhibition in Cyclic-Nucleotide Dependent Protein Kinases
Author: Jung Ah Byun, Honours B.Sc. (McMaster University)
Supervisor: Professor Giuseppe Melacini
Number of Pages: xii, 170

Lay Abstract

Cyclic-nucleotide dependent protein kinases are critical to translate extracellular signals into intracellular processes. Malfunctioning kinases within our body or kinases in pathogens are related to cancerous and infectious diseases, respectively. Hence, it is of great interest to find ways to inhibit these kinases, which can be achieved through compounds (*i.e.* inhibitors) that bind to these kinases and stop their function. Allosteric sites are distant from the active site of a kinase, yet when perturbed by binding of a small allosteric molecule, such effect can be relayed down to the active site. Allosteric inhibitors provide selectivity and potency in kinase inhibition. Here, we use NMR spectroscopy, in conjunction with simulations and allosteric modelling, to elucidate the molecular mechanisms underlying the allosteric inhibition of Protein Kinase A and *Plasmodium falciparum* Protein Kinase G. Understanding such mechanisms will aid in designing new drug leads and developing therapeutic strategies, including multi-drug combinations.

Thesis Abstract

Allosteric inhibition of kinases provides high selectivity and potency due to lower evolutionary pressure in conserving allosteric *vs.* orthosteric sites. The former are regions distinct from the kinase active site, yet, when perturbed through allosteric effectors, induce conformational and/or dynamical changes that in turn modulate kinase function. Protein kinases involved in cyclic nucleotide signalling are important targets for allosteric inhibition due to their association with diseases, from infections to Cushing's syndrome. This dissertation specifically focuses on elucidating the molecular mechanism of allosteric inhibition in the cAMP-dependent protein kinase (PKA) and the *Plasmodium falciparum* cGMP-dependent protein kinase (*Pf*PKG), which are targets for a generalized tumor predisposition commonly referred to as Carney Complex and for malaria, respectively. In chapters 2 and 3, we focus on the agonism-antagonism switch (*i.e.* allosteric pluripotency) observed as the phosphorothioate analog of cAMP, Rp-cAMPS (Rp), binds to PKA. Utilizing Nuclear Magnetic Resonance (NMR), Molecular Dynamics (MD) simulations and Ensemble Allosteric Model (EAM), we determined that two highly homologous cAMP-binding domains respond differently to Rp, giving rise to a conformational ensemble that includes excited inhibition-competent states. The free energy difference between this state and the ground inhibition-incompetent state is tuned to be similar to the effective free energy of association of the regulatory (R) and catalytic (C) subunits, leading to allosteric pluripotency depending on conditions that perturb the R:C affinity. The general significance of these results is a re-definition of the concept of allosteric target to include not only the isolated allosteric receptor, but also its metabolic and proteomic sub-cellular environment. In chapter 4, we utilize a mutant that silences allosteric pluripotency to reveal that the agonism-antagonism switch of PKA not only arises from the mixed response of tandem domains, but also from the mixed response of allosteric regions within a single domain that mediates interactions with Rp. In chapter 5, the allosteric inhibition of *Pf*PKG associated with malaria is induced through base-modified cGMP-analogs and the underlying inhibitory mechanism is determined. We show that, when bound to a *Pf*PKG antagonist, the regulatory domain of *Pf*PKG samples a mixed intermediate state distinct from the native inhibitory and active conformations. This mixed state stabilizes key cGMP-binding regions, while perturbing the regions critical for activation, and therefore it provides an avenue to preserve high affinity, while promoting significant inhibition. Overall, in this thesis, previously elusive mechanisms of allosteric inhibition were elucidated through the combination of NMR, MD, and EAM methods. Through this integrated approach, we have unveiled an emerging theme of inhibitory 'mixed' states, either within a single domain or between domains, which offer a simple but effective explanation for functional allostery in kinases.

Acknowledgements

First and foremost, I would like to thank my supervisor, Professor Giuseppe Melacini for all his guidance over the past 6 years. It was a true blessing to be able to learn and grow under your supervision. Thank you for your continuous patience and encouragements, which I needed the most and those really allowed me to achieve all that I have done. Your endless passion for research and science has inspired me in many ways. I will always remember all that I have learned from you and I sincerely thank you for everything.

I would also like to thank all the members of the Melacini Lab whom I have had the privilege to work with. To Dr. Madoka Akimoto, thank you for your wonderful mentorship and friendship. I have learned so much from you in many different ways. You allowed me to recognize my abilities and reach higher and I am really grateful for that. To Dr. Rashik Ahmed, whom I have walked the path of graduate career together, thank you for your friendship and motivating me to work harder (but I would never be able to do like you do). All the great advices, encouragements, and support helped me to persevere. To Dr. Stephen Boulton, thank you for answering all those questions I asked you and sorry I have bugged you with so many. Thank you for teaching me how to analyze different data and important tips for carrying out experiments. To Naeimeh, thank you for your friendship and kindness. I'm thankful that I had you to ask if I'm doing things right, whenever I doubted myself, and I would always get reassurance from you. To Dr. Bryan VanSchouwen, thank you for your wonderful MD simulations and also teaching me how to analyze 3D data and assign chemical shifts. To Jinfeng, thank you for being so kind and bringing delicious food to share together. You were really patient when we were working on the MD simulations and I'm truly thankful for that. To Karla, Heba, and Hongzhao, thank you for the friendships and all the good times. To Kody, thank you for your supervision for my undergraduate thesis in the Melacini Lab. You were a great mentor and taught me how to work independently, which helped me to learn many things. To my thesis students, Katherine, Tomas, and Nishi, thank you for your partnerships in working through our projects together. What you have done have served as steppingstones for making those manuscripts fly.

Next, I would like to thank my committee members Dr. Gerry Wright, Dr. Russell Bishop, and Dr. Alba Guarne for their support and guidance. I would always get reminded of what the most important questions are from the committee meetings, which helped me refocus my minds. All the great advices will be treasured, thank you.

To all my friends, especially YK, Hansol, and Susie, who would always tell me I'm the best and should never lose my confidence. Whenever I talk about science, you would never get bored, but rather appreciate what I'm doing. Thank you for being there through all my ups and downs.

Lastly, I would like to sincerely thank my family with my whole heart. I could not have done this without your overflowing love, support and sacrifice. You would always be so proud of me from even the smallest things I do. All the opportunities and privileges I had come from you. I could not have asked for more. I am truly blessed to be your daughter, your granddaughter and your sister. 감사합니다. 사랑합니다.

Table of Contents

List of Main Text Figures

CHAPTER 1

CHAPTER 2

CHAPTER 3

CHAPTER 4

CHAPTER 5

CHAPTER 6

List of Supplementary Figures

CHAPTER 4

CHAPTER 5

List of Tables

CHAPTER 3

List of Supplementary Tables

CHAPTER 5

Abbreviations

δ	Chemical shift (ppm)
ATP	Adenosine triphosphate
BBR	Base binding region
BME	β-mercaptoethanol
cAMP	Adenosine 3ʺ,5ʺ-cyclic monophosphate
CBD	cAMP-binding domain
CCS	Compounded ^{15}N-^{1}H chemical shift
CEST	Chemical-exchange saturation transfer
cGMP	Guanosine 3ʺ,5ʺ-cyclic monophosphate
CHESPA	Chemical shift projection analysis
CHESCA	Chemical shift covariance analysis
C-subunit	Catalytic subunit of PKA
DRM	Disease-related mutant
DTT	Dithiothreitol
EAM	Ensemble allosteric model
FEL	Free-energy landscape
K_a	Equilibrium association constant
K_d	Equilibrium dissociation constant
K_m	Michaelis-Menten constant
EPAC	Exchange protein activated by cAMP
HCN	Hyperpolarization-activated cyclic nucleotide-gated ion channel
H/D	Hydrogen-deuterium exchange
HSQC	Heteronuclear single quantum coherence
MD	Molecular Dynamics
MTSL	*S*-(1-oxyl-2,2,5,5-tetramethyl-2,5-dihydro-1H-pyrrol-3-yl) methyl methanesulfonothioate
MW	Molecular weight
NMR	Nuclear magnetic resonance
NNE	Near-neighbour effects
PBC	Phosphate binding cassette
PDB	Protein Data Bank
PF	Protection factor
*Pf*D	cGMP-binding domain D of *P. falciparum* cGMP-dependent kinase
*Pf*PKG	*P. falciparum* cGMP-dependent kinase
PKA	Protein kinase A (cAMP-dependent protein kinase)
PRE	Paramagnetic relaxation enhancement
R1a	Isoform Iα of regulatory subunit of PKA
RMSD	root-mean-square deviation
ROESY	rotating frame Overhauser effect spectroscopy
Rp	Adenosine- 3', 5'- cyclic monophosphorothioate (Rp-cAMPS)
SPR	surface plasmon resonance
STD	Saturation transfer difference
TROSY	Transverse relaxation-optimized spectroscopy
WT	Wild type

Chapter 1

Introduction

1.1 Kinases as drug targets and the role of allostery

Protein kinases are essential cellular regulators. They modify the function of their target proteins by adding a phosphate group from an ATP substrate. Phosphorylation induces changes in conformation and consequently in function, including enzymatic activity, membrane transport, signal transduction, protein-protein interactions and protein degradation (1, 2). As it can be inferred from such a broad range of mechanisms they are involved in, different kinases with defective functions can lead to multiple diseases, such as cancer (3–6), neurological (7, 8), immunological (9–11), infections (12–14), and developmental disorders (15, 16). Hence, kinases serve as attractive drug targets.

More than 500 kinases are encoded in the human genome, suggesting that essentially every process within a signalling network is directly or indirectly connected to a phosphorylation cascade (17). This suggests a perturbation of the activity of a kinase can lead to a significant physiological response, pointing to how kinase inhibitors can be effective drugs for therapeutic purposes. Indeed, kinases are one of the most targeted system for drug development (2).

Inhibition of a kinase could be promoted by targeting the catalytic core of the kinase, where the transfer of the ATP phosphate to the protein substrate occurs. The inhibitor would competitively bind and replace the ATP, thus halting the phospho-transfer reaction. In fact, the majority of kinase inhibitors exhibit such mechanism (2). However, one main drawback of targeting the active site of kinases is its highly conserved nature among different kinases as needed to preserve the function, leading to selectivity issues and to potential side effects of these ATP-mimicking inhibitors (18). An alternative way to address this selectivity issue is through targeting loci distinct from the ATP-binding site, called “allosteric sites”. These sites are more specific to a particular kinase due to lower evolutionary pressure and when perturbed

through an allosteric ligand binding, the effect is allosterically relayed down to the active site leading to functional changes.

1.2 Kinases in cyclic nucleotide signalling

Cell-to-cell communication relies on the conversion of extracellular stimuli into tightly regulated intracellular responses. A key step in this transduction process is the relay of external signals by second messengers, including cyclic nucleotides (cNMPs). For example, increased intracellular cAMP concentrations are generated in response to hormones binding to G-protein-coupled receptors that lead to the activation of adenylyl cyclase. cAMP then binds to regulatory proteins and causes conformational changes that modulate specific cellular functions. For instance, cAMP activates protein kinase A (PKA), which regulates cellular differentiation, proliferation and metabolism. Defects in the cAMP-dependent activation of PKA in humans result in cancer and developmental disorders (4, 5, 19, 20). In addition, cNMPs are critical for infectious diseases. cGMP activates protein kinase G in the malaria parasite *Plasmodium falciparum* (*Pf*PKG) and controls essential stages of the *Plasmodium* life cycle (12, 21–23). Therefore, the pathways controlled by PKA and *Pf*PKG are ideal therapeutic targets.

1.2.1 PKA: Physiological Relevance, Domain Architecture, and Regulatory Mechanism

PKA has been used for many studies for decades as a prototype for protein kinase superfamily. It is responsible for regulating important cellular processes, such as inflammatory immune responses, cell proliferation, gene expression, and metabolism (24–28). It exists in two forms: the inactive tetrameric holoenzyme and the active dissociated catalytic subunit (C) (29–31). In the inactive holoenzyme, two C-subunits are bound to a dimeric regulatory subunit (R). Upon binding cAMP, the R-subunits undergo a conformational change that releases C-subunits to phosphorylate substrate proteins. PKA over-activation was observed by the deletion of the gene for the isoform 1a of the R-subunit (R1a). Such over-activation has shown to induce multiple types of tumours, including breast cancer, thyroid, pancreatic, and pituitary tumours, suggesting the PKA R1a is an essential tumour suppressor (4, 5, 19, 20, 32, 33).

The R1a consists of an N-terminal dimerization/docking domain, a flexible linker that bridges the inhibitory site and two cAMP binding domains (CBD), CBD-A and CBD-B, which mediate the interaction with the C-subunit and also contain the phosphate binding cassette (PBC), a helix loop region responsible for interacting with the ribose-phosphate of cAMP and is highly conserved between other cNMP binding proteins (Figure 1A). Both CBDs share a typical α/β subdomain architecture, with the β- barrels embedding the two cAMP binding sites and with the non-contiguous α-helical subdomains joined at the interface between the two domains. The flexible inhibitory linker N-terminal to CBD-A interacts with C and is important for the inhibition of the complex (Figure 1B) (30, 34). This interaction site in C is the activation loop where both the substrate and MgATP also bind. Activation mechanism of PKA revealed by structures demonstrates binding of cAMP to CBD-B first, which allows CBD-A to bind to the second cAMP, followed by capping of the cAMP in CBD-A by W260 of CBD-B (Figure 1C) (30). This leads to formation of a compact globular R and facilitates the dissociation and activation of C. CBD-B regulates the access of cAMP to CBD-A, while the inhibitory linker and CBD-A mediate key inhibitory interactions with C.

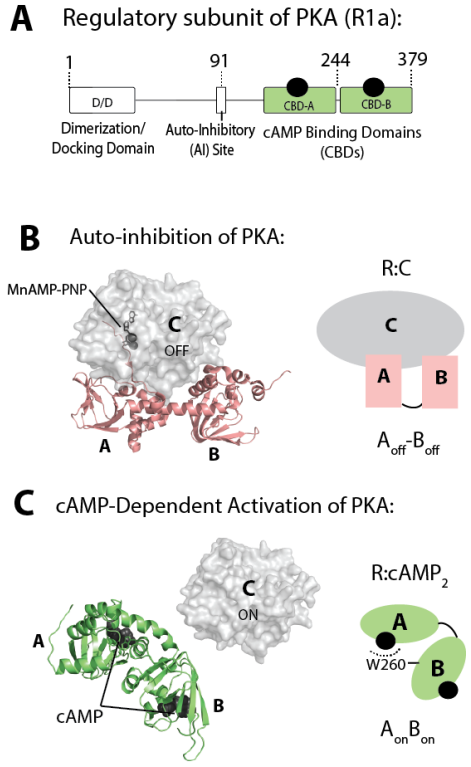

Figure 1. *PKA regulatory subunit.* (A) Domain organization of the regulatory subunit R1a (R). (B) PKA holoenzyme, where the R subunit shown in ribbon diagram inhibits the catalytic subunit (C) shown in gray. The flexible inhibitory linker binds to the active site of C subunit. The cAMP-binding domains (CBD) A and B confer to the 'off' state. (PDB:2QCS) (C) cAMPs bind to each CBD. Conformational shift to the 'on' state of these CBDs lead to the release of the C subunit. (PDB:1RGS)

1.2.2 PfPKG: Physiological Relevance and Domain Architecture

*Pf*PKG plays a major role in both replication and transmission of the *Plasmodium* parasite, including exflagellation and gametogenesis in the asexual blood stage, invasion of hepatocytes by sporozoites, and gliding motility of ookinetes (22, 35–38). *Pf*PKG consists of an N-terminal regulatory domain followed by a C-terminal catalytic domain (Fig. 1A) (39). In the absence of cGMP, the regulatory domain auto-inhibits the catalytic domain. When the regulatory domain binds to cGMPs, it undergoes conformational changes that allow the catalytic domain to be activated. The regulatory domain is organized into four cyclic-cGMP binding domains (CBDs): A, B, C and D. CBD-C is degenerate and does not bind to cGMP (40). Among CBD-A, B, and D, the C-terminal CBD-D that is directly linked to the catalytic domain, exhibits the highest affinity and

selectivity towards cGMP and is the main CBD responsible for the auto-inhibition and the activation of *Pf*PKG (23, 40). Similar to other CBDs, *Pf*PKG CBD-D is composed of a contiguous β-subdomain and noncontiguous α-subdomain (Fig. 1B). The β-subdomain includes the base-binding region (BBR) and the PBC, which are critical for cGMP recognition and binding. The α-subdomain includes the N-terminal helices called the N3A and the two C-terminal helices, which are important for mediating the inhibitory interaction with the catalytic region (23, 41, 42).

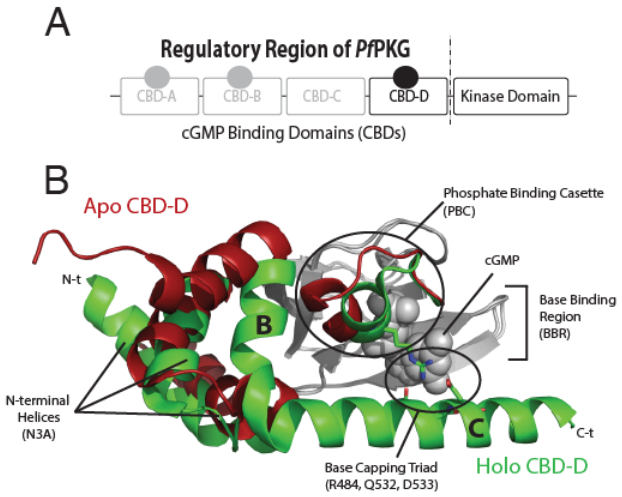

Figure 2. *CBD-D is the key regulatory domain of PfPKG. (A) Domain organization of PfPKG.* (B) Structures of apo (red) and cGMP-bound holo (green) CBD-D. The invariant β-subdomains are shown in gray. (PDB: 4OFF, 4OFG)

1.3 Thesis Overview and the Key Questions Addressed

A common theme that emerges from the previous sections is the allosteric inhibition of kinases, specifically PKA and *Pf*PKG. Allosteric modulation of these kinases can be achieved through targeting the CBD of the regulatory region. In this thesis, we elucidate the molecular mechanism of allosteric inhibition of PKA and *Pf*PKG induced by cNMP-analogs. Biophysical methods, including NMR, MD simulations and allosteric modelling, along with functional assays and affinity measurements are utilized. Brief summaries of the findings are outlined below. Detailed discussion of the results can be found in Chapters 2, 3, 4 and 5.

1.3.1 Mechanism of Rp-cAMPS induced agonism-antagonism switch in PKA

The only allosteric inhibitor for PKA known to date is Rp-cAMPS, a phosphorothioate analog of cAMP. However, it was shown that Rp-cAMPS acts as both an agonist and an antagonist for PKA depending on the environmental condition, specifically the concentration of MgATP (43). Another challenge is that the crystal structure of Rp-bound PKA R1a (91-379; spanning the inhibitory linker, CBD-A and CBD-B) shows that both domains adopt to a similar structure as the cAMP-bound structure (44), suggesting that there must be other mechanisms, through dynamics, which allow Rp to function as an antagonist for PKA. In Chapter 2, we discuss how we utilize Nuclear Magnetic Resonance (NMR) spectroscopy, MD simulations, Ensemble Allosteric Modelling (EAM) and the functional kinase assay to tackle the previously unknown mechanism of inhibition of Rp-cAMPS and the agonism-antagonism switch. Using NMR methods, we show that the two homologous CBDs exhibit divergent response to Rp. Such differential response perturbs the domain-domain interaction, which is also confirmed through MD simulations. This leads to a conformational ensemble, where the inhibitory-competent states (*i.e.* states competent to bind and inhibit C-subunit) are excited high free energy states, providing a viable explanation for the Rp-induced antagonism. The EAM built based on the input parameters measured from the NMR methods show that the Rp-induced agonism can be observed under conditions where the effective R:C binding affinity is low, due to factors such as lower MgATP concentration, presence of high affinity kinase substrate, or the presence of a mutation. In such scenarios, the inhibitory-competent states remain higher in free energy than the ground inhibitory-incompetent state, leading to PKA activation.

1.3.2 Ensemble Allosteric Model for PKA

Allosteric modelling is also crucial in providing insights on observable allosteric phenomena. When allostery was initially conceptualized, the two leading allosteric models were the Monod-Wyman-Changeux's (MWC) (45) and the Koshland-Nemethy-Filmer's (KNF) (46), also known as the 'symmetric' and 'sequential' models, respectively. These two models explain allostery of multimeric proteins, where the subunits undergo conformational change between two major structural end states, the low-affinity and high-affinity forms. The main idea of the MWC model is the pre-existing conformational equilibrium that shifts with conservation of symmetry upon binding of a regulator or ligand (45). On the other hand, the KNF model

postulates that each subunit undergoes conformational change upon binding of the ligand (*i.e.* induced-fit), and that this propagates to adjacent subunits, thus changing the affinity of those binding sites, and hence giving rise to cooperativity (46). However, these models cannot be applied to all allosteric systems, and do not provide explanations on how the allosteric modulation can occur without structural changes or how an allosteric switch could occur between agonism and antagonism upon binding to the same ligand. The ensemble allosteric model (EAM) successfully addresses these limitations by interpreting the dynamics of allostery in terms of thermodynamic ensembles of microstates. In the EAM, the populations of each microstate are modeled through normalized Boltzmann factors, which are in turn dictated by the free energies of conformational change within each (sub)domain and of inter-(sub)domain interactions (47–51). Knowledge of such populations enables the prediction of key observables, such as affinities and degrees of activation/inhibition, hence the relation between experimental findings to the observed function. In Chapter 3, using PKA as our model system, we discuss how the input parameters are measured on the basis of the populations and the free energies determined by NMR methods and how the EAM is built based on these input parameters.

1.3.3 Dissecting the drivers of allosteric pluripotency in Protein Kinase A

Allosteric pluripotency observed with PKA and its allosteric effector, Rp-cAMPS, was shown to be lost with a domain-silencing mutant, R209K: the Rp-cAMPS induced consistent agonism regardless of the presence of MgATP (43). To elucidate the mechanism underlying such loss in agonism-antagonism switch, in hopes to dissect the key drivers of allosteric pluripotency, we utilized the R209K mutation, in combination with the EAM and NMR methods. In Chapter 4, we show the R209K perturbs the 'on' vs. 'off' equilibrium of CBD-A:Rp to sample a larger fraction of the 'on' state compared to WT, stabilizing the inhibitory-incompetent ground state. However, the extent of this shift is not enough to silence the agonism-antagonism switch, as predicted through the EAM modelling. Our results indicate that the enhanced inter-domain interaction also significantly contributes to the observed consistent Rp-induced agonism. Performing a double-mutant cycle, where we introduced the R209K mutation and CBD-B (which contributes as a lid for the base of Rp), and measuring the affinity of Rp to CBD-A, we dissected the allosteric drivers that are responsible for determining the stabilization of the inter-domain interaction and hence the allosteric pluripotency. The coupling between the R209K mutation and the lid

engagement suggests when both the R209 (PBC) and W260 (lid) engage in the interaction with Rp, steric frustration arises due to the bulky phosphorothioate moiety of Rp, leading to partial destabilization of the closed topology inhibitory-incompetent ground state. This gives rise to a conformational ensemble responsible for driving the allosteric pluripotency. With the R209K mutation, such steric frustration is relieved, leading to stabilization of the closed topology inhibitory-incompetent ground state and to the consistent Rp-induced agonism.

1.3.4 Mechanism of allosteric inhibition of *Pf*PKG

The mechanism underlying the *Pf*PKG allosteric inhibition has the potential to offer important insights for the rational design of *Pf*PKG-selective allosteric inhibitors. However, information on such mechanism was sparse. We utilized a set of based-modified cGMP-analogs that induces a range of kinetic *Pf*PKG activations. The conformational states sampled by CBD-D of *Pf*PKG bound to these cGMP-analogs were characterized through NMR chemical shift analyses. Our data indicates that an antagonist (*i.e.* 8-NBD-cGMP), instead of simply reversing the two-state inactive-active equilibrium to the inactive state, promotes CBD-D to sample an additional "mixed" intermediate state. The MD simulations and NMR analysis combined with site-directed mutagenesis show the antagonist perturbs critical interactions within the CBD-D that are required for activation. Our analysis suggests that the mixed intermediate state, through the C-terminal lid disengagement, exhibits an inhibitory potential similar to the native inactive state. Furthermore, the engagement of key cGMP-binding regions, including the PBC, suggests that the mixed intermediate state provides an avenue for the inhibitors to preserve high affinity towards CBD-D, which was confirmed through surface plasmon resonance.

1.4 NMR methods to dissect the molecular mechanisms of disease-related mutations (DRMs): Understanding how DRMs remodel functional free energy landscapes.

The work presented in this section (1.4) has previously been published and is reproduced with permission from the Elsevier B.V. Full citation is as follows:

Byun, JA and Melacini, G. 2018. NMR methods to dissect the molecular mechanisms of disease-related mutations (DRMs): Understanding how DRMs remodel functional free energy landscapes. *Methods.* 148:19-27.

The main purpose of including this section is to introduce the NMR methods used to dissect the molecular mechanisms of perturbations such as disease-related mutations or an allosteric inhibition through effector binding. This publication focused on the disease-related mutation as an example of such perturbation, however, the methods discussed here can be applied in a more general manner and in part, were also utilized in experimental approaches taken in studies included in this thesis.

1.4.2 Introduction

Thanks to genomic and proteomic efforts, the databases of disease-related mutations (DRMs) linked to a wide array of inherited diseases are rapidly growing (52). In addition, DRMs are a central aspect of personalized precision medicine, whereby therapies are optimized based on the specific genetic fingerprint of a patient (53). The clinical and pharmacological phenotypes induced by DRMs may arise through multiple mechanisms. For instance, they can alter the expression levels of the protein associated with the mutated gene, leading to either pathologically excessive or insufficient amounts of expressed proteins. Alternatively, DRMs could induce disease-related phenotypes by impairing the function of the expressed protein through changes in protein structure and/or dynamics and/or folding pathways. Such changes typically affect protein function. For example, DRMs in signaling hubs often perturb the regulation of downstream cell metabolism, thus leading to mis-regulation and pathologies such as cancer predisposition or hormonal resistance (15, 54, 55).

Elucidating the changes in structure, dynamics and folding pathways induced by DRMs is a fundamental first step towards understanding the molecular etiology of inherited pathologies and thus towards the development of therapies. For this purpose, classical structural biology methods such as X-ray crystallography, electron microscopy (EM), and nuclear magnetic resonance (NMR) are extensively utilized to identify the structural perturbations induced by DRMs. However, in multiple instances no major differences could be detected

between the DRM and wild-type (WT) structures (56–59). A possible explanation for the apparent absence of DRM *vs.* WT structural differences, is that the solved structures typically capture the most populated state ("ground state") of the conformational ensemble sampled by a protein, whereas DRMs may remodel other functionally relevant attributes of the free-energy landscape (FEL). For example, the FEL of allosteric regulatory proteins includes not only the ground state, but also accessible excited states residing in local minima at higher relative free-energy levels and kinetically separated from the ground conformation by free energy barriers. Understanding how DRMs perturb these thermodynamic and kinetic FEL features is a critical step for determining the mechanism of action underlying the functional and/or clinical phenotype of a DRM.

The simplest possible functional FEL for an allosteric regulatory protein is based on a four-state thermodynamic cycle, in which a two-state conformational equilibrium is coupled to an allosteric effector-binding equilibrium (Fig. 3A) (45, 60, 61). The conformational equilibrium is usually between inactive and active states, which differ at the allosteric effector-binding site, as well as, at functional sites distinct from the allosteric site. The effector typically exhibits different affinities towards the two states, and whichever state the effector binds with the higher affinity, will be stabilized upon binding (Fig. 3B). An example of a FEL for this allosteric model is shown in Fig. 3C. The relative depths of the free-energy wells of the inactive *vs.* active states in the apo sample determine the relative population of each state prior to effector binding, and therefore control the position of the auto-inhibitory equilibrium and constitutive activity. The state-specific association constants define the extent of activation upon effector binding and dictate whether the allosteric effector acts as an activator, a partial agonist, antagonist or reverse agonist. Furthermore, the state-specific association constants, together with the position of the apo auto-inhibitory equilibrium, determine the overall thermodynamic affinity for the allosteric effector (62). In addition, the widths of the free-energy wells and the free energy barrier between the apo and effector-bound forms affect the off kinetics for effector release and signal termination (63, 64). The DRMs may induce changes in all these functionally relevant FEL attributes, *i.e.* the depths and widths of local minima as well as barriers separating them. Hence, it is clear that DRM-induced phenotypes may arise from multiple concurrent perturbations of the FEL (Fig. 3) and therefore dissecting the molecular mechanism of a DRM is a complex exercise.

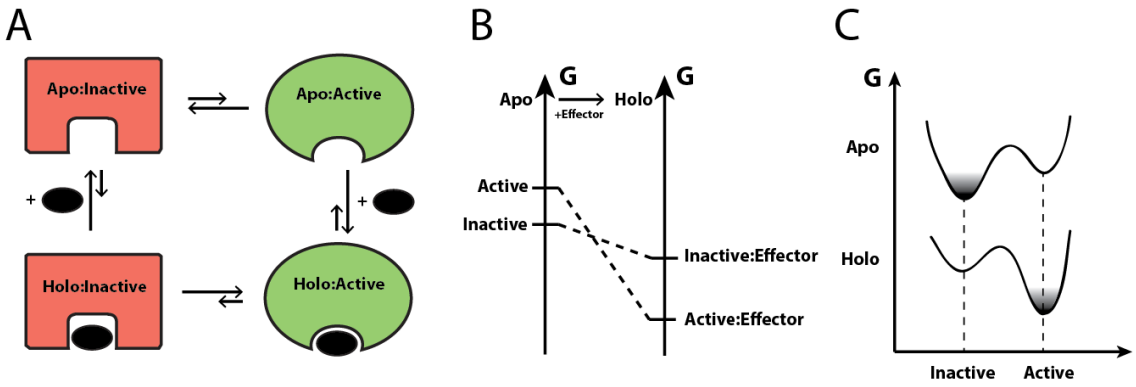

Figure 3. *Model of a four-state thermodynamic allosteric cycle obtained through coupling of two two-state equilibria.* (A) Thermodynamic cycle arising from the coupling of a two-state conformational equilibrium (active *versus* inactive) and an allosteric effector-binding equilibrium (apo *versus* holo). Inactive and active states differ at least at the level of the functional site and of the effector-binding site. (B) Free-energy diagram illustrating the thermodynamic cycle in (A). An activating effector exhibits higher affinity towards the active conformation, resulting in a selective lowering of the free energy of the active conformer upon binding of the effector. (C) Free energy landscape showing the inactive-active equilibria in the apo and holo forms, highlighting free energy barriers and minima with higher populations (shaded region).

An experimental technique ideally suited to dissect the complexity of DRM effects on FELs is NMR spectroscopy. NMR is an excellent technique to map how DRMs perturb FELs with near-atomic resolution. This review will discuss NMR methods ideally suited to understand the molecular basis of DRMs by mapping how DRMs modify the FEL of allosteric regulation, *i.e.* how DRMs alter the thermodynamics and kinetics of conformational and binding transitions that are critical for the regulation of protein function (Fig. 3). For the sake of illustration, we will focus on our recent work on a bradycardia-related point mutation reported for the hyperpolarization and cyclic-nucleotide channel (HCN) (56). While it is clear that this example does not exhaustively encompass the depth and breadth of all recent seminal work on the molecular mechanisms of DRMs (58, 59, 65–76), it illustrates the effectiveness of NMR in dissecting the molecular mechanisms through which DRMs cause clinical phenotypes. Specifically, this article is articulated into three main sections: the CHEmical Shift Projection Analyses (CHESPA), which aim at measuring active *vs.* inactive state populations (i.e. the thermodynamics of fast-exchanging inhibitory equilibria), NMR spin relaxation measurements, which probe the width of FEL wells, and NMR measurements of binding thermodynamics (K_d) and kinetics (k_{on} and k_{off}). By combining these complementary NMR analyses, it is possible to reconstruct a comprehensive

picture of how DRMs remodel functional FELs, rationalizing clinical and pharmacological phenotypes.

1.4.3 The CHEmical Shift Projection Analysis (CHESPA)

Chemical shifts are excellent probes to detect changes caused by DRMs as they are exquisitely sensitive to structural and dynamical changes (61, 77–82). The magnitude of the chemical shift change reports on variations in the local chemical and/or structural environment. Therefore, a systematic analysis of the size of chemical shift changes reveals regions affected by a DRM, both at the site of mutation and at more remote loci (*i.e.* allosteric effects) (77, 83). The direction of chemical shift change is another valuable observable to consider. For example, when the exchange between two conformations, such as the inactive and active states of a protein, is fast on the chemical shift NMR time scale, the NMR chemical shifts are linear averages and therefore the peak position reports on the relative populations of the two conformations, *i.e.* chemical shift changes conforming to a linear pattern sense the position of a two-state conformational equilibrium. The CHESPA quantifies both the magnitude and the direction of chemical shift changes caused by perturbations, such as mutations or ligand-effector binding (15, 78–80). The CHESPA is thus useful to analyze mutation-induced perturbations of allosteric conformational equilibria at residue resolution, which in turn provides information on the relative depth of the free energy well of the inactive vs. active states.

The CHESPA analysis starts with defining two vectors. The first vector is the reference vector (vector B), which typically joins the inactive and the active state of WT (Fig. 4A). Examples of such states are the apo (non-bound) and holo (bound) state, especially when functional assays confirm lack of appreciable constitutive activity in the absence of effector ligand and maximal activation in the presence of saturating amounts of the effector ligand. The second vector (vector A) connects the mutant-apo or the mutant-holo to the WT-apo or the WT-holo, respectively. Under the assumption of fast exchange, the normalized projection of vector A onto vector B allows for the measurement of the fractional shift towards inhibition or activation induced by a mutation. The fractional shift is denoted as *X* and is calculated as the ratio of the magnitude of the component of vector A along vector B and of vector B:

$$X = \frac{\overrightarrow{|A|}}{\overrightarrow{|B|}} cos\theta \qquad (1)$$

where θ is the angle between vectors A and B. Hence, cos(θ) can be computed as:

$$cos\theta = \frac{\vec{A}\cdot\vec{B}}{|\vec{A}||\vec{B}|} \quad (2)$$

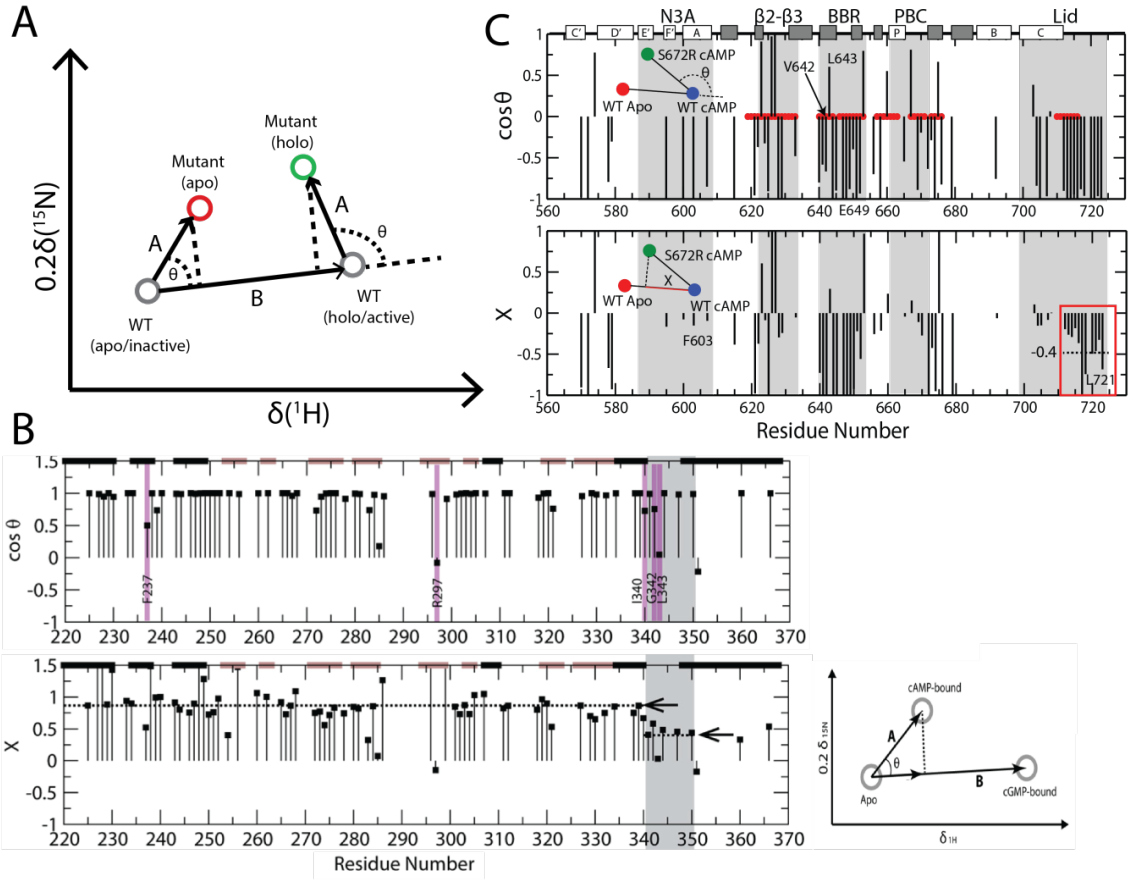

Figure 4. *Mapping mutation-induced perturbations through CHESPA.* (A) General CHESPA scheme. The mutant to WT chemical shift vector (vector A) is projected onto a reference vector connecting WT apo and WT holo (vector B). Through this projection, the fractional shift (*X*) and the cos(θ) are measured. The compounded chemical shift (CCS) is extracted from measuring the magnitude of vector A. (B) An example of CHESPA data, where cos(θ) and *X* are plotted *vs*. the residue number. The CHESPA pattern is indicative of a three-state equilibrium. The secondary structural elements are indicated on the top of the graphs (black = α-helices, brown = β-strands). The residues highlighted with purple vertical bars indicate outlier residues that exhibit notably low cos(θ) values. The dotted black line and the arrows in the *X* plot indicate the average fractional shift toward activation of two different regions, where the *X* values are quite homogenous within each region compared to the difference between the *X* values in the two regions. Figure adapted from Ref.(81). Copyright 2015 the American Society for Biochemistry and Molecular Biology. (C) An example of CHESPA analysis, where the DRM-induced perturbations lead to complex dynamics and sampling of a conformational manifold. The red highlights in the cos(θ) plot indicate residues that are within 15 Å of the mutation site. The red box highlights lid residues with significantly negative *X* values, indicating a significant shift toward the inactive state. Figure adapted from Ref.(56). Copyright 2017 the American Society for Biochemistry and Molecular Biology.

1.4.3.1 Analysis of CHESPA data

The fractional shift, *X*, and the angle between vector A and B, θ, usually reported as cos(θ), are computed for each residue to create a map of the perturbations caused by a mutation. The cos(θ) reports on the direction of the equilibrium shift. For residues with $|\cos(\theta)| \sim 1$, vectors A and B are approximately co-linear, as expected for a two-state equilibrium in the fast exchange regime. For these residues, the *X* value provides a direct gauge of the conformational shift induced by the perturbation (*i.e*. mutation or ligand modification). A positive *X* value suggests the mutation shifts the equilibrium to an active state, whereas a negative *X* value suggests a shift of the equilibrium to an inactive or less active state, provided vectors A and B are defined similarly to Fig. 4A. However, the meaning of *X* and cos(θ) may vary depending on how vectors A and B are defined and how vector A is projected onto vector B. For residues with $|\cos(\theta)|$ significantly <1 (e.g. typically $|\cos(\theta)| < 0.90–0.95$), vectors A and B are not co-linear, an indication of "outliers" that deviate from the two-state active-inactive conformational equilibrium. Examples of such outliers include residues that are sufficiently close in space to ligand binding pockets or mutation sites that are perturbed through near-neighbour effects (NNEs). In the absence of NNEs, a perturbation that causes a shift in a two-state conformational equilibrium, will skew the distribution of $|\cos(\theta)|$ values towards unity and the *X* values for all the residues will be similar in magnitude. In the presence of NNEs, the distribution of both $|\cos(\theta)|$ and *X* will be less homogenous and selected residues will exhibit $|\cos(\theta)| < 1$, with the *X* values not necessarily reflecting the degree of conformational shift for all residues.

Another interesting scenario occurs when DRMs introduce not only NNEs, but also a shift from two- to three-state conformational exchange. For example, if DRMs or other perturbations result in a distinct third conformer in fast exchange with the two states that recapitulate the conformational equilibrium of the WT or unperturbed protein, a dual pattern of fractional activations is often observed. For example, residues with $|\cos(\theta)| \sim 1$ may cluster into two regions with different *X* values. The *X* values within each region are quite homogenous compared to the difference between the *X* values in the two regions. Residues with $|\cos(\theta)| < 1$ may include not only sites subject to NNEs, but also residues at the interface between the two regions exhibiting different *X* values. These interface residues sense the three-state conformational exchange, which causes deviations from linearity. This was the pattern observed by VanSchouwen *et al.* (81) when the cNMP-binding domain B (CBD-B) of PKGIb was perturbed by replacing the primary

allosteric effector, cGMP, with its partial agonist, cAMP. The dual CHESPA pattern observed for the ternary apo *vs.* cGMP *vs.* cAMP comparative analyses of PKGIb (Fig. 4B) revealed that cAMP partially stabilizes a third state that is distinct from the two states populated by the apo and cGMP-bound PKGIb, yet it includes elements of both conformers into a single state. The 'mixed' third state helped rationalize the partial agonism of cAMP. Furthermore, the CHESPA *X* values were used to compute the populations of the three conformers accessed by cAMP-bound PKGIb CBD-B. This example illustrates the effectiveness of CHESPA in identifying three-state fast exchanging equilibria and in elucidating the mechanism of action of partial agonists, and possibly DRMs.

Occasionally, two or three-state equilibria and NNEs alone may not be sufficient to rationalize the observed CHESPA patterns. For example, when the *X* distribution is highly scattered, e.g. significant residue-specific variations in *X* values are observed in more than two regions of the protein and several residues exhibit $|\cos(\theta)| < 1$, it is likely that complex dynamics are induced by the perturbation and a manifold (>3) of conformers is being sampled with multiple regions undergoing at least partial disengagement from the native fold. This was observed by Boulton *et al.* for the HCN4 mutation, S672R, which causes familial sinus bradycardia (56). This mutation, which is located in the cAMP-binding domain (CBD) of the intracellular region (IR) of HCN4, causes abnormally low resting heart rates and more negative activation voltages than WT in either the absence or the presence of cAMP, indicating a loss-of-function phenotype (84–88). However, the crystal structure of the cAMP-bound S672R IR tetramer does not show major structural changes compared to the WT (89–91) Hence, CHESPA was performed as a first step to understand how the mutation causes the loss-of-function phenotype, and thus to test the hypothesis that S672R either causes partial reversal of the two-state equilibrium toward the inactive conformation or gives rise to additional states that are not fully active nor fully inactive (56).

The CHESPA analysis of holo (*i.e.* cAMP-bound)-S672R showed that the mutation shifts the equilibrium toward a less activated state, indicated by $\cos(\theta)$ values of ~ -1 and negative *X* values for the majority of residues (Fig. 4C). However, residue-specific variations in *X* values indicated that this reversal in equilibrium did not completely follow the two-state equilibrium and pointed to a partially de-correlated state. For example, the C-terminal lid region showed *X* values ranging from 0.2 to 1, while the N-terminal motif, known as N3A, showed *X* values close

to 0.1. These regions are distant from the mutation site and are not directly involved in binding cAMP and thus report only on the position of the conformational equilibrium. This partial de-correlation is also reflected by several residues exhibiting |cos(θ)| <1 in the holo-S672R CHESPA. In the case of the apo-S672R CHESPA, a distinct active- or inactive-skewed pattern was not observed, *i.e.* cos(θ) and *X* values are quite homogeneously scattered from 1 to −1, suggesting that the mutation-induced perturbations in apo HCN4 cause extensive de-correlated deviations from the two-state equilibrium and possibly lead to enhanced dynamics. This was independently confirmed through additional NMR experiments, such as ^{15}N-relaxation and cAMP-binding kinetics, as discussed below in Sections 1.4.4 and 1.4.5.

1.4.3.2 Troubleshooting CHESPA

Critical parameters for a reliable CHESPA analysis include the cut-off threshold values for both the reference vector (|B|) and the mutant *versus* WT CCS (|A|) (Fig. 2A). Since |B| is used to normalize the *X* values, as a per Eqs. (1), (2), and a small value of |B| will amplify experimental errors. For this reason, it is advisable that the |B| cut-off value be large enough to minimize amplification of such errors, possibly leading to false positives, but not too large to the extent where informative *X* values, that may report on functionally relevant conformational shifts, are lost, resulting in false negatives. With an excessively low |B| cut-off, a nearly random distribution of *X* and cos(θ) values may prevail and meaningful patterns or distributions may become hidden, making it difficult to analyze the CHESPA data. With an excessively high |B| cut-off, the *X* and cos(θ) values for potentially revealing residues will be filtered out and lead to an incomplete and partial CHESPA analysis.

The |A| cut-off value is also important for minimizing errors in the *X* values and especially, the cos(θ) values, since |A| appears in the denominator of the cos(θ) Eq. (2). Previous studies have shown that using residues with |B| and |A| >0.05 ppm provided reliable CHESPA results (56, 79–81). However, it is a good practice to optimize these parameters for a specific system by testing multiple cut-off threshold values, when analyzing a given chemical shift data set. For our systems, cut-off values typically fall in the 0.03–0.10 ppm range, but a broader window may be required for other applications depending on the precision and accuracy of chemical shift measurements, which is related to the linewidths and therefore to the size of the system and the extent of intermediate chemical exchange. Setting the optimal cut-off values will filter out *X*

values that are largely affected by errors, while keeping meaningful *X* values for informative residues, thus achieving a viable compromise between false negatives and positives. In addition, if the purpose of the chemical shift analysis is to find residues that report primarily on two-state fast exchanging conformational equilibria, it is advisable to impose stringent cut-off thresholds directly on the $|\cos(\theta)|$ values as well (*i.e.* values ~1) (62).

Another aspect to consider when troubleshooting CHESPA data, is that CHESPA offers only an initial assessment of the multiple perturbations caused by a mutation (*e.g.* distortions or NNEs vs. shifts in the conformational equilibrium of a protein). However, it is possible to further separate the NNEs from conformational equilibrium changes using the CHEmical Shift Covariance Analysis (CHESCA) approach. CHESCA relies on a targeted library of functionally characterized perturbations, such as a series of mutations as opposed to only a single mutant, and therefore goes beyond the simple ternary comparisons at the basis of CHESPA (61, 78, 92, 93). CHESCA allows for the identification of correlated residues in a functionally relevant allosteric network through perturbations from mutations or chemically modified ligand effectors. The distinct perturbations within a CHESCA set are typically selected to lock the active *vs.* inactive conformational equilibrium at different positions, as confirmed by functional assays. Sampling intermediate degrees of activation between the fully inactive and active extremes is essential to dissect the allosteric networks linked to activation. Residue pairs that belong to the same allosteric network give rise to perturbation-dependent chemical shift changes that are linearly correlated, even when the magnitudes of these changes are different (Fig. 5A). This allows for identifying correlations between residues that are undergoing conformational changes with major chemical shift variations and residues undergoing dynamical changes rather than major structural changes. The residues in the latter case thus exhibit only minor, yet still significant, chemical shift variations. This means that the CHESCA analysis is able to detect subtle conformational/dynamical changes that are possibly relevant for allosteric signal propagation and are often elusive to commonly used structure determination methods.

Once the correlated residues are identified, they are partitioned into groups of coupled residues or "clusters" (Fig. 5B). Each cluster is a network of residues that exhibit a similar response to the common set of perturbations and are responsible for a specific functional role, such as allosteric contribution or effector binding. Such roles are assigned to each identified cluster through a transposed agglomerative clustering analysis or singular value decomposition (SVD).

Since CHESCA extensively relies on linear correlations and is based on four or more states to identify such correlations, as opposed to the ternary comparative analysis typical of CHESPA, it serves as an excellent complementary method to elucidate the network of residues that sense the position of the active/inactive equilibrium and are minimally perturbed by NNEs arising from the mutation. For example, CHESCA analyses for a series of mutations utilized as perturbation sets have been performed by Axe *et al.* to study the amino acid networks that regulate the catalytic cycle of tryptophan synthase (67, 94). In addition, comparative wt *vs.* mutant CHESCA analyses are an effective means to reveal allosteric sub-clusters perturbed by DRMs.

Similarly, to CHESPA, meaningful CHESCA results rely on careful choices of the CCS cut-off values, to ensure that the smallest chemical shift changes across the CHESCA perturbation set are only minimally affected by experimental errors. In addition, both CHESPA and CHESCA assume fast exchange between active and inactive conformations. When this assumption fails, alternative methods should be utilized to probe the thermodynamics and kinetics of conformational transitions, such as NMR dispersion (NMRD) in the case of intermediate exchange (95) and Nz-exchange or CEST in the case of slow exchange (59, 96–100). Another complementary method to evaluate long-range allosteric effects of DRMs relies on double-mutant cycles monitored through global unfolding analyses, such as chemical unfolding monitored by fluorescence and/or thermal unfolding monitored by H/D exchange (101, 102). Often these methods are applicable to high molecular weight (MW) proteins that are not easily accessible to NMR and therefore they provide an opportunity to validate in full-length integral proteins the results obtained by NMR on truncated constructs.

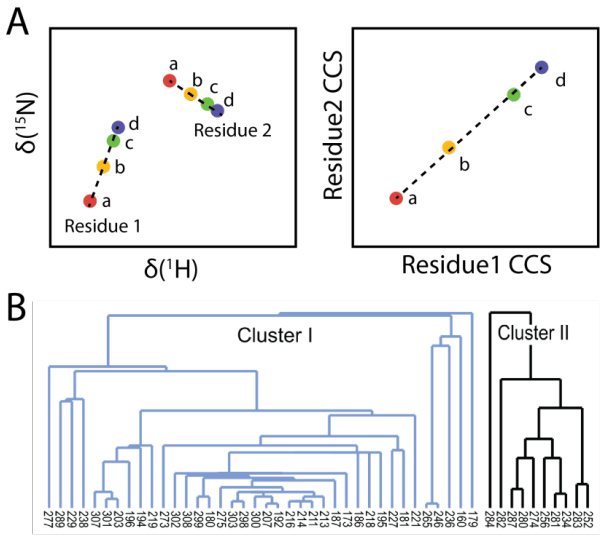

Figure 5. *Mapping mutation-induced perturbations through CHESCA.* (A) Two representative residues exhibiting a concerted response to a common perturbation set (a–d), such as a set of mutations or chemically modified ligand effectors (left), resulting in a linearly correlated pairwise inter-residue plot (right). The two axis report chemical shift changes. (B) An example of a dendrogram generated from agglomerative clustering. The horizontal lines indicate the linked residues, while the vertical axis reports on the magnitude of the correlation coefficient. Figure adapted from Ref. (78). Copyright 2011 National Academy of Sciences.

1.4.4 NMR spin relaxation measurements

Chemical shift changes probing the position of the conformational equilibria and allosteric networks might not be sufficient alone to fully capture all the FEL perturbations induced by a DRM. Local enhancement or quenching of dynamics also plays a significant role in explaining how a mutation alters protein function and thus leads to a disease phenotype. A wide array of advanced NMR spin relaxation methods is available to probe protein dynamics at atomic resolution and these experiments have been already extensively reviewed elsewhere (103–106). Even the simplest NMR relaxation experiments, *i.e.* T_1, T_2, and HN-NOE measurements, have proven to be extremely useful in monitoring changes of picosecond to nanosecond and microsecond to millisecond dynamics induced by disease-related mutations (56, 74–76, 107–109). Variations in dynamics within these time scales are effective means to evaluate long-range perturbations, possibly reaching functional regions of the protein or distant allosteric loci, even in the absence of resolvable structural changes. For example, in the Exchange Protein directly

activated by cAMP (EPAC), long-range enhancements of dynamics generate an entropic penalty that weakens inhibitory interactions (110).

Comparative NMR spin relaxation analyses serve also as an excellent complementary method to confirm hypotheses generated based on CHESPA about DRM-induced de-correlations, *e.g.* deviations from the two-state active *vs.* inactive equilibrium. For example, for both the cAMP-binding domain of WT and of the bradycardia-related S672R mutant of HCN4 the ^{15}N T_1, T_2, and HN-NOE observables were converted into reduced spectral densities, which were then utilized to estimate order parameters (S^2) (56). The latter quantify the amplitude of ps-ns dynamics and offer a valuable proxy of conformational entropy (111, 112), which is related to the width of the free energy wells in the FEL. Therefore, the differences in the distribution of the overall S^2 order parameters between the WT and the mutant reveal the effect of the mutation on the width of the main free energy well for either the apo or holo sample. Such width changes provide a basis for proposing hypotheses on how DRM modify the apo-to-holo free energy barrier. These hypotheses can be further confirmed through measurement of effector-binding kinetics, as discussed below. For instance, the apo state of the S672R mutant of HCN4 exhibited a redistribution of the S^2 order parameters towards lower values compared to the apo WT (Fig. 6A), whereas WT holo and mutant holo do not reveal such significant shift (Fig. 6B) (56). The redistribution observed for the apo states points to an increased amplitude in the ps-ns motions and thus to the widening of the free energy well of the apo S672R *vs.* WT (Fig. 6C). The broadening of the main apo free energy well suggests that the mutation shifts the equilibrium of the apo state to an inactive state not through a simple two-state exchange, but rather through a more complex mechanism involving partial de-correlation, which is consistent with the CHESPA analysis. The widening of the FEL well also suggests lowering of the free energy barrier for the apo-holo exchange, which was further confirmed through measurements of the cAMP binding kinetics (discussed in Section 1.4.5.2).

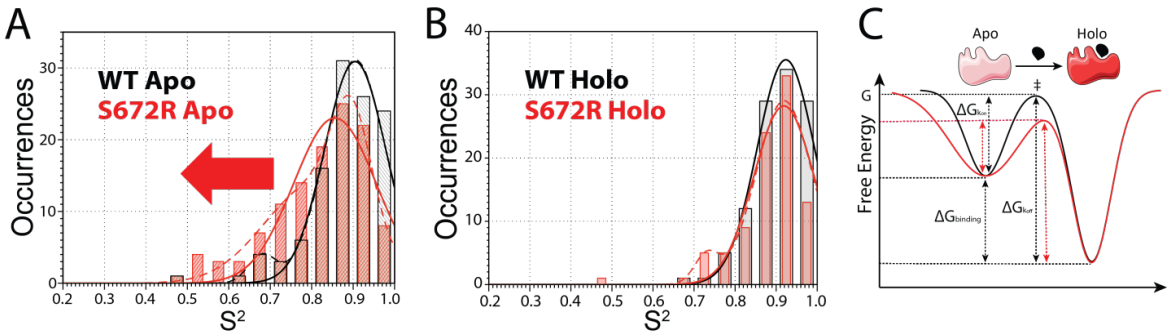

Figure 6. *Probing changes in the width of the free energy landscape of allosteric regulation through measurement of net shifts in S^2 order parameters extracted from NMR spin relaxation experiments.* (A) S^2 order parameter distribution of WT and mutant apo, showing a net shift of order parameters to lower values. (B) Comparison of WT holo and mutant holo does not reveal a significant shift. (C) The net shift in S^2 order parameter distribution points to broadening of the free energy well of the apo conformation of the mutant (red) compared to the WT (black). Figures adapted from Ref. (56). Copyright 2017 the American Society for Biochemistry and Molecular Biology.

1.4.4.1 Troubleshooting relaxation measurement experiments

Mutation-induced perturbations may cause partial protein unfolding, exposing hydrophobic sites and resulting in aggregation. Aggregates may in turn lead to inaccurate measurements of T_2 times, which are highly sensitive to the effective MW. A useful means to identify systematic aggregation-induced errors in the measured T_2 values relies on HYDRONMR (113). HYDRONMR predicts the T_2 values based on the protein structure and thus if the sample undergoes aggregation or if multimerization of the solved structure occurs, the T_2 values will be systematically lower than the values predicted by HYDRONMR. Another method to confirm the accuracy of T_2 measurements is to perform a dilution control. If dilution reduces formation of aggregates, the T_2 relaxation times will increase as the sample is diluted.

1.4.5 Measurements of effector binding dynamics

The previous sections focused on how to probe the relative inactive *vs*. active depths and widths for the free energy wells in either apo or holo samples. However, a thorough map of the DRM-modified free energy landscape requires also a determination of the relative apo *vs.* holo free energy well depths (*i.e.* measurement of thermodynamic binding constants) as well as an assessment of the free energy barrier between the apo and holo states (*i.e.* measurement of kinetic binding constants).

1.4.5.1 Measurement and interpretation of thermodynamic constants for ligand-effector binding

An important step to understand an observed physiological phenotype of a DRM is to investigate how it influences the affinity for a cognate ligand-effector. For example, a simple explanation for a loss-of-function phenotype mutation is that the DRM weakens the interactions between the receptor and the ligand-effector responsible for activation, resulting in an increase in dissociation constants (K_d). While a wide array of techniques are available for measuring K_d values, here we focus primarily on NMR methods. In particular, we discuss both ligand-based methods, such as Saturation Transfer Difference (STD) experiments (114–120), and protein-based approaches, such as HSQC-monitored titrations (77). In either case, it is critical that the total protein concentration be <10 K_d to ensure a gradual transition between the initial binding region and the final saturation plateau of the dose-response binding isotherm. Such gradual transition is essential to enhance the precision and accuracy of the K_d measurement. Hence, HSQC-monitored titrations are usually suitable to measure K_d values in the high µM–mM range. For K_d values in this range, the corresponding k_{off} are often sufficiently high to ensure a fast apo-holo exchange at least for cross-peaks subject to minimal, yet still significant, chemical shift changes upon ligand-effector binding and especially in the presence of large excess of free ligand. In these cases, the fast apo-holo exchange ensures that the peak position (*i.e.* the chemical shifts) is a population weighted average of the apo and holo states, which reports on the position of the binding equilibrium. This allows for accurate quantification of the fraction of bound protein through measuring the chemical shift changes at increasing ligand-effector concentrations (77). The STD, on the other hand, looks at the ligand signal to measure the extent of interaction with the protein (114–120). The protein signal is selectively saturated and this saturation is transferred to the interacting ligand through the nuclear Overhauser effect. This transfer of saturation is measured through the intensity measurement of the ligand signal, which correlates with the extent of binding. The applications of STD in biological systems and for quantitative measurement of protein-ligand interaction have been reviewed in depth elsewhere (121–124). The STD experiments can be used to measure K_d values in the ~µM–mM range. However, it is important to note that the efficiency of the saturation transfer, and hence the STD signal, decreases as the K_d values approach the nM range. In this case, a competitive

binding STD experiment is recommended, whereby a protein is pre-loaded with an excess amount of a weaker binding ligand for the same binding site where the high affinity ligand binds. The excess of competitive ligand is used to modulate the effective apparent K_d for the ligand of interest and bring it within a range suitable for STD applications (62, 125). Alternatively, K_d values can also be obtained by measuring apo *vs*. holo global unfolding free energies as computed, for example, based on maximal protection factors from H/D exchange NMR (61, 83, 126–128).

The measurement of K_d values serves as an initial assessment of the DRM-induced changes. It is also possible to extend the analysis further and determine which factors cause the DRM-induced variations in the K_d values. For example, the DRM may perturb non-covalent interactions between the ligand and the protein that directly alter its affinity. However, K_d changes may also arise from a shift in the position of the active-inactive equilibrium in the apo state. This is because the observed association constant is a population weighted average of the state specific association constants. As the populations of the conformational equilibrium change, the weighting on the state specific association constants will modify the observed average affinity. For example, when the ligand is known to exhibit a higher affinity for the active *vs*. inactive state, a DRM-induced shift of the apo inhibitory equilibrium towards the inactive state will increase the observed K_d value compared to WT. The effect of DRMs on the apo active-inactive fast-exchanging equilibrium can be assessed through CHESPA, providing valuable insight on how DRMs modulate ligand affinities.

1.4.5.2 Measurement and interpretation of kinetic constants for ligand-effector binding

It is possible that DRM-induced changes in affinities, as quantified by the K_d thermodynamics constants, are necessary but not sufficient to fully explain the underlying molecular mechanism of mutation-induced perturbations. For example, the kinetics of HCN channel closing is controlled by cAMP binding and the S672R HCN4 bradycardia mutation is known to accelerate channel deactivation. Boulton *et al.* observed that the S672R HCN4 mutant exhibited similar K_d values for cAMP as WT HCN4 (56). Nevertheless, they were able to explain the faster S672R *vs.* WT channel deactivation by measuring the kinetic rate constants (*i.e.* k_{off} and k_{on}). The DRM *vs.* WT comparison of kinetic rate constants revealed that the DRM reduced the free energy barrier for the apo-holo exchange and led to an accelerated on/off cAMP exchange, thus explaining, at least in part, the faster deactivation of HCN caused by the mutation.

An effective means to measure on/off rate constants is the Nz-exchange experiment (99, 100). In the presence of sub-stoichiometric ratios of a ligand, residues that undergo slow exchange give rise to distinct apo and holo HSQC cross-peaks. The Nz-exchange method is ideally suited for systems with relatively low on/off exchange rates (k_{ex} <100 s^{-1}) (129). This means that for systems with high on/off exchange rates, a low ligand concentration is required to observe a slow-exchange regime (Eq. (1)), which results in a weak holo peak, limiting the ability to use the Nz-exchange experiment to quantify on/off rate constants.

$$k_{ex} = [\text{Ligand}]_{free} \cdot k_{on} + k_{off} \quad (1)$$

In such cases, a less quantitative approach can be taken, whereby chemical exchange regimes in HSQC spectra are compared between the WT and the mutant (56). This approach takes advantage of the fact that different exchange regimes are observed for different residues depending on the differences in Hz between the apo and the holo resonance frequencies ($\Delta\nu_{A-H}$) at a specific k_{ex} value. When $k_{ex} << \Delta\nu_{A-H}$, the peak for this residue will appear in the slow exchange regime (Fig. 7A). When $k_{ex} \approx \Delta\nu_{A-H}$, the residue will be in the intermediate exchange regime. When $k_{ex} >> \Delta\nu_{A-H}$, the residue will appear in the fast exchange regime. By assessing the chemical exchange regimes for each amino acid and sorting them in a decreasing order of $\Delta\nu_{A-H}$ values, a qualitative comparison of kex values for WT *vs.* the mutant is possible. For example, this simple HSQC analysis was performed with the S672R mutant of HCN (56). The $\Delta\nu_{A-H}$ values were plotted sorted in decreasing order for both WT and the S672R mutant and the $\Delta\nu_{A-H}$ range exhibiting intermediate regimes were defined and compared (Fig. 7B and C). For the S672R mutant, the intermediate regime was observed at higher $\Delta\nu_{A-H}$ values than for WT, suggesting that the k_{ex} is significantly faster for the mutant *vs.* the WT. Alternatively, more quantitative protein-based NMR approaches are available to measure the on-off exchange kinetics of binding, such as CEST or NMRD, even when the minor state is not directly detectable in HSQC or TROSY spectra (95–99).

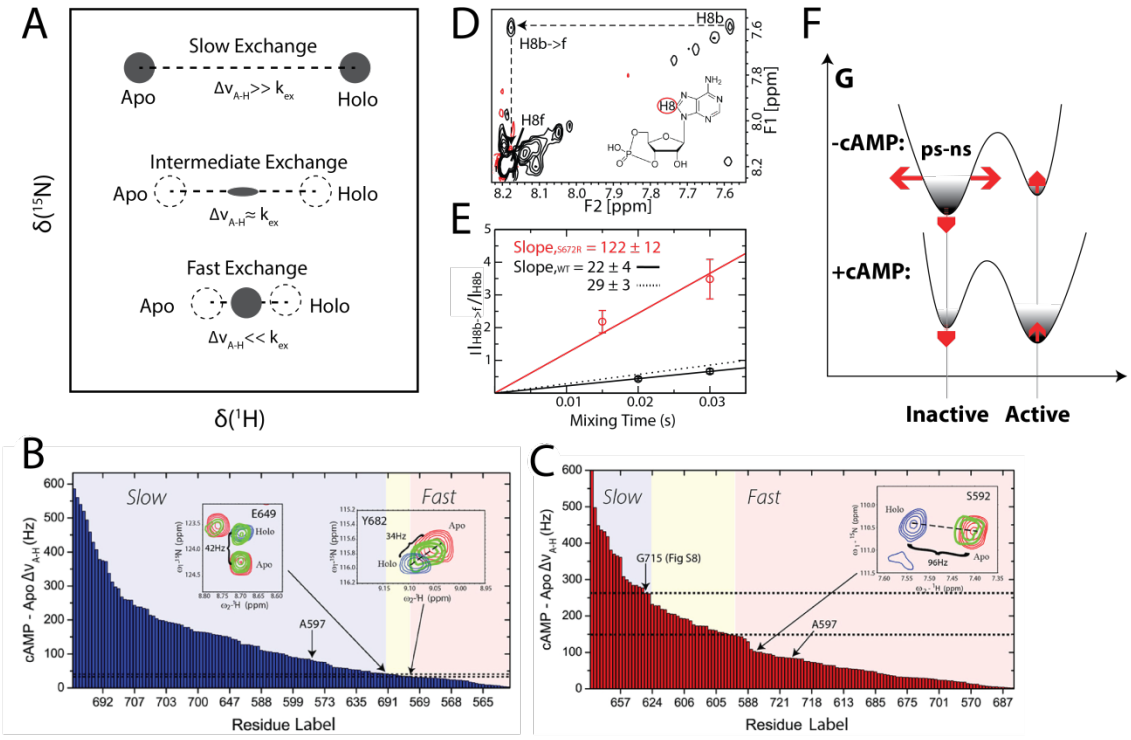

Figure 7. *Protein- and ligand-based analyses of on-off chemical exchange regimes for assessing kinetic rate constants.* (A) Schematic illustration of different chemical exchange regime between apo and holo states and the rationale for the comparison of k_{ex} and the differences in Hz between the apo and the holo resonance frequencies ($\Delta\nu_{A-H}$). (B, C) The sorted $\Delta\nu_{A-H}$ vs. residue label plot for WT (B) and the S672R mutant of HCN4 (C). The chemical exchange regime is assessed for each residue and reported on the sorted $\Delta\nu_{A-H}$ plot. The dashed lines indicated the $\Delta\nu_{A-H}$ range corresponding to the intermediate regime. (D) ROESY spectra of the ligand-effector (cAMP) in the presence of protein (HCN4). Diagonal peaks indicate the H8 of cAMP in either the bound (H8b) or the free (H8f) states. The cross-peak arising from the chemical exchange between the bound and free state is indicated by H8b->f. (E) The cross-peak *vs.* diagonal bound peak intensity ratio plotted against the ROESY mixing time. The initial slopes (s^{-1}) are indicated in the figure. (F) Schematic summary of the S672R-induced remodelling of the free energy landscape (red arrows) for the HCN4 cAMP-binding domain, which provides a basis for understanding the molecular mechanism of familial bradycardia. The horizontal arrows represent the enhanced conformational entropy of the inactive state. The vertical arrows indicate that the S672R mutation shifts the inhibitory equilibrium by destabilizing the active state and/or stabilizing the inactive state. Figures adapted from Ref. (56). Copyright 2017 the American Society for Biochemistry and Molecular Biology.

The protein-NMR based methods to quantify on/off kinetic rates can be complemented by ligand-based NMR experiments, such as ROESY, which provide an independent assessment of the on/off exchange rates (56, 130). With ligand-based NMR experiments, Eq. (1) is modified to:

$$k_{ex} = [Protein]_{free} \cdot k_{on} + k_{off} \quad (2)$$

Eq. (2) implies that, when ROESY spectra are acquired with excess ligand, slow exchange is observed between the free and bound ligand peaks, even when fast exchange is detected between the free and bound protein peaks under the same experimental conditions. The slow exchange between the free and bound ligand peaks allows for the detection of ROESY cross-peaks separated from the diagonal and with the same sign as the diagonal peaks (Fig. 5D). The intensity of the ROESY cross-peak arising from the chemical exchange from bound to free state is typically measured at different ROESY mixing times. The cross-peak *vs.* diagonal bound peak intensity ratio is then plotted against the ROESY mixing time and the off-exchange rate is extracted from the initial slope (Fig. 5E).

1.4.6 Conclusions

Remodelling of the FEL for allosteric regulation is one of the main mechanisms through which DRMs lead to altered functional phenotypes and NMR is ideally suited to elucidate how DRMs remodel the FEL at near-atomic resolution. Specifically, the NMR CHESPA and CHESCA analyses enable the measurements of the relative populations of fast exchanging conformational states and therefore report on DRM-induced changes in the relative depth of the respective free energy wells. Furthermore, CHESPA is also useful to identify deviations from two-state transitions and de-correlations that can be independently confirmed through measurements of local ps-ns dynamics using spin relaxation measurements. The latter provide the S^2 order parameters, which in turn report on the width of the free energy well. Changes in the width of the free energy well may point to modulations of free energy barriers, which can be assessed independently through kinetic binding measurements (*i.e.* k_{off}, k_{on}). The latter rely on ligand-based NMR experiments, such as ROESY, and/or protein-based experiments, such as Nz exchange and CEST or simply comparisons of chemical exchange regimes in the HSQC

spectra of WT and mutant proteins. Last but not least, affinity measurements (K_d) are necessary to complete the assessment of the apo *vs.* holo free energy changes. In conclusion, the NMR methods discussed here provide a thorough picture of the multiple concurrent perturbations induced by DRMs on different FEL attributes (Figs. 6C and 7F), which is a necessary step towards dissecting the molecular mechanisms underlying the pathological phenotypes of DRMs and disease etiology.

1.5 References

1. Rauch, J., Volinsky, N., Romano, D., and Kolch, W. (2011) The secret life of kinases: functions beyond catalysis. *Cell Commun. Signal.* **9**, 23
2. Zhang, J., Yang, P. L., and Gray, N. S. (2009) Targeting cancer with small molecule kinase inhibitors. *Nat. Rev. Cancer*. **9**, 28–39
3. Paul, M. K., and Mukhopadhyay, A. K. (2004) Tyrosine kinase – Role and significance in Cancer. *Int. J. Med. Sci.* 10.7150/ijms.1.101
4. Beristain, A. G., Molyneux, S. D., Joshi, P. A., Pomroy, N. C., Di Grappa, M. A., Chang, M. C., Kirschner, L. S., Privé, G. G., Pujana, M. A., and Khokha, R. (2015) PKA signaling drives mammary tumorigenesis through Src. *Oncogene*. **34**, 1160–1173
5. Saloustros, E., Salpea, P., Starost, M., Liu, S., Faucz, F. R., London, E., Szarek, E., Song, W.-J., Hussain, M., and Stratakis, C. A. (2017) Prkar1a gene knockout in the pancreas leads to neuroendocrine tumorigenesis. *Endocr. Relat. Cancer*. **24**, 31–40
6. Bhullar, K. S., Lagarón, N. O., McGowan, E. M., Parmar, I., Jha, A., Hubbard, B. P., and Rupasinghe, H. P. V. (2018) Kinase-targeted cancer therapies: progress, challenges and future directions. *Mol. Cancer*. **17**, 48
7. Mueller, B. K., Mack, H., and Teusch, N. (2005) Rho kinase, a promising drug target for neurological disorders. *Nat. Rev. Drug Discov.* **4**, 387–398
8. Alessi, D. R., and Sammler, E. (2018) LRRK2 kinase in Parkinson's disease. *Science (80-.).* **360**, 36–37
9. Cohen, P. (2014) Immune diseases caused by mutations in kinases and components of the ubiquitin system. *Nat. Immunol.* **15**, 521–529
10. Szilveszter, K. P., Németh, T., and Mócsai, A. (2019) Tyrosine Kinases in Autoimmune and Inflammatory Skin Diseases. *Front. Immunol.* 10.3389/fimmu.2019.01862
11. Patterson, H., Nibbs, R., McInnes, I., and Siebert, S. (2014) Protein kinase inhibitors in the treatment of inflammatory and autoimmune diseases. *Clin. Exp. Immunol.* **176**, 1–10
12. Alam, M. M., Solyakov, L., Bottrill, A. R., Flueck, C., Siddiqui, F. A., Singh, S., Mistry, S., Viskaduraki, M., Lee, K., Hopp, C. S., Chitnis, C. E., Doerig, C., Moon, R. W., Green, J. L., Holder, A. A., Baker, D. A., and Tobin, A. B. (2015) Phosphoproteomics reveals malaria parasite Protein Kinase G as a signalling hub regulating egress and invasion. *Nat. Commun.* **6**, 7285
13. Mondal, A., Dawson, A. R., Potts, G. K., Freiberger, E. C., Baker, S. F., Moser, L. A., Bernard, K. A., Coon, J. J., and Mehle, A. (2017) Influenza virus recruits host protein kinase C to control assembly and activity of its replication machinery. *Elife*. 10.7554/eLife.26910
14. Kang, Y.-L., Chou, Y., Rothlauf, P. W., Liu, Z., Soh, T. K., Cureton, D., Case, J. B., Chen, R. E., Diamond, M. S., Whelan, S. P. J., and Kirchhausen, T. (2020) Inhibition of PIKfyve kinase prevents infection by Zaire ebolavirus and SARS-CoV-2. *Proc. Natl. Acad. Sci.* **117**, 20803–20813
15. Linglart, A., Menguy, C., Couvineau, A., Auzan, C., Gunes, Y., Cancel, M., Motte, E., Pinto, G., Chanson, P., Bougnères, P., Clauser, E., and Silve, C. (2011) Recurrent PRKAR1A mutation in acrodysostosis with hormone resistance. *N. Engl. J. Med.* **364**, 2218–26
16. McDonell, L. M., Kernohan, K. D., Boycott, K. M., and Sawyer, S. L. (2015) Receptor tyrosine kinase mutations in developmental syndromes and cancer: two sides of the same coin. *Hum. Mol. Genet.* **24**, R60–R66
17. Manning, G. (2002) The Protein Kinase Complement of the Human Genome. *Science*

(80-.). **298**, 1912–1934
18. Cohen, P. (2002) Protein kinases — the major drug targets of the twenty-first century? *Nat. Rev. Drug Discov.* **1**, 309–315
19. Palorini, R., Votta, G., Pirola, Y., De Vitto, H., De Palma, S., Airoldi, C., Vasso, M., Ricciardiello, F., Lombardi, P. P., Cirulli, C., Rizzi, R., Nicotra, F., Hiller, K., Gelfi, C., Alberghina, L., and Chiaradonna, F. (2016) Protein Kinase A Activation Promotes Cancer Cell Resistance to Glucose Starvation and Anoikis. *PLOS Genet.* **12**, e1005931
20. Molyneux, S. D., Di Grappa, M. A., Beristain, A. G., McKee, T. D., Wai, D. H., Paderova, J., Kashyap, M., Hu, P., Maiuri, T., Narala, S. R., Stambolic, V., Squire, J., Penninger, J., Sanchez, O., Triche, T. J., Wood, G. A., Kirschner, L. S., and Khokha, R. (2010) Prkar1a is an osteosarcoma tumor suppressor that defines a molecular subclass in mice. *J. Clin. Invest.* **120**, 3310–3325
21. Diaz, C. A., Allocco, J., Powles, M. A., Yeung, L., Donald, R. G. K., Anderson, J. W., and Liberator, P. A. (2006) Characterization of Plasmodium falciparum cGMP-dependent protein kinase (PfPKG): Antiparasitic activity of a PKG inhibitor☆. *Mol. Biochem. Parasitol.* **146**, 78–88
22. Taylor, H. M., McRobert, L., Grainger, M., Sicard, A., Dluzewski, A. R., Hopp, C. S., Holder, A. A., and Baker, D. A. (2010) The Malaria Parasite Cyclic GMP-Dependent Protein Kinase Plays a Central Role in Blood-Stage Schizogony. *Eukaryot. Cell*. **9**, 37–45
23. Kim, J. J., Flueck, C., Franz, E., Sanabria-Figueroa, E., Thompson, E., Lorenz, R., Bertinetti, D., Baker, D. A., Herberg, F. W., and Kim, C. (2015) Crystal Structures of the Carboxyl cGMP Binding Domain of the Plasmodium falciparum cGMP-dependent Protein Kinase Reveal a Novel Capping Triad Crucial for Merozoite Egress. *PLOS Pathog.* **11**, e1004639
24. Berman, H. M., Ten Eyck, L. F., Goodsell, D. S., Haste, N. M., Kornev, A., and Taylor, S. S. (2005) The cAMP binding domain: An ancient signaling module. *Proc. Natl. Acad. Sci.* **102**, 45–50
25. Taylor, S. S., and Kornev, A. P. (2011) Protein kinases: evolution of dynamic regulatory proteins. *Trends Biochem. Sci.* **36**, 65–77
26. Serezani, C. H., Ballinger, M. N., Aronoff, D. M., and Peters-Golden, M. (2008) Cyclic AMP: master regulator of innate immune cell function. *Am. J. Respir. Cell Mol. Biol.* **39**, 127–132
27. Stork, P. J. ., and Schmitt, J. M. (2002) Crosstalk between cAMP and MAP kinase signaling in the regulation of cell proliferation. *Trends Cell Biol.* **12**, 258–266
28. ALBERINI, C. M., GHIRARDI, M., HUANG, Y.-Y., NGUYEN, P. V., and KANDEL, E. R. (1995) A Molecular Switch for the Consolidation of Long-Term Memory: cAMP-Inducible Gene Expression. *Ann. N. Y. Acad. Sci.* **758**, 261–286
29. Taylor, S. S., Ilouz, R., Zhang, P., and Kornev, A. P. (2012) Assembly of allosteric macromolecular switches: lessons from PKA. *Nat. Rev. Mol. Cell Biol.* **13**, 646–658
30. Kim, C., Cheng, C. Y., Saldanha, S. A., and Taylor, S. S. (2007) PKA-I holoenzyme structure reveals a mechanism for cAMP-dependent activation. *Cell*. **130**, 1032–43
31. Huang, L. J., and Taylor, S. S. (1998) Dissecting cAMP Binding Domain A in the R I α Subunit of cAMP-dependent Protein Kinase. *J. Biol. Chem.* **273**, 26739–26746
32. Wilson, G. R., Cramer, A., Welman, A., Knox, F., Swindell, R., Kawakatsu, H., Clarke, R. B., Dive, C., and Bundred, N. J. (2006) Activated c-SRC in ductal carcinoma in situ correlates with high tumour grade, high proliferation and HER2 positivity. *Br. J. Cancer*. **95**, 1410–1414
33. Elsberger, B., Tan, B. A., Mitchell, T. J., Brown, S. B. F., Mallon, E. A., Tovey, S. M., Cooke, T.

G., Brunton, V. G., and Edwards, J. (2009) Is Expression or Activation of Src Kinase Associated with Cancer-Specific Survival in ER-, PR- and HER2-Negative Breast Cancer Patients? *Am. J. Pathol.* **175**, 1389–1397

34. Kim, C., Xuong, N.-H., and Taylor, S. S. (2005) Crystal structure of a complex between the catalytic and regulatory (RIalpha) subunits of PKA. *Science*. **307**, 690–6
35. Hopp, C. S., Bowyer, P. W., and Baker, D. A. (2012) The role of cGMP signalling in regulating life cycle progression of Plasmodium. *Microbes Infect.* **14**, 831–837
36. Moon, R. W., Taylor, C. J., Bex, C., Schepers, R., Goulding, D., Janse, C. J., Waters, A. P., Baker, D. A., and Billker, O. (2009) A Cyclic GMP Signalling Module That Regulates Gliding Motility in a Malaria Parasite. *PLoS Pathog.* **5**, e1000599
37. McRobert, L., Taylor, C. J., Deng, W., Fivelman, Q. L., Cummings, R. M., Polley, S. D., Billker, O., and Baker, D. A. (2008) Gametogenesis in Malaria Parasites Is Mediated by the cGMP-Dependent Protein Kinase. *PLoS Biol.* **6**, e139
38. Govindasamy, K., Jebiwott, S., Jaijyan, D. K., Davidow, A., Ojo, K. K., Van Voorhis, W. C., Brochet, M., Billker, O., and Bhanot, P. (2016) Invasion of hepatocytes by Plasmodium sporozoites requires cGMP-dependent protein kinase and calcium dependent protein kinase 4. *Mol. Microbiol.* **102**, 349–363
39. Baker, D. A., and Deng, W. (2005) Cyclic GMP-dependent protein kinases in protozoa. *Front. Biosci.* **10**, 1229
40. Deng, W., Parbhu-Patel, A., Meyer, D. J., and Baker, D. A. (2003) The role of two novel regulatory sites in the activation of the cGMP-dependent protein kinase from Plasmodium falciparum. *Biochem. J.* **374**, 559–565
41. Franz, E., Knape, M. J., and Herberg, F. W. (2018) cGMP Binding Domain D Mediates a Unique Activation Mechanism in Plasmodium falciparum PKG. *ACS Infect. Dis.* **4**, 415–423
42. El Bakkouri, M., Kouidmi, I., Wernimont, A. K., Amani, M., Hutchinson, A., Loppnau, P., Kim, J. J., Flueck, C., Walker, J. R., Seitova, A., Senisterra, G., Kakihara, Y., Kim, C., Blackman, M. J., Calmettes, C., Baker, D. A., and Hui, R. (2019) Structures of the cGMP-dependent protein kinase in malaria parasites reveal a unique structural relay mechanism for activation. *Proc. Natl. Acad. Sci.* **116**, 14164–14173
43. Dostmann, W. R., and Taylor, S. S. (1991) Identifying the molecular switches that determine whether (Rp)-cAMPS functions as an antagonist or an agonist in the activation of cAMP-dependent protein kinase I. *Biochemistry*. **30**, 8710–6
44. Wu, J., Jones, J. M., Nguyen-Huu, X., Ten Eyck, L. F., and Taylor, S. S. (2004) Crystal structures of RIalpha subunit of cyclic adenosine 5′-monophosphate (cAMP)-dependent protein kinase complexed with (Rp)-adenosine 3′,5′-cyclic monophosphothioate and (Sp)-adenosine 3′,5′-cyclic monophosphothioate, the phosphothioate analogues of cA. *Biochemistry*. **43**, 6620–9
45. Monod, J., Wyman, J., and Changeux, J.-P. (1965) On the nature of allosteric transitions: A plausible model. *J. Mol. Biol.* **12**, 88–118
46. Koshland, D. E., Némethy, G., and Filmer, D. (1966) Comparison of Experimental Binding Data and Theoretical Models in Proteins Containing Subunits *. *Biochemistry*. **5**, 365–385
47. Byun, J. A., Akimoto, M., VanSchouwen, B., Lazarou, T. S., Taylor, S. S., and Melacini, G. (2020) Allosteric pluripotency as revealed by protein kinase A. *Sci. Adv.* **6**, eabb1250
48. Motlagh, H. N., and Hilser, V. J. (2012) Agonism/antagonism switching in allosteric ensembles. *Proc. Natl. Acad. Sci.* **109**, 4134–4139

49. Hilser, V. J., Wrabl, J. O., and Motlagh, H. N. (2012) Structural and Energetic Basis of Allostery. *Annu. Rev. Biophys.* **41**, 585–609
50. Motlagh, H. N., Wrabl, J. O., Li, J., and Hilser, V. J. (2014) The ensemble nature of allostery. *Nature*. **508**, 331–339
51. White, J. T., Li, J., Grasso, E., Wrabl, J. O., and Hilser, V. J. (2018) Ensemble allosteric model: energetic frustration within the intrinsically disordered glucocorticoid receptor. *Philos. Trans. R. Soc. B Biol. Sci.* **373**, 20170175
52. Stenson, P. D., Mort, M., Ball, E. V., Evans, K., Hayden, M., Heywood, S., Hussain, M., Phillips, A. D., and Cooper, D. N. (2017) The Human Gene Mutation Database: towards a comprehensive repository of inherited mutation data for medical research, genetic diagnosis and next-generation sequencing studies. *Hum. Genet.* **136**, 665–677
53. Hamburg, M. A., and Collins, F. S. (2010) The Path to Personalized Medicine. *N. Engl. J. Med.* **363**, 301–304
54. Casey, M., Mah, C., Merliss, A. D., Kirschner, L. S., Taymans, S. E., Denio, A. E., Korf, B., Irvine, A. D., Hughes, A., Carney, J. A., Stratakis, C. A., and Basson, C. T. (1998) Identification of a novel genetic locus for familial cardiac myxomas and Carney complex. *Circulation*. **98**, 2560–6
55. Greene, E. L., Horvath, A. D., Nesterova, M., Giatzakis, C., Bossis, I., and Stratakis, C. A. (2008) In vitro functional studies of naturally occurring pathogenic PRKAR1A mutations that are not subject to nonsense mRNA decay. *Hum. Mutat.* **29**, 633–9
56. Boulton, S., Akimoto, M., Akbarizadeh, S., and Melacini, G. (2017) Free energy landscape remodeling of the cardiac pacemaker channel explains the molecular basis of familial sinus bradycardia. *J. Biol. Chem.* **292**, 6414–6428
57. Yun, J.-H., Kim, M., Kim, K., Lee, D., Jung, Y., Oh, D., Ko, Y.-J., Cho, A. E., Cho, H.-S., and Lee, W. (2015) Solution structure of the transmembrane 2 domain of the human melanocortin-4 receptor in sodium dodecyl sulfate (SDS) micelles and the functional implication of the D90N mutant. *Biochim. Biophys. Acta - Biomembr.* **1848**, 1294–1302
58. Kim, J., Masterson, L. R., Cembran, A., Verardi, R., Shi, L., Gao, J., Taylor, S. S., and Veglia, G. (2015) Dysfunctional conformational dynamics of protein kinase A induced by a lethal mutant of phospholamban hinder phosphorylation. *Proc. Natl. Acad. Sci. U. S. A.* **112**, 3716–21
59. Sekhar, A., Rumfeldt, J. A. O., Broom, H. R., Doyle, C. M., Sobering, R. E., Meiering, E. M., and Kay, L. E. (2016) Probing the free energy landscapes of ALS disease mutants of SOD1 by NMR spectroscopy. *Proc. Natl. Acad. Sci.* **113**, E6939–E6945
60. Akimoto, M., Moleschi, K., Boulton, S., VanSchouwen, B., Selvaratnam, R., Taylor, S. S., and Melacini, G. (2014) Allosteric linkers in cAMP signalling. *Biochem. Soc. Trans.* **42**, 139–144
61. Akimoto, M., Selvaratnam, R., McNicholl, E. T., Verma, G., Taylor, S. S., and Melacini, G. (2013) Signaling through dynamic linkers as revealed by PKA. *Proc. Natl. Acad. Sci. U. S. A.* **110**, 14231–6
62. Moleschi, K. J., Akimoto, M., and Melacini, G. (2015) Measurement of State-Specific Association Constants in Allosteric Sensors through Molecular Stapling and NMR. *J. Am. Chem. Soc.* **137**, 10777–85
63. Krishnamurthy, S., Moorthy, B. S., Xin Xiang, L., Xin Shan, L., Bharatham, K., Tulsian, N. K., Mihalek, I., and Anand, G. S. (2014) Active site coupling in PDE:PKA complexes promotes resetting of mammalian cAMP signaling. *Biophys. J.* **107**, 1426–40

64. Krishnamurthy, S., Tulsian, N. K., Chandramohan, A., and Anand, G. S. (2015) Parallel Allostery by cAMP and PDE Coordinates Activation and Termination Phases in cAMP Signaling. *Biophys. J.* **109**, 1251–63
65. Schütz, A. K., Rennella, E., and Kay, L. E. (2017) Exploiting conformational plasticity in the AAA+ protein VCP/p97 to modify function. *Proc. Natl. Acad. Sci. U. S. A.* 10.1073/pnas.1707974114
66. Bouvignies, G., Vallurupalli, P., Hansen, D. F., Correia, B. E., Lange, O., Bah, A., Vernon, R. M., Dahlquist, F. W., Baker, D., and Kay, L. E. (2011) Solution structure of a minor and transiently formed state of a T4 lysozyme mutant. *Nature*. **477**, 111–4
67. Axe, J. M., O'Rourke, K. F., Kerstetter, N. E., Yezdimer, E. M., Chan, Y. M., Chasin, A., and Boehr, D. D. (2015) Severing of a hydrogen bond disrupts amino acid networks in the catalytically active state of the alpha subunit of tryptophan synthase. *Protein Sci.* **24**, 484–494
68. Chen, W., Gamache, E., Rosenman, D. J., Xie, J., Lopez, M. M., Li, Y.-M., and Wang, C. (2014) Familial Alzheimer's mutations within APPTM increase Aβ42 production by enhancing accessibility of ε-cleavage site. *Nat. Commun.* 10.1038/ncomms4037
69. Vostrikov, V. V., Soller, K. J., Ha, K. N., Gopinath, T., and Veglia, G. (2015) Effects of naturally occurring arginine 14 deletion on phospholamban conformational dynamics and membrane interactions. *Biochim. Biophys. Acta - Biomembr.* **1848**, 315–322
70. Lu, S., Banerjee, A., Jang, H., Zhang, J., Gaponenko, V., and Nussinov, R. (2015) (intro) GTP Binding and Oncogenic Mutations May Attenuate Hypervariable Region (HVR)-Catalytic Domain Interactions in Small GTPase K-Ras4B, Exposing the Effector Binding Site. *J. Biol. Chem.* **290**, 28887–28900
71. Nelson, S. E. D., Ha, K. N., Gopinath, T., Exline, M. H., Mascioni, A., Thomas, D. D., and Veglia, G. (2018) Effects of the Arg9Cys and Arg25Cys mutations on phospholamban's conformational equilibrium in membrane bilayers. *Biochim. Biophys. Acta - Biomembr.* **1860**, 1335–1341
72. Chandak, M. S., Nakamura, T., Makabe, K., Takenaka, T., Mukaiyama, A., Chaudhuri, T. K., Kato, K., and Kuwajima, K. (2013) The H/D-Exchange Kinetics of the Escherichia coli Co-Chaperonin GroES Studied by 2D NMR and DMSO-Quenched Exchange Methods. *J. Mol. Biol.* **425**, 2541–2560
73. Smith, M. J., Neel, B. G., and Ikura, M. (2013) NMR-based functional profiling of RASopathies and oncogenic RAS mutations. *Proc. Natl. Acad. Sci.* **110**, 4574–4579
74. Schuetz, A. K., and Kay, L. E. (2016) A Dynamic molecular basis for malfunction in disease mutants of p97/VCP. *Elife*. 10.7554/eLife.20143
75. Wang, J., Kawasaki, R., Uewaki, J., Rashid, A., Tochio, N., and Tate, S. (2017) Dynamic Allostery Modulates Catalytic Activity by Modifying the Hydrogen Bonding Network in the Catalytic Site of Human Pin1. *Molecules*. **22**, 992
76. Deacon, O. M., Karsisiotis, A. I., Moreno-Chicano, T., Hough, M. A., Macdonald, C., Blumenschein, T. M. A., Wilson, M. T., Moore, G. R., and Worrall, J. A. R. (2017) Heightened Dynamics of the Oxidized Y48H Variant of Human Cytochrome c Increases Its Peroxidatic Activity. *Biochemistry*. **56**, 6111–6124
77. Williamson, M. P. (2013) Using chemical shift perturbation to characterise ligand binding. *Prog. Nucl. Magn. Reson. Spectrosc.* **73**, 1–16
78. Selvaratnam, R., Chowdhury, S., VanSchouwen, B., and Melacini, G. (2011) Mapping allostery through the covariance analysis of NMR chemical shifts. *Proc. Natl. Acad. Sci. U.*

S. A. **108**, 6133–8
79. Selvaratnam, R., VanSchouwen, B., Fogolari, F., Mazhab-Jafari, M. T., Das, R., and Melacini, G. (2012) The Projection Analysis of NMR Chemical Shifts Reveals Extended EPAC Autoinhibition Determinants. *Biophys. J.* **102**, 630–639
80. Selvaratnam, R., Mazhab-Jafari, M. T., Das, R., and Melacini, G. (2012) The auto-inhibitory role of the EPAC hinge helix as mapped by NMR. *PLoS One*. **7**, e48707
81. VanSchouwen, B., Selvaratnam, R., Giri, R., Lorenz, R., Herberg, F. W., Kim, C., and Melacini, G. (2015) Mechanism of cAMP Partial Agonism in Protein Kinase G (PKG). *J. Biol. Chem.* 10.1074/jbc.M115.685305
82. Akimoto, M., McNicholl, E. T., Ramkissoon, A., Moleschi, K., Taylor, S. S., and Melacini, G. (2015) Mapping the Free Energy Landscape of PKA Inhibition and Activation: A Double-Conformational Selection Model for the Tandem cAMP-Binding Domains of PKA RIα. *PLoS Biol.* **13**, e1002305
83. Das, R., Abu-Abed, M., and Melacini, G. (2006) Mapping allostery through equilibrium perturbation NMR spectroscopy. *J. Am. Chem. Soc.* **128**, 8406–7
84. Schweizer, P. A., Duhme, N., Thomas, D., Becker, R., Zehelein, J., Draguhn, A., Bruehl, C., Katus, H. A., and Koenen, M. (2010) cAMP Sensitivity of HCN Pacemaker Channels Determines Basal Heart Rate But Is Not Critical for Autonomic Rate Control. *Circ. Arrhythmia Electrophysiol.* **3**, 542–552
85. Schulze-Bahr, E., Neu, A., Friederich, P., Kaupp, U. B., Breithardt, G., Pongs, O., and Isbrandt, D. (2003) Pacemaker channel dysfunction in a patient with sinus node disease. *J. Clin. Invest.* **111**, 1537–1545
86. Milanesi, R., Baruscotti, M., Gnecchi-Ruscone, T., and DiFrancesco, D. (2006) Familial Sinus Bradycardia Associated with a Mutation in the Cardiac Pacemaker Channel. *N. Engl. J. Med.* **354**, 151–157
87. DiFrancesco, D. (2013) Funny channel gene mutations associated with arrhythmias. *J. Physiol.* **591**, 4117–4124
88. Baruscotti, M., Bucchi, A., Milanesi, R., Paina, M., Barbuti, A., Gnecchi-Ruscone, T., Bianco, E., Vitali-Serdoz, L., Cappato, R., and DiFrancesco, D. (2017) A gain-of-function mutation in the cardiac pacemaker HCN4 channel increasing cAMP sensitivity is associated with familial Inappropriate Sinus Tachycardia. *Eur. Heart J.* **38**, 280–288
89. Zagotta, W. N., Olivier, N. B., Black, K. D., Young, E. C., Olson, R., and Gouaux, E. (2003) Structural basis for modulation and agonist specificity of HCN pacemaker channels. *Nature*. **425**, 200–205
90. Xu, X., Vysotskaya, Z. V., Liu, Q., and Zhou, L. (2010) Structural Basis for the cAMP-dependent Gating in the Human HCN4 Channel. *J. Biol. Chem.* **285**, 37082–37091
91. Xu, X., Marni, F., Wu, S., Su, Z., Musayev, F., Shrestha, S., Xie, C., Gao, W., Liu, Q., and Zhou, L. (2012) Local and Global Interpretations of a Disease-Causing Mutation near the Ligand Entry Path in Hyperpolarization-Activated cAMP-Gated Channel. *Structure*. **20**, 2116–2123
92. Boulton, S., Akimoto, M., Selvaratnam, R., Bashiri, A., and Melacini, G. (2015) A Tool Set to Map Allosteric Networks through the NMR Chemical Shift Covariance Analysis. *Sci. Rep.* **4**, 7306
93. Boulton, S., Selvaratnam, R., Ahmed, R., and Melacini, G. (2018) Implementation of the NMR CHEmical Shift Covariance Analysis (CHESCA): A Chemical Biologist's Approach to Allostery, pp. 391–405, 10.1007/978-1-4939-7386-6_18

94. Axe, J. M., Yezdimer, E. M., O'Rourke, K. F., Kerstetter, N. E., You, W., Chang, C. A., and Boehr, D. D. (2014) Amino Acid Networks in a (β/α) 8 Barrel Enzyme Change during Catalytic Turnover. *J. Am. Chem. Soc.* **136**, 6818–6821
95. Massi, F., Johnson, E., Wang, C., Rance, M., and Palmer, A. G. (2004) NMR R 1 ρ Rotating-Frame Relaxation with Weak Radio Frequency Fields. *J. Am. Chem. Soc.* **126**, 2247–2256
96. Fawzi, N. L., Ying, J., Ghirlando, R., Torchia, D. A., and Clore, G. M. (2011) Atomic-resolution dynamics on the surface of amyloid-β protofibrils probed by solution NMR. *Nature*. **480**, 268–272
97. Vallurupalli, P., Bouvignies, G., and Kay, L. E. (2012) Studying "Invisible" Excited Protein States in Slow Exchange with a Major State Conformation. *J. Am. Chem. Soc.* **134**, 8148–8161
98. Sekhar, A., Rumfeldt, J. A., Broom, H. R., Doyle, C. M., Bouvignies, G., Meiering, E. M., and Kay, L. E. (2015) Thermal fluctuations of immature SOD1 lead to separate folding and misfolding pathways. *Elife*. 10.7554/eLife.07296
99. Farrow, N. A., Zhang, O., Forman-Kay, J. D., and Kay, L. E. (1994) A heteronuclear correlation experiment for simultaneous determination of 15N longitudinal decay and chemical exchange rates of systems in slow equilibrium. *J. Biomol. NMR*. **4**, 727–734
100. Robson, S. A., Peterson, R., Bouchard, L.-S., Villareal, V. A., and Clubb, R. T. (2010) A Heteronuclear Zero Quantum Coherence N z -Exchange Experiment That Resolves Resonance Overlap and Its Application To Measure the Rates of Heme Binding to the IsdC Protein. *J. Am. Chem. Soc.* **132**, 9522–9523
101. Horovitz, A. (1996) Double-mutant cycles: a powerful tool for analyzing protein structure and function. *Fold. Des.* **1**, R121–R126
102. Boyer, J. A., Clay, C. J., Luce, K. S., Edgell, M. H., and Lee, A. L. (2010) Detection of Native-State Nonadditivity in Double Mutant Cycles via Hydrogen Exchange. *J. Am. Chem. Soc.* **132**, 8010–8019
103. Boulton, S., and Melacini, G. (2016) Advances in NMR Methods To Map Allosteric Sites: From Models to Translation. *Chem. Rev.* **116**, 6267–6304
104. Palmer, A. G. (2004) NMR Characterization of the Dynamics of Biomacromolecules. *Chem. Rev.* **104**, 3623–3640
105. Mittermaier, A. K., and Kay, L. E. (2009) Observing biological dynamics at atomic resolution using NMR. *Trends Biochem. Sci.* **34**, 601–611
106. Kay, L. E. (2016) New Views of Functionally Dynamic Proteins by Solution NMR Spectroscopy. *J. Mol. Biol.* **428**, 323–331
107. Loh, A. P., Guo, W., Nicholson, L. K., and Oswald, R. E. (1999) Backbone Dynamics of Inactive, Active, and Effector-Bound Cdc42Hs from Measurements of 15 N Relaxation Parameters at Multiple Field Strengths †. *Biochemistry*. **38**, 12547–12557
108. Wang, C., Pawley, N. H., and Nicholson, L. K. (2001) The role of backbone motions in ligand binding to the c-Src SH3 domain. *J. Mol. Biol.* **313**, 873–887
109. Fayos, R., Melacini, G., Newlon, M. G., Burns, L., Scott, J. D., and Jennings, P. A. (2003) Induction of Flexibility through Protein-Protein Interactions. *J. Biol. Chem.* **278**, 18581–18587
110. Das, R., Mazhab-Jafari, M. T., Chowdhury, S., SilDas, S., Selvaratnam, R., and Melacini, G. (2008) Entropy-driven cAMP-dependent Allosteric Control of Inhibitory Interactions in Exchange Proteins Directly Activated by cAMP. *J. Biol. Chem.* **283**, 19691–19703
111. Popovych, N., Sun, S., Ebright, R. H., and Kalodimos, C. G. (2006) Dynamically driven

protein allostery. *Nat. Struct. Mol. Biol.* **13**, 831–838
112. Bracken, C., Carr, P. A., Cavanagh, J., and Palmer, A. G. (1999) Temperature dependence of intramolecular dynamics of the basic leucine zipper of GCN4: implications for the entropy of association with DNA 1 1Edited by P. E. Wright. *J. Mol. Biol.* **285**, 2133–2146
113. García de la Torre, J., Huertas, M. ., and Carrasco, B. (2000) HYDRONMR: Prediction of NMR Relaxation of Globular Proteins from Atomic-Level Structures and Hydrodynamic Calculations. *J. Magn. Reson.* **147**, 138–146
114. Mayer, M., and Meyer, B. (1999) Characterization of Ligand Binding by Saturation Transfer Difference NMR Spectroscopy. *Angew. Chemie Int. Ed.* **38**, 1784–1788
115. Assadi-Porter, F. M., Tonelli, M., Maillet, E., Hallenga, K., Benard, O., Max, M., and Markley, J. L. (2008) Direct NMR Detection of the Binding of Functional Ligands to the Human Sweet Receptor, a Heterodimeric Family 3 GPCR. *J. Am. Chem. Soc.* **130**, 7212–7213
116. Raditsis, A. V., Milojevic, J., and Melacini, G. (2013) Aβ Association Inhibition by Transferrin. *Biophys. J.* **105**, 473–480
117. Milojevic, J., and Melacini, G. (2011) Stoichiometry and Affinity of the Human Serum Albumin-Alzheimer's Aβ Peptide Interactions. *Biophys. J.* **100**, 183–192
118. Milojevic, J., Costa, M., Ortiz, A. M., Jorquera, J. I., and Melacini, G. (2013) In Vitro Amyloid-β Binding and Inhibition of Amyloid-β Self-Association by Therapeutic Albumin. *J. Alzheimer's Dis.* **38**, 753–765
119. Mazhab-Jafari, M. T., Das, R., Fotheringham, S. A., SilDas, S., Chowdhury, S., and Melacini, G. (2007) Understanding cAMP-Dependent Allostery by NMR Spectroscopy: Comparative Analysis of the EPAC1 cAMP-Binding Domain in Its Apo and cAMP-Bound States. *J. Am. Chem. Soc.* **129**, 14482–14492
120. Akimoto, M., Zhang, Z., Boulton, S., Selvaratnam, R., VanSchouwen, B., Gloyd, M., Accili, E. A., Lange, O. F., and Melacini, G. (2014) A Mechanism for the Auto-inhibition of Hyperpolarization-activated Cyclic Nucleotide-gated (HCN) Channel Opening and Its Relief by cAMP. *J. Biol. Chem.* **289**, 22205–22220
121. Bhunia, A., Bhattacharjya, S., and Chatterjee, S. (2012) Applications of saturation transfer difference NMR in biological systems. *Drug Discov. Today*. **17**, 505–513
122. Angulo, J., and Nieto, P. M. (2011) STD-NMR: application to transient interactions between biomolecules—a quantitative approach. *Eur. Biophys. J.* **40**, 1357–1369
123. Cala, O., Guillière, F., and Krimm, I. (2014) NMR-based analysis of protein–ligand interactions. *Anal. Bioanal. Chem.* **406**, 943–956
124. Wagstaff, J. L., Taylor, S. L., and Howard, M. J. (2013) Recent developments and applications of saturation transfer difference nuclear magnetic resonance (STD NMR) spectroscopy. *Mol. BioSyst.* **9**, 571–577
125. Wang, Y.-S., Liu, D., and Wyss, D. F. (2004) Competition STD NMR for the detection of high-affinity ligands and NMR-based screening. *Magn. Reson. Chem.* **42**, 485–489
126. Gardino, A. K., Villali, J., Kivenson, A., Lei, M., Liu, C. F., Steindel, P., Eisenmesser, E. Z., Labeikovsky, W., Wolf-Watz, M., Clarkson, M. W., and Kern, D. (2009) Transient Non-native Hydrogen Bonds Promote Activation of a Signaling Protein. *Cell*. **139**, 1109–1118
127. McNicholl, E. T., Das, R., SilDas, S., Taylor, S. S., and Melacini, G. (2010) Communication between Tandem cAMP Binding Domains in the Regulatory Subunit of Protein Kinase A-Iα as Revealed by Domain-silencing Mutations. *J. Biol. Chem.* **285**, 15523–15537
128. Abu-Abed, M., Das, R., Wang, L., and Melacini, G. (2007) Definition of an electrostatic relay switch critical for the cAMP-dependent activation of protein kinase A as revealed

by the D170A mutant of RIalpha. *Proteins*. **69**, 112–24

129. Kleckner, I. R., and Foster, M. P. (2011) An introduction to NMR-based approaches for measuring protein dynamics. *Biochim. Biophys. Acta - Proteins Proteomics*. **1814**, 942–968
130. Das, R., Chowdhury, S., Mazhab-Jafari, M. T., SilDas, S., Selvaratnam, R., and Melacini, G. (2009) Dynamically Driven Ligand Selectivity in Cyclic Nucleotide Binding Domains. *J. Biol. Chem.* **284**, 23682–23696

Chapter 2

Allosteric Pluripotency as Revealed by Protein kinase A

2.1 Author's Preface

The work presented in this chapter has previously been published and is reproduced here with permission from the Science Advances, AAAS. Full citation is as follows:

Byun, J. A., Akimoto, M., VanSchouwen, B., Lazarou, T. S., Taylor, S. S., and Melacini, G. (2020) Allosteric pluripotency as revealed by protein kinase A. Sci. Adv. 6, eabb1250.

I co-designed and co-conducted most of the experiments necessary for the manuscript and analyzed the data with Dr. Madoka Akimoto. Dr. Bryan VanSchouwen performed all the MD simulations. Tomas S. Lazarou assisted in sample preparations for the paramagnetic relaxation enhancement experiments. Dr. Susan S. Taylor provided plasmids and helpful discussions. Dr. Giuseppe Melacini contributed to designing the experiments and developed the ensemble allosteric model. I co-wrote the manuscript with Dr. Madoka Akimoto and Dr. Giuseppe Melacini.

* The supplementary materials for this manuscript are presented in Chapter 3. Please refer to Chapter 3 for supplementary figures, tables, and texts mentioned in this chapter.

2.2 Abstract

The functional response of a signaling system to an allosteric stimulus often depends on sub-cellular conditions, a phenomenon known as pluripotent allostery. For example, a single allosteric modulator of the prototypical Protein Kinase A (PKA) switches from antagonist to agonist depending on MgATP levels. However, the mechanism underlying such pluripotent allostery has remained elusive for decades. Using NMR spectroscopy, ensemble models, kinase assays and molecular dynamics simulations, we show that allosteric pluripotency arises from surprisingly divergent responses of highly homologous tandem domains. The differential responses perturb domain-domain interactions and remodel the free energy landscape of inhibitory excited states sampled by the regulatory subunit of PKA. The resulting activation threshold values are comparable to the effective free energy of regulatory and catalytic subunit binding, which depends on metabolites, substrates and mutations, explaining pluripotent allostery and warranting a general redefinition of allosteric targets to include specific sub-cellular environments.

2.3 Introduction

Allosteric modulation is a proven approach to increase selectivity for target receptors (1–6). Allosteric modulators are typically more selective than orthosteric ligands, which target highly conserved active sites (3). However, the functional response of an allosteric system to an allosteric stimulus may vary depending on the experimental conditions, a phenomenon known as pluripotent allostery (7–10). For example, the breast cancer drug tamoxifen serves its intended antagonist role for estrogen receptors (ERs) in breast tissue, but it acts as an agonist for uterus ERs, enhancing the risk of endometrial cancer (8). Such undesired side effects are rationalized through a three ligand-binding trimer model, which effectively explains the therapeutically-relevant agonism-antagonism switch in ERs (*7*). However, pluripotent allostery in other systems, such as kinases, remains still poorly understood. For example, the Rp-cAMPS phosphorothioate analog of cAMP (Rp; Fig. 1A) has been known for decades to act as an effective allosteric inhibitor of isoform 1a Protein Kinase A (PKA) in the presence of excess MgATP, but as an allosteric agonist in the absence of excess MgATP (Fig. 1, C and D) (11). Yet, the mechanism underlying the MgATP-dependent allosteric switch of Rp is currently still elusive.

Understanding pluripotent allostery in PKA is a central unmet challenge in the kinase field, not only because PKA serves as a prototype for the protein kinase superfamily, but also because PKA is a cancer driver (12–14). Given the cancer predisposition caused by defective PKA inhibition, hundreds of cAMP analogs have been screened for PKA antagonism (15, 16). Yet, to date the only known cAMP antagonist of PKA is Rp (Fig. 1A), which remains the best currently available lead for allosteric inhibition of PKA (15, 16). Hence, it is essential to understand the Rp mechanism of action, including pluripotent allostery.

The PKA regulatory subunit (R) functions as a cAMP-dependent competitive inhibitor of the PKA catalytic subunit (C) (*17-19*). In the inhibited PKA holoenzyme, two catalytic subunit molecules bind to a dimeric regulatory subunit (R_2) (Fig. 1B) (17). Upon cAMP binding, each inhibitory R-subunit undergoes a conformational change, unleashing the catalytic activity of the C-subunit to phosphorylate substrate proteins (Fig. 1B) (17). The full-length R-subunit, *i.e.* R1a (1-379), includes an *N*-terminal dimerization domain, followed by a linker and two cAMP-binding domains (CBD-A and CBD-B; Fig. 1E) (17). The linker includes an auto-inhibitory region (Fig. 1E), and the monomeric R-subunit construct spanning this region and CBD-A and -B, *i.e.* R1a

(91-379), or R_{AB} (Fig. 1E), is sufficient for full inhibition and cAMP-dependent activation of PKA (18–20).

In the inhibitory C:R_{AB} complex, both CBDs adopt a conformation denoted as 'off' and interact with the C-subunit, although the CBDs are not in close contact with one another (red triangles, Fig. 1F). This inhibitory-competent CBD topology is denoted here as A_{off}-B_{off}, with the hyphen between A and B indicating that CBD-A and CBD-B are not interacting (18, 20). In the non-inhibitory R_{AB}:$cAMP_2$ complex (Fig. 1G), both CBDs switch to a conformation denoted as 'on' and come into contact with one another (green rectangles, Fig. 1G). This inhibitory-incompetent CBD topology is denoted as $A_{on}B_{on}$, with the absence of the hyphen indicating that CBD-A and -B are interacting (18–21). Hence, the terms 'on/off' refer to the inability/ability of each CBD to promote inhibitory interactions of R with C that make C inaccessible to the substrate to be phosphorylated. Allosteric effectors typically act by controlling the on/off transitions of each CBD, which modulate the binding affinity of R for C and consequently the inhibition of PKA.

Rp binds both CBDs of R1a, but, unlike cAMP, forms a stable inhibitory complex in the presence of MgATP, *i.e.* Rp_4:R_2:C_2 (Fig. 1C) (15, 16, 22, 23). Despite extensive crystallization attempts, the structure of this inhibitory complex is currently unknown. The closest system amenable to crystallization so far has been R_{AB}:Rp_2 without C, but the structure of R_{AB}:Rp_2 is surprisingly very similar to that of R_{AB}:$cAMP_2$, which cannot bind C (RMSD = 0.47 Å; Fig. 1, G and H) (23). Therefore the structure of R_{AB}:Rp_2 may explain the agonism observed for Rp in the absence of excess MgATP (Fig. 1D), but alone is not sufficient to rationalize the antagonism of Rp in the presence of excess MgATP. Why does replacing cAMP with Rp in R_{AB}:$cAMP_2$ make R_{AB} competent to bind and inhibit C without changing the structure of R_{AB}? Without an answer to this question the mechanism of action for Rp remains unclear, limiting further development of allosteric inhibitors for PKA.

We hypothesize that the primary difference between the inhibitory R_{AB}:Rp_2 and the non-inhibitory R_{AB}:$cAMP_2$ complexes is in the conformational dynamics. Here, we test this hypothesis by investigating the interactions of Rp with R_{AB} and C:R_{AB} by NMR. Our comparative NMR analyses reveal how Rp remodels the conformational ensemble accessible to PKA R1a and provide a foundation to build an Ensemble Allosteric Model (EAM) for PKA. We show how to measure input EAM parameters by NMR (24–27) and how based on the PKA EAM it is possible

to relate microscopic dynamics to kinase function as measured by enzymatic assays, explaining allosteric pluripotency.

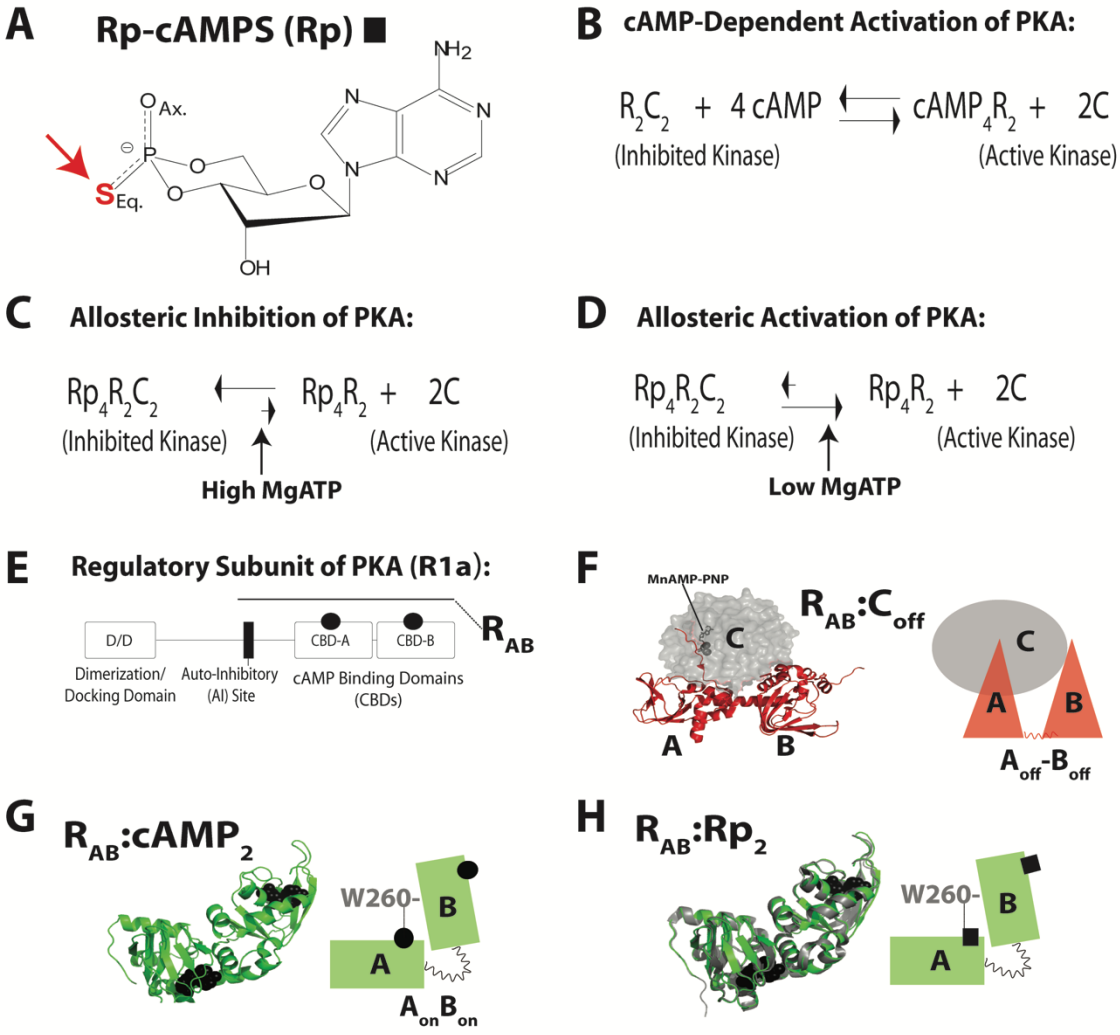

Figure 1. *Rp-cAMPS as Prototype of Allosteric Pluripotency.* **(A)** The Rp-cAMPS cAMP analog. **(B)** Activation equilibrium of Protein Kinase A (PKA). **(C, D)** Pluripotent allostery of Rp, which functions as an allosteric antagonist or agonist in the presence or absence of excess MgATP, respectively (11). **(E)** Domain organization of the regulatory (R)-subunit R1a and of the R_{AB} construct (91-379). **(F, G)** Crystal structures and respective cartoons of C:R_{AB} (PDB:2QCS) (18) and R_{AB}:$cAMP_2$ (PDB: 1RGS) (28), with the cAMP-binding domains (CBDs) bridged by W260 of CBD-B interacting with cAMP in CBD-A. Bound nucleotides are shown as stick or sphere representation. **(H)** As (G), but for the crystal structure of the R_{AB}:Rp_2 complex (PDB: 1NE4, grey ribbon) (23) superimposed to the structure of R_{AB}:$cAMP_2$ (PDB: 1RGS, green ribbon). The two structures are virtually identical (RMSD = 0.47 Å).

2.4 Results

2.4.1 Rp-cAMPS Acts as an Antagonist for CBD-A and as an Agonist for the Homologous CBD-B in the Absence of Inter-Domain Interactions

As a first step to understand the effect of Rp on the 'off' *vs.* 'on' conformational equilibria of R_{AB}, we analyzed the W260A R_{AB} mutant, which selectively silences the inter-domain interactions without substantially perturbing the allosteric network within each domain (20). The analysis of the W260A R_{AB}:Rp_2 complex is expected to reveal how Rp controls the 'off' *vs.* 'on' conformational equilibrium of each separate domain. For this purpose, we compared the HN TROSY spectrum of W260A R_{AB}:Rp_2 to three key reference ^{1}H,^{15}N TROSY spectra, *i.e.*, R_{AB}:C (MW ~73 kDa), which traps the conformation of R_{AB} domains in the 'off' state, R_{AB}:$cAMP_2$ (MW ~33 kDa), which is assumed to represent the 'on' state of each CBD, and the fully unbound apo R_{AB} spectrum. Our comparative analyses focused on cross peaks arising from R_{AB} residues that are sufficiently distant from the C- and cAMP-binding interfaces to report primarily on the 'off' *vs.* 'on' equilibria. For example, the cross peaks of L221 and S297 specifically report on the conformational equilibria of CBD-A and CBD-B, respectively, and exhibit a linear pattern for the aforementioned reference states (*i.e.,* R_{AB}:C, R_{AB}:$cAMP_2$ and apo R_{AB}), as shown in Fig. 2, A and B. Such linearity points to a fast 'off' *vs.* 'on' exchange regime, in which linear chemical shift averaging implies that cross-peak positions reflect the relative populations of 'off' and 'on' states within each domain. The intermediate position of the apo R_{AB} cross peaks relative to those of R_{AB}:C and R_{AB}:$cAMP_2$ (Fig. 2, A and B) means that each apo domain samples a nearly degenerate equilibrium with comparable populations of 'on' and 'off' CBD conformers.

The comparative TROSY analysis of W260A R_{AB}:Rp_2 relative to the three reference states reveals that in the absence of inter-domain interactions, Rp shifts the conformational equilibrium of apo CBD-A slightly to the 'off' state (Fig. 2A). In striking contrast to CBD-A, CBD-B samples mostly the 'on' state in W260A R_{AB}:Rp_2, similar to R_{AB}:$cAMP_2$ (Fig. 2B). Given the homology between the two tandem domains, the differential CBD-A *vs.* -B response to Rp is surprising and therefore we extended our analysis of W260A R_{AB}:Rp_2 to a broader set of conformational equilibria-sensing residues (Fig. 2, C and D). This broader analysis provides a more quantitative measurement of the 'off' *vs.* 'on' state populations, ensuring that they are not biased by the choice of a single residue within each domain. Specifically, the slopes of the ($\delta_{W260A\ R:Rp2} - \delta_{R:cAMP2}$) *vs.* ($\delta_{R:C} - \delta_{R:cAMP2}$) chemical shift correlation plots for CBD-A (Fig. 2C) and CBD-B (Fig.

2D) indicate that the average fraction of the 'off' state sampled by W260A R_{AB}:Rp_2 is ~60% for CBD-A and ~5% for CBD-B. Overall, the chemical shift analyses of W260A R_{AB}:Rp_2 unexpectedly reveal that, in the absence of inter-domain interactions, Rp acts as an antagonist for CBD-A, but as an agonist for the homologous CBD-B. We then examined how the two CBDs respond to Rp in WT R_{AB}.

2.4.2 WT R_{AB}:Rp_2 Samples a Conformational Ensemble with a Ground State in a Closed $A_{on}B_{on}$ Topology Similar to WT R_{AB}:$cAMP_2$ but Excited States in an Open Topology Lacking Inter-Domain Interactions

To probe the contribution of inter-domain interactions to the conformational equilibria sampled by R_{AB}:Rp_2, we also acquired an HN TROSY spectrum of WT R_{AB}:Rp_2 (Fig. 2, E and F). We observed that CBD-B samples mostly the 'on' state, similar to W260A R_{AB}:Rp_2, where the inter-domain interactions are negligible (Fig. 2, F and H). Unlike CBD-B, CBD-A residues surprisingly exhibit two sets of peaks in slow exchange and with different intensities (Fig. 2, E and G). The major and minor peaks are at positions similar to WT R_{AB}:$cAMP_2$ and W260A R_{AB}:Rp_2, respectively. This unexpected observation indicates that in WT R_{AB}:Rp_2, CBD-A samples a conformational ensemble with ground and excited (*i.e.* higher energy) states. In the ground state, CBD-A is in the 'on' conformation similar to WT R_{AB}:$cAMP_2$, in which CBD-A interacts with the 'on' CBD-B through the stacking of the W260 indole and the adenine base. This suggests that the inter-domain interactions selectively stabilize the 'on' state of CBD-A.

In the excited state, the inter-domain interactions that stabilize the ground state are lost and CBD-A samples a fast-exchanging equilibrium between 'on' and 'off' conformers. This result is supported by the excellent match between the chemical shifts of the minor peaks in WT R_{AB}:Rp_2 and of W260A R_{AB}:Rp_2 (Fig. 2, E and I). Furthermore, the chemical shifts of the minor peaks of CBD-A in WT R_{AB}:Rp_2 match also those of the isolated CBD-A:Rp (Fig. 2J), confirming that the minor peaks of CBD-A in WT R_{AB}:Rp_2 arise from open topologies, where CBD-A does not interact with CBD-B. The overall population of the open-topology excited state corresponding to the minor peaks is 17 ± 5 %, after correcting for the differential relaxation of open *vs.* closed topologies (fig. S1). Considering that the population of 'off' state in the open topology is ~60% (Fig. 2C), the excited state of WT R_{AB}:Rp_2 includes 10 ± 3 % and 7 ± 2 % of CBD-A in the 'off' and

'on' conformations, respectively, while CBD-B remains in the 'on' conformer in all the detectable states of the ensemble accessed by WT R_{AB}:Rp_2 (Fig. 3C).

Interestingly, when the C-subunit of PKA is added to WT R_{AB}:Rp_2 in the presence of excess $MgCl_2$ and AMP-PNP, a non-hydrolazable analog of MgATP, it selectively binds to and stabilizes the 'off' conformer of CBD-A (~90% 'off'; Fig. 2, K and M, and fig. S2A). However, the C-subunit only partially shifts the conformational equilibrium of CBD-B to yield a ~45% 'off' state (Fig. 2, L and N, and fig. S2A), resulting in a two state conformational ensemble for C:R_{AB}:Rp_2 (Fig. 3F). Hence, the excited state in the ternary R_{AB}:Rp_2 complex with an open topology and CBD-A and B in the 'off' and 'on' conformers, respectively, is inhibition-competent, because it becomes a ground state in the inhibited quaternary C:R_{AB}:Rp_2 complex (Fig. 3, C and F). To better understand how these two complexes form upon Rp binding, we titrated Rp into the apo R_{AB} and C:R_{AB} samples and monitored the titration through HN TROSY spectra to measure domain-specific binding affinities for Rp (fig. S3). The results show that Rp binds C:R_{AB} with an 'A-to-B' order, which is opposite to cAMP binding, and Rp binds to Apo R_{AB} with a 'B-to-A' order similar to cAMP (fig. S3 and Supplementary Text S1). Based on these results, it is possible to propose a qualitative mechanism for the Rp antagonism-agonism switch in PKA, *i.e.* for pluripotent allostery (Fig. 3, A to F).

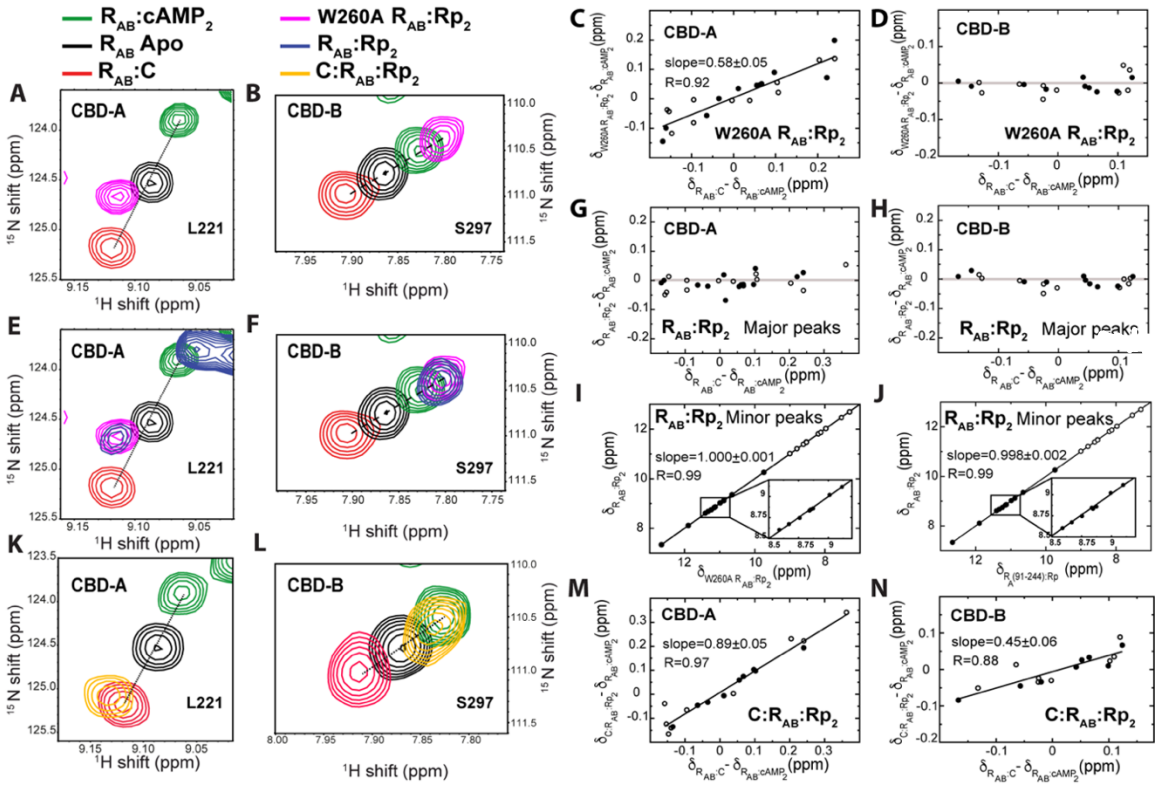

Figure 2. *Identifying the States Accessible to the R_{AB} Ensemble in the Presence of Rp-cAMPS.* **(A, B)** Representative TROSY cross-peaks of ^{15}N,^{2}H-labeled W260A R_{AB}:Rp_2 (pink) for residues sensing primarily the 'on' *vs.* 'off' equilibria of CBD-A and CBD-B. The corresponding cross-peaks in apo R_{AB} (black), R_{AB}:$cAMP_2$ (green) and WT R_{AB}:C (red) are also show as comparison benchmarks. **(C)** Fractional inhibition of CBD-A in W260A R_{AB}:Rp_2 through the chemical shift (δ) correlation slope. Closed and open circles in (C-N) indicate ^{1}H and ^{15}N chemical shifts downscaled by a 0.2 factor, respectively. **(D)** As (C) for CBD-B. **(E, F)** As (A, B) including WT R_{AB}:Rp_2 (blue). **(G, H)** As (C, D) for the major cross-peaks of WT R_{AB}:Rp_2. **(I)** Correlation between the chemical shifts of the minor peaks in WT R_{AB}:Rp_2 and the W260A R_{AB}:Rp_2 mutant. **(J)** As panel (I) but *vs.* the isolated CBD-A construct R1a (91-244) bound to Rp-cAMPS. **(K, L)** As (A, B) replacing W260A R_{AB}:Rp_2 with the WT C: R_{AB}:Rp_2 quaternary complex (orange). **(M, N)** As (C, D) for the WT C:R_{AB}:Rp_2 quaternary complex.

2.4.3 A Qualitative Mechanism of Pluripotent Allostery in PKA

In the absence of the C-subunit, apo R_{AB} samples an ensemble of states that are accessible within a nearly degenerate free energy landscape (20). This consists of four states with each non-interacting domain in fast-exchange between comparable populations of 'off' and the 'on' conformations (Fig. 3A) (20). Upon addition of Rp, it preferentially occupies CBD-B first selectively stabilizing the 'on' conformation of CBD-B, while CBD-A remains unoccupied and thus inter-domain interactions are still negligible (Fig. 3B). As the concentration of Rp increases further, Rp also binds to CBD-A, facilitating inter-domain interactions that partially stabilize a

closed topology, where both domains of R_{AB}:Rp_2 are in the 'on' conformation ($A_{on}B_{on}$; Fig. 3C). However, R_{AB}:Rp_2 also samples substantial populations (~20%) of open topologies, where CBD-A is in fast exchange between the 'off' and the 'on' conformations, *i.e.,* A_{off}-B_{on} and A_{on}-B_{on}, respectively (Fig. 3C).

When Rp is added to C:R_{AB}, it preferentially binds to CBD-A first, stabilizing it in the 'off' state, and then to CBD-B, promoting a partial 'off'-to-'on' transition (Fig. 3, D to F). When the quaternary C:R_{AB}:Rp_2 complex forms, R_{AB} samples the A_{off}-B_{on} and A_{off}-B_{off} states (Fig. 3F). In marked contrast to Rp, when cAMP is added to C:R_{AB}, it preferentially binds to CBD-B first, transiently sampling the C:R_{AB}:cAMP binding intermediate with R_{AB} in the A_{off}-B_{on} state (Fig. 3, G and H). Then cAMP binds also to CBD-A, stabilizing both domains in an 'on' conformation and releasing the C-subunit (Fig. 3I) (18). Hence, the Rp antagonism arises from the stabilization by Rp of two inhibitory states of C:R_{AB}:Rp_2, *i.e.,* A_{off}-B_{off} as in the inhibited C:R_{AB} complex, and A_{off}-B_{on}, which is a transient intermediate along the cAMP-dependent activation pathway, but is stably trapped by C:R_{AB}:Rp_2 (Fig. 3, D to I).

The model of Fig. 3 offers a qualitative rationalization of the Rp agonism-antagonism switch in PKA. The ensemble of R_{AB}:Rp_2 includes three main conformations: a ground closed state, $A_{on}B_{on}$, and two excited open states: A_{on}-B_{on} and A_{off}-B_{on} (Fig. 3C). The first two states are also sampled by the R_{AB}:$cAMP_2$ complex, albeit with different populations (Fig. 3I), and are inhibitory incompetent given their negligible affinity for the C-subunit. The third state (A_{off}-B_{on}) represents instead a unique feature of R_{AB}:Rp_2 that differentiates it from R_{AB}:$cAMP_2$, and is inhibitory competent because it is populated also in the stable C:R_{AB}:Rp_2 inhibited complex (Fig. 3F). As a result, the mixed A_{off}-B_{on} excited state sampled by R_{AB}:Rp_2 drives Rp to act as an antagonist when C binds R_{AB} with sufficiently high affinity to selectively stabilize A_{off}-B_{on} relative to $A_{on}B_{on}$ and A_{on}-B_{on}, resulting in a stable C:R_{AB}:Rp_2 complex and PKA inhibition. However, if the affinity of C for R_{AB} is reduced, for example due to lower MgATP levels (29–31), the inhibitory A_{off}-B_{on} state remains excited in the presence of C, while the ground, most populated state is still $A_{on}B_{on}$, which, being inhibition incompetent, leads to PKA activation. Hence, the model of Fig. 3 (A to F) provides a viable framework to explain the MgATP-dependent Rp agonism-antagonism switch observed for PKA (11).

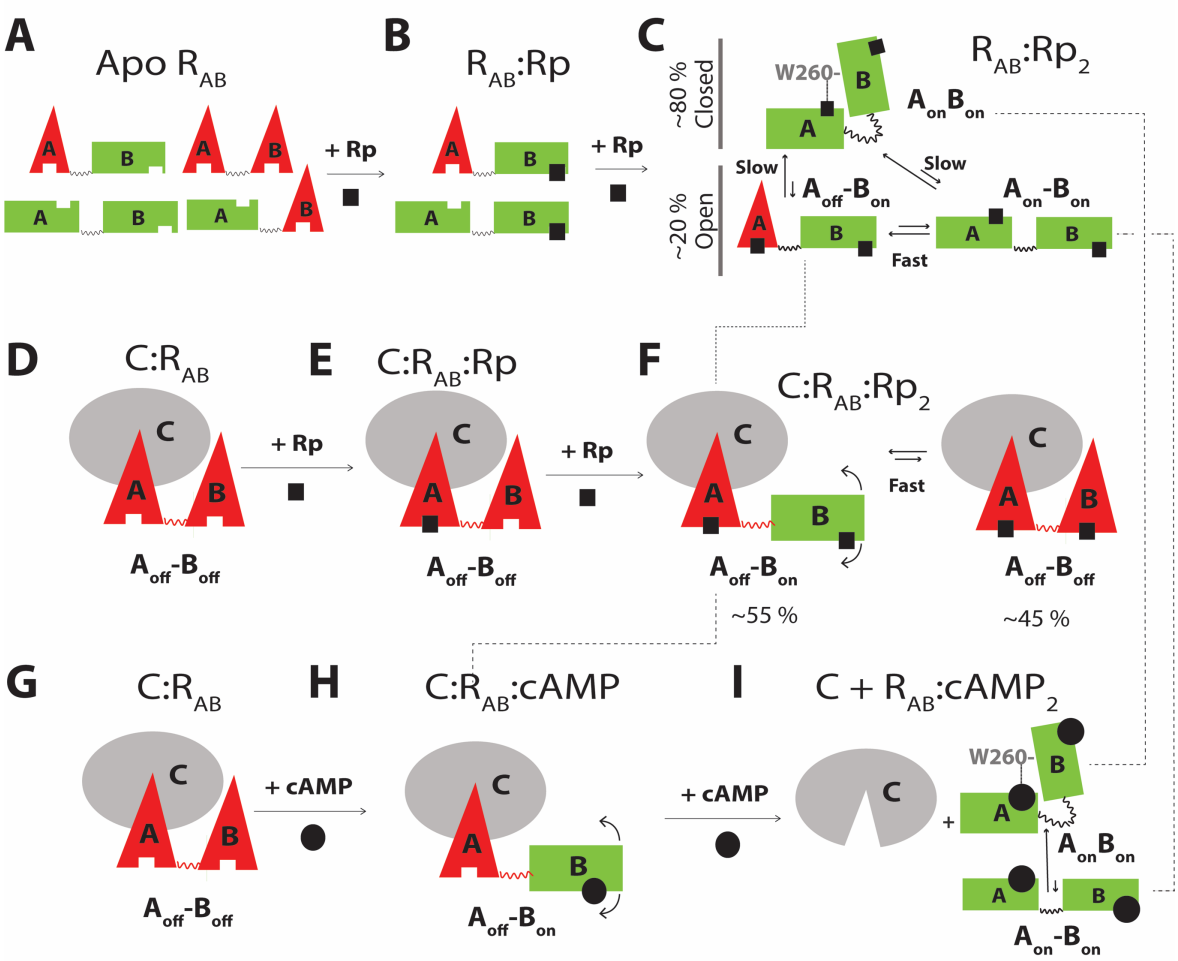

Figure 3. *Conformational Ensembles Accessible to Apo and C-Bound R_{AB} as a Function of Rp-cAMPS Binding.* **(A)** States accessible within the degenerate free energy landscape of apo R_{AB} (20). Red triangles and green rectangles denote 'off' and 'on' conformations of each CBD, respectively. The 'on/off' notation refers to the inability/ability of each CBD to promote inhibitory interactions of R with C. **(B)** States accessible to R_{AB}:Rp. No interdomain interactions occur when CBD-A is apo. **(C)** States accessible to R_{AB}:Rp_2. The dashed lines indicate that the A_{off}-B_{on} excited open state sampled by R_{AB}:Rp_2 is also sampled by C:R_{AB}:Rp_2 and is a transient intermediate along the cAMP-dependent activation pathway. **(D, E)** Rp binds first preferentially to CBD-A of C-bound R_{AB} further stabilizing the inhibitory conformation of CBD-A. **(F)** States accessible to the quaternary complex C:R_{AB}:Rp_2, showing that when CBD-B is bound to Rp it samples the 'on' conformation as well. **(G-I)** Traditional sequential binding of cAMP to C:R_{AB}, resulting in PKA activation. Unlike the case of Rp binding to C:R_{AB}, cAMP binds first to CBD-B and then CBD-A (18). The dashed lines illustrate that the inhibition-incompetent R_{AB}:$cAMP_2$ complex samples the same ground states as R_{AB}:Rp_2 as well as one of the excited states.

Given the potential of the model in Fig. 3 to account for the Rp agonism-antagonism switch, we sought to validate it further by additional investigations of how inter-domain interactions are coupled to the on-off equilibria within each domain. Such coupling is a central

feature of our model (Fig. 3), as it suggests that when both domains are bound to cyclic nucleotides, inter-domain interactions occur only if both CBDs are in the 'on' state (Fig. 3). When either CBD adopts the 'off' state, domain-domain interactions are weakened and, conversely, when inter-domain interactions are present, the conformational equilibrium of each CBD shifts to the 'on' state. In order to refine this hypothesis, we performed MD simulations of both R_{AB}:Rp_2 and C:R_{AB}:Rp_2 (Fig. 4, A, D and F, and figs. S4 to S6).

2.4.4 The Allosteric Pluripotency Mechanism Predicts that Domain-Domain Interactions Are Coupled to Intra-Domain On-Off Equilibria

The MD simulations of R_{AB}:Rp_2 were executed starting from the $A_{on}B_{on}$ and A_{off}-B_{off} reference states as well as the mixed A_{off}-B_{on} state. The $A_{on}B_{on}$ and A_{off}-B_{off} states are based on the crystal structures of R_{AB}:Rp_2 (PDB code: 1NE4) (23) and C:R_{AB} (PDB code: 2QCS) (18), respectively, while the hybrid A_{off}-B_{on} states were generated by combining CBD-A from the crystal structure of C:R_{AB} and CBD-B from the crystal structure of R_{AB}:Rp_2 with three different A/B boundaries within the helices that connect the two domains, *i.e.*, residues 242, 231, and 225 (Fig. 4A and fig. S4, A to F), which reside close to the hinge points for the closed-to-open transition (18). The A/B boundary dictates whether the center-of-mass (CM) distance between the two domains approaches the closed *vs.* open topologies of the $A_{on}B_{on}$ *vs.* A_{off}-B_{off} structures, with 242 and 231 sampling the open topology, and 225 approaching the closed topology (Fig. 4A).

To assess the structural propensities of each domain within the hybrid R_{AB} structures, RMSDs of the CBD-A and CBD-B from the R_{AB}:Rp_2 and C:R_{AB} X-ray structures were computed (Fig. 4, D and F, and fig. S5, A, D, F and G). As expected, CBD-B remains close to the conformation in the 1NE4 control structure for all three hybrid structures (Fig. 4F and fig. S5G). Meanwhile, the CBD-A domain remains close to the conformation in the C:R_{AB} control structure for the 231 and 242 hybrid structures, but shifts to the conformation in the R_{AB}:Rp_2 control structure for the 225 hybrid structure (Fig. 4D and fig. S5F). Therefore, a shift of the R-subunit to its closed conformation, as in the 225 hybrid, appears to promote a shift of CBD-A to its 'on' conformation, further corroborating our hypotheses based on the chemical shift analysis of R_{AB}:Rp_2 (Fig. 3C).

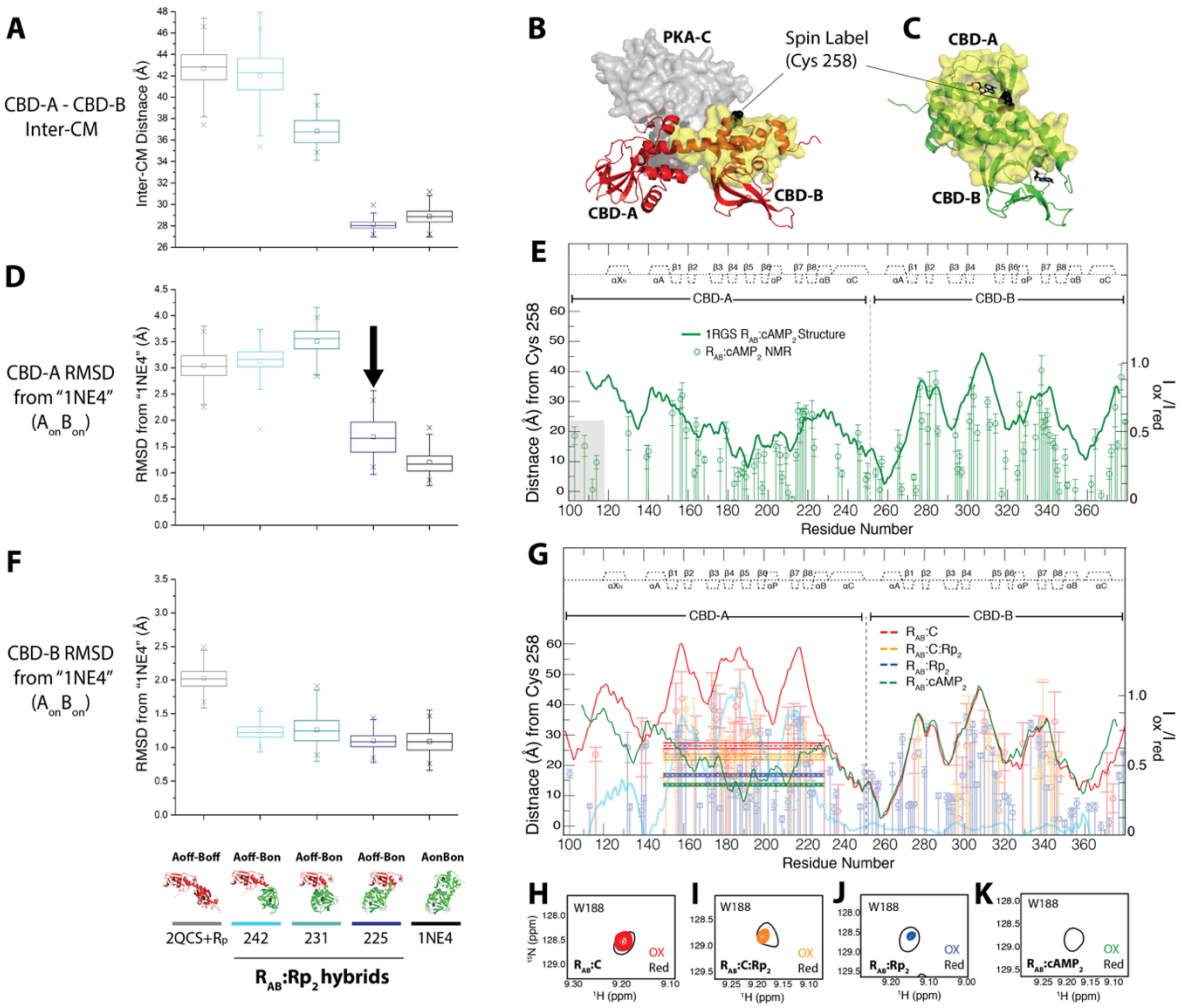

Figure 4. *R_{AB} Inter-Domain Interactions Probed through MD Simulations and Paramagnetic Relaxation Enhancements (PREs).* **(A)** Simulated center-of-mass (CM) distances between CBD-A and B for R_{AB}:Rp_2 in the A_{off}-B_{off}, $A_{on}B_{on}$ and hybrid A_{off}-B_{on} models with three different A/B boundaries (*i.e.* residues 242, 231 and 225, as shown in the bottom of panel (F)). **(B, C)** PRE design. The spin label is at Cys258 in CBD-B. Yellow surfaces are within 25 Å of the spin-label. In C-bound ($cAMP_2$-bound) R_{AB} inter-domain interactions are minimal (maximal). **(D)** CBD-A RMSD *vs.* $A_{on}B_{on}$. The closed topology induces the A_{off}-B_{on} → $A_{on}B_{on}$ transition (black arrow). **(E)** PRE control. The I_{ox}/I_{red} ratios (green circles) track the distance from the spin-label (dark green line). Deviations occur in dynamic regions, *e.g.* flexible linker (grey highlight) (20, 32). **(F)** As (D), but for CBD-B. **(G)** I_{ox}/I_{red} ratios for the R_{AB}:C (red), R_{AB}:C:Rp_2 (orange), and R_{AB}:Rp_2 (blue) complexes. Dashed lines indicate the average I_{ox}/I_{red} ratio for the region with the largest 2QCS (red) *vs.* 1RGS (green) difference (cyan) in distance from the spin-label. Solid lines mark the respective average +/- one standard deviation. **(H-K)** Representative HN-TROSY cross-peaks of oxidized and reduced samples. Contour levels were adjusted according to the intensity normalization as per Materials and Methods to account for aggregation.

The MD simulations outlined above were also repeated in the presence of C-subunit (fig. S4, G to I, fig. S5, B, C and E, and fig. S6). As in the case of the hybrid 225 R_{AB}:Rp_2 complex, the hybrid 225 A_{off}-B_{on} structure shifts to the $A_{on}B_{on}$ state (fig. S6, E, G, I and J) with a closed topology similar to cAMP-bound R_{AB} (fig. S5C and fig. S6, A and C) and dissociates from the C-subunit (fig. S5, B and E, and fig. S6, B, D and F). On the contrary, the more open hybrid 231 and 242 A_{off}-B_{on} structures do not shift to the $A_{on}B_{on}$ closed state (fig. S6, E, G, I and J) and preserve an open topology (fig. S5C and fig. S6, A and C), enabling CBD-A to remain in its 'off' state and bound to the C-subunit (fig. S5B and fig. S6, B and D). However, CBD-B in the hybrid 231 and 242 A_{off}-B_{on} structures is displaced away from the C-subunit more than in the A_{off}-B_{off} case (fig. S5E and fig. S6F), and as a result the A-B distance remains consistently shorter than in the canonical C:R_{AB} complex (*i.e.,* A_{off}-B_{off}; fig. S5C), yet larger than in the closed $A_{on}B_{on}$ topology (fig. S5C) because CBD-A is still stabilized in the 'off' conformer by its binding interaction with the C-subunit. Overall, based on the MD simulations, the A – B interdomain distances are predicted to decrease in the order: C:R_{AB} > C:R_{AB}:Rp_2 > R_{AB}:Rp_2 > R_{AB}:$cAMP_2$. We tested this prediction through Paramagnetic Relaxation Enhancement (PRE) NMR measurements (Fig. 4, B, C, E and G to K).

2.4.5 PRE Experiments Confirm The Coupling of Domain-Domain Interactions and Intra-Domain On-Off Equilibria

PRE measurements are ideally suited to probe inter-domain distances by engineering a spin label in one domain and observing the relaxation enhancement induced in the other domain. In the case of R_{AB}, we introduced a cysteine mutation at residue 258 to covalently link the spin label to CBD-B and observe the relaxation enhancement in CBD-A, with the goal of probing the transition between open and closed domain topologies (Fig. 4, B and C).

The PRE data were acquired for four different samples: R_{AB}:$cAMP_2$, R_{AB}:Rp_2, C:R_{AB} and C:R_{AB}:Rp_2 (Fig. 4, E and G to K). The I_{ox}/I_{red} PRE ratios for R_{AB}:$cAMP_2$ correlate well with the distances from residue 258 predicted based on the crystal structure of R_{AB}:$cAMP_2$ (PDB code 1RGS; Fig. 4E) (28), confirming the correct positioning of the spin-label at residue 258 and its efficacy in inducing relaxation enhancements. To probe the inter-domain separation, we focused on the region of CBD-A subject to the largest variations in the distance from residue 258 when going from the C-bound (A_{off}-B_{off}) to the cAMP-bound structure ($A_{on}B_{on}$), *i.e.*, residues 150-230 (Fig. 4G,

cyan trace). We then calculated the average I_{ox}/I_{red} PRE ratios within this region for the R_{AB}:$cAMP_2$, R_{AB}:Rp_2, C:R_{AB} and C:R_{AB}:Rp_2 samples (Fig. 4G, dashed bars).

The average PRE ratios scale in the order: C:R_{AB} > C:R_{AB}:Rp_2 > R_{AB}:Rp_2 > R_{AB}:$cAMP_2$, as expected based on the proposed chemical shift-based Rp-antagonism-agonism model and MD simulations (Fig. 3, Fig. 4. A, D and F, and figs. S4 to S6). Overall, the PRE data consistently confirm the dependence of domain-domain interactions on the intra-domain on-off equilibria predicted by the Rp-antagonism-agonism switch mechanism (Fig. 3, A to F), *i.e.* they confirm that the probability of having CBD-A and/or CBD-B in the 'off' state scales with the weakening of the inter-domain interactions. We then utilized the validated Rp-antagonism-agonism switch mechanism (Fig. 3, A to F) to build and parametrize a general Ensemble Allosteric Model (EAM) (33, 34) of pluripotent allostery for PKA, which enables quantitative predictions of kinase activity and therefore stringent comparisons to data from kinase assays.

2.4.6 A Quantitative Ensemble Allosteric Model (EAM) of Pluripotent Allostery in PKA

In order to quantitatively relate the R_{AB} dynamics (Fig. 3) to the regulation of kinase function, we built an EAM of PKA inhibition and activation, as explained in the Supplementary Text (Section S2). The EAM relies on four sets of input parameters (table S1): *i.* the 'on' *vs.* 'off' free energy difference for each apo CBD, denoted as ΔG_A and ΔG_B; *ii.* the state-specific association constants of Rp for each isolated domain; *iii.* the free energy of interaction between the two CBDs both in the 'on' state with CBD-A bound to the cyclic nucleotide, denoted as ΔG_{AB}; *iv.* the state-specific affinities of the C subunit for R_{AB}. The key assumptions of our EAM are that (*a*) ΔG_A and ΔG_B are not affected by C- or cNMP-binding; (*b*) ΔG_{AB} is not affected by binding of C or a second cNMP molecule to CBD-B; (*c*) the inhibition of PKA arises uniquely from R binding C and competing with the kinase substrates; (*d*) allosteric effectors act by controlling the affinity of R for C.

The EAM input parameters were measured based on the populations and free energies determined by NMR chemical shift analyses and by H/D exchange protection factors for WT *vs.* W260A, as explained in the Supplementary Materials (Text Section S3, table S1, and figs. S1 and S2). In addition, a single scaling factor (γ) was introduced for the state-specific association constants of the C subunit (table S1), to account for the dependence of the R:C affinity on the

concentration of MgATP (29). For example, at low [MgATP], the effective R:C affinity decreases, requiring γ values < 1. Based on input parameters *i.-iv.* (table S1), we modeled how cyclic nucleotide binding rescales the normalized thermodynamic statistical weights for each of the 18 possible states of the R_{AB} ensemble, resulting from the combination of on/off, open/close and apo/holo equilibria for the two domains in R_{AB} (table S2). Starting from the ensembles of both apo and cyclic nucleotide-bound R_{AB}, we utilized binding polynomials to compute R:C affinities in both scenarios, which were in turn used to calculate the change in kinase activity occurring upon addition of cyclic nucleotides (Supplementary Text and fig. S7).

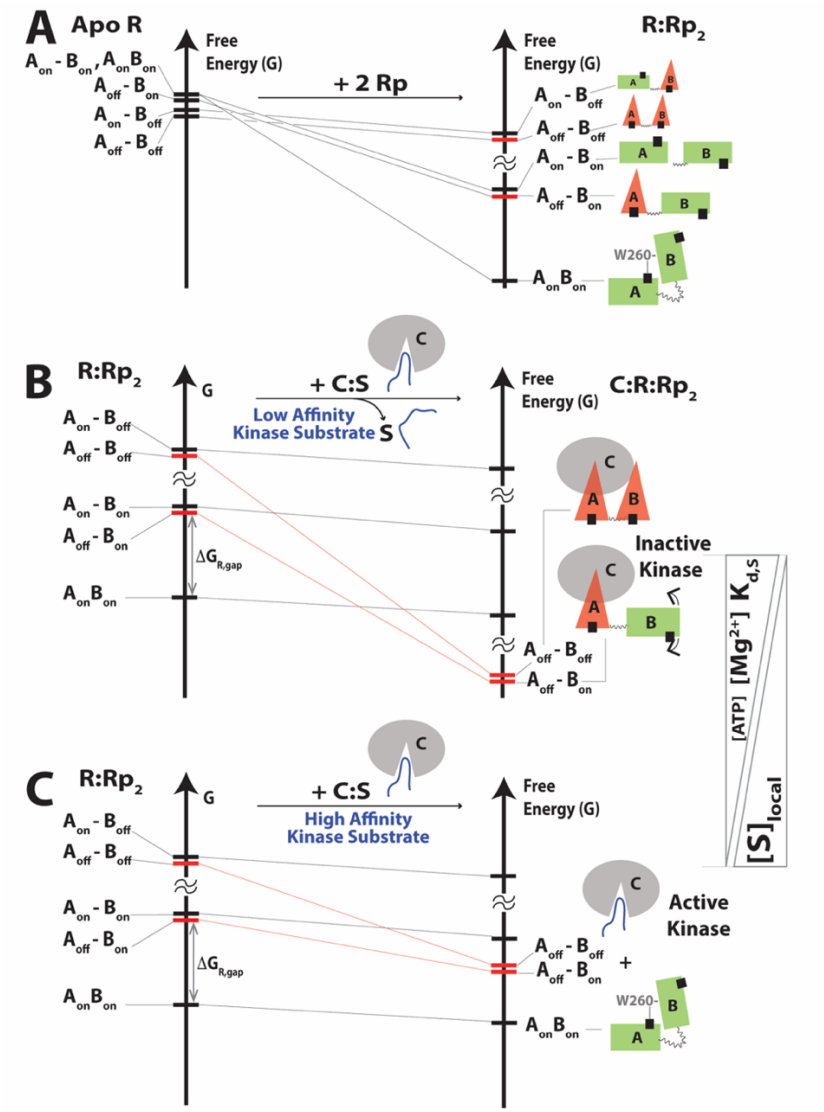

Figure 5. *Remodeling of the Free Energy Landscape of apo R_{AB} by Rp and the PKA C-Subunit Explains Allosteric Pluripotency.* **(A)** Effect of Rp binding on the ensemble of states accessible to apo R_{AB}. As the Boltzmann populations of the state decrease, the size of the cartoon is reduced. The inhibitory-competent conformations of R_{AB}:Rp_2 (red) are excited states. **(B)** Effect of PKA C-subunit binding on the ensemble of states accessible to R_{AB}:Rp_2. If the binding of the substrate to the kinase is sufficiently weak and the MgATP level is sufficiently high, the inhibitory states "A_{off} – B_{off}" and "A_{off} – B_{on}" become the most stable conformations of R_{AB} in the C:R_{AB}:Rp_2 ensemble. The kinase is inactive. $\Delta G_{R,gap}$ is the inhibitory excited *vs.* non-inhibitory ground state free energy difference. **(C)** In the case of substrates that bind C with sufficiently high affinity to compete with R_{AB} or when the MgATP level decreases, due to the lower effective affinity of R_{AB}:Rp_2 for C, the most stable conformation of R_{AB} accessible to the C:R_{AB}:Rp_2 ensemble is the "$A_{on}B_{on}$" state, which is non inhibitory. Hence, the kinase is active.

To illustrate how the EAM explains the pluripotent allostery of PKA, we simulated how the free energy hierarchy of the states accessible to the apo R_{AB} ensemble is remodeled by Rp and C-subunit binding (Fig. 5). When excess Rp binds to apo R_{AB} in the absence of C, the $A_{on}B_{on}$ closed state, the ground state, while the remaining states, which include the inhibitory-competent states (*i.e*. the A_{off}-B_{off} and A_{off}-B_{on} states), are at excited free energy levels (Fig. 5A). When the C-subunit is introduced, the R_{AB}:Rp_2 free energy level hierarchy is further remodeled according to the effective affinity of C for R_{AB}.

When the effective R_{AB}:C affinity is high, *e.g.* presence of excess [MgATP] and a competing kinase substrate with low affinity and/or concentration, the free energy levels of the excited inhibitory states are lowered to the ground level by C binding, resulting in the formation of a stable C:R_{AB}:Rp_2 complex and PKA inhibition (Fig. 5B). When the effective R_{AB}:C affinity is low, *e.g.* lower [MgATP] or presence of a competing substrate with high affinity and/or concentration, then the inhibitory states are not sufficiently stabilized by C binding to reach the ground level. In this case, the C:R_{AB}:Rp_2 inhibitory complex is unstable, resulting in PKA activation (Fig. 5C). Hence, we hypothesize that not only the concentration of MgATP, but also the affinity and concentration of the kinase substrate modulate the effect of Rp on PKA and trigger the Rp-antagonism-agonism switch. In order to test this EAM-based prediction on the determinants of pluripotent allostery and further validate the model, we compared the fractional changes in kinase activity (ϕ) computed through the EAM to experimental data from kinase assays.

2.4.7 The MgATP Concentration and Kinase Substrate Affinity Control the Pluripotent Allostery of PKA by Remodeling the Free Energy Landscape of the R-Subunit

In order to test our predictions on how the MgATP concentration and the affinity of competing kinase substrates modulate the activity of Rp bound PKA, we first computed the Rp-dependent kinase activity (ϕ) in the presence ($\gamma = 1$) and in the absence of high [MgATP] ($\gamma = 10^{-3}$) using the EAM and the measured input parameters (table S1). The predicted dose-dependent kinase activity profiles clearly reflect the antagonism-agonism switch of PKA by Rp-cAMPS (Fig. 6A), in agreement with previous observations (11). In fact, the K_a values and the Hill coefficient predicted from the EAM are in excellent agreement with the experimental values measured for full-length R1a subunit (Fig. 6A) (11), validating the EAM. Furthermore, based on the EAM, it is possible to dissect the determinants of pluripotent allostery. For example, the EAM model

reveals that when the effective R:C affinity is weak ($\gamma = 10^{-3}$), partial activation surprisingly remains even in the absence of inter-domain interaction ($\Delta G_{AB} = 0$ RT). Considering that CBD-A is in the 'off' state when the two tandem domains don't interact (Fig. 3, A to F), this means that the main drivers of the antagonism-to-agonism switch observed for the PKA – Rp system are both domain-domain interactions and the ability of Rp to shift CBD-B to the 'on' state. The significant contribution of CBD-B to the activation of PKA was largely unexpected given the homology between the two tandem domains (28).

We also hypothesized that increasing the apparent affinity of the kinase substrates triggers the antagonism-to-agonism switch of Rp, as kinase substrates and the inhibitory linker of R compete for the active site of C, thus weakening the effective R:C affinity. In order to test this hypothesis, we utilized two substrates with different apparent affinities: PKS ($K_m = 1.5 \pm 0.2$ μM) and PKS2 ($K_m = 26 \pm 4$ μM) (Fig. 6, B and C) and we compared the respective experimental kinase activities to the EAM predictions (Fig. 6E). As expected from our hypothesis, upon binding of excess Rp, almost full agonism is observed with the high affinity substrate (*i.e.* PKS), while only partial agonism is observed with the low affinity substrate (*i.e.* PKS2). Moreover, the predicted kinase activities from the EAM are in agreement with the experimental values measured for full-length R1a subunit, further validating the relevance of our model of pluripotent allostery for the full-length integral PKA system.

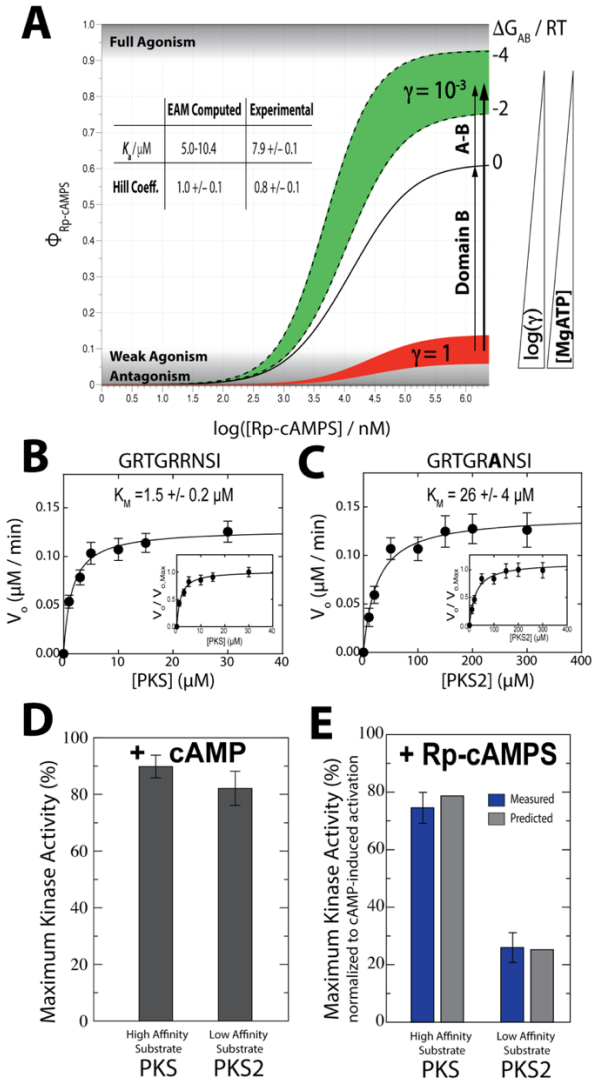

Figure 6. *Changes in MgATP and/or Substrate Affinity Trigger the Rp Antagonism-to-Agonism Switch for PKA R1a.* **(A)** Antagonism-to-agonism switch triggered by [MgATP] reduction. Dose-dependent kinase activation (ϕ) in the presence (red, $\gamma = 1$) and absence of MgATP (green, $\gamma = 10^{-3}$). The γ scaling factor models the reduction in R:C affinity occurring upon removal of MgATP (table S1). **(B-E)** Antagonism-to-agonism switch triggered by substrate affinity increases. The substrates PKS and PKS2 exhibit K_m values different by ~one order of magnitude (B, C) and the increase in apparent affinity causes a switch to almost full agonism for Rp-cAMPS (E), while cAMP acts as an activator for both substrates, irrespective of the apparent affinity (D). In panel (E) blue bars are from kinase assays, while gray bars are computed based on the EAM (see Materials and Methods). Error bars reflect the standard deviation from triplicate measurements.

2.5 Discussion

2.5.1 An Ensemble Allosteric Model of Pluripotent Allostery in PKA

Based on our comparative NMR analysis of C:R_{AB}:Rp_2, R_{AB}:Rp_2, W260A R_{AB}:Rp_2, R_{AB}:$cAMP_2$ and apo R_{AB}, we propose an ensemble model of pluripotent allostery for PKA (Fig. 5). The proposed model addresses the long standing question of why Rp functions as an antagonist under some conditions, but as an agonist under others. The main difference between R_{AB}:$cAMP_2$ and R_{AB}:Rp_2 lies in the free energy gap between the inhibitory-competent excited states (A_{off}-B_{on} and A_{off}-B_{off}) and the inhibitory-incompetent ground state ($A_{on}B_{on}$), which is common to both ternary complexes. This free energy gap is denoted here as $\Delta G_{R,gap}$. The $\Delta G_{R,gap}$ is lower in R_{AB}:Rp_2 than in R_{AB}:$cAMP_2$ and when the C-subunit binds the A_{off}-B_{on} and A_{off}-B_{off} states of R_{AB} with high affinity (*e.g.* in the presence of excess MgATP), they become more stable than the $A_{on}B_{on}$ state, resulting in the formation of the C:R_{AB}:Rp_2 inhibited complex and in Rp antagonism (Fig. 5B). When the affinity of the C-subunit for the excited inhibitory states is reduced (*e.g.* in the absence of excess MgATP), the $A_{on}B_{on}$ state remains the ground state even in the presence of C and a stable inhibited complex cannot form, leading to Rp agonism (Fig. 5C). In the case of R_{AB}:$cAMP_2$, the free energy gap between the inhibitory-competent excited states and the inhibitory-incompetent ground state is too large to result in antagonism, even in the presence of excess MgATP.

The proposed model not only provides a simple but general rationalization of pluripotent allostery, but it also offers an unprecedented view of the previously elusive C:R_{AB}:Rp_2 quaternary inhibitory complex, resolving prior apparent discrepancies in the available R_{AB} crystal structures. We show that while the C:R_{AB}:Rp_2 complex locks CBD-A in its off state, CBD-B samples a degenerate free energy landscape with comparable populations of 'on' and 'off' states (Fig. 3F and Fig. 5B). When in the 'on' state, CBD-B is disengaged from both the C-subunit and CBD-A and becomes inherently dynamic, explaining why the C:R_{AB}:Rp_2 complex is refractory to crystallization attempts. Interestingly, the A_{off}-B_{on} R_{AB} state in the C:R_{AB}:Rp_2 complex (Fig. 3F) resembles a transient cAMP-binding intermediate (Fig. 3H), given the B-to-A binding order of cAMP, which is opposite to Rp. Our model also explains why the crystal structures of R_{AB}:$cAMP_2$ and R_{AB}:Rp_2 are virtually identical (Fig. 1H) and why in the absence of CBD-B, CBD-A adopts similar conformations when bound to C or 8-Br-Rp-cAMPS (35). The R_{AB}:$cAMP_2$ and R_{AB}:Rp_2 complexes share similar ground states with a closed topology, stabilized by inter-domain

interactions that selectively favor the $A_{on}B_{on}$ state (Fig. 5A). However, upon deletion of CBD-B, the CBD-A/B contacts are lost and Rp-bound CBD-A samples the 'off' state, as in the open topology of R_{AB}:Rp_2. Hence, our model is fully consistent with the previous crystallographic data. While these structures offer an essential framework to understand the interactions between Rp and the ground states of the R-subunit, it is clear that dynamics of the excited states sampled by R must be factored in to explain the inhibitory mechanism of Rp and pluripotent allostery in general (Fig. 5).

Another unique aspect of the model of Figure 5 is that it unveils the key drivers of pluripotent allostery in PKA. The proposed EAM shows that agonism is driven by two key factors. First, Rp acts as an agonist for the isolated CBD-B, but as an antagonist for the isolated CBD-A. The CBD-B agonism was unexpected given the homology between the two tandem CBDs, but it is a primary driver of PKA activation because it reduces the affinity of R for C (Fig. 6A). Second, the A/B interdomain interactions promote agonism as they selectively stabilize the inhibitory-incompetent $A_{on}B_{on}$ ground state with a closed inter-domain topology relative to the excited states with open topologies (Fig. 5A), as consistently shown by both MD simulations and PRE experiments (Fig. 4 and figs. S4 to S6). Together, the Rp-induced stabilization of the 'on' state of CBD-B and the CBD-A/B interactions favor agonism, while the Rp-induced stabilization of the 'off' state of CBD-A promotes antagonism. The balance between these agonism- and antagonism-driving interactions controls the free energy gap that separates the excited inhibitory states from the ground non-inhibitory state of R_{AB}:Rp_2 ($\Delta G_{R,gap}$). The $\Delta G_{R,gap}$ defines a critical threshold that must be overcome by the R:C affinity in order for antagonism to prevail over agonism (Fig. 5, B and C).

2.5.2 Metabolomic, Proteomic and Genomic Triggers of Pluripotent Allostery in PKA

Based on the proposed threshold model of pluripotent allostery, the antagonism-agonism switch occurs whenever the binding free energy for the association of the C-subunit with the R-subunit inhibitory excited states exceeds the $\Delta G_{R,gap}$ (Fig. 5, B and C). This simple notion not only addresses the long-outstanding question of why the allosteric response of PKA to Rp is MgATP-dependent (Fig. 6A), but it also reveals that the pluripotent allostery of PKA is a general phenomenon, with the antagonism-agonism switch controlled by other factors as well. These include the concentration and apparent affinity of kinase substrates (Fig. 6, B to E) and

disease-related genetic mutations that weaken the R:C affinity. For example, Cushing's syndrome driver mutations reduce the affinity of C for R, leading to aberrant constitutive activation of PKA (36). The Rp antagonism observed for WT PKA may suggest that Rp offers a viable means to reduce the overactivation of PKA typical of Cushing's disease. However, given the marginal binding free energy between the mutated C-subunit and R, our pluripotent allosteric model indicates that Rp is more likely to function as an agonist for Cushing's patients.

The Cushing's example illustrates the need to redefine the concept of allosteric drug target beyond the allosteric receptor to also account for conditions. The definition of allosteric target should include also the local metabolomic (*e.g.* MgATP), proteomic (*e.g.* kinase substrates) and genomic (*e.g.* disease-related mutations) contexts, as they serve as critical determinants of pluripotent allostery. An important implication of this broader redefinition of allosteric drug target is that the response to a given stimulus by a given receptor may vary depending on sub-cellular localization and on the specific signalosome in which PKA is integrated. Sub-cellular localization and signalosomes dictate the effective local concentrations and types of substrates and metabolites to which PKA is exposed (37, 38), potentially affecting pluripotent allostery.

2.5.3 Concluding Remarks

We have shown that the allosteric response of the prototypical cAMP-dependent kinase cannot be recapitulated by a simple on-off switch as in traditional allostery, but is more similar to a three-way switch. In the latter, the response to one on-off switch is contingent upon another switch, as expected for pluripotent allostery. We show that one of the simplest but most effective explanations of such pluripotent allostery is a threshold response model in which the outcome of a given allosteric stimulus depends primarily on the free energy gap that separates the excited inhibitory states from the ground non-inhibitory state of the cNMP-bound R-subunit ($\Delta G_{R,gap}$). Notably, if both tandem domains responded similarly to Rp, $\Delta G_{R,gap}$ would be either too low or too high relative to the free energy of R:C binding, resulting in either antagonism or agonism irrespective of experimental conditions. However, the differential response of the two CBDs to Rp ensures that $\Delta G_{R,gap}$ is tuned to values more similar to the effective free energy of R:C association, leading to pluripotent allostery.

As part of the pluripotent allosteric model of PKA, we have mapped through NMR the sought-after dynamic conformational ensembles of the R_{AB}:Rp_2 and C:R_{AB}:Rp_2 complexes. These ensembles serve as the foundation for a model of kinase pluripotent allostery, which in turn enables quantitative predictions of kinase activity based on EAM input parameters measured through NMR. Hence, the approaches utilized here illustrate a general strategy, in which ensemble allosteric models bridge between dynamics as revealed by NMR and function as measured by enzyme assays. We anticipate the results and the experimental design proposed here to be transferable to other multidomain proteins functioning as molecular switches and signal transducers.

2.6 Materials and Methods

Materials and Protein Expression and Purification

Rp-cAMPS (>99% purity) was purchased from Biolog, while cAMP (>98.5% purity) was purchased from Sigma and S-(1-oxyl-2,2,5,5-tetramethyl-2,5-dihydro- 1H-pyrrol-3-yl) methyl methanesulfonothioate (MTSL) was purchased from Toronto Research Chemicals. PKA R1a (91-379, 33 kDa) , (119-379, 29 kDa) and (91-244, 17 kDa) constructs were expressed and purified according to previously published protocols (32, 39). PKA C-subunit (40 kDa) was expressed (32) or purchased (P2645, Sigma-Aldrich). AMP-PNP was purchased from Sigma. The kinase substrates, PKS (GRTGRRNSI) and PKS2 (GRTGRANSI), were synthesized and purchased from GenScript. The Kinase-Glo reagents were purchased from Promega.

General NMR Spectroscopy

NMR data were acquired on a Bruker Avance 700 MHz spectrometer equipped with a 5-mm TCI cryo-probe. Unless otherwise specified, we processed the NMR data either using NMRpipe or Bruker's Topspin with linear prediction, and a resolution enhancing 60° shifted sine squared bell window function. Spectral analysis was implemented in NMRFAM-SPARKY using Gaussian line-fitting. All experiments were acquired at 306 K in the NMR buffer (50 mM MOPS pH 7.0, 100 mM NaCl, 10 mM $MgCl_2$, 5 mM DTT, and 0.02 % sodium azide) with 5% ^2H_2O, unless otherwise specified. TROSY triple-resonance 3D experiments (*i.e.* CBCA(CO)NH, HNCACB, HNCA and HN(CO)CA) and/or spectral comparisons, if no ambiguities were present, were utilized for spectral assignments

Chemical Shift Analyses

Uniformly ^{2}H,^{15}N-labeled PKA R1a (91-379) wild type, W260A and (91-244) wild type were concentrated to 50 or 100 µM in the NMR buffer (50 mM MOPS, pH 7.0, 100 mM NaCl, 10 mM $MgCl_2$, 5 mM DTT, with or without 1 mM cAMP or 2 mM Rp-cAMPS, 0.02 % sodium azide and 5 % $^{2}H_2O$). The C-subunit-bound R1a (91-379) complex was prepared with 1 mM AMP-PNP (Sigma-Aldrich) and with or without 2 mM Rp-cAMPS in the NMR buffer, as previously described (32). Transverse-relaxation optimized spectroscopy (TROSY) 2D experiments were recorded using 12 or 16 scans and a recycle delay of 1.7s with 80 and 1024 complex points and spectral widths of 31.8 and 15.9 ppm for the ^{15}N and ^{1}H dimensions, respectively. CHEmical Shift Projection Analyses (CHESPA) were implemented as previously described (32). The positions of the 'on' *vs.* 'off' equilibria of W260A R1a (91-379), wild type R1a (91-379) and C-bound wild type R1a (91-379) were evaluated through chemical shift correlation slope analyses in the presence of 2 mM Rp-cAMPS to ensure both Rp-cAMPS binding sites were saturated. Residues 156, 157, 159, 162, 179, 215, 216, 217, 220, 221, 223 were used for the CBD-A chemical shift correlation analyses and residues 293, 296, 297, 317, 320, 339, 340, 343, 345, 347 were used for CBD-B.

Measurement of R1a Domain-Specific K_D Constants of Rp-cAMPS

Binding of Rp-cAMPS to the apo and C-bound R1a (91-379) were monitored by titration of Rp-cAMPS into 30 µM apo ^{2}H, ^{15}N-labeled R1a (91-379) or 50 µM ^{2}H, ^{15}N-labeled R1a (91-379):C samples and acquiring for each titration point ^{15}N-^{1}H 2D TROSY spectra using 128 scans and a recycle delay of 1.7s with 80 and 1024 complex points and spectral widths of 31.8 and 15.9 ppm for the ^{15}N and ^{1}H dimensions, respectively. Peak intensity or chemical shifts were measured for the probe residues N186, G193 and S297 to extract the K_D values of Rp-cAMPS for CBD-A and CBD-B. The K_D constants of Rp-cAMPS for R1a (91-379):C were determined from binding isotherms built through chemical shift changes, as the bound/unbound exchange is fast in the Rp-cAMPS titration into R1a (91-379):C (fig. S3). The K_D constants of Rp-cAMPS for apo R1a (91-379) were determined from binding isotherms built through cross-peak intensities, as the bound/unbound exchange is slow in the Rp-cAMPS titration into apo R1a (91-379) (fig. S3). Dilution effects for the titration of the apo R1a (91-379) sample were corrected by using a peak of a residue in the β-barrel that did not undergo significant chemical shift change upon binding of Rp-cAMPS (*i.e.* R340).The intensity or chemical shift change of the last titration point was used

for normalization to calculate the domain-specific fraction bound (<*v*>). The domain-specific dissociation constants and respective errors were estimated through linear Scatchard regressions.

H/D Exchange Experiments

Protection Factor (PF) values were measured by NMR monitored H/D amide exchange for the wild type and the W260A mutant of the R1a (119-379) construct. For this purpose, the protein was concentrated to 100 µM in 50 mM MES (pH 6.5), 100 mM NaCl, 5 mM DTT, 2 mM EDTA, 2 mM EGTA, 0.02 % sodium azide and 5 % $^{2}H_2O$. The cAMP-bound sample was prepared by adding excess 100 µM cAMP. Heteronuclear single-quantum coherence (HSQC) spectra using a recycle delay of 1.0 s with 128 and 1024 complex points and spectral widths of 31.8 ppm and 15.9 ppm for the ^{15}N and ^{1}H dimensions, respectively, were recorded. For the first 30 HSQC spectra, 4 scans were acquired, while for the remaining 60 HSQC spectra 8 scans were utilized. To provide data points for the slow decaying peaks, additional HSQC spectra were acquired once per week. H/D exchange rates were measured using Levenberg-Marquardt non-linear least square exponential fitting, as previously described (39). The maximal protection factor (PF) value for domain A (*i.e.* residues 119-244) was determined by identifying first the maximum logPF value and then selecting other CBD-A logPF values that fell within error from the maximum. The average and the standard deviation of the logPF values selected according to this protocol were utilized as the $logPF_{max}$ and the related error, respectively, in both WT and W260A R1a (119-379) constructs. The WT *vs.* W260A difference in the average $logPF_{max}$ values resulted in the $\Delta logPF_{max}$ utilized for equation (56) (Supplementary Text S3).

Paramagnetic Relaxation Enhancement Analysis

Position 258 was selected as spin-label attachment point as it meets multiple requirements for optimal PRE measurements. Residue 258 is sufficiently removed from the C and cAMP binding sites and the inter-domain interfaces to avoid significant perturbations of these interactions by the introduction of the mutation and of the spin-labeled cysteine (Fig. 4B). Residue 258 is also sufficiently distant from CBD-A in the absence of inter-domain interaction (>30Å; Fig. 4B), but sufficiently close to CBD-A in the presence of inter-domain interaction (<30Å; Fig. 4C) to efficiently probe by PRE the transition between open and closed domain topologies.

R1a (91-379) includes two Cysteines and both are located in CBD-B (*i.e.* residue 345 and 360). These cysteines are shielded from solvent in both the cAMP- and C-bound structures (pdb: 1RGS and 2QCS, respectively), exhibiting SASA values of 1.73 $Å^2$ (residue 345) and 1.96 $Å^2$ (residue 360) in the 1RGS structure and 1.23 $Å^2$ (residue 345) and 1.17 $Å^2$ (residue 360) in the 2QCS structure. Thus, we expect minimal or negligible attachment of MTSL to these Cysteines.

The Asp258Cys PKA R1a (91-379) mutant was prepared according to the protocol used for WT R1a 91-379. The reducing reagent in the buffer was removed using a PD10 column before the addition of the spin label (1- 1-oxyl-2,2,5,5-tetra-methyl-pyrroline-3-methyl-16methanethiosulfonate; MTSL). The reduced Asp258Cys PKA R1a (91-379) was incubated with threefold molar excess of MTSL for 3h at room temperature. Excess MTSL was then removed with a PD10 column. The protein sample was then concentrated to 30 µM and 2 mM of cAMP or Rp-cAMPS were added. For the R1a (91-379):C and R1a (91-379):C:Rp_2 samples, the MTSL was first covalently attached to the Asp258Cys R1a (91-379) mutant, as described above. After removing the excess MTSL with a PD10 column, the R:C complex was formed by incubating the Asp258Cys R1a (91-379) attached to MTSL with 1.5 molar excess of C-subunit overnight at 4 °C in the presence of 1 mM AMP-PNP and then performing Size Exclusion Chromatography (SEC) to isolate the R:C complex. ^{15}N-^{1}H 2D TROSY spectra using a recycle delay of 1.7s with 80 and 1024 complex points and spectral widths of 31.8 and 15.9 ppm for the ^{15}N and ^{1}H dimensions, respectively, were acquired for the paramagnetic samples. To obtain the diamagnetic control, 5 mM DTT was added and incubated for 1 h at room temperature, after which we re-acquired TROSY spectra. The total data acquisition time for PRE experiments was 30 h for each complex, resulting in partial signal losses, presumably from partial aggregation of proteins, that needed to be corrected for a reliable analysis of PRE experiments. For this purpose, two independent approaches were taken. The first approach was to quantify the extent of sample decay by monitoring the residue-specific cross-peak intensities over time through the acquisition of multiple replicate TROSY spectra for each sample (*i.e.* oxidized or reduced). The average intensity loss was then calculated for both the oxidized (paramagnetic) and the reduced (diamagnetic) samples. Based on the average intensity losses, the sample decay occurring during PRE data acquisition was quantified and used to correct the PRE intensities accordingly. The second approach was taken to validate the first method and relies on the residues in β7 of

CBD-B, which do not undergo changes in distance from 258 in the 'off' and the 'on' conformations. These residues were used as reference to normalize all other residues. For all four complexes analyzed by PRE (R:C, R:C:Rp_2, C:Rp_2 and R:$cAMP_2$) the two approaches resulted in oxidized *vs.* reduced ratios within experimental error. The analysis resulting from the first approach was used for the PRE plots in Fig. 4, E and G to K. The error bars were generated starting from the errors on the intensities estimated using the signal-to-noise ratios of each peak and propagating these errors to the PRE intensity ratios (I_{ox}/I_{red}).

Measurement of Michaelis-Menten Constants Through Kinase Assay

Phosphorylation in the presence of 10 nM PKA C-subunit (P2645, Sigma-Aldrich) and increasing concentration of PKS (GRTGRRNSI; 0 µM – 30 µM; Genscript) or PKS2 (GRTGR**A**NSI; 0 µM – 300 µM; Genscript) was allowed to progress for 25 min in 50 µL of the assay buffer (40 mM Tris pH 7.5, 20 mM $MgCl_2$, 10 µM ATP, 0.1 mg/mL BSA). To reach the final reacting concentrations stated above, we diluted the stock concentrations of PKA C-subunit and the substrates 10-fold. The kinase-catalyzed reaction was terminated by adding 50 µL of the Kinase-Glo Luciferase Reagent (Promega) and was incubated for 10 min at room temperature before measuring the luminescence with a BioTek CYTATION 5 spectrophotometer in triplicates. The Michaelis-Menten constant (K_m) was determined through a non-linear fitting of the V_o *vs.* [S] plot using the Michaelis-Menten equation ($V_o = V_{o.max}$ [S]/(K_m+[S]).

Measurement of PKA Holoenzyme Activation by cAMP and Rp-cAMPS

Full-length PKA R1a (1-379) was purified following a protocol previously described (40). The activity of PKA C subunit (P2645, Sigma-Aldrich) was determined by the luminescent kinase assay (Kinase Glo, Promega). The reaction mixture of 10 nM PKA C-subunit, 12 nM R1a (1-379) and 50 µM cAMP or 100 µM Rp-cAMPS was prepared in 40 mM Tris (pH 7.5), 20 mM $MgCl_2$, 10 µM ATP, 0.1 mg/mL BSA. The reaction mixture was incubated for 15 min at room temperature, after which 50 µM substrate (PKS or PKS2) was added and allowed to react for 2 h in 50 µL of the reaction mixture. To reach the final reacting concentrations stated above, we diluted the stock concentrations of PKA C-subunit, PKA R1a, cyclic nucleotides and the substrates 10-fold. The kinase-catalyzed reaction was terminated by adding 50 µL Kinase-Glo Luciferase Reagent (Promega) and was incubated for 10 min at room temperature before measuring the

luminescence with a BioTek CYTATION 5 spectrophotometer in triplicates. The relative kinase activity was calculated by normalizing based on the luminescence values corresponding to maximum activity of C (*i.e.* in the absence of R1a and cNMP) and maximum inhibition of C (*i.e.* in the presence of R1a but in the absence of cNMP), as per equation (41) (Supplementary Text S2). The kinase activation data measured under these experimental conditions are consistent with ΔG_{AB} and γ values of -4 (-2) RT and 0.4 (0.07), respectively.

Molecular Dynamics (MD) Simulations

MD simulations in explicit solvent were performed starting from several "hybrid" structures of the PKA R1a (91-379) construct containing both CBDs of PKA R1a, either unbound or in complex with the PKA 1a catalytic subunit (C-subunit; fig. S4 and table S3). The initial conformations for the simulations were constructed based on X-ray crystal structures of the R-subunit with Rp-cAMPS ligands bound to both CBD domains (representing the 'on' state of each CBD; PDB ID "1NE4"), and the R-subunit/C-subunit complex without bound Rp-cAMPS (representing the 'off' state of each CBD; PDB ID "2QCS"). The simulations starting from the "1NE4" and "2QCS" X-ray structures served as controls during analysis (fig. S4 and table S3). With the exception of the 2QCS control structure, all structures were simulated with Rp-cAMPS ligands bound to both CBD domains (table S3), and when Rp-cAMPS needed to be added to the 2QCS-derived CBD-A and CBD-B domains, the addition was achieved *via* overlay of the CBD-A and CBD-B domains with PDB structures "3PLQ" and "1NE4", respectively (23, 35).

Initial Structure Preparation for MD Simulations

A construct spanning residues 91-379 of R1a was used for the Rp-cAMPS-bound R-subunit simulations, and an additional construct spanning residues 13-350 of the PKA 1a C-subunit was included for all C-subunit-bound R-subunit simulations (fig. S4 and table S3). Initial structures for the 1NE4 and 2QCS structure control simulations (fig. S4, A and F) were obtained by first deleting all water molecules, and any R-subunit residues N-terminal to residue 91 or C-terminal to residue 379, from the respective PDB structures, and using SwissPDB Viewer to reconstruct partially missing side chains on the protein surface (41). In addition, other non-protein components besides bound Rp-cAMPS were deleted from the structures, with the exception of bound AMP-PNP and Mn^{2+} ligands found in the C-subunit of the 2QCS PDB

structure, which were modified to ATP and Mg^{2+} by editing the PBD text file, in accordance with the conditions used in kinase assays. An Rp-cAMPS-bound version of the 2QCS structure was then obtained by docking Rp-cAMPS ligands into both CBD domains (table S3). The docking of Rp-cAMPS into the CBD-A domain was achieved by overlaying the X-ray structure of the 8-Br-Rp-cAMPS-bound CBD-A domain (PDB ID "3PLQ") onto the CBD-A domain of the 2QCS structure at residues 152-226 (*i.e.* the CBD-A β-core), deleting the 8-Br substituent to obtain bound Rp-cAMPS, while docking of Rp-cAMPS into the CBD-B domain was achieved by overlaying the "1NE4" X-ray structure onto the CBD-B domain of the 2QCS structure at the CBD-B base-binding region (BBR; *i.e.* residues 297-302 and 311-316) and phosphate binding cassette (PBC; *i.e.* residues 323-335) regions. An Rp-cAMPS-bound version of the 2QCS structure R-subunit lacking the bound C-subunit was also constructed, by deleting the atomic coordinates for the C-subunit (and its bound ATP and Mg^{2+} ligands) from the Rp-cAMPS-bound 2QCS structure (fig. S4C and table S3).

Initial structures for the "hybrid" structure simulations were obtained from the 1NE4 control and Rp-cAMPS-bound 2QCS structures by grafting the CBD-B domain from the 1NE4 control structure onto the CBD-A domain of the Rp-cAMPS-bound 2QCS structure *via* backbone superimposition at three different locations along the intervening α-helical region between the two CBD domains, saving the atomic coordinates for the 2QCS-derived CBD-A domain residues and 1NE4-derived CBD-B domain residues as a new structure (fig. S4, C to E, G to I, and table S3). The three graft locations were selected in accordance with kinks that were observed in the intervening α-helical region of the 1NE4 structure, but not in the 2QCS structure, resulting in three distinct CBD-A/CBD-B grafts (fig. S4, C to E, G to I, and table S3). The atomic coordinates for the 2QCS-derived C-subunit (and its bound ATP and Mg^{2+} ligands) were deleted from the grafted structures to obtain the three hybrid R-subunit structures lacking the bound C-subunit (fig. S4, C to E, and table S3), but were retained to achieve the respective C-subunit-bound hybrid structures (fig. S4, G to I, and table S3). Molecular structure topology and CHARMM parameters for Rp-cAMPS were calculated using the SwissParam software, as previously described (42).

MD Simulation Protocol

All MD simulations were performed using a previously described protocol (42) with box dimensions of 108 Å for the 1NE4 control structure, 116 Å for the three hybrid R-subunit

structures, or 134 Å for the C-subunit-bound structures, and utilized 2.1 GHz 32-core Broadwell compute nodes accelerated with two NVIDIA Pascal GPUs per node. These runs were executed for 400 ns at constant temperature and pressure, saving structures every 100000 timesteps (*i.e.* 100.0 ps) for subsequent analysis, resulting in a *total simulation time of 4.0 μs*.

Analysis of PKA Structural Dynamics

As an assessment of R-subunit structural propensities, root-mean-square deviations (RMSDs) from the "1NE4" and "2QCS" X-ray structures were computed for the CBD-A/CBD-B region of the R-subunit (*i.e.* residues 119-357 of PKA R1a), and the CBD-A and CBD-B domains (*i.e.* residues 119-231 and 243-357, respectively), over the course of all simulations. While the simulated PKA structures contain additional structural regions at the N- and C-termini of the R-subunit, these more flexible regions were excluded from the RMSD calculations to avoid the possibility of dynamics in these regions obscuring the structural dynamics of interest. These flexible regions consist of R-subunit residues N-terminal to residue 119 (*i.e.* the N-terminal linker) and C-terminal to residue 357 (i.e. the CBD-B domain C-helix and C-terminal tail, which adopt a more disordered structure in "2QCS"). In addition, RMSDs from the "2QCS" X-ray structure were computed for the CBD-A/CBD-B region of the R-subunit, and the CBD-A and CBD-B domains, together with the bound C-subunit over the course of all C-subunit-bound structure simulations to assess dynamics of the R- and C-subunits relative to one another, and the corresponding RMSDs of the C-subunit alone from the "2QCS" X-ray structure (considering all C-subunit residues present in the structure) were computed to check for structural dynamics (if any) contributed by the C-subunit itself. The first 50 ns in each trajectory were not included in the computations to account for equilibration. Inter-center-of-mass distances between domains were computed as previously described (*42*). As in the RMSD calculations, residues 119-231 and 243-357 of the R-subunit were considered in the calculation of the centers of mass for the CBD-A and CBD-B domains, respectively, while all C-subunit residues present in the structure were considered in the calculation of the center of mass for the C-subunit. As for the RMSD computations, the first 50 ns in each trajectory were excluded.

Summary of Experimental Error Analyses

The errors on the populations of each conformational states were estimated from the errors on the slopes of the linear regressions in Fig. 2, C and D, G and H, M and N. The errors on the dissociation constants (K_D) were estimated from the errors on the slopes of the Scatchard regressions (fig. S3). The errors associated with the Protection Factors (PFs) in Fig. S1 were propagated from the errors on the H/D exchange rates obtained in the exponential fits. The errors on the minor *vs*. major peak intensity ratio of R:Rp_2 and the errors on the WT *vs*. W260A R_{AB}:$cAMP_2$ TROSY intensity ratio were calculated through the standard deviations of the intensity ratios distributions (fig. S1A). Similarly, the errors for the average fractional inhibition of C:R_{AB}:Rp_2 were calculated through the standard deviation of the fractional inhibition distribution from multiple residues (fig. S2A). The errors for the PRE intensity ratios (I_{ox}/I_{red}) were obtained from the errors on the intensities estimated based on the signal-to-noise ratio of each peak and error propagation. The errors for the kinase activities were obtained from the standard deviation of triplicate measurements. Other reported errors were obtained through error propagation. As to the boxplots used for the MD simulation data, the middle, bottom, and top lines of the central box correspond to the median, 25th percentile, and 75th percentile of the data set, respectively, while the whiskers denote points falling within 1.5*IQR above the 75th percentile or below the 25th percentile. The IQR is the difference between the 75th and 25th percentiles. The square symbol within the box and the two "x" symbols represent the mean and the 1st and 99th percentiles of the data set, respectively.

2.7 Acknowledgements

We thank L. Konermann, K. Green, C. Kalodimos, R. Ahmed, N. Jafari, S. Boulton, and K. Van for helpful discussions.

2.8 References

1. De Smet, F., Christopoulos, A., and Carmeliet, P. (2014) Allosteric targeting of receptor tyrosine kinases. *Nat. Biotechnol.* **32**, 1113–1120
2. Wodak, S. J., Paci, E., Dokholyan, N. V, Berezovsky, I. N., Horovitz, A., Li, J., Hilser, V. J., Bahar, I., Karanicolas, J., Stock, G., Hamm, P., Stote, R. H., Eberhardt, J., Chebaro, Y., Dejaegere, A., Cecchini, M., Changeux, J.-P., Bolhuis, P. G., Vreede, J., Faccioli, P., Orioli, S., Ravasio, R., Yan, L., Brito, C., Wyart, M., Gkeka, P., Rivalta, I., Palermo, G., McCammon, J. A., Panecka-Hofman, J., Wade, R. C., Di Pizio, A., Niv, M. Y., Nussinov, R., Tsai, C.-J., Jang, H., Padhorny, D., Kozakov, D., and McLeish, T. (2019) Allostery in Its Many Disguises: From Theory to Applications. *Structure*. **27**, 566–578
3. Cohen, P. (2002) Protein kinases — the major drug targets of the twenty-first century? *Nat. Rev. Drug Discov.* **1**, 309–315
4. Whittier, S. K., Hengge, A. C., and Loria, J. P. (2013) Conformational Motions Regulate Phosphoryl Transfer in Related Protein Tyrosine Phosphatases. *Science (80-.).* **341**, 899–903
5. Saleh, T., Rossi, P., and Kalodimos, C. G. (2017) Atomic view of the energy landscape in the allosteric regulation of Abl kinase. *Nat. Struct. Mol. Biol.* **24**, 893–901
6. Huang, R., Ripstein, Z. A., Rubinstein, J. L., and Kay, L. E. (2019) Cooperative subunit dynamics modulate p97 function. *Proc. Natl. Acad. Sci.* **116**, 158–167
7. Motlagh, H. N., and Hilser, V. J. (2012) Agonism/antagonism switching in allosteric ensembles. *Proc. Natl. Acad. Sci.* **109**, 4134–4139
8. Lu, N. Z., and Cidlowski, J. A. (2005) Translational Regulatory Mechanisms Generate N-Terminal Glucocorticoid Receptor Isoforms with Unique Transcriptional Target Genes. *Mol. Cell*. **18**, 331–342
9. Nguyen, T. T., Ghirlando, R., and Venditti, V. (2018) The oligomerization state of bacterial enzyme I (EI) determines EI's allosteric stimulation or competitive inhibition by α-ketoglutarate. *J. Biol. Chem.* **293**, 2631–2639
10. Boulton, S., Selvaratnam, R., Blondeau, J.-P., Lezoualc'h, F., and Melacini, G. (2018) Mechanism of Selective Enzyme Inhibition through Uncompetitive Regulation of an Allosteric Agonist. *J. Am. Chem. Soc.* **140**, 9624–9637
11. Dostmann, W. R., and Taylor, S. S. (1991) Identifying the molecular switches that determine whether (Rp)-cAMPS functions as an antagonist or an agonist in the activation of cAMP-dependent protein kinase I. *Biochemistry*. **30**, 8710–6
12. Saloustros, E., Salpea, P., Starost, M., Liu, S., Faucz, F. R., London, E., Szarek, E., Song, W.-J., Hussain, M., and Stratakis, C. A. (2017) Prkar1a gene knockout in the pancreas leads to neuroendocrine tumorigenesis. *Endocr. Relat. Cancer*. **24**, 31–40
13. Veugelers, M., Wilkes, D., Burton, K., McDermott, D. A., Song, Y., Goldstein, M. M., La Perle, K., Vaughan, C. J., O'Hagan, A., Bennett, K. R., Meyer, B. J., Legius, E., Karttunen, M., Norio, R., Kaariainen, H., Lavyne, M., Neau, J.-P., Richter, G., Kirali, K., Farnsworth, A., Stapleton, K., Morelli, P., Takanashi, Y., Bamforth, J.-S., Eitelberger, F., Noszian, I., Manfroi, W., Powers, J., Mochizuki, Y., Imai, T., Ko, G. T. C., Driscoll, D. A., Goldmuntz, E., Edelberg, J. M., Collins, A., Eccles, D., Irvine, A. D., McKnight, G. S., and Basson, C. T. (2004) Comparative PRKAR1A genotype-phenotype analyses in humans with Carney complex and prkar1a haploinsufficient mice. *Proc. Natl. Acad. Sci.* **101**, 14222–14227

14. Boikos, S. A., and Stratakis, C. A. (2007) Carney complex: the first 20 years. *Curr. Opin. Oncol.* **19**, 24–29
15. Wit, R. J. W., Hoppe, J., Stec, W. J., Baraniak, J., and Jastorff, B. (1982) Interaction of cAMP Derivatives with the "Stable" CAMP-Binding Site in the CAMP-Dependent Protein Kinase Type I. *Eur. J. Biochem.* **122**, 95–99
16. Poppe, H., Rybalkin, S. D., Rehmann, H., Hinds, T. R., Tang, X.-B., Christensen, A. E., Schwede, F., Genieser, H.-G., Bos, J. L., Doskeland, S. O., Beavo, J. A., and Butt, E. (2008) Cyclic nucleotide analogs as probes of signaling pathways. *Nat. Methods*. **5**, 277–278
17. Taylor, S. S., Ilouz, R., Zhang, P., and Kornev, A. P. (2012) Assembly of allosteric macromolecular switches: lessons from PKA. *Nat. Rev. Mol. Cell Biol.* **13**, 646–658
18. Kim, C., Cheng, C. Y., Saldanha, S. A., and Taylor, S. S. (2007) PKA-I holoenzyme structure reveals a mechanism for cAMP-dependent activation. *Cell*. **130**, 1032–43
19. Huang, L. J., and Taylor, S. S. (1998) Dissecting cAMP Binding Domain A in the R I α Subunit of cAMP-dependent Protein Kinase. *J. Biol. Chem.* **273**, 26739–26746
20. Akimoto, M., McNicholl, E. T., Ramkissoon, A., Moleschi, K., Taylor, S. S., and Melacini, G. (2015) Mapping the Free Energy Landscape of PKA Inhibition and Activation: A Double-Conformational Selection Model for the Tandem cAMP-Binding Domains of PKA RIα. *PLoS Biol.* **13**, e1002305
21. Hao, Y., England, J. P., Bellucci, L., Paci, E., Hodges, H. C., Taylor, S. S., and Maillard, R. A. (2019) Activation of PKA via asymmetric allosteric coupling of structurally conserved cyclic nucleotide binding domains. *Nat. Commun.* **10**, 3984
22. Anand, G. S., Krishnamurthy, S., Bishnoi, T., Kornev, A., Taylor, S. S., and Johnson, D. A. (2010) Cyclic AMP- and (Rp)-cAMPS-induced conformational changes in a complex of the catalytic and regulatory (RI{alpha}) subunits of cyclic AMP-dependent protein kinase. *Mol. Cell. Proteomics*. **9**, 2225–37
23. Wu, J., Jones, J. M., Nguyen-Huu, X., Ten Eyck, L. F., and Taylor, S. S. (2004) Crystal structures of RIalpha subunit of cyclic adenosine 5′-monophosphate (cAMP)-dependent protein kinase complexed with (Rp)-adenosine 3′,5′-cyclic monophosphothioate and (Sp)-adenosine 3′,5′-cyclic monophosphothioate, the phosphothioate analogues of cA. *Biochemistry*. **43**, 6620–9
24. Marsiglia, W. M., Katigbak, J., Zheng, S., Mohammadi, M., Zhang, Y., and Traaseth, N. J. (2019) A Conserved Allosteric Pathway in Tyrosine Kinase Regulation. *Structure*. **27**, 1308-1315.e3
25. Bonin, J. P., Sapienza, P. J., Wilkerson, E., Goldfarb, D., Wang, L., Herring, L., Chen, X., Major, M. B., and Lee, A. L. (2019) Positive Cooperativity in Substrate Binding by Human Thymidylate Synthase. *Biophys. J.* **117**, 1074–1084
26. De Simone, A., Richter, B., Salvatella, X., and Vendruscolo, M. (2009) Toward an accurate determination of free energy landscapes in solution states of proteins. *J. Am. Chem. Soc.* **131**, 3810–1
27. Narayanan, C., Bernard, D. N., Bafna, K., Gagné, D., Chennubhotla, C. S., Doucet, N., and Agarwal, P. K. (2018) Conservation of Dynamics Associated with Biological Function in an Enzyme Superfamily. *Structure*. **26**, 426-436.e3
28. Su, Y., Dostmann, W. R., Herberg, F. W., Durick, K., Xuong, N. H., Ten Eyck, L., Taylor, S. S., and Varughese, K. I. (1995) Regulatory subunit of protein kinase A: structure of deletion mutant with cAMP binding domains. *Science*. **269**, 807–13
29. Herberg, F. W., Dostmann, W. R. G., Zorn, M., Davis, S. J., and Taylor, S. S. (1994) Crosstalk

between Domains in the Regulatory Subunit of cAMP-Dependent Protein Kinase: Influence of Amino Terminus on cAMP Binding and Holoenzyme Formation. *Biochemistry*. **33**, 7485–7494

30. Lu, T.-W., Wu, J., Aoto, P. C., Weng, J.-H., Ahuja, L. G., Sun, N., Cheng, C. Y., Zhang, P., and Taylor, S. S. (2019) Two PKA RIα holoenzyme states define ATP as an isoform-specific orthosteric inhibitor that competes with the allosteric activator, cAMP. *Proc. Natl. Acad. Sci.* **116**, 16347–16356
31. Herberg, F. W., Doyle, M. L., Cox, S., and Taylor, S. S. (1999) Dissection of the Nucleotide and Metal−Phosphate Binding Sites in cAMP-Dependent Protein Kinase †. *Biochemistry*. **38**, 6352–6360
32. Akimoto, M., Selvaratnam, R., McNicholl, E. T., Verma, G., Taylor, S. S., and Melacini, G. (2013) Signaling through dynamic linkers as revealed by PKA. *Proc. Natl. Acad. Sci. U. S. A.* **110**, 14231–6
33. Motlagh, H. N., Wrabl, J. O., Li, J., and Hilser, V. J. (2014) The ensemble nature of allostery. *Nature*. **508**, 331–339
34. Hilser, V. J., Wrabl, J. O., and Motlagh, H. N. (2012) Structural and Energetic Basis of Allostery. *Annu. Rev. Biophys.* **41**, 585–609
35. Badireddy, S., Yunfeng, G., Ritchie, M., Akamine, P., Wu, J., Kim, C. W., Taylor, S. S., Qingsong, L., Swaminathan, K., and Anand, G. S. (2011) Cyclic AMP analog blocks kinase activation by stabilizing inactive conformation: conformational selection highlights a new concept in allosteric inhibitor design. *Mol. Cell. Proteomics*. **10**, M110.004390
36. Walker, C., Wang, Y., Olivieri, C., Karamafrooz, A., Casby, J., Bathon, K., Calebiro, D., Gao, J., Bernlohr, D. A., Taylor, S. S., and Veglia, G. (2019) Cushing's syndrome driver mutation disrupts protein kinase A allosteric network, altering both regulation and substrate specificity. *Sci. Adv.* **5**, eaaw9298
37. Musheshe, N., Schmidt, M., and Zaccolo, M. (2018) cAMP: From Long-Range Second Messenger to Nanodomain Signalling. *Trends Pharmacol. Sci.* **39**, 209–222
38. Aggarwal-Howarth, S., and Scott, J. D. (2017) Pseudoscaffolds and anchoring proteins: the difference is in the details. *Biochem. Soc. Trans.* **45**, 371–379
39. McNicholl, E. T., Das, R., SilDas, S., Taylor, S. S., and Melacini, G. (2010) Communication between tandem cAMP binding domains in the regulatory subunit of protein kinase A-Ialpha as revealed by domain-silencing mutations. *J. Biol. Chem.* **285**, 15523–37
40. Wu, J., Brown, S., Xuong, N.-H., and Taylor, S. S. (2004) RIα Subunit of PKA: A cAMP-free Structure Reveals a Hydrophobic Capping Mechanism for Docking cAMP into Site B. *Structure*. **12**, 1057–1065
41. Guex, N., and Peitsch, M. C. (1997) SWISS-MODEL and the Swiss-Pdb Viewer: An environment for comparative protein modeling. *Electrophoresis*. **18**, 2714–2723
42. VanSchouwen, B., and Melacini, G. (2018) Role of Dimers in the cAMP-Dependent Activation of Hyperpolarization-Activated Cyclic-Nucleotide-Modulated (HCN) Ion Channels. *J. Phys. Chem. B*. **122**, 2177–2190

Chapter 3

Ensemble Allosteric Model for PKA

3.1 Author's Preface

The work presented in this chapter has previously been published as supplementary materials and is reproduced here with permission from the Science Advances, AAAS. Full citation is as follows:

Byun, J. A., Akimoto, M., VanSchouwen, B., Lazarou, T. S., Taylor, S. S., and Melacini, G. (2020) Allosteric pluripotency as revealed by protein kinase A. *Sci. Adv.* **6**, eabb1250.

I co-designed and co-conducted most of the experiments necessary for the manuscript and analyzed the data with Dr. Madoka Akimoto. Dr. Bryan VanSchouwen performed all the MD simulations. Tomas S. Lazarou assisted in sample preparations for the paramagnetic relaxation enhancement experiments. Dr. Susan S. Taylor provided plasmids and helpful discussions. Dr. Giuseppe Melacini contributed to designing the experiments and developed the ensemble allosteric model. I co-wrote the manuscript with Dr. Madoka Akimoto and Dr. Giuseppe Melacini.

* Please refer to Chapter 2 for main text figures mentioned in this chapter.

3.2 S1. Rp Binds C:R_{AB} with an 'A-to-B' Order Opposite to cAMP and to Apo R_{AB} with a 'B-to-A' Order Similar to cAMP.

The apo/holo exchange falls in the fast exchange regime during the Rp titration onto the C:R_{AB} complex (fig. S3, D and F), suggesting that chemical shifts are population-weighted averages and are suitable to build domain-specific Rp binding isotherms (fig. S3B). Figure S3B shows that Rp binds CBD-A with one-order of magnitude higher affinity than CBD-B (table S1), resulting in a 'A-to-B' binding order (Fig. 3, D to F), which is the reversal of what is expected for cAMP binding to C:R_{AB} (Fig. 3, G to I) *(1)*. However, when the titration starts from apo R_{AB}, slow apo/holo exchange is observed (fig. S3, C and E) and the CBD-A *vs.* B affinities of Rp are switched, with CBD-B exhibiting now the highest affinity (fig. S3A, Fig. 3, A to C, and table S1). The 'A-to-B' to 'B-to-A' switch in Rp binding order in going from C:R_{AB} to apo R_{AB} (Fig. 3, A to F), reflects the different positions of the 'off' *vs.* 'on' CBD equilibria prior to adding Rp, *i.e.* both CBDs sample primarily the 'off' state in C:R_{AB}, while both CBDs shift to comparable 'off' *vs.* 'on' populations in apo R_{AB} *(2)*. This result is in full agreement with Rp functioning as an antagonist for the isolated CBD-A, whereby Rp exhibits 'off' *vs.* 'on' state selectivity for CBD-A, and as an agonist for CBD-B, whereby Rp exhibits a reversed 'on' *vs.* 'off' state selectivity for CBD-B (Fig. 2, A to D).

3.3 S2. An Ensemble Allosteric Model (EAM) for Protein Kinase A Pluripotent Allostery

To build an ensemble allosteric model (EAM) of PKA inhibition and activation, we focused first on the ensemble of apo R1a, *i.e.* R1a in the absence of cyclic nucleotides and of catalytic subunit, as this represents the simplest starting point.

S2.1. The Apo R1a Ensemble. Previous NMR investigations of a two-domain construct of apo R1a, *i.e.* R1a (91-379) *(2),* have shown that *(a)* each cAMP-binding domain (CBD) samples two conformations, an 'off' state, denoted as "0", which is similar to the C-bound structure *(1),* and 'on' state, denoted as "1", which is similar to the cAMP-bound structure *(3)*; *(b)* in the absence of cyclic nucleotide the two tandem CBDs do not interact *(2)*. Hence, apo R1a samples four states (*i.e.* "00", "01", "10" and "11", where the first binary digit denotes the state of CBD-A and the

second the state of CBD-B) with Boltzmann statistical weights ($S_{apo,i}$) simply dictated by the "1" *vs.* "0" free energy difference for each CBD, denoted as ΔG_A and ΔG_B:

$$S_{apo,00} = 1 \quad (1)$$

$$S_{apo,10} = e^{-\Delta G_A/RT} \quad (2)$$

$$S_{apo,01} = e^{-\Delta G_B/RT} \quad (3)$$

$$S_{apo,11} = e^{-(\Delta G_A + \Delta G_B)/RT} \quad (4)$$

The corresponding probabilities are obtained by normalizing with respect to the binding polynomial for apo R1a:

$$Q_{apo} = S_{apo,00} + S_{apo,10} + S_{apo,01} + S_{apo,11} \quad (5)$$

Yielding:

$$P_{apo,00} = \frac{S_{apo,00}}{Q_{apo}} \quad (6)$$

$$P_{apo,10} = \frac{S_{apo,10}}{Q_{apo}} \quad (7)$$

$$P_{apo,01} = \frac{S_{apo,01}}{Q_{apo}} \quad (8)$$

$$P_{apo,11} = \frac{S_{apo,11}}{Q_{apo}} \quad (9)$$

The next step to build the EAM of PKA is to quantify how cyclic nucleotide binding remodels the free energy landscape accessible to the apo R1a ensemble and the respective statistical weights.

S2.2. Remodeling of the Apo R1a Ensemble by Cyclic Nucleotide Binding. Cyclic nucleotide mono phosphates (cNMPs), such as cAMP or Rp-cAMPS, bind both CBDs of R1a with state-specific association constants that depend both on the CBD (*i.e.* A *vs.* B) and the state it adopts (*i.e.* "0"

vs. "1"). Hence, in the absence of inter-CBD interactions, the statistical weights of the four states accessed by R1a are modulated by cNMP-binding according to:

$$S_{cNMP,00} = (1 + K_{A0}x)(1 + K_{B0}x) \quad (10)$$

$$S_{cNMP,10} = (1 + K_{A1}x)(1 + K_{B0}x)e^{-\Delta G_A/RT} \quad (11)$$

$$S_{cNMP,01} = (1 + K_{A0}x)(1 + K_{B1}x)e^{-\Delta G_B/RT} \quad (12)$$

$$S_{cNMP,11} = (1 + K_{A1}x)(1 + K_{B1}x)e^{-(\Delta G_A + \Delta G_B)/RT} \quad (13)$$

where x denotes the concentration of unbound (free) cNMP, K_{A0} and K_{A1} the association constants of the cNMP ligand for states "0" and "1" of CBD-A, respectively, and K_{B0} and K_{B1} the association constants of cNMP for states "0" and "1" of CBD-B, respectively.

In the presence of cNMP, it is essential to consider that CBD-B in state "1" interacts with the cNMP bound to CBD-A in state 1, as the indole of W260 in CBD-B caps the base of the cNMP in CBD-A ("*trans*-domain lid") *(3, 4)*. This means that equation (13) for state "11" needs to be modified as follows to take into account that inter-domain interactions stabilize the bound form in CBD-A such that a correction is needed for K_{A1}:

$$S'_{cNMP,11} = \left[1 + K_{A1}\left(\frac{1+e^{-\frac{\Delta G_{AB}}{RT}}}{2}\right)x\right](1 + K_{B1}x)e^{-(\Delta G_A + \Delta G_B)/RT} \quad (14)$$

ΔG_{AB} is the free energy of interaction between the two CBDs when both are in the 'on' state ("1") with CBD-A bound to the cNMP. The ΔG_{AB} free energy is negative for stable inter-domain interactions between the 'on' states of CBD-A and B. The $e^{-\Delta GAB/RT}$ term in equation (14) effectively scales up the affinity of cNMP for CBD-A in the 11 state ($K_{A1'}$), as a result of the interaction of CBD-B with the cNMP bound to CBD-A, which stabilizes the 'closed' inter-domain 11 topology:

$$K_{A1\prime} = K_{A1}\left(\frac{1+e^{-\frac{\Delta G_{AB}}{RT}}}{2}\right) \quad (15)$$

The "1" addendum in this equation takes into account residual populations of 'open' inter-domain topology, in which the two domains do not interact. Division by 2 is required for internal normalization of the K_{A1} scaling factor, so that when $\Delta G_{AB} = 0$, equation (14) becomes equivalent to equation (13), as expected. The respective state populations in the presence of cNMP are obtained by normalizing through the binding polynomial for cNMP-bound R1a:

$$Q_{cNMP} = S_{cNMP,00} + S_{cNMP,10} + S_{cNMP,01} + S'_{cNMP,11} \quad (16)$$

Yielding:

$$P_{cNMP,00} = \frac{S_{cNMP,00}}{Q_{cNMP}} \quad (17)$$

$$P_{cNMP,10} = \frac{S_{cNMP,10}}{Q_{cNMP}} \quad (18)$$

$$P_{cNMP,01} = \frac{S_{cNMP,01}}{Q_{cNMP}} \quad (19)$$

$$P_{cNMP,11} = \frac{S\prime_{cNMP,11}}{Q_{cNMP}} \quad (20)$$

In the absence of cNMP (*i.e.* $x = 0$), equations (17-20) are equivalent to equations (6-9) above, respectively, as expected. In the presence of cNMP (*i.e.* $x > 0$), the statistical weights and probabilities of each microstate are computed through equations (10-20) (table S2). If saturation by the cNMP is reached, *i.e.* $x >>$ max ($1/K_{A1}$, $1/K_{A0}$, $1/K_{B1}$, $1/K_{B0}$), then equations (17-20) become considerably simpler:

$$P_{cNMP_{Sat},00} = \lim_{x\to\infty} P_{cNMP,00} = \frac{1}{Q_{cNMP_{Sat}}} \quad (21)$$

$$P_{cNMP_{Sat},10} = \lim_{x\to\infty} P_{cNMP,10} = \frac{\rho_A e^{-\Delta G_A/RT}}{Q_{cNMP_{Sat}}} \quad (22)$$

$$P_{cNMP_{Sat},01} = \lim_{x\to\infty} P_{cNMP,01} = \frac{\rho_B e^{-\Delta G_B/RT}}{Q_{cNMP_{Sat}}} \quad (23)$$

$$P_{cNMP_{Sat},11} = \lim_{x\to\infty} P_{cNMP,11} = \frac{0.5\rho_A\rho_B\left(1+e^{-\frac{\Delta G_{AB}}{RT}}\right)e^{-(\Delta G_A+\Delta G_B)/RT}}{Q_{cNMP_{Sat}}} \quad (24)$$

where ρ_A and ρ_B are the ratio of state specific association constants for CBD-A and B, respectively:

$$\rho_A = {K_{A1}}/{K_{A0}} \quad (25)$$

$$\rho_B = {K_{B1}}/{K_{B0}} \quad (26)$$

and the binding polynomial at cNMP saturation becomes:

$$Q_{cNMP_{Sat}} = 1 + \rho_A e^{-\Delta G_A/RT} + \rho_B e^{-\Delta G_B/RT} + 0.5\rho_A\rho_B\left(1+e^{-\frac{\Delta G_{AB}}{RT}}\right)e^{-(\Delta G_A+\Delta G_B)/RT} \quad (27)$$

Equations (6-9) and (21-27) define the populations of the four states accessible to the tandem domains of R1a either in the absence of cNMP or in the presence of saturating amounts of cNMP, respectively, and provide the foundation for computing the affinity of the catalytic subunit of PKA (C) in both scenarios.

S2.3. Computation of R:C Affinities and of cNMP-Induced Changes in Kinase Activity. When the C subunit binds R1a in the absence of cNMP, the binding polynomial of apo R1a becomes:

$$Q_{C,no\ cNMP} = \sum_{i=00,01,10,11} S_{apo,i}(1 + K_{Ci}[C]) \quad (28)$$

where [*C*] is the concentration of unbound (free) catalytic subunit, the *i* subscript is a state index and K_{C00}, K_{C01}, K_{C10} and K_{C11} are the association constants for C binding to states "00", "01", "10" and "11", respectively. From equation (28), it is possible to calculate the average fractional saturation of R1a by C as *(5)*:

$$\langle \nu \rangle_{C,no\ cNMP} = \frac{\partial \ln Q_{C,no\ cNMP}}{\partial \ln[C]} \quad (29)$$

or:

$$\langle \nu \rangle_{C,no\ cNMP} = \frac{\sum_{i=00,01,10,11} S_{apo,i} K_{Ci}[C]}{\sum_{i=00,01,10,11} S_{apo,i}(1+K_{Ci}[C])} \quad (30)$$

which can be re-written as:

$$\langle \nu \rangle_{C,no\ cNMP} = \frac{\langle K_{C,no\ cNMP} \rangle [C]}{1+\langle K_{C,no\ cNMP} \rangle [C]} \quad (31)$$

where:

$$\langle K_{C,no\ cNMP} \rangle = \sum_{i=00,01,10,11} P_{apo,i} K_{Ci} \quad (32)$$

is the affinity of C for R1a in the absence of cNMP and of substrate, as a function of the apo state populations provided by equations (6-9). Essentially, equation (32) means that the effective association constant of the complex between C and apo R1a is an average of the state-specific association constants and the weighing coefficients in the average are the populations of the apo R1a states prior to C binding.

When the C subunit binds R1a in the presence of saturating amounts of cNMP, the binding polynomial of cNMP-saturated R1a becomes:

$$Q_{C,cNMP_{Sat}} = \sum_{i=00,01,10,11} S_{cNMP_{Sat},i}(1 + K_{Ci}[C]) \quad (33)$$

Proceeding similarly to equations (29-32), the average fraction of cNMP-saturated R1a bound to C is *(5)*:

$$\langle \nu \rangle_{C,cNMP_{Sat}} = \frac{\partial \ln Q_{C,cNMP_{Sat}}}{\partial \ln[C]} = \frac{\langle K_{C,cNMP_{Sat}} \rangle [C]}{1 + \langle K_{C,cNMP_{Sat}} \rangle [C]} \quad (34)$$

where:

$$\langle K_{C,cNMP_{Sat}} \rangle = \sum_{i=00,01,10,11} P_{cNMP_{Sat},i} K_{Ci} \quad (35)$$

is the affinity of the C-subunit for cNMP-saturated R1a as a function of the populations provided by equations (21-27). Similar to equation (32), equation (35) formulates the effective association constant of the complex between C and cNMP-saturated R1a in the absence of substrate as an average of the state-specific association constants, where the weighing coefficients are the R-subunit state populations prior to C-subunit binding. If the concentration of cNMP is not sufficiently high to reach full saturation, the weighting factors for the state-specific affinities (K_{Ci}) are computed utilizing equations (17-20) rather than (21-24):

$$\langle K_{C,cNMP} \rangle = \sum_{i=00,01,10,11} P_{cNMP,i} K_{Ci} \quad (36)$$

The effective R:C association constants provided by equations (32) and (36) enable the computation of the concentration of R-subunit not bound to the C-subunit in the absence and presence of excess cNMP (*i.e.* $[R]_{no\ cNMP}$ and $[R]_{cNMP}$, respectively). Simply utilizing a classical quadratic equation, if the total concentrations of R and C are $[R]_{Tot.}$ and $[C]_{Tot.}$, then:

$$[R]_{no\ cNMP} = [R]_{Tot.} - 0.5(b_{no\ cNMP} - \sqrt{b^2_{no\ cNMP} - 4[R]_{Tot.}[C]_{Tot.}}) \quad (37)$$

with: $$b_{no\ cNMP} = [R]_{Tot.} + [C]_{Tot.} + (\frac{1}{\langle K_{C,no\ cNMP} \rangle}) \quad (38)$$

And similarly, for the concentration of R-subunit not bound to C-subunit in the presence of cNMP:

$$[R]_{cNMP} = [R]_{Tot.} - 0.5(b_{cNMP} - \sqrt{b_{cNMP}^2 - 4[R]_{Tot.}[C]_{Tot.}}) \quad (39)$$

with: $$b_{cNMP} = [R]_{Tot.} + [C]_{Tot.} + (\frac{1}{\langle K_{C,cNMP} \rangle}) \quad (40)$$

Once the concentration of C-unbound R-subunit is computed in the absence and presence of excess cNMP through equations (37-40), the fractional change of kinase activity (ϕ) caused by the addition of cNMP is quantified as:

$$\phi = \frac{V_{cNMP} - V_{no\ cNMP}}{V_{no\ R,\ no\ cNMP} - V_{no\ cNMP}} \quad (41)$$

where the initial phosphorylation rates (*V*) are obtained through the Michaelis-Menten equations in the absence and presence of competitive inhibition by the R-subunit, computed assuming that the substrate S is present in excess (*i.e.* $[S]_{Tot} >> [C]_{Tot}$):

$$V_{no\ R,\ no\ cNMP} = \frac{k_{cat}[C]_{Tot.}[S]_{Tot.}}{[S]_{Tot.} + K_m} \quad (42)$$

$$V_{no\ cNMP} = \frac{k_{cat}[C]_{Tot.}[S]_{Tot.}}{[S]_{Tot.} + K_m(1 + \langle K_{C,no\ cNMP} \rangle [R]_{no\ cNMP})} \quad (43)$$

$$V_{cNMP} = \frac{k_{cat}[C]_{Tot.}[S]_{Tot.}}{[S]_{Tot.} + K_m(1 + \langle K_{C,cNMP} \rangle [R]_{cNMP})} \quad (44)$$

While k_{cat} is included in equations (42-44) for the sake of completeness, it is clear that ϕ does not dependent on k_{cat} and therefore the substrate-dependency of ϕ is dictated primarily by the Michaelis-Menten constant K_m as well as $[S]_{Tot}$.

In summary, the ensemble allosteric model formalized by equations (1-44) enables us to quantify the extent of kinase activation or inhibition (*i.e.* ϕ) occurring upon binding of a given cNMP ligand to the R-subunit. The computed ϕ value is a function of the following input parameters:

i. the free energies of the 'off' ("0") to 'on' ("1") state conformational transition for the apo domain A (ΔG_A) and B (ΔG_B);
ii. the ratio of state-specific association constants for each isolated (non-interacting) domain ($\rho_A = K_{A,1}/K_{A,0}$ and $\rho_B = K_{B,1}/K_{B,0}$). If the cNMP does not reach full saturation, the ratios of state-specific association constants are not sufficient, and the actual state-specific affinities ($K_{A,1}$, $K_{A,0}$, $K_{B,1}$ and $K_{B,0}$) are needed to implement equations (17-20).
iii. the free energy of interaction between the cNMP-bound 'on' states ("11") of the two tandem domains (ΔG_{AB}) when the cNMP ligand is bound to CBD-A;
iv. the state-specific affinities of the catalytic kinase subunit C for R (K_{C00}, K_{C01}, K_{C10} and K_{C11});
v. the total concentrations of R and C ($[R]_{Tot.}$ and $[C]_{Tot.}$);
vi. the substrate concentration and the respective Michaelis-Menten constant ($[S]_{Tot.}$ and K_m)

The measurement of these PKA EAM input parameters is outlined in the next section and a summary of all the EAM input parameters and their sources is provided in table S1.

3.4 S3. Measurement of Input Parameters for the EAM Model

S3.1. EAM Input i. The ΔG_A and ΔG_B free energies are determined considering that the exchange between the "0/1" states of each domain is fast in the NMR chemical shift time scale for both apo CBD-A and apo CBD-B in two-domain R1a constructs and therefore the observed chemical shifts are linear averages of those in the "0" and "1" states for each domain *(2)*. If the C-bound and cAMP-bound samples are assumed to represent the "0" and "1" states of each CBD, respectively, correlative NMR chemical shift analyses, such as CHESPA, indicate that apo CBD-A samples the "0" and "1" states with similar probabilities (*i.e.* $\Delta G_A = 0$), while CBD-B samples the "0" and "1" states with 70% and 30% populations, respectively (*i.e.* $\Delta G_B = 0.85$ RT) *(2, 6)*. Considering that RT is ~0.6 kcal/mol under physiological conditions, these data suggest that apo

R1a accesses a highly degenerate free energy landscape with comparable populations for the four accessible states, "00", "01", "10" and "11" (Fig. 5A) *(2)*.

S3.2. EAM Input ii. The ratio of state-specific association constants for each isolated (non-interacting) domain (ρ_A and ρ_B) are measured by quantifying the shift in the 0 *vs.* 1 conformational equilibrium of each CBD that occurs upon binding saturating amounts of the Rp-cAMPS in the absence of inter-domain interactions. This is because in the presence of a large excess of free Rp ligand (*i.e.* $K_{A,0}$ [Rp] >> 1, $K_{A,1}$ [Rp] >> 1, $K_{B,0}$ [Rp] >> 1 and $K_{B,1}$ [Rp] >> 1):

$$\rho_A \cong \frac{\left(1-x_{Rp_{Sat},A0}\right)/\, x_{Rp_{Sat},A0}}{\left(1-x_{Apo,A0}\right)/\, x_{Apo,A0}} \qquad (45)$$

where $x_{Rp\ Sat,A0}$ and $x_{Apo,A0}$ are the average fractions of 'off' ("0") states for CBD-A in the Rp-saturated and apo samples, respectively (44). Similarly, for CBD-B:

$$\rho_B \cong \frac{\left(1-x_{Rp_{Sat},B0}\right)/\, x_{Rp_{Sat},B0}}{\left(1-x_{Apo,B0}\right)/\, x_{Apo,B0}} \qquad (46)$$

While $x_{Apo,A0}$ and $x_{Apo,B0}$ are already available from input *i.* as explained above (*i.e.* $x_{Apo,A0}$ = 0.5 and $x_{Apo,B0}$ = 0.7), $x_{Rp\ Sat,A0}$ and $x_{Rp\ Sat,B0}$ are measured at cNMP saturation through chemical shift correlation analyses given the fast "0" *vs.* "1" conformational exchange *(2, 7, 8)*. These chemical shift analyses were applied to the W260A mutant to ensure that domain-domain interactions are silenced, as ρ_A and ρ_B are defined in terms of association constant for cNMP binding in the absence of domain – domain interactions. If the R:C and R:cAMP$_2$ complexes lock the CBDs in the "0" and "1" states, respectively, the slope of the plot of $\delta_{W260A,Rp}$ - $\delta_{WT,cAMP}$ *vs.* $\delta_{WT:C}$ - $\delta_{WT,cAMP}$ chemical shift differences yield directly the $x_{Rp\ Sat,A0}$ and $x_{Rp\ Sat,B0}$ values, provided that such a plot is confined to residues that report primarily on the 0 *vs.* 1 conformational equilibria as opposed to binding or nearest neighbor effects (Fig. 2, C and D) *(2, 7, 8)*. Figure 2, C and D indicate that $x_{Rp\ Sat,A0}$ = 0.6 +/- 0.1 and $x_{Rp\ Sat,B0}$ ~ 0. This result means that $\rho_A \cong$ 0.7 +/- 0.3, whereas ρ_B >> 1.

Considering that $x_{Rp\ Sat,B0}$ approaches a null value, it remains challenging to accurately measure ρ_B through chemical shift correlations alone and equation (46). Hence, we resorted to titrating Rp into R_{AB}, either in the absence or presence of the C-subunit, to measure the state-specific association constants that define ρ_B, *i.e.* $K_{B,0}$ and $K_{B,1}$ (fig. S3, A and B). The dissociation constants for Rp from CBD-B in the C:R:Rp_2 and R:Rp_2 complexes (table S1) provide a valuable means to determine ρ_B. If CBD-B is assumed to adopt the 'off' ("0") state in the R:C complex, then $K_{B,0}$ = 1/127 μM^{-1}. If CBD-B in apo R_{AB} samples the "0" and "1" states with 70% and 30% probabilities, respectively, then:

$$\frac{1}{1.3\ \mu M} = 0.3K_{B1} + \frac{0.7}{127\ \mu M} \qquad (47)$$

Hence, $K_{B1} \cong$ 2.6 +/- 0.4 μM^{-1} and, based on equation (26), ρ_B = 330 +/- 57. Furthermore, if CBD-A is in the 'off' ("0") state in the R:C complex, then $1/K_{A0} \cong$ 8 μM and, since ρ_A = 0.7 +/- 0.3, K_{A1} can be estimated based on equation (25) as: $1/K_{A1} \cong 1/(\rho_A K_{A0}) \cong$ 8-20 μM.

S3.3. EAM Input iii. The free energy of interactions between the two domains (ΔG_{AB}) was measured through two independent approaches. The first approach is based on the intensity of the minor TROSY peak observed for R:Rp_2 (Fig. 2A), while the second relies on the WT *vs.* W260A difference in the domain-specific free energy of unfolding as gauged through H/D exchange kinetics. The first method capitalizes on the notion that the minor and major set of peaks observed for R:Rp_2 (Fig. 2A) correspond to the open and closed domain topologies in slow exchange (Fig. 3C) and therefore the relative minor *vs.* major peak intensities report on the free energy of domain-domain interactions (ΔG_{AB}). However, the minor *vs.* major intensities are also affected by the different relaxation rates of the open *vs.* closed domain conformations. In the open topology the two tandem domains do not interact and therefore the effective correlation time is expected to be shorter than in the closed topology. In order to take into account the effect of the open *vs.* closed topology differential relaxation, the minor *vs.* major intensity ratios for R:Rp_2 were corrected based on the WT *vs.* W260A R:$cAMP_2$ intensity ratios, resulting in an open *vs.* closed population ratio of 0.21 +/- 0.07, *i.e.* in an open topology fraction of 17 +/- 5% (fig. S1A).

The next step focused on translating the experimental open topology fraction measured for the R:Rp_2 sample into a ΔG_{AB} determination. For this purpose, we relied on the EAM and inputs *i.* and *ii.* The state populations of R:Rp_2 are provided by equations (21-24) and based on them it is possible to compute the open topology fraction as a function of ΔG_{AB}:

$$P_{Open\ Topology,R:Rp2} = \frac{0.5\rho_A\rho_B e^{-(\Delta G_A + \Delta G_B)/RT} + \rho_B e^{-\Delta G_B/RT}}{1 + \rho_A e^{-\Delta G_A/RT} + \rho_B e^{-\Delta G_B/RT} + 0.5\rho_A\rho_B\left(1+e^{-\frac{\Delta G_{AB}}{RT}}\right)e^{-(\Delta G_A + \Delta G_B)/RT}} \quad (48)$$

This equation stems from the observation that the open topology corresponding to the minor peak includes both the open "01" and the open "11" states (Fig. 2). Using the data for input *i.* and *ii.* (table S1), equation (48) results in the $P_{open\ topology}$ *vs.* ΔG_{AB} plot shown in figure S1B. Figure S1B indicates that ΔG_{AB} must fall in the [-2.6 RT, -3.3 RT] range in order to reproduce the experimental value of the open topology fraction (17 +/- 5%), measured based on the minor peak intensities of R:Rp_2 (fig. S1A).

As an independent validation of the ΔG_{AB} measurement through TROSY peak intensities, we also probed the strength of domain-domain interactions through a second and independent method based on H/D exchange, which exploits the relationship between free energies of unfolding of the holo (*e.g.* cAMP-bound) samples and the respective cAMP affinity:

$$\Delta G_{unf,WT,holo} \cong \Delta G_{unf,WT,apo} + RTln(1 + K_{A1'}[cAMP]) + RTln(1 + K_{B1}[cAMP]) \quad (49)$$

$$\Delta G_{unf,W260A,holo} \cong \Delta G_{unf,W260A,apo} + RTln(1 + K_{A1}[cAMP]) + RTln(1 + K_{B1}[cAMP]) \quad (50)$$

Assuming that the W260 indole does not significantly affect the affinity of cAMP for CBD-B and the free energy of unfolding for the apo samples, since the stacking and hydrogen-bond interactions with the W260 indole are lost in the absence of ligand *(2)*, the difference of equations (49) and (50) leads to:

$$\Delta\Delta G_{unfolding,holo} = RTln\left(\frac{1+K_{A1'}[cAMP]}{1+K_A[cAMP]}\right) \quad (51)$$

The $\Delta\Delta G_{unfolding,holo}$ is measured based on the WT *vs.* W260A difference in the maximal H/D exchange protection factors for CBD-A of WT and W260A R-subunit (fig. S1C), denoted as $\Delta logPF_{max}$:

$$\Delta\Delta G_{unfolding,holo} = RTln(10^{\Delta logPF_{max}}) \quad (52)$$

Combining equations (51) and (52), we obtain:

$$10^{\Delta logPF_{max}} = \frac{1+K_{A1}'[cAMP]}{1+K_A[cAMP]} \quad (53)$$

Considering that the H/D exchange data was acquired in the presence of 100 μM excess free cAMP (*i.e.* [cAMP] = 100 μM), which is more than two orders of magnitude higher than the dissociation constants for cAMP from R1a *(6),* equation (53) can be simplified as:

$$10^{\Delta logPF_{max}} = \frac{K_{A1}'}{K_A} \quad (54)$$

which, based on equation (15), becomes:

$$10^{\Delta logPF_{max}} = \frac{1+e^{-\frac{\Delta G_{AB}}{RT}}}{2} \quad (55)$$

or: $$\Delta G_{AB} = -RT \ln (2 * 10^{\Delta logPF_{max}} - 1) \quad (56)$$

Hence, if $\Delta logPF_{max}$ = 1.0 +/- 0.2 (fig. S1C and Materials and Methods section), the ΔG_{AB} free energy of interactions between the two domains falls in the [-2.5 RT, -3.4 RT] range. This ΔG_{AB} range is remarkably similar to the range independently determined above through the minor peak intensities of R:Rp_2 and the EAM model, *i.e.* [-2.6 RT, -3.3 RT]. Based on this agreement, we conservatively conclude that ΔG_{AB} falls in the [-2 RT, -4 RT] range.

S3.4. EAM Input iv. The state-specific association constants of C for R were determined assuming that K_{C01} and K_{C11} are in first approximation provided by the affinities of R1a (91-244) for the C-subunit measured in the presence of excess Rp or cAMP, *i.e.* K_d values of $4*10^{-11}$ and $3*10^{-8}$ M, respectively *(9)*. Hence, considering the population of CBD-A in Rp:R1a (91-244) is ~0.5 *(6)*, we obtained: $K_{C01} = (2/4)*10^{11} = 50$ (1/nM) and $K_{C11} = (1/3)*10^{8} = (1/3)*10^{-1}$ (1/nM). In order to take into account that the R:C affinities depend on the concentration of ATP and Mg^{2+} ions *(10, 11)* which may vary in different experiments, we introduce a scaling factor (γ) so that: $K_{C01} = 50\ \gamma$ (1/nM) and $K_{C11} = (\gamma/3)*10^{-1}$ (1/nM). The two remaining state-specific R:C association constants (*i.e.* K_{C00} and K_{C10}) were determined based on the CBD-B "0" *vs.* "1" populations in the C:R:Rp_2 complex, as measured by chemical shift correlations (Fig. 2N). For this purpose, we modeled the state populations of the C:R:Rp_2 quaternary complex by modifying equations (21-24) for the state populations of R:Rp_2 to take into account the effect of C-binding:

$$P_{C:R:Rp_2,00} = \frac{(1+[C]K_{C00})}{Q_{C:R:Rp_2}} \tag{57}$$

$$P_{C:R:Rp_2,10} = \frac{\rho_A e^{-\Delta G_A/RT}(1+[C]K_{C10})}{Q_{C:R:Rp_2}} \tag{58}$$

$$P_{C:R:Rp_2,01} = \frac{\rho_B e^{-\Delta G_B/RT}(1+[C]K_{C01})}{Q_{C:R:Rp_2}} \tag{59}$$

$$P_{C:R:Rp_2,11} = \frac{0.5\rho_A\rho_B\left(1+e^{-\frac{\Delta G_{AB}}{RT}}\right)e^{-(\Delta G_A+\Delta G_B)/RT}(1+[C]K_{C11})}{Q_{C:R:Rp_2}} \tag{60}$$

where the binding polynomial for R:C:Rp_2 (*i.e.* $Q_{C:R:Rp2}$) is the sum of the numerators in equations (57-60). If we define the ratio of state specific association constants for CBD-B as:

$$\rho_C = {}^{K_{C00}}/_{K_{C01}} = {}^{K_{C10}}/_{K_{C11}} \tag{61}$$

then it is possible to compute the fraction of CBD-B sampling the "0" state within the R:C:Rp_2 complex as a function of ρ_C using equations (57) and (58):

$$x_{CBD\text{-}B0 \text{ in C:R:Rp2}} = P_{C:R:Rp_2,00} + P_{C:R:Rp_2,10} \quad (62)$$

The plot of $x_{CBD\text{-}B0}$ in C:R:Rp2 *vs.* $\log(\rho_C)$ indicates that $\rho_C = 1.2 \times 10^2$ +/- 22 reproduces the experimental value of $x_{CBD\text{-}B0}$ (0.45 +/- 0.06) (Fig. 2N). This result still applies, if K_{C10} equals K_{C11} as opposed to $\rho_C K_{C11}$ (fig. S2B), showing that the measurement of $\rho_C = 1.2 \times 10^2$ +/- 22 is robust with respect to the assumption in equation (61) about the K_{C10}/K_{C11} ratio. Once ρ_C is determined from equation (61), together with the K_{C01} and K_{C11} values determined above, it provides the values for K_{C00} and K_{C10} (table S1).

S3.5. EAM Inputs v. and vi. The total concentrations of R and C ($[R]_{Tot.}$ and $[C]_{Tot.}$) are typically in nM – tens of nM range *(12)*. Finally, the concentration of free substrate [S] is often assumed to match the total concentration of substrate, as typically $[S]_{Tot.} >> [C]_{Tot.}$, while the respective Michaelis-Menten constants (Fig. 6, B and C) were measured as explained in Materials and Methods section.

3.5 Supplementary Figures

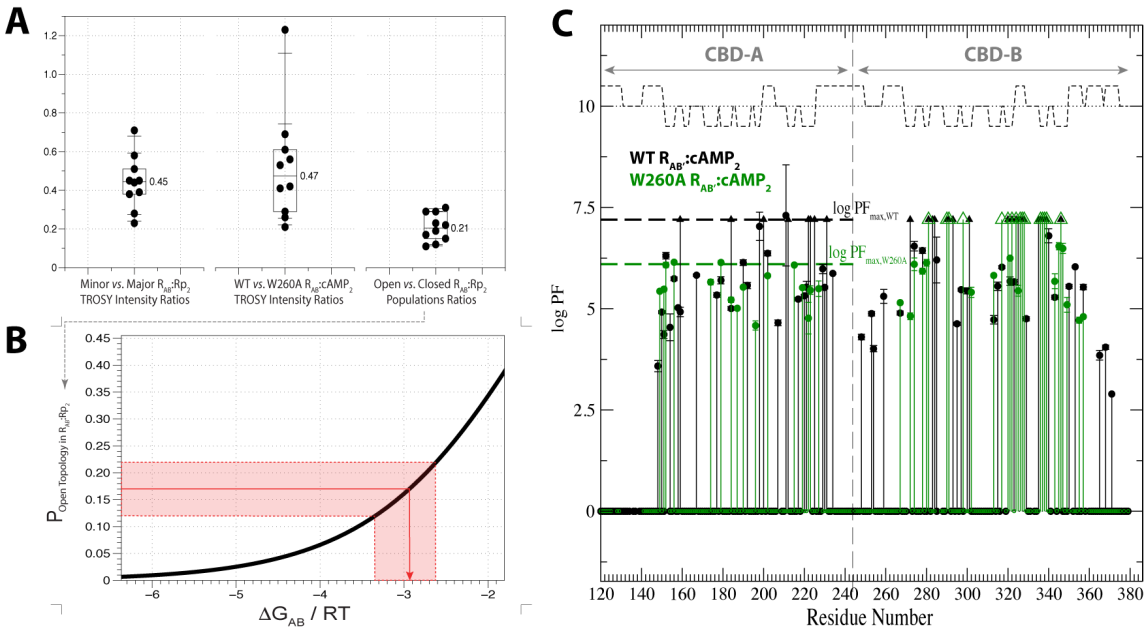

Figure S1. *Measurements of the inter-domain interaction free energy (ΔG$_{AB}$, EAM input .iii).* **(A)** Box plot illustrating how the open *vs*. closed R:Rp$_2$ population ratio was measured. The minor *vs*. major TROSY cross-peak intensity ratios were first measured for CBD-A residues for which a well-resolved minor peak was detected in TROSY spectra of R$_{AB}$:Rp$_2$ (leftmost box plot). Then we utilized the WT *vs*. W260A R$_{AB}$:cAMP$_2$ TROSY intensity ratios for the same residues to correct for the enhanced relaxation of the open *vs*. closed R$_{AB}$ topology (central box plot). The product of these two ratios provides the open vs. closed R$_{AB}$:Rp$_2$ population ratio (0.21 +/- 0.07). Based on this average ratio we determined the experimental population of open R$_{AB}$:Rp$_2$ states (0.21/1.21=0.17), which was compared with the respective populations calculated based on the EAM model using equation (48), as shown in **(B).** The ΔG$_{AB}$ measurement was obtained by comparing the calculated (black line) and experimental (red area) populations of the open domain topology in R:Rp$_2$. To correct for concentration differences when measuring the WT *vs*. W260A R$_{AB}$:cAMP$_2$ TROSY intensity ratios, all intensities were normalized to the C-terminal intensity for residue 379, as this residue is highly dynamic in the ps-ns time scale *(2)* and only minimally sensitive to the changes in overall tumbling rates between the closed and open topologies. In all box plots, whiskers are 2.5, 10, 90 and 97.5 percentiles and median values are shown for each type of ratio. **(C)** ΔG$_{AB}$ measurement through the Protection Factors (PF). PF values were measured by NMR monitored H/D amide exchange for WT (black circles) and W260A (green circles) R$_{AB'}$, *i.e.* R1a (119–379), constructs. The residues that exchanged completely at the first acquired HSQC spectrum are shown as circles at a PF of 0. The triangles indicate the residues which did not exchange appreciably during the H/D exchange experiment. Secondary structure is reported as dashed lines.

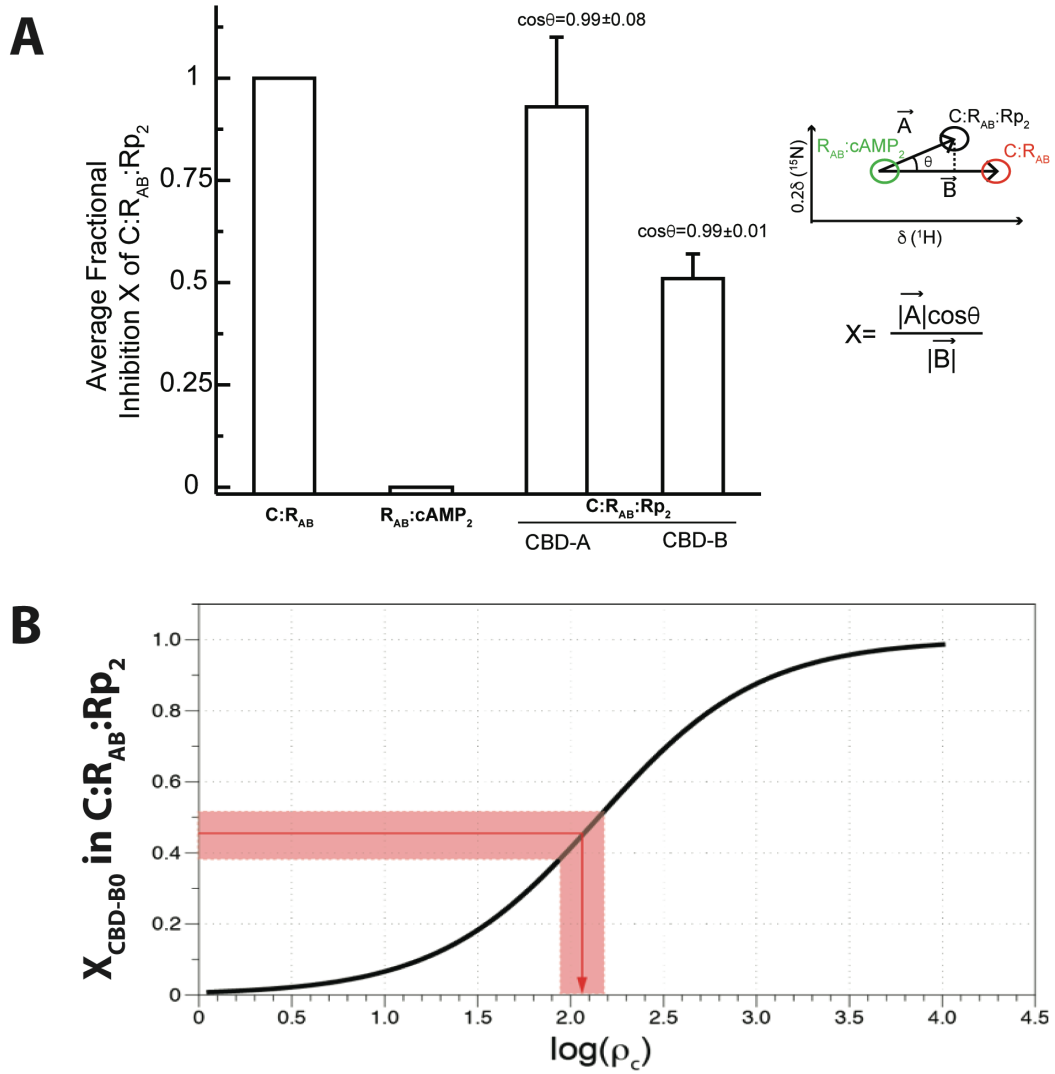

Figure S2. *Measurements of "1" vs. "0" relative C affinities of CBD-B ($\rho_C = K_{C00}/K_{C01}$; EAM input .iv).* **(A)** Domain-specific CHESPA analysis of the C:R_{AB}:Rp_2 complex. The panel on the right illustrates the definition of the CHESPA vectors, where vector B serves as reference onto which vector A is projected. **(B)** Plot of the calculated fraction of CBD-B in the "0" state for the C:R_{AB}:Rp_2 quaternary complex in the presence of saturating amount of Rp, $[C]_{Tot.} = 60$ μM, $[R]_{Tot.} = 50$ μM. The red arrow indicates the ρ_C value corresponding to the experimental fraction of CBD-B in the "0" state from Fig. 2N. No significant variations are observed if ΔG_{AB} switches from -2.6 RT to -3.3 RT or if K_{C10} varies from K_{C11} to $\rho_C K_{C11}$.

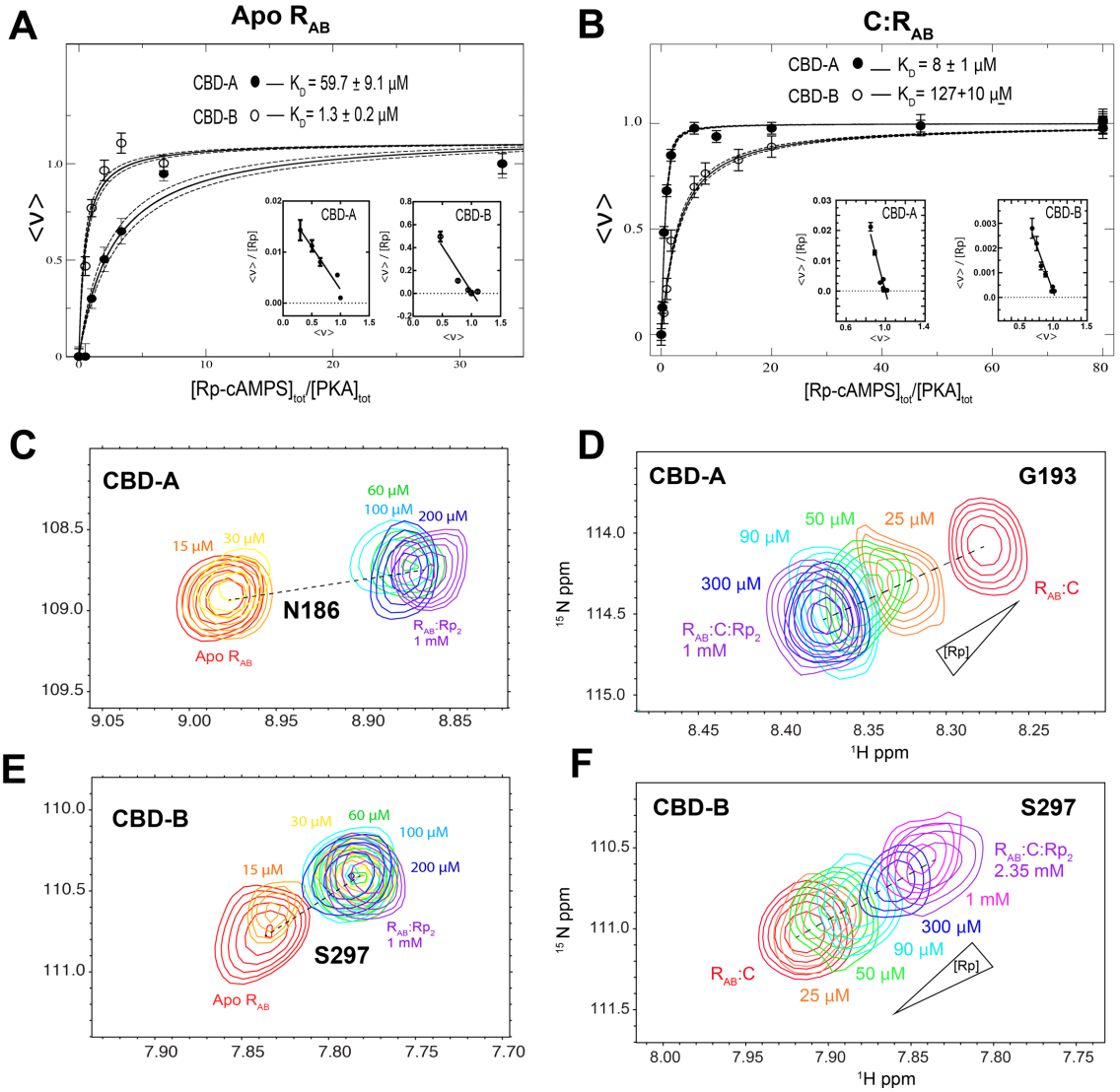

Figure S3. *Rp Binding Isotherms From NMR Monitored Titrations of Apo and C-Bound R_{AB} with Rp-cAMPS.* **(A)** Isotherms for the binding of Rp to each CBD of apo R_{AB}. **(B)** Isotherms for the binding of Rp to each CBD of C:R_{AB} . In panels (A) and (B), three binding isotherms are shown corresponding to the main K_D value (solid curve) +/- the respective error (dashed curves). The Scatchard plots are shown as insets in A and B. **(C)** Titration of Rp-cAMPS into apo R_{AB} as monitored by intensity changes in TROSY cross-peaks for representative residues in CBD-A (N186). Cross-peak intensities are used to gauge the fraction bound in each CBD due to the slow bound-unbound exchange. **(D)** Titration of Rp-cAMPS into C:R_{AB} as monitored by changes in TROSY cross-peak positions for representative residues in CBD-A (G193). Cross-peak positions are used to gauge the fraction bound in each CBD, due to the fast bound-unbound exchange. **(E, F)** As (C, D) but for CBD-B using residue S297.

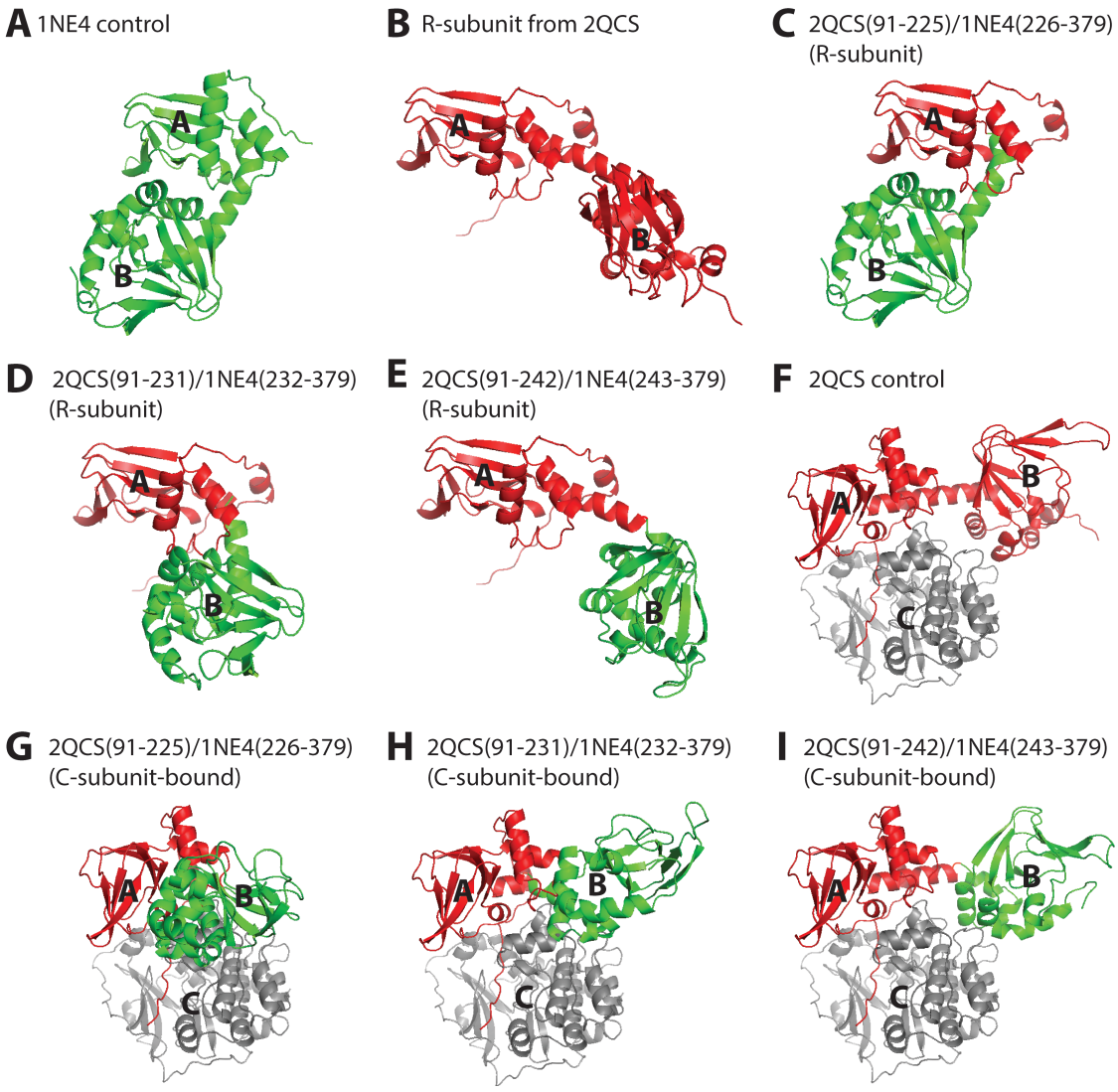

Figure S4. *Outline of the hybrid R-subunit and C-subunit-bound R-subunit starting structures used in the MD simulations of PKA 1a.* **(A)** Control '$A_{on}B_{on}$' R-subunit, derived from PDB structure "1NE4"; **(B)** R-subunit portion of the PDB structure "2QCS"; **(C-E)** hybrid R-subunit structures, consisting of the CBD-A domain from PDB structure "2QCS", and the CBD-B domain from PDB structure "1NE4", grafted together at residues 225-226, 231-232 or 242-243, respectively; **(F)** control 'A_{off}-B_{off}', C-subunit-bound R-subunit, derived from PDB structure "2QCS"; **(G-I)** hybrid C-subunit-bound R-subunit structures, consisting of the CBD-A domain and C-subunit from PDB structure "2QCS", and the CBD-B domain from PDB structure "1NE4". In all panels, the R-subunit and C-subunit residues derived from PDB structure "2QCS" are shown as red and gray ribbons, respectively, the R-subunit residues derived from PDB structure "1NE4" are shown as green ribbons, and the CBD-A ("A") and CBD-B ("B") domains and C-subunit ("C") are labelled. To facilitate comparison of the structures, the R-subunit structures in panels (A-E) are all shown with their CBD-A domain β-cores in the same orientation, and the C-subunit-bound R-subunit structures in panels (F-I) are all shown with their CBD-A domain β-cores and C-subunits in the same orientation.

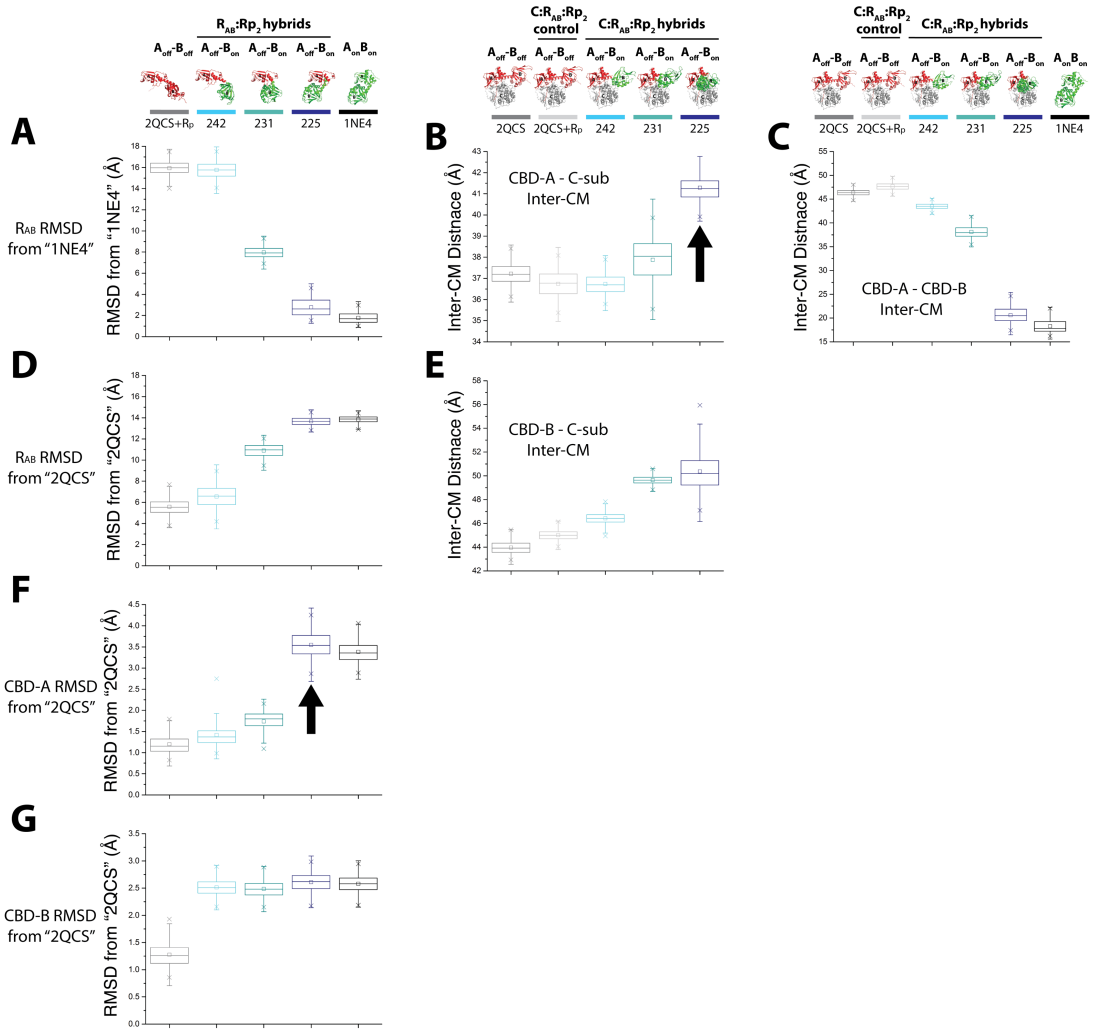

Figure S5. *MD simulations of R_{AB}:Rp_2 and C:R_{AB}:Rp_2* **(A)** Boxplots of the RMSD relative to the full-length 1NE4 structure with the closed $A_{on}B_{on}$ topology. The same MD simulation trajectories for R_{AB}:Rp_2 and color codes as in Fig. 4, A, D and F are utilized in this figure. The header at the top of the figure illustrates the initial structures utilized for the MD simulations of R_{AB}:Rp_2 and the respective color code. **(B)** Boxplots of the center-of-mass (CM) distance between CBD-A and the C-subunit for the C:R_{AB}:Rp_2 simulations. The headers at the top of the figure illustrate the initial structures utilized for the MD simulations of C:R_{AB}:Rp_2 and the respective color code. A notable shift toward CM distance values similar to the 1NE4 structure that was observed in the simulations is indicated by a black arrow. **(C)** As in panel (B), but for the CBD-B / C-subunit distances. **(D)** As in panel (A), but for the RMSD relative to the full-length 2QCS structure with the open A_{off}-B_{off} topology. **(E)** As in panel (B), but for the CBD-A / B distances. For the CBD-A / B distances presented here, only residues from CBD-A and CBD-B that were probed by the paramagnetic relaxation enhancement (PRE) experiments (*i.e.* CBD-A residues 150-230 and CBD-B residue 258) were considered in the CM calculation, in order to facilitate comparison of the results with the corresponding PRE data. **(F)** As in panel (D), but for the RMSD confined to CBD-A. **(G)** As in panel (D), but for the RMSD confined to CBD-B. A notable shift toward RMSD values similar to the 1NE4 structure is indicated by a black arrow.

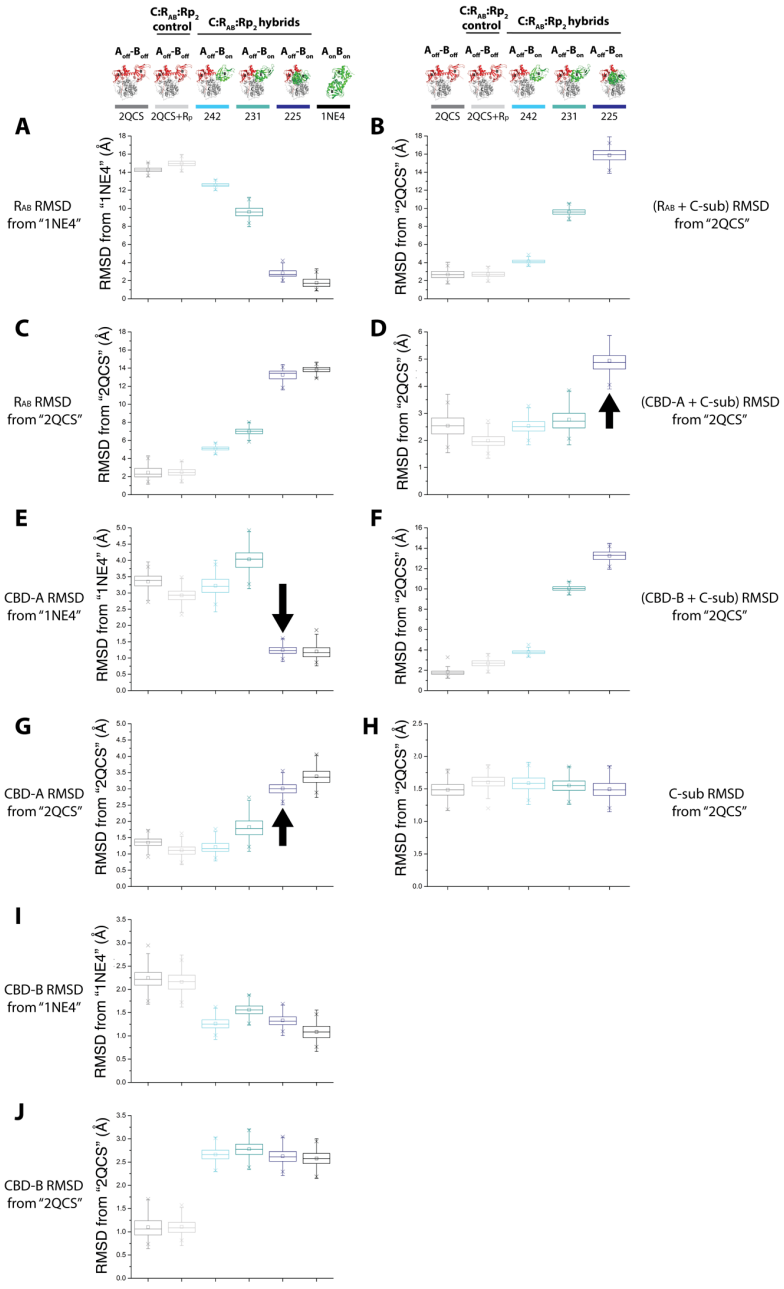

Figure. S6. *MD simulations of C:R_{AB}:Rp_2 – RMSD Analyses.* Boxplots of the RMSDs of the C:R_{AB}:Rp_2 complex relative to either the closed $A_{on}B_{on}$ structure of the R_{AB}:Rp_2 complex (1NE4), or the C:R_{AB} complex with an open A_{off}-B_{off} R_{AB} topology (2QCS). The RMSD values are calculated for different moieties of the C:R_{AB}:Rp_2 complex: R-subunit relative to 1NE4 **(A)**; R- and C-subunits together **(B)**; R-subunit relative to 2QCS **(C)**; CBD-A and C-subunit together **(D)**; CBD-A alone relative to 1NE4 **(E)**; CBD-B and C-subunit together **(F)**; CBD-A alone relative to 2QCS **(G)**; C-subunit alone **(H)**; and CBD-B alone **(I, J)**. and The headers at the top of the figure illustrate the initial structures utilized for the MD simulations of C:R_{AB}:Rp_2 and the respective color code. Notable shifts toward RMSD values similar to the 1NE4 structure that were observed from the simulations are indicated by black arrows.

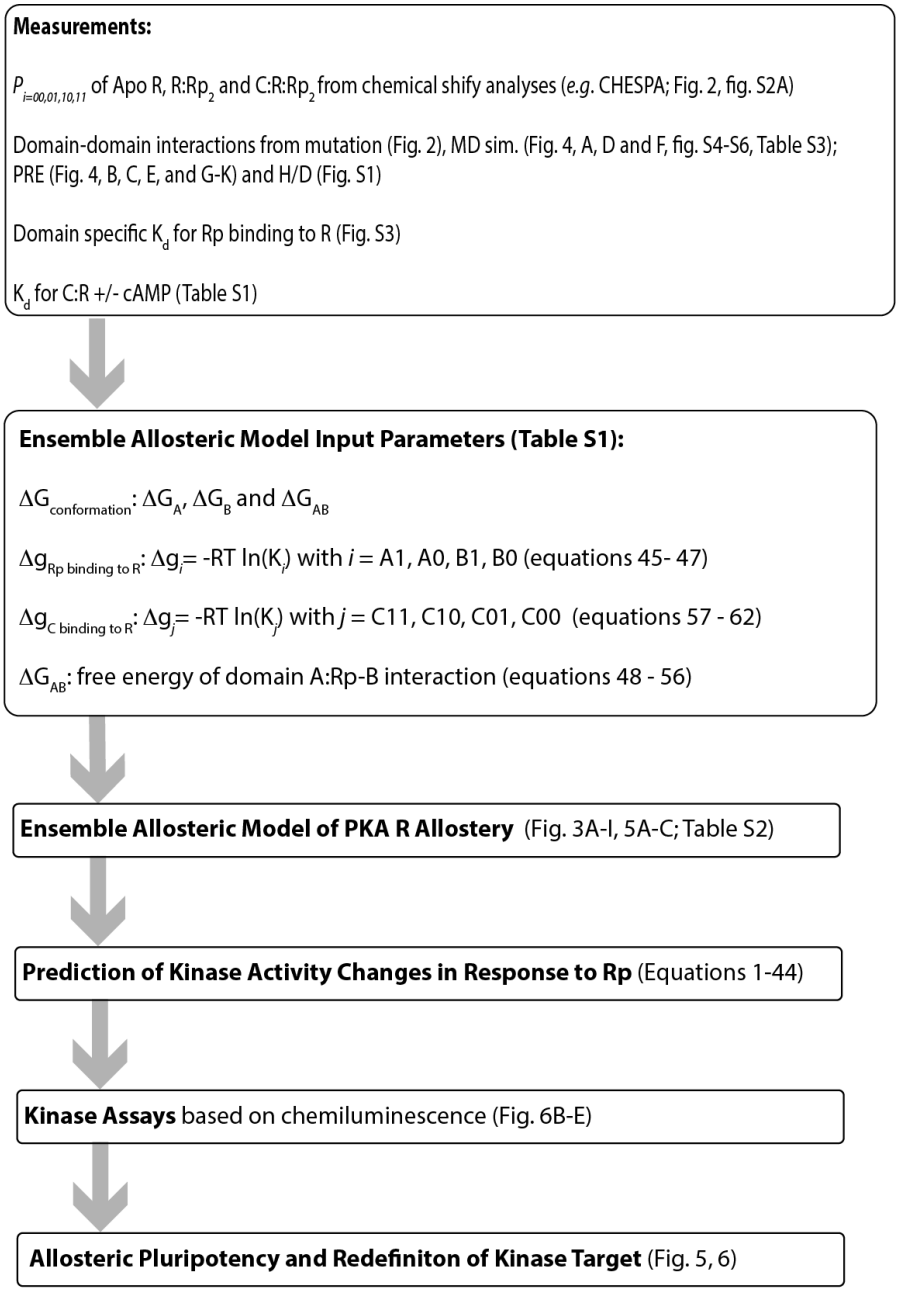

Figure S7. *General Scheme for Building the Ensemble Allosteric Model (EAM) of PKA***.** The NMR and affinity data are utilized to measure the free energies required by the EAM, which is essential to relate the dynamics of the R ensemble to kinase assays and predict how PKA function is modulated by allosteric ligands. Relevant Tables, Figures and equations for each step are specified.

3.6 Supplementary Tables

Table S1. *Summary of Input Parameters Required for the Ensemble Allosteric Model (EAM) of PKA Allosteric Pluripotency*

Input	***CBD-A***	***CBD-B***	***Source***
i. ΔG of apo CBD 1 *vs*. 0	$\Delta G_A = 0$ RT	$\Delta G_B = 0.85$ RT	CHESPA of apo R **(20)**
ii. State-specific association constant for each isolated domain	$1/K_{A0}$ = 8 +/- 1 μM $\rho_A = K_{A1}/ K_{A0}$ = 0.7 +/- 0.3	$1/K_{B0}$ = 127 +/- 10 μM $\rho_B = K_{B1}/ K_{B0}$ = 330 +/- 57	Rp titrations (fig. S3)
iii. Free energy of interaction between domains both in state 1	ΔG_{AB} = [-2, -4] RT		TROSY minor peak intensities and WT *vs*. W260A ΔPF H/D (fig. S1)
iv. State-specific affinities of C for R	$K_{C01} = \gamma 50$ (1/nM) $K_{C11} = (\gamma/3)*10^{-1}$ (1/nM) $K_{C00} = \rho_C K_{C01}$ $K_{C10} = [K_{C11}, \rho_C K_{C11}]$ with $\rho_C = 1.2 * 10^2$ +/- 22		Ref. **(22)** and CHESPA of C:R:Rp_2 (Fig. 2; fig. S2)

Table S2. *States of the Ensemble Allosteric Model of R1a (91-379)*

	State [a]	Symbol	$\Delta G_{Conformation}$	$\Delta g_{Ligand\ Binding}$	Statistical Weights (S_i) [b]
1		00	0	0	1
2		00	0	Δg_{A0}	$K_{A0}\,x$
3		00	0	Δg_{B0}	$K_{B0}\,x$
4		00	0	$\Delta g_{A0} + \Delta g_{B0}$	$K_{A0}\,K_{B0}\,x^2$
5		10	ΔG_A	0	$exp(-\Delta G_A/RT)$
6		10	ΔG_A	Δg_{A1}	$exp(-\Delta G_A/RT)\,K_{A1}\,x$
7		10	ΔG_A	Δg_{B0}	$exp(-\Delta G_A/RT)\,K_{B0}\,x$
8		10	ΔG_A	$\Delta g_{A1} + \Delta g_{B0}$	$exp(-\Delta G_A/RT)\,K_{A1}\,K_{B0}\,x^2$
9		01	ΔG_B	0	$exp(-\Delta G_B/RT)$
10		01	ΔG_B	Δg_{A0}	$exp(-\Delta G_B/RT)\,K_{A0}\,x$
11		01	ΔG_B	Δg_{B1}	$exp(-\Delta G_B/RT)\,K_{B1}\,x$
12		01	ΔG_B	$\Delta g_{A0} + \Delta g_{B1}$	$exp(-\Delta G_B/RT)\,K_{A0}\,K_{B1}\,x^2$
13		11	$\Delta G_A + \Delta G_B$	0	$exp(-\Delta G_A/RT)\,exp(-\Delta G_B/RT)$
14		11	$\Delta G_A + \Delta G_B$	Δg_{A1}	$0.5\,exp(-\Delta G_A/RT)\,exp(-\Delta G_B/RT)\,K_{A1}\,x$
15		11	$\Delta G_A + \Delta G_B$	Δg_{B1}	$exp(-\Delta G_A/RT)\,exp(-\Delta G_B/RT)\,K_{B1}\,x$
16		11	$\Delta G_A + \Delta G_B$	$\Delta g_{A1} + \Delta g_{B1}$	$0.5\,exp(-\Delta G_A/RT)\,exp(-\Delta G_B/RT)\,K_{A1}K_{B1}\,x^2$
17		11 closed	$\Delta G_A + \Delta G_B + \Delta G_{AB}$	Δg_{A1}	$0.5\,exp(-\Delta G_A/RT)\,exp(-\Delta G_B/RT)\,exp(-\Delta G_{AB}/RT)\,K_{A1}\,x$
18		11 closed	$\Delta G_A + \Delta G_B + \Delta G_{AB}$	$\Delta g_{A1} + \Delta g_{B1}$	$0.5\,exp(-\Delta G_A/RT)\,exp(-\Delta G_B/RT)\,exp(-\Delta G_{AB}/RT)\,K_{A1}K_{B1}\,x^2$

[a] For each domain, red triangles denote the inhibitory or "0" conformation, while green rectangles represent the non- inhibitory or "1" conformation. Black squares indicate the bound ligands, *e.g.* the Rp-cAMPS cyclic nucleotide. Microstates 1, 5, 9 and 13 are all apo. Unless otherwise specified, microstates are "open", *i.e.* the two tandem domains do not interact. A "closed" inter-domain topology, where the tandem domains interact, is possible for the 11 conformation in the presence of cNMP bound to domain A. [b] The degeneracy of each microstate is one. x is the concentration of free ligand, $\Delta g_i = -RT\ln(K_i)$ or $K_i = \exp(-\Delta g_i/RT)$, with i = A1, A0, B1 or B0. The sum of the 18 statistical weights results in the partition function Q_{cNMP} in equation (16). Normalization of each statistical weight (S_j) through the partition function results in the probability or population (P_j) of each state j = 1-18.

Table S3. *Summary of the Initial PKA 1α Structures Used in the MD Simulations*[a]

Structure	R-Subunit Residues			Bound R_p-cAMPS included? (Y/N)		C-subunit included? (Y/N)
	from 2QCS	from 1NE4	for grafting[b]	In CBD-A?	In CBD-B?	
1NE4 control	n/a	91-379	n/a	Y	Y	N
2QCS control	91-379	n/a	n/a	N	N	Y
R_p-cAMPS-bound 2QCS	91-379	n/a	n/a	Y	Y	Y
R_p-cAMPS-bound 2QCS R-subunit	91-379	n/a	n/a	Y	Y	N
2QCS(91-225)/1NE4(226-379) hybrid R-subunit	91-225	226-379	219-226	Y	Y	N
2QCS(91-231)/1NE4(232-379) hybrid R-subunit	91-231	232-379	227-231	Y	Y	N
2QCS(91-242)/1NE4(243-379) hybrid R-subunit	91-242	243-379	237-242	Y	Y	N
2QCS(91-225)/1NE4(226-379) C-subunit-bound hybrid	91-225	226-379	219-226	Y	Y	Y
2QCS(91-231)/1NE4(232-379) C-subunit-bound hybrid	91-231	232-379	227-231	Y	Y	Y
2QCS(91-242)/1NE4(243-379) C-subunit-bound hybrid	91-242	243-379	237-242	Y	Y	Y

[a] The total simulation time is 4.0 μs. [b]During construction of the hybrid structures, backbone superimposition of the "2QCS" and "1NE4" structures at these residues was used to align the structures, in order to achieve the desired graft between the structures. Further details are available in the Materials and Methods section.

3.7 References

1. C. Kim, C. Y. Cheng, S. A. Saldanha, S. S. Taylor, PKA-I holoenzyme structure reveals a mechanism for cAMP-dependent activation. *Cell*. **130**, 1032–1043 (2007).
2. M. Akimoto, E. T. McNicholl, A. Ramkissoon, K. Moleschi, S. S. Taylor, G. Melacini, Mapping the Free Energy Landscape of PKA Inhibition and Activation: A Double-Conformational Selection Model for the Tandem cAMP-Binding Domains of PKA RIα. *PLoS Biol.* **13**, e1002305 (2015).
3. Y. Su, W. R. Dostmann, F. W. Herberg, K. Durick, N. H. Xuong, L. Ten Eyck, S. S. Taylor, K. I. Varughese, Regulatory subunit of protein kinase A: structure of deletion mutant with cAMP binding domains. *Science*. **269**, 807–13 (1995).
4. J. Wu, J. M. Jones, X. Nguyen-Huu, L. F. Ten Eyck, S. S. Taylor, Crystal structures of RIalpha subunit of cyclic adenosine 5′-monophosphate (cAMP)-dependent protein kinase complexed with (Rp)-adenosine 3′,5′-cyclic monophosphothioate and (Sp)-adenosine 3′,5′-cyclic monophosphothioate, the phosphothioate analogues of cA. *Biochemistry*. **43**, 6620–6629 (2004).
5. K. A. Dill, S. Bromberg, *Molecular Driving Forces. Statistical Thermodynamics in Biology, Chemistry, Physics, and Nanoscience* (Garland Science, New York, 2010).
6. M. Akimoto, R. Selvaratnam, E. T. McNicholl, G. Verma, S. S. Taylor, G. Melacini, Signaling through dynamic linkers as revealed by PKA. *Proc. Natl. Acad. Sci. U. S. A.* **110**, 14231–14236 (2013).
7. K. J. Moleschi, M. Akimoto, G. Melacini, Measurement of State-Specific Association Constants in Allosteric Sensors through Molecular Stapling and NMR. *J. Am. Chem. Soc.* **137**, 10777–10785 (2015).
8. R. Selvaratnam, S. Chowdhury, B. VanSchouwen, G. Melacini, Mapping allostery through the covariance analysis of NMR chemical shifts. *Proc. Natl. Acad. Sci. U. S. A.* **108**, 6133–6138 (2011).
9. G. S. Anand, S. Krishnamurthy, T. Bishnoi, A. Kornev, S. S. Taylor, D. A. Johnson, Cyclic AMP- and (Rp)-cAMPS-induced conformational changes in a complex of the catalytic and regulatory (RIα) subunits of cyclic AMP-dependent protein kinase. *Mol. Cell. Proteomics*. **9**, 2225–2237 (2010).
10. F. W. Herberg, W. R. G. Dostmann, M. Zorn, S. J. Davis, S. S. Taylor, Crosstalk between Domains in the Regulatory Subunit of cAMP-Dependent Protein Kinase: Influence of Amino Terminus on cAMP Binding and Holoenzyme Formation. *Biochemistry*. **33**, 7485–7494 (1994).
11. M. J. Knape, L. G. Ahuja, D. Bertinetti, N. C. G. Burghardt, B. Zimmermann, S. S. Taylor, F. W. Herberg, Divalent Metal Ions Mg 2+ and Ca 2+ Have Distinct Effects on Protein Kinase A Activity and Regulation. *ACS Chem. Biol.* **10**, 2303–2315 (2015).
12. B. T. Gjertsen, G. Mellgren, A. Otten, E. Maronde, H. G. Genieser, B. Jastorff, O. K. Vintermyr, G. S. McKnight, S. O. Døskeland, Novel (Rp)-cAMPS analogs as tools for inhibition of cAMP-kinase in cell culture. Basal cAMP-kinase activity modulates interleukin-1 beta action. *J. Biol. Chem.* **270**, 20599–20607 (1995).

Chapter 4

State-Selective Frustration as a Key Driver of Allosteric Pluripotency

4.1 Author's Preface

I conducted most of the experiments necessary for the manuscript and analyzed the data. Nishi Parikh contributed to writing of the python script to build the contour plot and to the sample preparation of the NMR experiments with the R209K R_A construct and the following analysis. Dr. Madoka Akimoto acquired the NMR data on the reference states of WT R_A (*i.e.* cAMP-bound, apo, and C-subunit-bound). I co-wrote the manuscript and designed the research with Dr. Giuseppe Melacini.

4.2 Abstract

Allosteric pluripotency arises when an allosteric effector for a given receptor switches from agonism to antagonism depending on the experimental conditions. For example, in the case of Protein Kinase A (PKA), the Rp-cAMPS ligand switches from agonist to antagonist as the MgATP concentration increases and/or the substrate affinity or concertation decreases. Understanding allosteric pluripotency is essential to design effective allosteric therapeutics with minimal side effects. We have previously shown that the allosteric pluripotency of PKA arises from divergent allosteric responses of two homologous tandem cAMP-binding domains, resulting in a free energy landscape for the Rp-cAMPS-bound PKA regulatory subunit R1a in which the ground state is kinase inhibition-incompetent and the kinase inhibition-competent state is excited. The magnitude of the free energy between the ground non-inhibitory and excited inhibitory states (ΔG_{Gap}) relative to the effective free energy of R1a binding to the catalytic subunit of PKA ($\Delta G_{R:C}$) dictates whether the antagonism-to-agonism switch occurs. However, the key drivers of ΔG_{Gap} are not fully understood. Here, by analyzing a R1a mutant that silences allosteric pluripotency, we show that a major determinant of $\Delta G_{R,Gap}$ arises from state-selective frustration that destabilizes the ground inhibition-incompetent state of Rp-cAMPS-bound R1a. Such frustration is caused by steric clashes between the phosphate-binding cassette and the lid, which interact with the phosphate and base of Rp-cAMPS, respectively. These clashes are absent in the excited inhibitory state, thus reducing the $\Delta G_{R,Gap}$ to values comparable to $\Delta G_{R:C}$, as needed for allosteric pluripotency to occur.

4.3 Introduction

Allosteric inhibition, whereby an allosteric inhibitor targets and modulates a site distant from the orthosteric active site, provides enhanced selectivity for target systems (1–3). However, some challenges may arise when the same allosteric inhibitor by targeting the same allosteric site, induces not only antagonism, but also agonism under different environmental conditions. Such phenomenon is defined as allosteric pluripotency (4–6). Allosteric pluripotency has been observed in clinical settings, but explanations on the underlying molecular mechanisms remain still very sparse. Recently, cAMP-dependent protein kinase (PKA) has been utilized as a model system to elucidate the molecular basis of allosteric pluripotency (5). PKA is an essential kinase in the cAMP signalling network and regulates critical cellular processes (7–11). PKA over-activation has been linked to tumors, such as breast and lung cancers as well as pancreatic, thyroid and pituitary tumours (12–15). Despite extensive screening for PKA antagonists (16, 17), the only known allosteric inhibitor of PKA to date is Rp-cAMPS (Rp) (Fig. 1A). Rp inhibits PKA isoform 1a in the presence of high [MgATP], but actives it in the absence of MgATP (18). Hence, Rp acts as an allosterically pluripotent ligand for the PKA regulatory subunit R1a.

The PKA regulatory subunit (R) is a cAMP-dependent inhibitor of the PKA catalytic subunit (C) (19–21). R is composed of an N-terminal dimerization domain, followed by a linker that includes an auto-inhibitory region and is followed by two cAMP-binding domains (CBDs; CBD-A and CBD-B) (Fig. 1B) (21). Although the PKA holoenzyme includes two C-subunits bound to a dimeric R-subunits, the monomeric R-subunit construct spanning the auto-inhibitory region, CBD-A and CBD-B, *i.e.,* R_{AB} (residues 91 to 379), is sufficient for full inhibition and cAMP-dependent activation of PKA (19, 20, 22). In the inhibited PKA, the R-subunit mediates interaction with the C-subunit mainly through the CBD-A and the inhibitory linker that binds to the active site of C-subunit (Fig. 1C) (19). This interaction is further stabilized through the binding of MgATP (23, 24). Upon cAMP binding, each CBD undergoes a conformational change and the indole sidechain of W260 in CBD-B caps the base of cAMP bound to CBD-A, facilitating inter-domain interactions and releasing the C-subunit to phosphorylate substrate proteins (Fig. 1D) (19).

The tandem CBDs of PKA R1a exhibit divergent responses to Rp, whereby Rp-bound CBD-A partially samples the ‘off’ state, but Rp-bound CBD-B samples mainly the ‘on’ state (5).

Additionally, the inter-domain interaction facilitates the conversion of CBD-A to the 'on' state (5). The interplay between the intra-domain on-off equilibrium and the inter-domain open-close equilibrium leads to a conformational ensemble of Rp-bound R1a where the ground state adopts a closed-topology with both domains in the 'on' state (*i.e.* $A_{on}B_{on}$), and the excited states feature an open-topology in which CBD-A samples the 'on' and the 'off' states (*i.e*. A_{on}-B_{on} and A_{off}-B_{on}) (Fig. 1G). The A_{off}-B_{on} state is the inhibitory-competent state that can bind the PKA C-subunit and inhibit the kinase (Fig. 1H). The free energy difference between the $A_{on}B_{on}$ and the A_{off}-B_{on} states is called the $\Delta G_{R,gap}$, and is the threshold that the effective free-energy of R:C association has to overcome in order to inhibit PKA. In the presence of excess MgATP or low-affinity substrates that stabilize the R:C affinity, the free-energy of R:C association is larger than $\Delta G_{R,gap}$ and PKA is inhibited. In the absence of MgATP or the presence of high-affinity substrates that de-stabilize the R:C affinity, this threshold is not reached, and the PKA remains active (5).

Interestingly, this agonism-antagonism switch is silenced by the R209K R1a mutation (18). For R209K R1a, Rp acts as an agonist both in the presence and the absence of excess MgATP (Fig. 1F) (18). R209 is a highly conserved phosphate-binding residue in the phosphate-binding cassette (PBC) of CBD-A and salt bridges with the phosphate moiety of cAMP (Fig. 1E) (25),(26). Due to its unique physiological response of consistent Rp-induced agonism, the R209K mutation, in combination with Ensemble Allosteric Modeling (EAM) (5) and Nuclear Magnetic Resonance (NMR) methods (4, 5, 27–29), serves as an excellent tool to identify the key drivers of allosteric pluripotency. The R:C affinity has been shown to increase with the R209K mutation compared to WT (26), as opposed to decreasing, as we would hypothesize based on our EAM model (5). Hence, the perturbation in the R:C affinity is not the main driver for the observed Rp-induced agonism, which opens up the question as to which factors within R1a are perturbed by R209K and how do they contribute to the loss of agonism-antagonism switch.

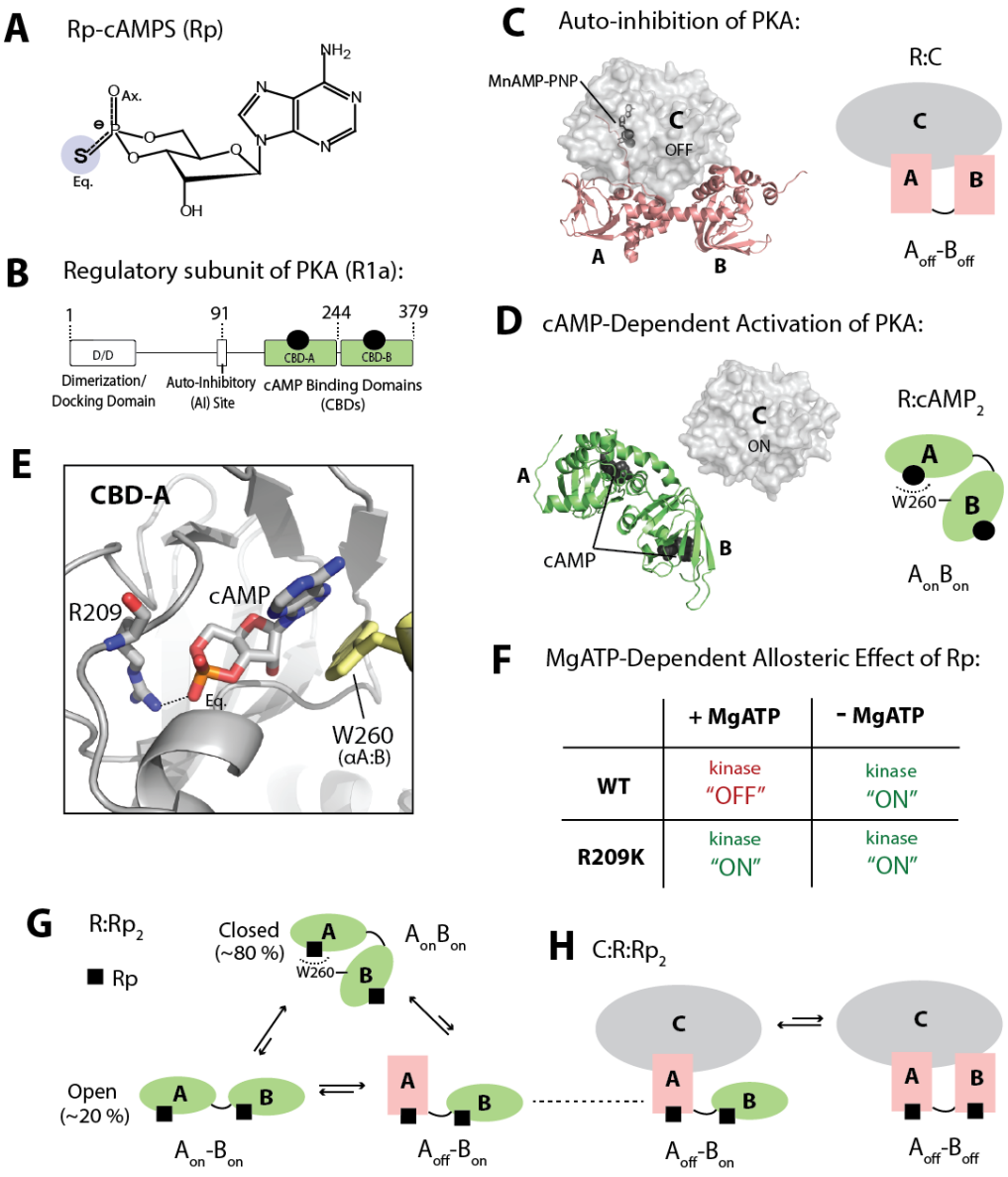

Figure 1. *PKA, Rp-cAMPS and its mechanism of action.* **(A)** Structure of Rp-cAMPS, a phosphorothioate analog of cAMP. **(B)** Domain architecture of the PKA R1a subunit. **(C, D)** Auto-inhibition and cAMP-dependent activation of PKA and the crystal structures of (C) R1a (91-379):C (PDB: 2QCS) (19) and (D) R1a (91-379):$cAMP_2$ (PDB: 1RGS) (25). cAMP binds to each of the cAMP-binding domain (CBD) of the regulatory subunit, R1a, which leads to release of the catalytic subunit, C. **(E)** cAMP (sticks) bound to CBD-A and its interaction with R209 in the phosphate binding cassette (PBC) of CBD-A and with W260 in CBD-B. **(F)** Summary of MgATP-dependent allosteric effects of Rp on PKA activity for WT and R209K. **(G)** Conformational ensemble of R (91-379):Rp_2, as revealed by NMR (5). **(H)** The C subunit selectively stabilizes the inhibition-competent states, where CBD-A is in the off state (5).

Here, we show that R209K shifts the equilibrium of CBD-A:Rp partially towards the 'on' state relative to wt, while stabilizing the inter-domain interaction typical of the closed-topology. As a result, R209K lowers the free-energy level of the closed $A_{on}B_{on}$ inhibition-incompetent ground state relative to the A_{off}-B_{on} inhibition-competent excited state and increases $\Delta G_{R,gap}$. The increased $\Delta G_{R,gap}$ value explains why for the R209K mutant Rp elicits agonism irrespective of whether MgATP is present or not. Using a double-mutant cycle and MD simulations, we also demonstrate that R209K stabilizes the ground closed $A_{on}B_{on}$ *vs.* excited open A_{off}-B_{on} state by selectively releasing frustration arising from steric clashes between the PBC and the adjacent B-helix in the closed topology of Rp-bound wt R1a. Overall, the R209K mutant reveals that state selective frustration is a major driver of allosteric pluripotency.

4.4 Results

4.4.1 The Rp-bound R209K CBD-A samples larger 'on' state populations compared to wt

One of the simplest explanations for the consistent activation induced by Rp in R209K is that the mutation increases the population of the 'on' state sampled by CBD-A:Rp. This would lead to a decrease in the population of the inhibitory-competent states where CBD-A is in the 'off' state, hence increasing the $\Delta G_{R,gap}$ and hindering the PKA inhibition. The EAM can be used to quantitatively predict the population of 'on' and 'off' states sampled by CBD-A:Rp needed to ensure PKA activation even in the presence of high [MgATP]. For such purpose, the critical EAM parameter is the ratio of state-specific association constant of Rp to CBD-A, denoted as ρ_A. The ρ_A value can be related to the fraction of 'off' CBD-A in the apo and in the Rp-bound form through equation (1):

$$\rho_A = {K_{A:on}}\Big/{K_{A:off}} \cong \frac{\left(1-x_{Rp_{Sat},A:off}\right)/\, x_{Rp_{Sat},A:off}}{\left(1-x_{Apo,A:\,off}\right)/\, x_{Apo,A:off}} \qquad (1)$$

where K_A refer to the state-specific association constant of Rp to CBD-A either in the 'on' or the 'off' state (5). The *x* refers to the fraction of 'off' state of CBD-A in either the apo form or in the presence of large excess of Rp.

Figure 2A shows a contour plot where the variables are the ρ_A value and the corresponding parameter for CBD-B, *i.e.* ρ_B. The contours in Figure 2A with different colors represent the predicted fractional change of kinase activity (ϕ) caused by addition of excess Rp in the presence of MgATP. Assuming that the mutation does not perturb the conformational equilibria of CBD-B and thus the ρ_B remains similar to WT, the minimal ρ_A value required for PKA to be activated beyond 90% is predicted to be ~90, which is two orders of magnitude larger than the ρ_A value of WT, *i.e.* 0.7.

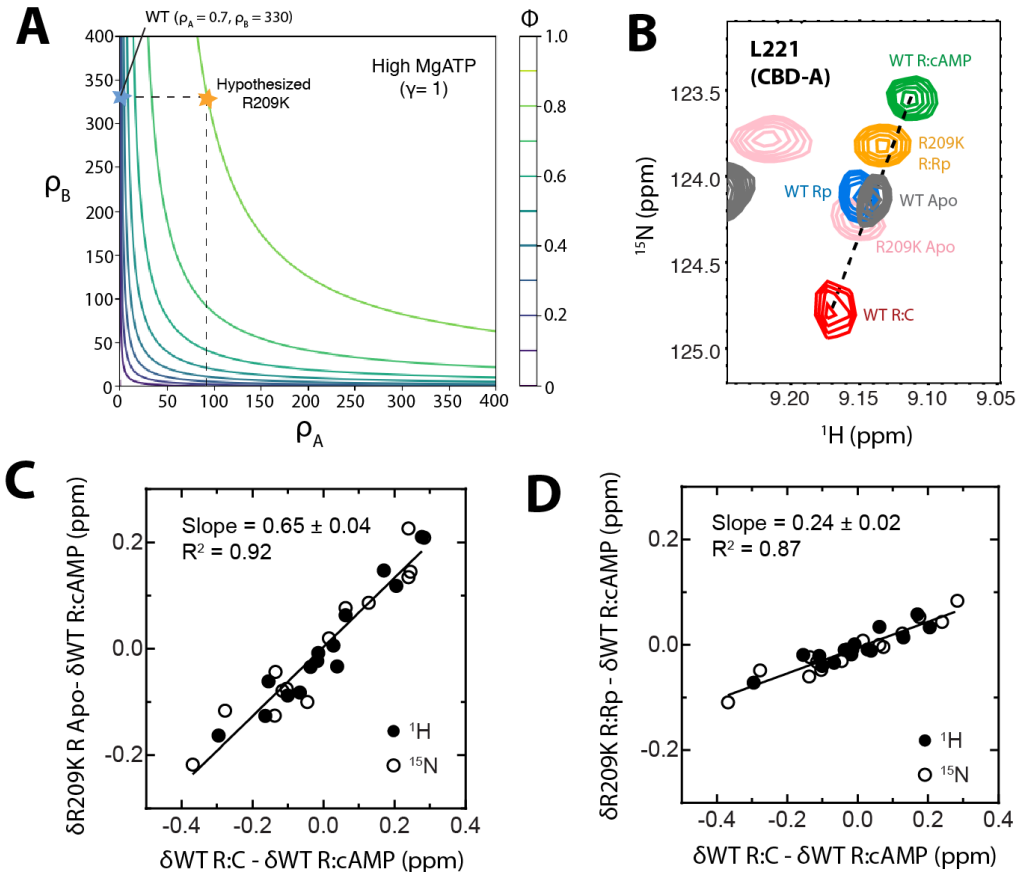

Figure 2. *Effect of R209K on the conformational equilibrium of CBD-A*. **(A)** Contour plot representing the effect of ρ_A and ρ_B on the maximal activation (φ) of PKA at high concentrations of MgATP (γ=1). With the experimentally determined ρ_B value of 330, PKA activation (φ ~ 0.8) at requires a ρ_A values of ~100 and above. The blue star represents the position for WT and the orange star represents the position where Rp would act as an agonist even in the presence of high [MgATP]. **(B)** Representative HSQC cross peaks of WT R_A (96-244):cAMP (green), WT R_A apo (grey), WT R_A:Rp (blue), R209K R_A:Rp (orange), R209K R_A apo (pink), and WT R (91-244):C (red). **(C)** Chemical shift correlation plot for apo R209K R (96 – 244). This graph compares ($\delta_{WT\ R:C} - \delta_{WT\ R:cAMP}$) to ($\delta_{R209K\ R\ Apo} - \delta_{WT\ R:cAMP}$). Open circles represent the downscaled ^{15}N chemical shifts (multiplied by 0.2), while the closed circles represent the ^{1}H chemical shifts. **(D)** Similar to panel (C) but for Rp-bound R209K R (96 – 244).

To test our hypothesis on the contribution of ρ_A, *i.e.* the conformational equilibrium of CBD-A:Rp, to the loss of agonism-antagonism switch in R209K, we acquired the ^{15}N-^{1}H HSQC NMR spectrum of R209K R1a CBD-A (*i.e.* R_A) apo and Rp-bound samples. Through comparative chemical shift analyses with reference samples (*i.e.* cAMP-bound sample assumed to represent the 'on' state and C-bound sample assumed to represent the 'off' state) (30), it is possible to estimate the position of the 'on' *vs*. 'off' conformational equilibrium for apo or Rp-bound R209K R_A. Such

estimation is legitimate when the 'on' vs. 'off' exchange regime is fast on the chemical shift NMR time scale, as suggested by the linear pattern that the reference samples conform to. Hence, the relative cross-peak positions reflect the relative population of 'on' and 'off' states for CBD-A, provided that such positions are measured for a residue sufficiently distant from the cAMP-binding sites to report primarily on the conformational equilibrium (Fig. 2B). Comparison with the WT reference states shows that R209K R_A:Rp samples larger population of the 'on' state compared to the WT R_A:Rp (Fig. 2B). the other hand, the R209K R_A apo samples slightly more of the 'off' state compared to the WT apo. Using multiple residues that meet the above mentioned criteria, similar to L221, and performing correlative analyses (Fig. 2C, D), we estimated the fraction of the 'off' states of the R209K R_A apo and Rp-bound to be 65% and 24%, respectively (Fig. 2C, D). Using these values, the ρ_A of R209K was calculated through equation (1) to be 5.88, which is approximately one order of magnitude higher than the WT. This finding confirmed our initial hypothesis on the increase in the population of the 'on' state of CBD-A:Rp and its contribution to the Rp-induced agonism in the presence of high [MgATP]. However, the experimental value of ρ_A is still lower than the predicted minimum ρ_A required to induce such physiological effect (*i.e.* ~90), suggesting that the perturbation on the 'on' vs. 'off' conformational equilibrium alone is not sufficient to explain the loss of agonism-antagonism switch in R209K and pointing to contributions from additional factors.

4.4.2 The R209K mutation stabilizes inter-domain interactions in the Rp-bound R-subunit

Another critical parameters of our EAM for allosteric pluripotency is the free energy of interaction between the two CBDs (*i.e.* ΔG_{AB}) when both are in the 'on' state and CBD-A is bound to Rp. A negative ΔG_{AB} value indicates stable CBD-A:Rp / CBD-B interactions. If ΔG_{AB} becomes more negative, the non-inhibitory ground state is stabilized relative to the inhibitory excited state and therefore $\Delta G_{R,Gap}$ increases, thus contributing to the Rp-induced agonism at high [MgATP]. The main driver of inter-CBD interactions is the capping of the cAMP base in CBD-A by W260 in CBD-B, which functions as a lid for cAMP. This inter-domain interaction facilitates the transition of CBD-A to the 'on' state (5). Therefore, a favourable inter-domain interaction, represented through a lower (more negative) ΔG_{AB} value, will shift the conformational equilibrium of Rp-bound

CBD-A to the 'on' state, thus selectively stabilizing the inhibition-incompetent $A_{ON}B_{ON}$ ground state relative to the inhibition-competent A_{OFF}-B_{ON} excited state and leading to PKA activation.

The EAM was used to quantitatively predict the effect of a decreased ΔG_{AB} value on the Rp-dependent fraction of PKA activation ($\phi_{Rp\text{-}cAMPS}$; Fig. 3A). In Figure 3A, the $\phi_{Rp\text{-}cAMPS}$ profiles were predicted at multiple ΔG_{AB} values ranging from -2 RT to -7 RT, which go beyond the ΔG_{AB} range of [-2, -4] RT expected for WT R1a (5). If R209K R1a exhibited a similar ΔG_{AB} range to WT, then the highest fraction of activation reached at high [MgATP] is ~50% (Fig. 3A). Hence, we hypothesized that ΔG_{AB} decreases to a more negative value, which leads to an enhanced PKA activation induced by Rp binding (Fig. 3A).

As a first step to test our ΔG_{AB} hypothesis, we acquired the ^{15}N-^{1}H TROSY NMR spectrum of R209K R1a 91-379 (*i.e.* R_{AB}), which spans both CBDs, in the presence of excess Rp. In WT, the overall population of the open-topology states, where the two CBDs do not interact, sampled by the R_{AB}:Rp_2 was measured to be ~20% (5). Such estimation is possible since the open- and closed-topology states are in slow exchange in NMR time scale, resulting in two separate cross peaks with different intensities (Fig. 3B, D). The minor and the major cross peaks of CBD-A residues arise from the open- and closed-topologies, respectively (5, 22). Through minor *vs.* major cross-peak intensity comparisons, the relative populations of open- and closed-topology states were measured, and from these the ΔG_{AB} for WT was determined (5). Here, if our ΔG_{AB} hypothesis for the R209K mutant is correct, we expect that the population of the open-topology states will decrease compared to WT, and therefore we anticipate a loss in the intensity of the minor peak. This is in fact what we observe. Figure 3B-E shows that in the R209K mutant the minor cross-peak detected for WT R_{AB}:Rp_2 disappears, despite similar signal-to-noise ratios to the WT spectrum, as shown by the CBD-B residue peak comparisons (Fig. 3G, H). Overall, the data in Figure 3B-H suggests a decrease in the population of the open topology, confirming our hypothesis that R209K leads to a more negative ΔG_{AB} value relative to WT.

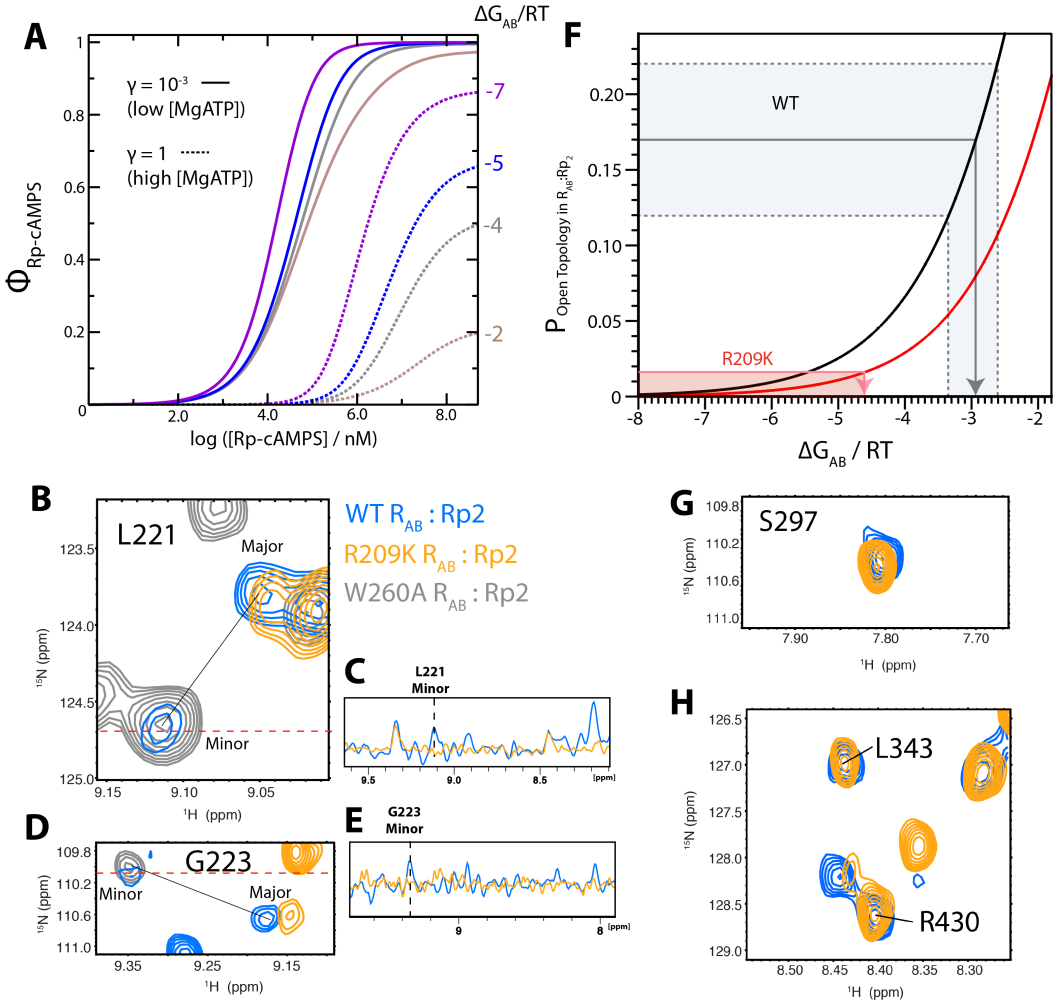

Figure 3. *The R209K mutation favors inter-domain interactions in R_{AB}:Rp_2.* **(A)** Predicted PKA kinase activation induced by Rp at low and high [MgATP] and multiple ΔG_{AB} values. The parameters for CBD-A, such as the ρ_A, ΔG_A (the 'on' vs. 'off' free energy difference for apo CBD-A), and the state specific association constants of Rp to CBD-A as measured by NMR and urea unfolding (Fig. 4; Fig. S1) were updated from the WT to the R209K values. **(B, D)** The enhanced inter-domain interactions of R209K R_{AB}:Rp_2 lead to loss in R209K R_{AB}:Rp_2 (orange) of the minor TROSY cross-peak of ^{15}N-^{2}H WT R_{AB}:Rp_2 (blue) for CBD-A. A W260A R_{AB}:Rp_2 TROSY spectrum expansion (grey) is also shown as reference. The proton 1D cross-sections at the ^{15}N dimension indicated by the red dashed lines are shown in **(C, E). (F)** The experimentally determined population of the open-topology of R_{AB}:Rp_2 can be used to estimate the ΔG_{AB} through comparison with the curves generated with eq. (2), which predicts how the population of the open-topology depends on ΔG_{AB}. The black curve and the shaded grey region are the computed and experimentally determined populations of open-topology for WT, respectively (5). The red curve and the shaded red region are the computed and experimentally determined populations of open-topology for the R209K mutant, respectively. The red arrow indicates the upper limit ΔG_{AB} value for R209K. **(G, H)** Representative TROSY cross-peak of ^{15}N-^{2}H WT R_{AB}:Rp_2 (blue) and R209K R_{AB}:Rp_2 (orange) from CBD-B.

In the case of WT, the ΔG_{AB} value was determined from the experimentally determined population of the open-topology (*i.e.* $P_{Open\ Topology,R:Rp2}$) as measured from the intensity ratio of the minor to the major peak corrected for differential relaxation effects (5). Such relationship is depicted through equation (2):

$$P_{Open\ Topology,R:Rp2} = \frac{0.5\rho_A\rho_B e^{-(\Delta G_A + \Delta G_B)/RT} + \rho_B e^{-\Delta G_B/RT}}{1 + \rho_A e^{-\Delta G_A/RT} + \rho_B e^{-\Delta G_B/RT} + 0.5\rho_A\rho_B\left(1+e^{-\frac{\Delta G_{AB}}{RT}}\right)e^{-(\Delta G_A + \Delta G_B)/RT}} \qquad (2)$$

where the ρ_A and ρ_B refer to the ratio of state-specific association constants of Rp to CBD-A and -B, respectively, and the ΔG_A and ΔG_B refer to the 'on' vs. 'off' free energy difference for apo CBD-A and -B, respectively. For WT, these parameters were measured by NMR and are inputted to build a function as shown in Fig. 3F (black plot). However, for R209K, the minor peaks representative of the open-topology states fall below the noise of our NMR spectrum. Based on the noise level, we can estimate the upper limit for the ΔG_{AB} value in R209K. The average noise was ~10 % of the signal, suggesting an upper limit for $P_{Open\ Topology,R:Rp2}$ of ~0.017. Using the EAM plot for R209K in Figure 3F (red), this $P_{Open\ Topology,R:Rp2}$ value translates into a ΔG_{AB} of -4.7 RT for R209K (Fig. 3F; red arrow). These are just upper limits, so the actual $P_{Open\ Topology,R:Rp2}$ and the ΔG_{AB} values are actually lower than 0.017 and -4.7 RT, respectively (Fig. 3F; red shaded region). For example, a ΔG_{AB} value of -7 RT, which leads to agonism in the presence of both high or low [MgATP] (Fig. 3A), is fully consistent with the NMR data in Figure 3B-H.

Taken together, our NMR data and EAM analyses suggest that the hypothesis that R209K lowers and stabilizes inter-CBD interactions is viable. To obtain a more quantitative assessment of ΔG_{AB} as well as to further elucidate the mechanism underlying the stabilization of the inter-domain interaction in R209K relative to WT and how this mechanism is involved in driving the allosteric pluripotency, we performed a double-mutant cycle that combines the R209K and CBD-B deletion mutations. This domain deletion was included because it is CBD-B that contribute the capping residue (*i.e.* W260) for cAMP in CBD-A, where R209 is located. The read-out measurement in this cycle was the K_d determination for Rp binding to CBD-A, either WT or R209K, in the presence and absence of CBD-B (Fig. 4A, B).

4.4.3 The measurement of Rp affinities for the R209K/CBD-B deletion double-mutant cycle provides a quantitative assessment of ΔG_{AB}

We assumed that the mutations-induced changes in the K_d value reflects mainly changes in the Rp-bound form and, therefore, that differences in K_d values provide insights on the coupling between the PBC (R209) and the lid (W260 in CBD-B). This assumption is supported by the negligible effect of CBD-B on apo CBD-A (22) and by the WT *vs.* R209K CBD-A similarities in the absence of Rp, as shown by the apo cross-peaks in Figure 2B. The K_d of Rp binding to R209K CBD-A in the absence of inter-domain interaction was measured by utilizing the R_A construct and monitoring the Rp titration through chemical shift changes, which were then translated into the fraction of Rp-bound CBD-A (Fig. 4C, E). The resulting K_d is 476 $\pm$ 77 μM for Rp binding to R209K CBD-A in the absence of inter-domain interactions. The corresponding K_d value in the presence of inter-domain interactions was measured by utilizing the R_{AB} construct and observing the chemical shift changes of a CBD-A residue, *i.e.* N218 (Fig. 4D, F). The resulting K_d value is 24 $\pm$ 6 μM, pointing to a significant increase in the affinity of Rp for R209K CBD-A upon addition of CBD-B (Fig. 4D).

The marked reduction in the K_d value for Rp binding to R209K CBD-A upon inclusion of CBD-B was independently confirmed through urea-induced unfolding experiments monitored by intrinsic fluorescence (Fig. S1). With the exception of W260, which serves as a link between CBD-A and CBD-B, the tryptophan residues of PKA R1a are clustered in CBD-A, therefore the K_d measurements with both the R_A and R_{AB} constructs obtained through the urea unfolding are assumed to reflect primarily the affinity of Rp for CBD-A. The K_d of Rp to CBD-A of R_A and R_{AB} measured through urea-induced unfolding are 396 $\pm$ 98 μM and 17 $\pm$ 3 μM, respectively, further validating the K_d values measured from NMR (Fig. 4B and Fig. S1). Similar experiments were also extended to WT R_A and R_{AB} in the same condition as R209K to ensure a reliable K_d comparison (Fig. S2). Interestingly, the K_d values measured for the WT do not exhibit significant difference between the R_A and R_{AB} constructs. This WT *vs.* R209K difference in the Rp K_d dependence on CBD-B is suggestive of a non-additive effect, whereby the Rp-binding free energy change caused by the double mutations are not recapitulated by the sum of the changes induced by the two single mutations. Such non-additivity reflects the coupling between two critical sites for cAMP binding, *i.e.* the PBC (R209K) and the lid (W260). The corresponding free energy of coupling ($\Delta G_{coupling}$) can be calculated as (31):

$$\Delta G_{coupling} = -RT\ ln \frac{K_{R_{A,}} K_{R_{AB,R209K}}}{K_{R_{AB}} K_{R_{A,R209K}}} \quad (3)$$

where the K_{RA}, K_{RAB}, $K_{RA,R209K}$ and $K_{RAB,R209K}$ refer to the respective association constants measured for CBD-A of WT R_A, WT R_{AB}, R209K R_A, and R209K R_{AB} constructs. Using the affinity measurements from the urea-induced unfolding experiment, the $\Delta G_{coupling}$ is calculated to be -3.4 RT, pointing to positive cooperativity between the R209K substitution and the introduction of the lid in Rp-binding. This positive cooperativity fully supports our hypothesis that R209K silences allosteric pluripotency also by stabilizing domain-domain interactions in the R1a:Rp_2 complex.

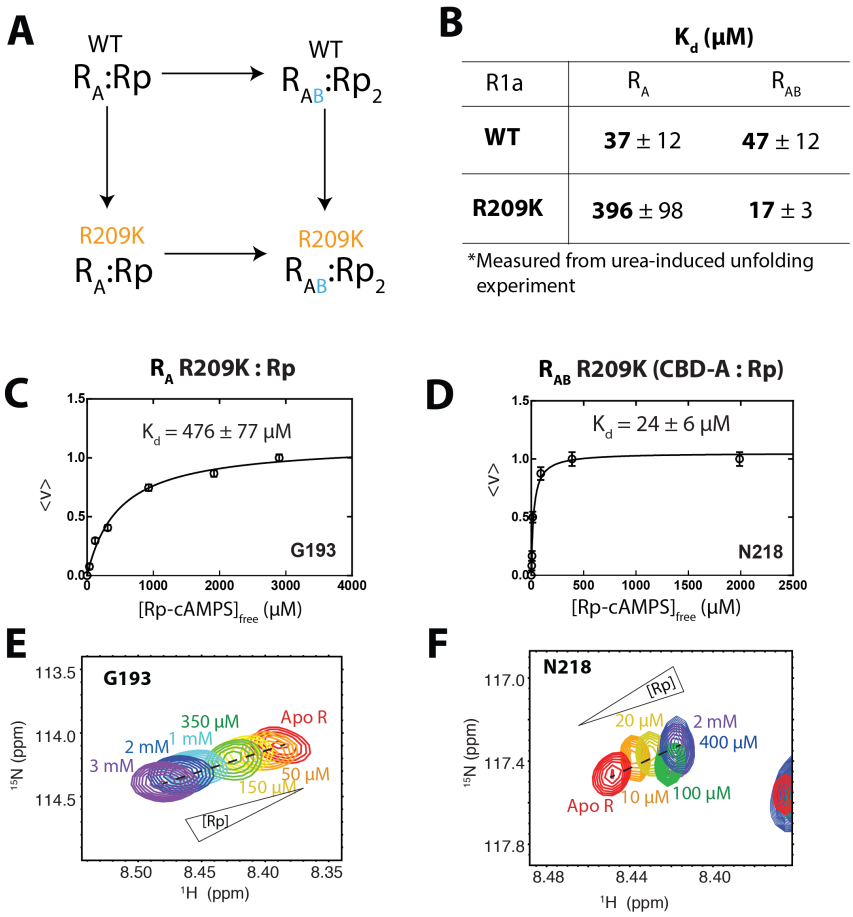

Figure 4. *Dissociation constants of Rp from R209K in the absence and presence of inter-domain interaction.* **(A)** Double-mutant thermodynamic cycle for the R209K mutation and the deletion of CBD-B, which mainly contributes as the W260 lid to Rp binding in CBD-A. This cycle is used to compute the coupling free energy of the R209 (PBC) and the W260 (lid) in the presence of Rp. **(B)** K_d values of Rp for WT and R209K R_A and R_{AB} constructs were measured through urea-induced unfolding (Fig. S1). **(C)** Isotherm for the binding of Rp to CBD-A in the absence of inter-domain interaction (*i.e.* R_A construct) using the NMR monitored titration shown in **(E)**. **(D)** Similar to panels (C) but in the presence of inter-domain interactions (*i.e.* R_{AB} construct). **(F)** Similar to panels (C) but in the presence of inter-domain interactions.

4.5 Discussion

Our results, based on comparative R209K *vs.* WT analyses combined with EAM computations and urea-induced unfolding experiments, have revealed two key drivers for the Rp agonism-antagonism switch in PKA, *i.e.* the conformational dynamics of the isolated CBD-A domain and the free energy of inter-domain interactions. The first allosteric pluripotency driver is the dynamic 'on' vs. 'off' conformational equilibrium within CBD-A, where shifting of the

equilibrium to the 'on' state increase the probability of Rp-induced agonism, whereas shifting of the equilibrium to the 'off' state increase the probability of Rp-induced antagonism. However, shifts in the CBD-A 'on'/'off' equilibrium alone are insufficient to fully recapitulate the observed silencing of allosteric pluripotency by the R209K mutation. The contribution of inter-domain interaction is also a critical factor for driving allosteric pluripotency.

Our analyses provide new insight on the determinants of inter-domain interactions in PKA R1a. The non-additivity of the R209K and CBD-B contributions to the free energy of Rp-binding to CBD-A is likely to arise from the steric frustration occurring in WT R1a when both R209 and W260 interact with Rp. This is clear from the K_d measurements for Rp binding to WT R1a, which shows the K_d for CBD-A does not significantly decrease upon introduction of inter-domain interactions, in clear contrast with R209K (Fig. 4E). Given the larger VanderWalls radius of sulfur relative to oxygen, the phosphorothioate substitution of Rp in CBD-A pushes the PBC towards an 'out' conformation. This in turn leads to a steric clash with the adjacent αB helix (*i.e.* αB:A), which is locked in the 'in' conformation due to the lid engagement driven by the base-capping interaction of W260 from αA of CBD-B (Fig. 1E, and Fig. 5).

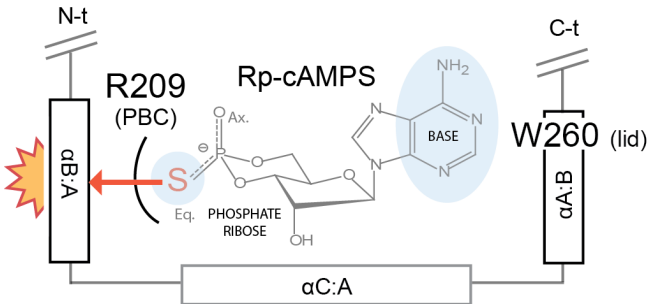

Figure 5. *Schematic showing the steric frustration caused by Rp-binding in CBD-A.* The R209 from the phosphate binding cassette (PBC) and W260 from the αA helix pf CBD-B (αA:B) interact with the phosphate and the base of Rp, respectively. When W260, which serves as the lid, caps the base and stabilizes the 'in' conformation, it brings the αB:A helix inward. However, the bulky phosphorothioate substitution at the equatorial position of the phosphate forces the PBC towards the 'out' conformation, causing a steric clash with the adjacent αB:A helix (red/orange star burst).

On one side, the Rp phosphorothioate forces the PBC and the αB:A towards the 'out' orientation, similar to the 'off' state, whereas on the other side, the Rp base engages the lid in the 'in' orientation, similar to the 'on' state (Fig. 5). These opposite tendencies lead to frustration in the close-topology of the R1a:Rp_2 complex and non-additive binding effect. The mixed response of the PBC and lid partially destabilizes the closed-topology ($A_{on}B_{on}$), leading to sampling of both the open and closed topology states in WT R1a:Rp_2. In such scenario, the free energy difference between the inhibition-competent state in the open-topology and the inhibition-incompetent state in the closed topology (*i.e.* $\Delta G_{R,gap}$) is tuned to be similar to the effective free energy of association of R:C complex (*i.e.* $\Delta G_{R:C\ binding}$), which in turn leads to allosteric pluripotency, *i.e.* Rp agonism or antagonism depending on the environmental conditions that modulate the R:C affinity (Fig. 6A, B) (5).

In the case of the R209K mutant, the Arg to Lys substitution in CBD-A allows the PBC to accommodate the bulky sulfur in the phosphorothioate group, allowing both the lid and the αB:A helix to remain in the 'in' conformations, relieving the steric frustration of the closed-topology observed in WT, and leading to selective stabilization of the closed-topology where both CBDs are in the 'on' state (Fig. 6C). This simple but effective model explains why the inter-domain interaction is more favourable in R209K relative to WT and why the ground non-inhibitory states is stabilized by R209K more than the excited inhibitory state. Hence, in R209K the $\Delta G_{R,gap}$ becomes larger than the free energy of association of R:C complex, providing a viable explanation for how the agonistic effect of Rp prevails and the allosteric pluripotency is silenced in the R209K mutant. We also anticipate that, if both the lid, the αB:A helix and the PBC all preferred the 'out' conformation, the closed-topology state would be de-stabilized, providing an avenue for consistent Rp-induced antagonism, with again suppression of allosteric pluripotency (Fig. 6D). It is only when the $\Delta G_{R,gap}$ and $\Delta G_{R:C\ binding}$ free energy differentials are tuned to comparable values by the frustration selectively present in the closed- but not open-topologies, as observed for the WT PKA R1a:Rp_2 complex (Fig. 6E, F), that allosteric pluripotency becomes possible.

To summarize, we were able to identify two key drivers for the Rp allosteric pluripotency observed in PKA. One is the conformational equilibrium of CBD-A sampling distinct populations of both 'off' and 'on' states. The other is the mixed response of the PBC (and its adjacent αB:A helix) and the lid region that causes steric frustration and destabilization of the closed-topology ground

state. Such frustration enables the R1a:Rp_2 complex to sample both the open and the closed topologies in significant populations. Together, these two drivers modulate the $\Delta G_{R,gap}$, *i.e.* the free-energy gap between the inhibition-competent excited state (A_{off}-B_{on}) and the inhibition-incompetent ground state ($A_{on}B_{on}$). Allosteric pluripotency occurs when the $\Delta G_{R,gap}$ is similar to the effective free energy of R:C association. When the identified drivers modulate the $\Delta G_{R,gap}$ to be significantly larger or smaller than the free energy of R:C association, then allosteric pluripotency is lost in favor of consistent agonism or antagonism. These results are significant for PKA, which serves as a prototype for other signaling hubs. In addition, we anticipate that the approaches illustrated here are applicable also to other allosteric systems exhibiting allosteric pluripotency.

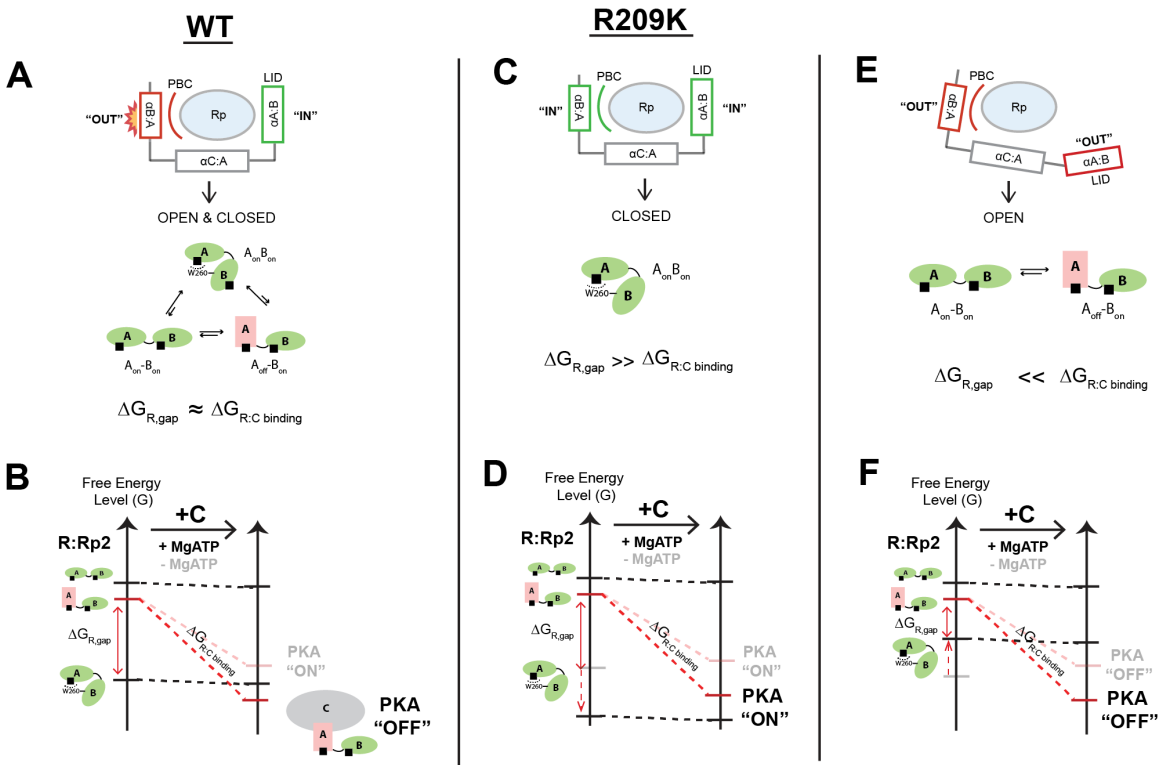

Figure 6. *The mixed response to the phosphate and base allosteric drivers within R1a leads to allosteric pluripotency.* **(A)** When PBC and the lid exhibit a mixed response, such as PBC 'out' and lid 'in' state, as in the case of WT, the closed-topology is only partially destabilized, leading to a conformational ensemble sampling both closed- and open-topologies, which is critical for driving allosteric pluripotency. **(B)** The free-energy landscape of WT R_{AB}:Rp_2 is remodelled by C-subunit binding. Since the $\Delta G_{R,gap}$ and the $\Delta G_{R:C\ binding}$ are similar, environmental conditions that modify $\Delta G_{R:C\ binding,}$ such as variations in MgATP levels, cause an agonism-antagonism switch (5, 18). **(C)** When both the PBC and the lid are 'in', as in the case of R209K, the closed topology state is stabilized and therefore $\Delta G_{R,gap} >> \Delta G_{R:C\ binding}$, leading to consistent agonism for Rp, as demonstrated by the free energy landscape shown in panel **(D).** **(E)** When both the PBC and the lid are 'out', the closed topology state is destabilized and therefore $\Delta G_{R,gap} << \Delta G_{R:C\ binding}$, leading to consistent antagonism for Rp, as demonstrated by the free energy landscape shown in panel **(F).**

4.6 Materials and Methods

NMR Acquisition

NMR data were acquired with a Bruker AVANCE or NEO 700-MHz spectrometer equipped with a 5 mm TCI cryopbrobe. All NMR experiments were acquired in the NMR buffer (50 mM MOPS pH 7.0, 100 mM NaCl, 10 mM $MgCl_2$, 5 mM dithiothreitol, and 0.02% sodium azide) with 5% ^2H_2O and at 306 K. NMR data were processed using either NMRPipe or Topspin. Spectral analyses were performed using NMRFAM-SPARKY (32) using Gaussian line fitting.

NMR Chemical shift analysis

Uniformly ^1H,^{15}N-labelled PKA R209K R_A (96-244) was expressed and purified following previously published protocols (30). The proteins were concentrated to 100 μM in the NMR buffer with and without 3 mM Rp-cAMPS (>99% purity; Biolog) and ^{15}N-^1H 2D HSQC experiments were acquired. The position of the 'on' *vs.* 'off' equilibria of R209K apo R_A and R209K R_A:Rp were measured through chemical shift correlation slope analyses using residues 104, 112, 114, 115, 151, 156, 157, 159, 162, 178, 180, 188, 221, and 223.

NMR cross-peak intensity comparison

Uniformly ^2H,^{15}N-labelled PKA R209K R_{AB} (91-379) was expressed and purified following previously published protocols (22, 30). The protein was concentrated to 20 μM in the NMR buffer and 2 mM of Rp-cAMPS was added prior to acquiring the ^{15}N-^1H 2D TROSY spectrum. The noise level of the R209K R_{AB}:Rp_2 spectrum near the position of the minor peak of WT R_{AB}:Rp_2 was measured through Topspin. Using multiple minor peak positions of WT R_{AB}:Rp_2, the average signal-to-noise ratio for the minor peaks was calculated. This value was used to estimate the upper limit population of the minor states in the R209K mutant.

Measurement of Rp-cAMPS K_d values for R1a CBD-A using NMR

Rp-cAMPS was titrated into either 100 μM ^1H,^{15}N-labelled PKA R209K R_A (96-244) or the 20 μM ^2H,^{15}N-labelled PKA R209K R_{AB} (91-379) and the binding was monitored by measuring the chemical shift of the cross peaks for G193 and N218, respectively, at each titration point. The

chemical shift change of the last titration point was used as a reference for normalization to determine the fraction of bound (<v>). The dissociation constants and the associated errors were calculated through fitting the curve to the equation $Y= B_{max}*X/(K_d+X)$ using GraphPad Prism (GraphPad Software), where Y refer to the fraction of bound and X refer to the $[Rp\text{-}cAMPS]_{free}$ (μM).

Measurement of Rp-cAMPS K_d values for R1a CBD-A using urea-induced unfolding

The WT and R209K R_A (91-244) and R_{AB} (91-379) constructs were expressed with BL21(DE3) *E. coli* using LB and 2xYT broth media, respectively, following previously published protocols (30). Urea-induced unfolding experiments were performed with 5 μM of R_A or R_{AB} construct either WT or R209K, in the absence and presence of excess Rp-cAMPS (500 μM for WT R_A, R_{AB} and R209K R_{AB}; 2 mM for R209K R_A). The dissociation constants were measured following previously published protocol (30).

Prediction of ρ_A and ΔG_{AB} values using the Ensemble Allosteric Model

A contour plot to illustrate the impact of ρ_A and ρ_B on the maximal activation of PKA in the presence of excess Rp-cAMPS and high concentration of MgATP (represented through γ = 1 (5) were generated using the following parameters: ΔG_{AB} = -4.00 RT, $[S]_{total}$ = 50 μM, K_m = 14 μM, $[R]_{total}$ = 12 nM, $[C]_{total}$ = 10 nM, [Rp-cAMPS] = 10^5 nM, ΔG_A = 0.00 RT, and ΔG_A = 0.85 RT. The contour plot was generated using a python script. The impact of ΔG_{AB} on the Rp-induced activation of R209K PKA was predicted in the presence of low and high [MgATP] (*i.e.* γ = 10^{-3} and γ = 1, respectively) and varying ΔG_{AB} values ranging from -2 to -7 RT. The following parameters were used: $[S]_{total}$ = 50 μM, K_m = 14 μM, $[R]_{total}$ = 12 nM, $[C]_{total}$ = 10 nM, ΔG_A = 0.62 RT, ΔG_B = 0.85 RT, ρ_A = 5.88, ρ_B = 330, and K_{A0} (association constant of Rp to 'off' state of CBD-A) = 1 / 1072 μM. The ΔG_A, ρ_A, and K_{A0} values were determined from the NMR and urea-induced unfolding experiments of R209K R1a. The K_{A0} was calculated using the K_d of Rp to R_A as measured from the urea-unfolding experiment (K_d = 386 μM) and using the fraction of 'off' and 'on' states sampled by the apo, which is 0.65 and 0.35, respectively. Then, the ρ_A = 5.88 was used to compute for K_{A0}.

4.7 References

1. Cohen, P. (2002) Protein kinases — the major drug targets of the twenty-first century? *Nat. Rev. Drug Discov.* **1**, 309–315
2. De Smet, F., Christopoulos, A., and Carmeliet, P. (2014) Allosteric targeting of receptor tyrosine kinases. *Nat. Biotechnol.* **32**, 1113–1120
3. Wodak, S. J., Paci, E., Dokholyan, N. V., Berezovsky, I. N., Horovitz, A., Li, J., Hilser, V. J., Bahar, I., Karanicolas, J., Stock, G., Hamm, P., Stote, R. H., Eberhardt, J., Chebaro, Y., Dejaegere, A., Cecchini, M., Changeux, J.-P., Bolhuis, P. G., Vreede, J., Faccioli, P., Orioli, S., Ravasio, R., Yan, L., Brito, C., Wyart, M., Gkeka, P., Rivalta, I., Palermo, G., McCammon, J. A., Panecka-Hofman, J., Wade, R. C., Di Pizio, A., Niv, M. Y., Nussinov, R., Tsai, C.-J., Jang, H., Padhorny, D., Kozakov, D., and McLeish, T. (2019) Allostery in Its Many Disguises: From Theory to Applications. *Structure*. **27**, 566–578
4. Motlagh, H. N., and Hilser, V. J. (2012) Agonism/antagonism switching in allosteric ensembles. *Proc. Natl. Acad. Sci.* **109**, 4134–4139
5. Byun, J. A., Akimoto, M., VanSchouwen, B., Lazarou, T. S., Taylor, S. S., and Melacini, G. (2020) Allosteric pluripotency as revealed by protein kinase A. *Sci. Adv.* **6**, eabb1250
6. Nguyen, T. T., Ghirlando, R., and Venditti, V. (2018) The oligomerization state of bacterial enzyme I (EI) determines EI's allosteric stimulation or competitive inhibition by α-ketoglutarate. *J. Biol. Chem.* **293**, 2631–2639
7. Berman, H. M., Ten Eyck, L. F., Goodsell, D. S., Haste, N. M., Kornev, A., and Taylor, S. S. (2005) The cAMP binding domain: An ancient signaling module. *Proc. Natl. Acad. Sci.* **102**, 45–50
8. Taylor, S. S., and Kornev, A. P. (2011) Protein kinases: evolution of dynamic regulatory proteins. *Trends Biochem. Sci.* **36**, 65–77
9. Serezani, C. H., Ballinger, M. N., Aronoff, D. M., and Peters-Golden, M. (2008) Cyclic AMP: master regulator of innate immune cell function. *Am. J. Respir. Cell Mol. Biol.* **39**, 127–132
10. Stork, P. J. ., and Schmitt, J. M. (2002) Crosstalk between cAMP and MAP kinase signaling in the regulation of cell proliferation. *Trends Cell Biol.* **12**, 258–266
11. ALBERINI, C. M., GHIRARDI, M., HUANG, Y.-Y., NGUYEN, P. V., and KANDEL, E. R. (1995) A Molecular Switch for the Consolidation of Long-Term Memory: cAMP-Inducible Gene Expression. *Ann. N. Y. Acad. Sci.* **758**, 261–286
12. Beristain, A. G., Molyneux, S. D., Joshi, P. A., Pomroy, N. C., Di Grappa, M. A., Chang, M. C., Kirschner, L. S., Privé, G. G., Pujana, M. A., and Khokha, R. (2015) PKA signaling drives mammary tumorigenesis through Src. *Oncogene*. **34**, 1160–1173
13. Saloustros, E., Salpea, P., Starost, M., Liu, S., Faucz, F. R., London, E., Szarek, E., Song, W.-J., Hussain, M., and Stratakis, C. A. (2017) Prkar1a gene knockout in the pancreas leads to neuroendocrine tumorigenesis. *Endocr. Relat. Cancer*. **24**, 31–40
14. Wilson, G. R., Cramer, A., Welman, A., Knox, F., Swindell, R., Kawakatsu, H., Clarke, R. B., Dive, C., and Bundred, N. J. (2006) Activated c-SRC in ductal carcinoma in situ correlates with high tumour grade, high proliferation and HER2 positivity. *Br. J. Cancer*. **95**, 1410–1414
15. Elsberger, B., Tan, B. A., Mitchell, T. J., Brown, S. B. F., Mallon, E. A., Tovey, S. M., Cooke, T. G., Brunton, V. G., and Edwards, J. (2009) Is Expression or Activation of Src Kinase Associated with Cancer-Specific Survival in ER-, PR- and HER2-Negative Breast Cancer Patients? *Am. J. Pathol.* **175**, 1389–1397

16. Boikos, S. A., and Stratakis, C. A. (2007) Carney complex: the first 20 years. *Curr. Opin. Oncol.* **19**, 24–29
17. WIT, R. J. W., HOPPE, J., STEC, W. J., BARANIAK, J., and JASTORFF, B. (1982) Interaction of cAMP Derivatives with the "Stable" CAMP-Binding Site in the CAMP-Dependent Protein Kinase Type I. *Eur. J. Biochem.* **122**, 95–99
18. Dostmann, W. R., and Taylor, S. S. (1991) Identifying the molecular switches that determine whether (Rp)-cAMPS functions as an antagonist or an agonist in the activation of cAMP-dependent protein kinase I. *Biochemistry*. **30**, 8710–6
19. Kim, C., Cheng, C. Y., Saldanha, S. A., and Taylor, S. S. (2007) PKA-I holoenzyme structure reveals a mechanism for cAMP-dependent activation. *Cell*. **130**, 1032–43
20. Huang, L. J., and Taylor, S. S. (1998) Dissecting cAMP Binding Domain A in the R I α Subunit of cAMP-dependent Protein Kinase. *J. Biol. Chem.* **273**, 26739–26746
21. Taylor, S. S., Ilouz, R., Zhang, P., and Kornev, A. P. (2012) Assembly of allosteric macromolecular switches: lessons from PKA. *Nat. Rev. Mol. Cell Biol.* **13**, 646–658
22. Akimoto, M., McNicholl, E. T., Ramkissoon, A., Moleschi, K., Taylor, S. S., and Melacini, G. (2015) Mapping the Free Energy Landscape of PKA Inhibition and Activation: A Double-Conformational Selection Model for the Tandem cAMP-Binding Domains of PKA RIα. *PLoS Biol.* **13**, e1002305
23. Herberg, F. W., Dostmann, W. R. G., Zorn, M., Davis, S. J., and Taylor, S. S. (1994) Crosstalk between Domains in the Regulatory Subunit of cAMP-Dependent Protein Kinase: Influence of Amino Terminus on cAMP Binding and Holoenzyme Formation. *Biochemistry*. **33**, 7485–7494
24. Herberg, F. W., Doyle, M. L., Cox, S., and Taylor, S. S. (1999) Dissection of the Nucleotide and Metal−Phosphate Binding Sites in cAMP-Dependent Protein Kinase †. *Biochemistry*. **38**, 6352–6360
25. Su, Y., Dostmann, W. R., Herberg, F. W., Durick, K., Xuong, N. H., Ten Eyck, L., Taylor, S. S., and Varughese, K. I. (1995) Regulatory subunit of protein kinase A: structure of deletion mutant with cAMP binding domains. *Science*. **269**, 807–13
26. Herberg, F. W., Taylor, S. S., and Dostmann, W. R. G. (1996) Active Site Mutations Define the Pathway for the Cooperative Activation of cAMP-Dependent Protein Kinase †. *Biochemistry*. **35**, 2934–2942
27. Hilser, V. J., Wrabl, J. O., and Motlagh, H. N. (2012) Structural and Energetic Basis of Allostery. *Annu. Rev. Biophys.* **41**, 585–609
28. Motlagh, H. N., Wrabl, J. O., Li, J., and Hilser, V. J. (2014) The ensemble nature of allostery. *Nature*. **508**, 331–339
29. White, J. T., Li, J., Grasso, E., Wrabl, J. O., and Hilser, V. J. (2018) Ensemble allosteric model: energetic frustration within the intrinsically disordered glucocorticoid receptor. *Philos. Trans. R. Soc. B Biol. Sci.* **373**, 20170175
30. Akimoto, M., Selvaratnam, R., McNicholl, E. T., Verma, G., Taylor, S. S., and Melacini, G. (2013) Signaling through dynamic linkers as revealed by PKA. *Proc. Natl. Acad. Sci. U. S. A.* **110**, 14231–6
31. Boulton, S., Van, K., VanSchouwen, B., Augustine, J., Akimoto, M., and Melacini, G. (2020) Allosteric Mechanisms of Nonadditive Substituent Contributions to Protein-Ligand Binding. *Biophys. J.* **119**, 1135–1146
32. Lee, W., Tonelli, M., and Markley, J. L. (2015) NMRFAM-SPARKY: enhanced software for biomolecular NMR spectroscopy. *Bioinformatics*. **31**, 1325–1327

4.8 Supplementary Materials

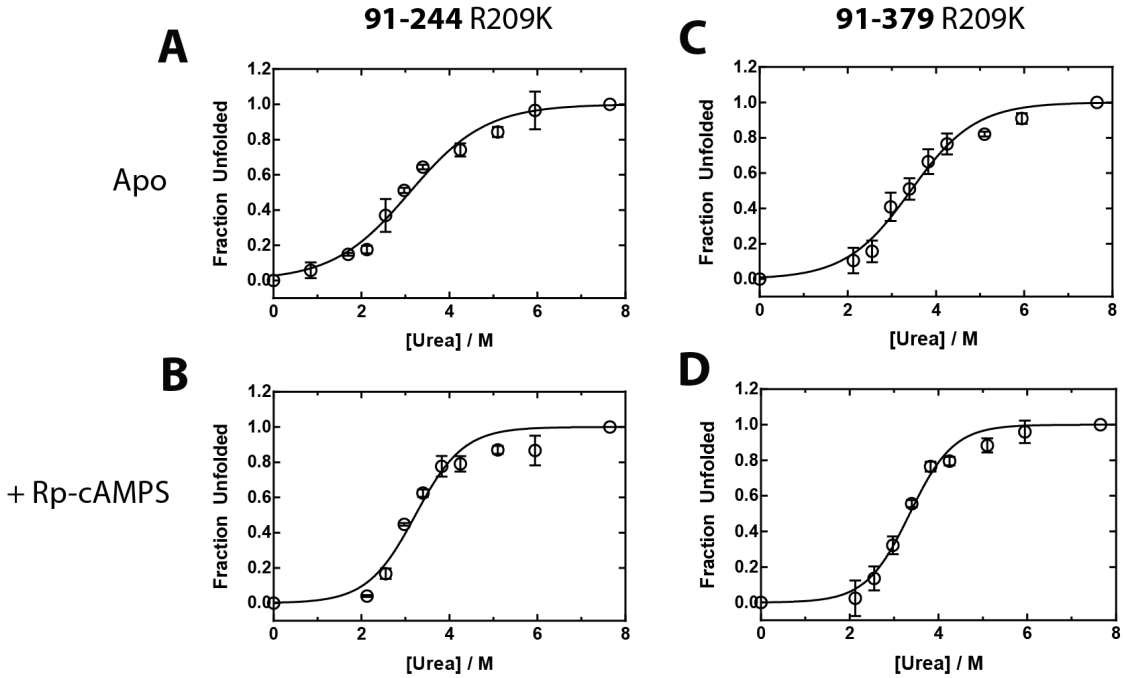

Figure S1. *Urea-induced unfolding curves for R209K.* **(A)** Urea-induced unfolding curve for apo R209K R_A (91-244). **(B)** Similar to (A) but in the presence of excess Rp-cAMPS (2 mM). **(C)** Similar to (A) but for the R_{AB} (91-379) construct. **(D)** Similar to (B) but in the presence of excess Rp-cAMPS (500 μM).

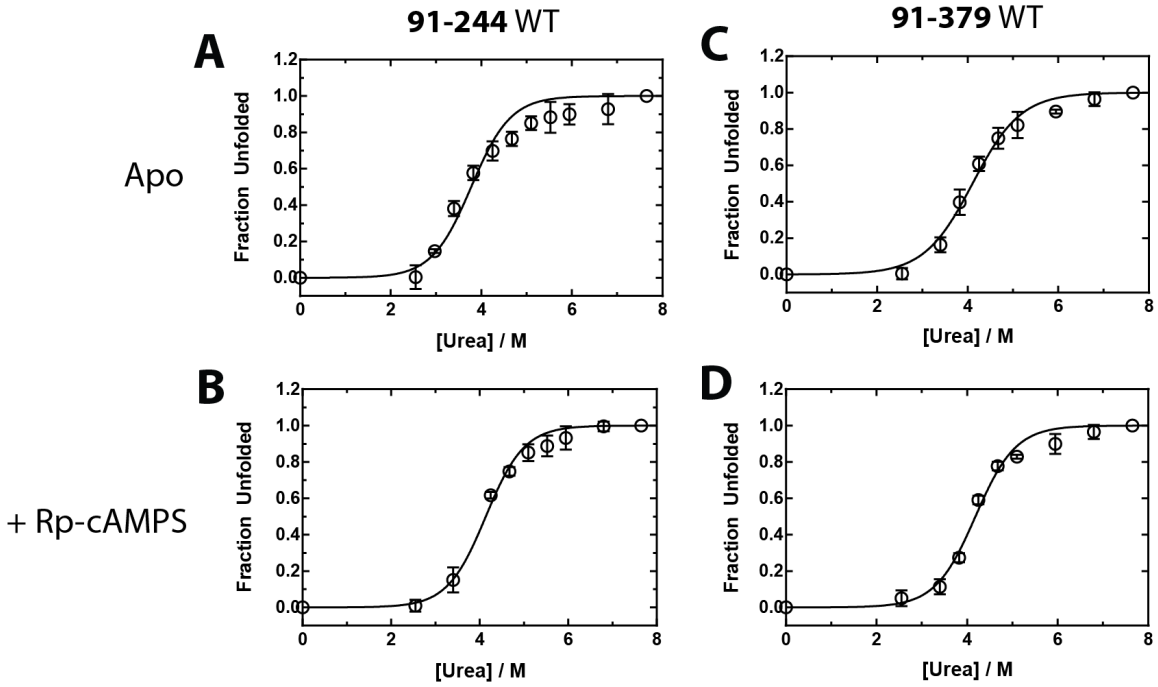

Figure S2. *Urea-induced unfolding curves for WT.* **(A)** Urea-induced unfolding curve for apo WT R_A (91-244). **(B)** Similar to (A) but in the presence of excess Rp-cAMPS (500 μM). **(C)** Similar to (A) but for the R_{AB} (91-379) construct. **(D)** Similar to (B) but for R_{AB} (91-379) construct.

Chapter 5

Mechanism of allosteric inhibition in the *Plasmodium falciparum* cGMP-dependent protein kinase

5.1 Author's Preface

The work presented in this chapter has previously been published and is reproduced here with permission from the Journal of Biological Chemistry, the American Society for Biochemistry and Molecular Biology. Full citation is as follows:

Byun, J. A., Van, K., Huang, J., Henning, P., Franz, E., Akimoto, M., Herberg, F. W., Kim, C., and Melacini, G. (2020) Mechanism of allosteric inhibition in the Plasmodium falciparum cGMP-dependent protein kinase. *J. Biol. Chem.* **295,** 8480–91.

I conducted and analyzed all NMR experiments. Katherine Van assisted in the NMR chemical shift assignments. Jinfeng Huang performed all the MD simulations. Philipp Henning and Eugene Franz prepared samples and performed kinase assays and direct binding measurements with support from Dr. Friedrich W. Herberg. Dr. Madoka Akimioto provided helpful discussions. Dr. Choel Kim provided the plasmids. I co-wrote the manuscript and designed the research with Dr. Giuseppe Melacini.

5.2 Abstract

Most malaria deaths are caused by the protozoan parasite *Plasmodium falciparum*. Its life cycle is regulated by a cGMP-dependent protein kinase (*Pf*PKG), whose inhibition is a promising antimalaria strategy. Allosteric kinase inhibitors, such as cGMP analogs, offer enhanced selectivity unlike competitive kinase inhibitors. However, the mechanisms underlying allosteric *Pf*PKG inhibition are incompletely understood. Here, we show that 8-NBD-cGMP is an effective *Pf*PKG antagonist. Using comparative NMR analyses of a key regulatory domain, *Pf*D, in its apo, cGMP-, and cGMP analog–bound states, we elucidated its inhibition mechanism of action. Using NMR chemical shift analyses, molecular dynamics simulations, and site-directed mutagenesis, we show that 8-NBD-cGMP inhibits *Pf*PKG not simply by reverting a two-state active *versus* inactive equilibrium, but by sampling also a distinct inactive 'mixed' intermediate. Surface-plasmon resonance indicate that the ability to stabilize a mixed intermediate provides a means to effectively inhibit *Pf*PKG, without losing affinity for the cGMP analog. Our proposed model may facilitate the rational design of *Pf*PKG-selective inhibitors for improved management of malaria.

5.3 Introduction

Malaria is a serious health risk for about 40 % of the world's population, with more than 200 millions of diagnoses and 400 thousands deaths globally estimated in 2018 (1). Most of malarial deaths are caused by *Plasmodium falciparum* with life cycles in both the human and the mosquito hosts (2, 3). The regulation of such cycles relies on cyclic-nucleotide signalling pathways (4).

Specifically, the *P. falciparum* cGMP-dependent kinase (*Pf*PKG) plays a major role in both replication and transmission of the *Plasmodium* parasite, including exflagellation and gametogenesis in the asexual blood stage, invasion of hepatocytes by sporozoites, and gliding motility of ookinetes (5–9). Hence, *Pf*PKG has emerged as a promising target for development of antimalaria therapies complementary to current malaria drugs, whose effectiveness is limited by increasing resistance (2, 10, 11). Furthermore, *Pf*PKG inhibition is an effective and novel strategy not only for malaria treatment, but also for malaria prophylaxis (2, 6, 12–15).

One strategy to inhibit *Pf*PKG is through targeting the active site in the kinase domain. Inhibitors that target such kinase active site are effective, but poorly selective, since the active sites are highly conserved among eukaryotic kinases (16). One approach to circumvent this is to target allosteric sites, such as the cGMP-binding sites in *Pf*PKG.

*Pf*PKG consists of an N-terminal regulatory region followed by a C-terminal catalytic domain (Fig. 1A), similarly to mammalian PKG (17–19). In the absence of cGMP, the regulatory region of *Pf*PKG auto-inhibits the catalytic domain. Upon cGMP binding to the regulatory region, the *Pf*PKG auto-inhibition is allosterically removed, resulting in activation. The regulatory domain is composed of four cGMP binding domains (CBDs): A, B, C and D (Fig. 1A). CBD-C is degenerate and does not bind to cGMP (20). CBD-D (here referred to as "*Pf*D") is adjacent to the catalytic domain (Fig. 1A) and exhibits the highest affinity and selectivity towards cGMP with a K_d of 40 nM, compared to $K_d \geq 1$ μM for CBD-A and CBD-B (14). In addition, the construct spanning only *Pf*D and the catalytic domain displays low basal activity in the *apo* state and is efficiently activated by cGMP (21). Hence, *Pf*D serves as the critical controlling unit for both *Pf*PKG auto-inhibition and activation.

*Pf*D is composed of a contiguous β-subdomain and non-contiguous α-subdomain (Fig. 1B) (14, 22). The β-subdomain forms a β-barrel critical for cGMP recognition and includes the Base Binding Region (BBR) and the Phosphate Binding Cassette (PBC) (Fig. 1B, C), whereas the α-

subdomain mediates inhibitory interactions with the catalytic domain and includes three N-terminal and two C-terminal helices, called N3A motif and αB-αC, respectively (Fig. 1B, D). In the *apo* form, the N3A contacts the β-barrel, while the C-terminal helices point away from it (Fig. 1B) (14). Upon cGMP binding, the N3A moves away from the β-subdomain, while the C-terminal helices are recruited to it by an arginine residue in the PBC, R484 (Fig. 1B). R484 bridges the PBC to two residues in the αC and defines a unique cGMP capping triad (Fig. 1B), markedly distinct from human PKG, in which cGMP is capped by a Tyr in the C-terminal helix (23). Disruption of the *Pf*PKG-specific capping triad by mutations blocks proliferation in *P. falciparum* (14), confirming that *Pf*D is an excellent target for treating malaria. Additionally, R528 in the αC plays a pivotal role in regulating *Pf*PKG activity by controlling the αC conformation through a hydrogen-bond with Y480, which stabilizes the active conformation (Fig. 1D) (14, 21, 24).

The allosteric transition of *Pf*D provides a simple model to rationalize the cGMP-dependent activation of the full length protein through a four-state allosteric thermodynamic cycle, which arises from the coupling of the *Pf*D inactive-active auto-inhibitory equilibrium and the *apo-holo* cGMP-binding equilibrium (Fig. 1E) (25–27). Out of the four states (Fig. 1E), the *holo*-inactive is particularly relevant for inhibition. This state is selectively stabilized by partial agonists and/or antagonists, which decouple binding from the intramolecular allosteric pathways necessary for activation. We hypothesize that the stabilization of the *holo*-inactive state arise from a reversal of the two-state inactive/active conformational equilibrium (Fig. 1F) or from a multi-state equilibrium sampling a distinct intermediate conformation that exhibits components of both the inactive and the active states of *Pf*D in different regions (Fig. 1G).

In order to test these hypotheses and understand the mechanism of action of allosteric partial agonists and antagonists that serve as leads for new *Pf*PKG selective inhibitors, we use comparative NMR to analyze *Pf*D in its *apo*, cGMP-bound, and cGMP-analog bound forms. The cGMP-analogs investigated here include 8-NBD-cGMP, 8-pCPT-cGMP, and PET-cGMP (Fig. 1I-K). Our results reveal that 8-NBD-cGMP and 8-pCPT-cGMP significantly reduce the kinase activity and induce major perturbations throughout *Pf*D by stabilizing an additional intermediate conformer that is distinct from both the native *apo*-inactive and *holo*-active conformations. This 'mixed' intermediate state exhibits comparable inhibitory potential to the *apo* inactive state, as the C-terminal lid is disengaged, but it preserves an affinity similar to cGMP, as the key cGMP binding regions, including the PBC and the adjacent αB, are still engaged. Hence, the

stabilization of an allosterically mixed intermediate emerges as a new strategy for selectively inhibiting *Pf*PKG with high potency and efficacy.

5.4 Results and Discussion

5.4.1 The apo *vs.* cGMP-bound comparative NMR analyses of *Pf*D reveal pervasive allosteric perturbations

As a first step to probe the allosteric effects of cGMP on the *Pf*D construct (401-542) used in our NMR studies, we acquired NH HSQC spectra of *apo* and cGMP-bound *Pf*D (Fig. 2A). The cGMP-bound spectrum was assigned through triple resonance NMR experiments and selective amino acid labelling. However, the *apo* construct was prone to precipitation during acquisition of 3D NMR data sets. Hence, the *apo* assignments were obtained by transferring the *holo* assignments to the *apo* spectrum through 2D-N_z-exchange (Fig. 2B, D) and 2D-difference N_z-exchange experiments acquired in the presence of sub-stoichiometric amounts of cGMP (Fig. 2C, E). Based on these assignments the cGMP-induced residue-specific compounded chemical shift changes (ΔCCS) were measured (Fig. 2F).

The majority of the residues exhibit significant ΔCCS values upon cGMP binding (Fig. 2F). As expected, significant ppm shifts are observed in the PBC and BBR regions, which directly interact with cGMP, as well as the β2-3 loop, which is adjacent to the PBC (Fig. 2F). Furthermore, major ppm changes are also detected for several α-helical regions, especially the αA, αB and αC helices (Fig. 2F). The ppm shifts in αB-αC are consistent with the cGMP-dependent structural changes for these regions, as shown by the local RMSD between the *apo vs.* cGMP-bound structures (Fig. 2G). The αB-αC structural changes also affect adjacent regions, such as the αA helix and the β8 strand (Fig. 2F), although such regions are not subject to major structural changes upon cGMP binding (Fig. 2G). Hence, the cGMP-dependent ΔCCS values (Fig. 2F) are in full agreement with the structures of *apo* and *holo Pf*D, providing an initial validation of our NMR assignments.

Our NMR assignments were further validated by the agreement between the measured and the computed Cα and Cβ chemical shift values based on the *apo* and *holo Pf*D structures (Fig. 2H,I). Once the NMR assignments were validated, we extended our analyses to evaluate the effects of cGMP analogs.

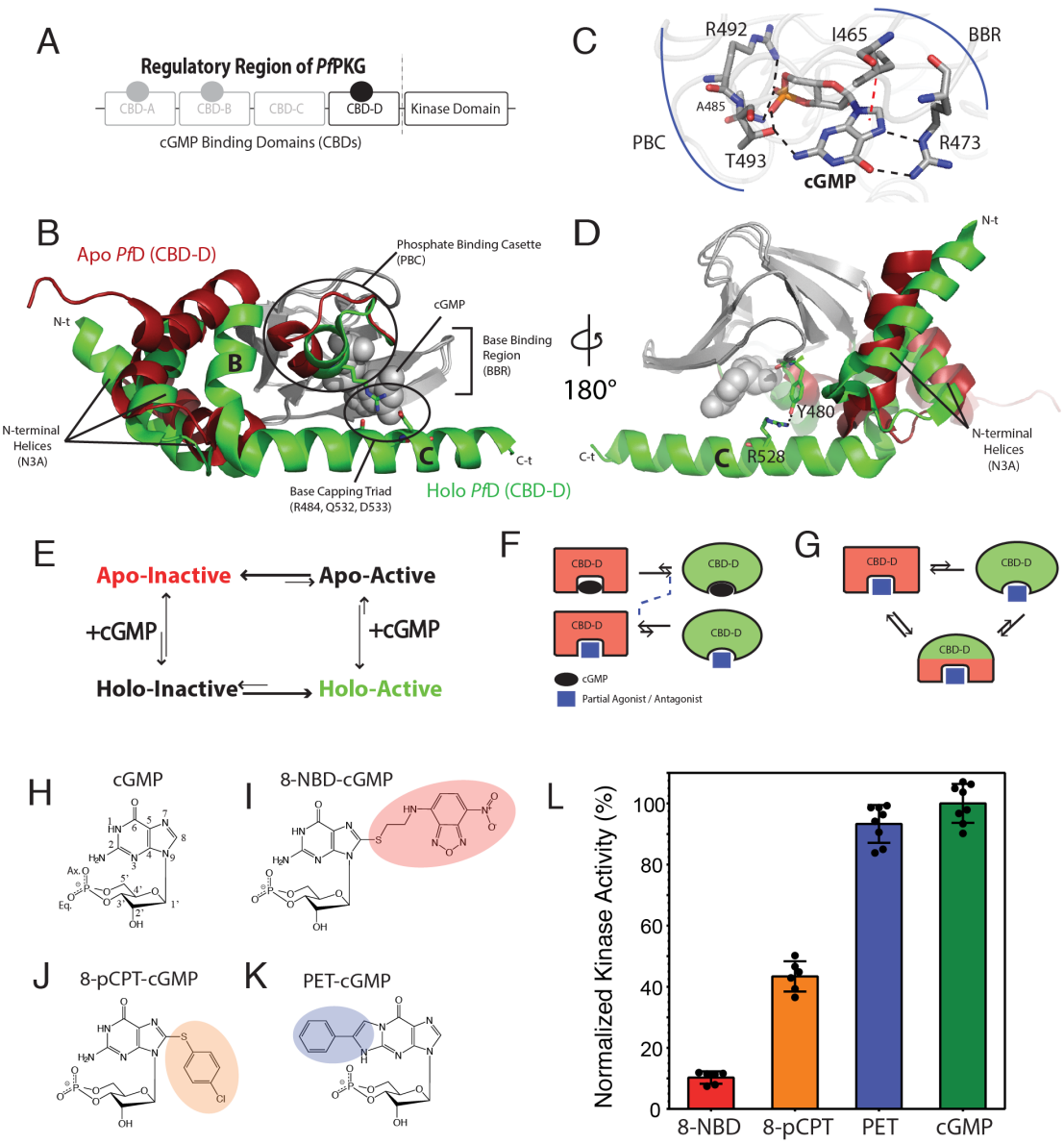

Figure 1. *Structural architecture of PfCBD-D and hypothetical models of inhibition.* **(A)** Domain organization of *Pf*PKG, including a regulatory region with four cyclic-nucleotide binding domains (CBD) and a C-terminal catalytic kinase domain. CBD-C is degenerate and does not bind cGMP. **(B)** Structures of *apo* (red) and cGMP-bound (green) CBD-D. The invariant β-subdomain is grey in both structures. **(C)** cGMP binding pocket of *Pf*D and selected cGMP-interacting residues. Black dashed lines represent hydrogen bonds. Red dashed line represents hydrophobic interaction. **(D)** Similar to panel (B) but with 180° vertical rotation, highlighting the Y480-R528 interaction. **(E)** Four-state thermodynamic equilibrium of the essential regulatory CBD (*i.e.* CBD-D). The apo CBD-D samples an auto-inhibitory equilibrium between inactive and active states, which is coupled to the cGMP-binding equilibrium. (**F, G)** Hypotheses to explain *Pf*PKG inhibition, as reversal of a two-state equilibrium (F) or stabilization of an intermediate with mixed active and inactive features and diminished activation competency (G). **(H-K)** Base-substituted cGMP-analogs investigated here. **(L)** Maximum *Pf*PKG kinase activities induced by cGMP and the cGMP-analogs in panels I-K.

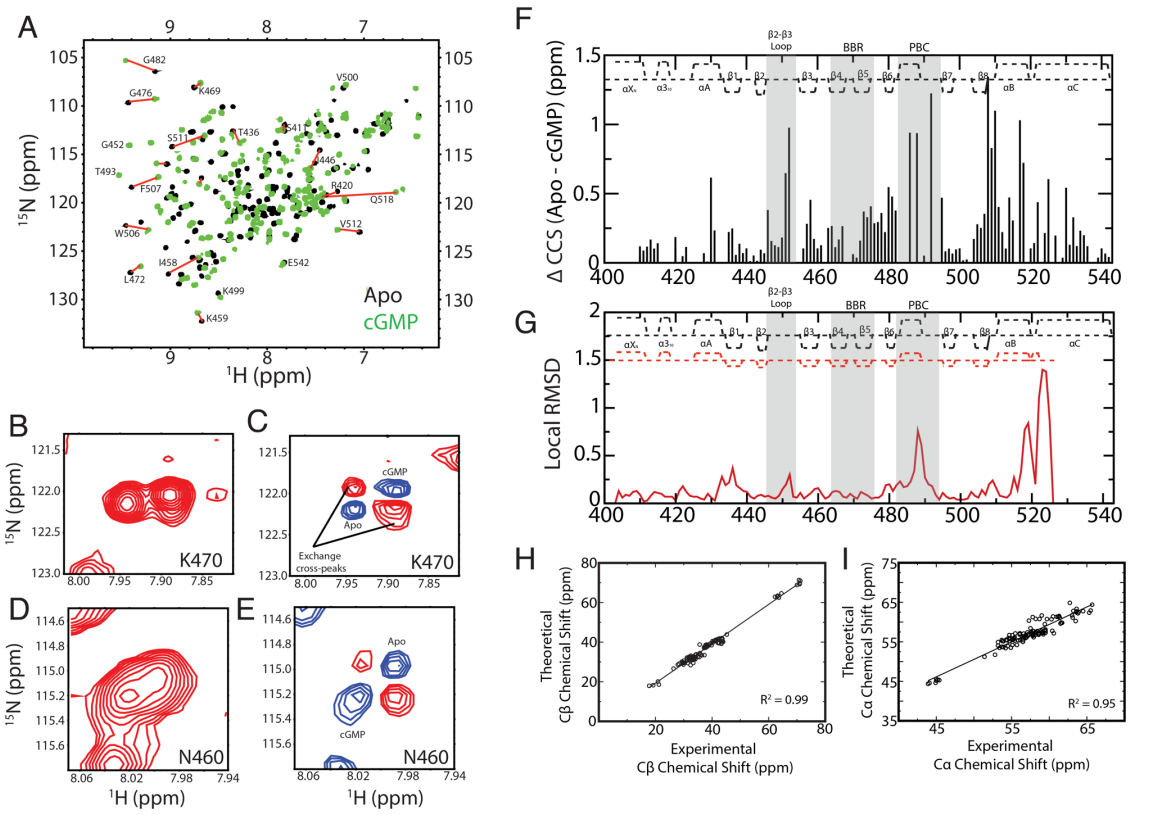

Figure 2. *The apo vs. cGMP-bound comparative NMR analyses of PfD reveal pervasive allosteric perturbations.* **(A)** Overlay of ^{15}N-^{1}H HSQC spectra of *apo* (black) and cGMP-bound (green) *Pf*D samples with representative assignments. N_z-Exchange **(B,D)** and N_z-exchange difference experiments **(C,E)** utilized to transfer the assignments from the cGMP-bound to the *apo* spectra. **(F)** Compounded ^{15}N-^{1}H Chemical Shift (CCS) differences between the *apo* and cGMP-bound samples. The secondary structure of *Pf*D is depicted on the top of the plot. The cGMP-binding regions BBR and PBC as well as the adjacent β2-3 loop are highlighted in grey background. **(G)** Local *apo* (PDB: 4OFF) *vs.* cGMP-bound (PDB: 4OFG) RMSD for *Pf*D. The secondary structures obtained from the *apo* and cGMP-bound crystals are reported as red and black dashed lines, respectively. **(H)** Cβ chemical shift values of cGMP-bound *Pf*D obtained from NMR triple resonance experiments *versus* the theoretical Cβ chemical shift values predicted form the structure (PDB code: 4OFG) using the ShiftX software (54). **(I)** Similar to (H) but for the Cα chemical shifts.

5.4.2 cGMP-Analog *vs.* cGMP chemical shift differences report on inhibitory conformational changes of *Pf*D

We focused on three cGMP analogs with distinct base modifications: 8-NBD-, 8-pCPT- and PET-cGMP (Fig. 1I-K), as they act as *Pf*PKG activators to different degrees. While PET-cGMP acts as an agonist as shown by kinase assays (Fig. 1L), 8-pCPT- and 8-NBD-cGMP elicit progressively increasing potential as antagonists. 8-NBD-cGMP is the most potent inhibitor of *Pf*PKG (Fig. S1), followed by 8-pCPT-cGMP. This range of kinase responses (Fig. 1L) makes this group of cGMP-analogs an excellent toolset to investigate the mechanisms underlying the allosteric inhibition of *Pf*PKG. For this purpose, we first measured the cGMP-analog *vs.* cGMP differences in compounded chemical shifts (Fig. 3A). The overall distributions of such ppm differences (Fig. 3B) rank in full agreement with the inhibitory potencies of the cGMP analogs (Fig. 1L). Furthermore, the pervasiveness of the effects caused by the cGMP modification (Fig. 3A, C-E) also reflects the extent of inhibition. The perturbations resulting from the replacement of cGMP with either 8-NBD-cGMP or 8-pCPT-cGMP extend throughout the *Pf*D structure, whereas, the least inhibitory analog, PET-cGMP, perturbs only a relatively limited region near the cGMP binding pocket (Fig. 3A, C-E).

Overall, the data of Fig. 3 suggest that chemical shifts are ideally suited to investigate the dynamical allosteric transitions underlying *Pf*PKG inhibition. This notion is fully consistent with the fast exchange between the inactive and the active states of CBDs (27–33), whereby the observed NMR peak positions are population-weighted averages of the pure inactive and active ppm values. Hence, chemical shifts report on the position of the dynamic inactive-active CBD conformational equilibrium. The CHemical Shift Projection Analysis (CHESPA) is an effective means to evaluate the perturbation of such dynamic equilibria caused by ligand modifications (28, 29, 31, 32). In the CHESPA analysis, the NMR peak positions of the cGMP-analog bound sample are evaluated relative to a reference vector connecting the peaks of the *apo* inactive and the cGMP-bound active samples (Fig. 4A, D). Specifically, the angle (θ) arising from the cGMP-analog bound *vs.* cGMP bound vector relative to the reference vector and the normalized projections onto the reference vector (*i.e.* fractional shift, *X*) are quantified through CHESPA (Fig. 4A, D). The cos(θ) values report on the direction of the cGMP-analog induced shifts, while the *X* values gauge the extent of such shift towards inhibition or activation.

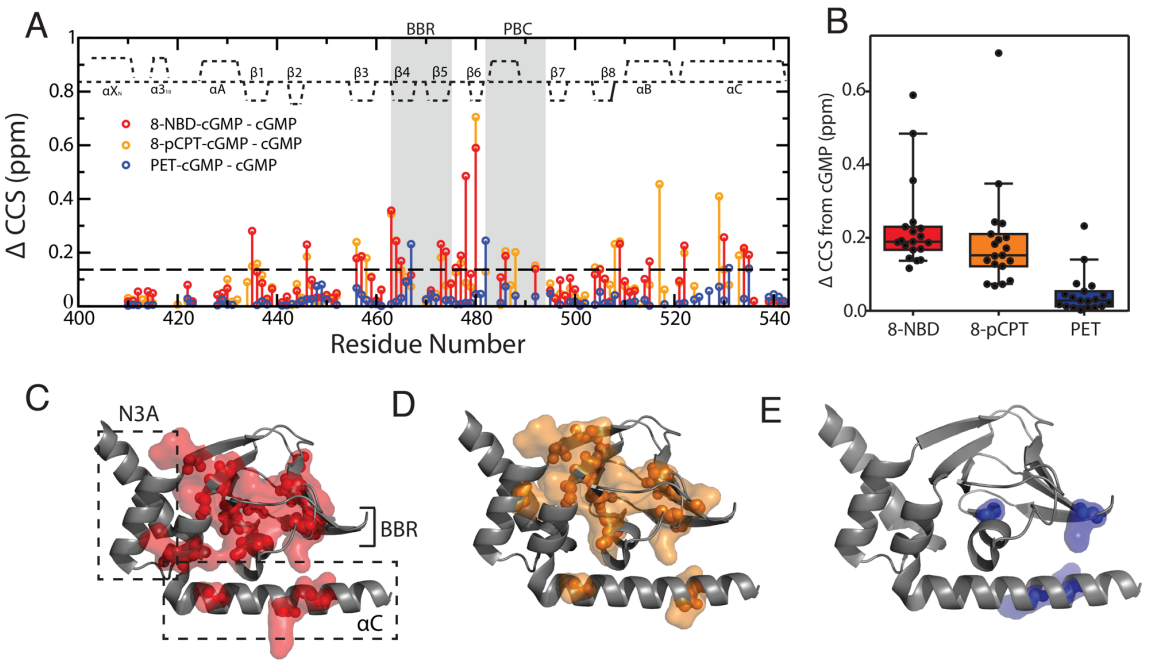

Figure 3. *cGMP-Analog vs. cGMP chemical shift differences report on inhibitory conformational changes of PfD.* **(A)** Compounded Chemical Shift difference (ΔCCS) between cGMP and 8-pCPT-cGMP (orange), 8-NBD-cGMP (red), PET-cGMP (blue) bound *Pf*D plotted against residue numbers. Dashed line indicates the average ΔCCS + 2 S.D. of PET-cGMP. **(B)** Box plot (10-90% percentile) of ΔCCS differences between cGMP-bound and the 8-NBD-cGMP, 8-pCPT-cGMP, and PET-cGMP-bound samples. Residues included in the box plot correspond to residues that are assigned in all samples and with at least one of the three ΔCCS > average + 2 S.D. of PET-cGMP (dashed line in Panel A). **(C-E)** Residues with CCS changes greater than the dashed line in (A) mapped onto the active structure of *Pf*D for the 8-NBD-cGMP (C), 8-pCPT-cGMP (D) and PET-cGMP (E) bound samples.

5.4.3 The CHemical Shift Projection Analyses (CHESPA) of the cGMP-analog bound *Pf*Ds reveal the presence of a third 'mixed' conformer with an engaged pre-lid but a disengaged lid

The CHESPA of 8-NBD-cGMP shows that the majority of residues exhibit negative *X* values (Fig. 4B), suggestive of most residues shifting towards the inactive state upon binding of 8-NBD-cGMP. However, the magnitudes of the *X* values are highly residue-dependent, pointing to deviations from the pure inactive-active two-state equilibrium, which predicts similar *X* values for residues outside the binding site. Another characteristic of a two-state model is the co-

linearity of the perturbation and reference vectors (*i.e.* $|\cos(\theta)| \sim 1$) for residues outside the binding site. However, the CHESPA of 8-NBD-cGMP reveals that several residues not in the binding site exhibit $|\cos(\theta)|$ values significantly < 1 (Fig. 4C), suggesting deviations from the two-state model and pointing to the presence of additional state(s) sampled by the *Pf*D:8-NBD-cGMP complex. Similar trends are observed for the 8-pCPT-cGMP-bound sample (Fig. 4E, F).

The presence of multiple conformational equilibria is further supported by the width of the *X* value distributions (Fig. 4G). The *X* distributions measured for 8-NBD-cGMP and 8-pCPT-cGMP bound *Pf*D are significantly wider compared to PET-cGMP (Fig. 4G), which is nearly a full agonist and samples mainly the active state (Fig. S2). These observations suggest that the *Pf*D:8-NBD-cGMP and *Pf*D:8-pCPT-cGMP complexes sample a multi-state ensemble, including not only the inactive and active conformers represented by the *apo* and cGMP-bound crystal structures, but also an additional state or states.

To simplify the analysis, we focused on the C-terminal helices that are directly linked to the catalytic domain and are one of the allosteric elements most critical in the inhibition and activation of the kinase (14, 21, 24). The C-terminal helices span two regions with clearly distinct average *X* values (<*X*>) in the *Pf*D:8-NBD-cGMP complex: residues 515-530, denoted as the pre-lid with <*X*> = -0.48, and residues 534-535, denoted as the lid with <*X*> = -0.88 (Fig. 4B, H, I). This means that for the *Pf*D:8-NBD-cGMP complex, the pre-lid only shifts ~halfway towards the inactive state, whereas the lid region shifts almost completely to the inactive state. A similar trend is observed for the *Pf*D:8-pCPT-cGMP complex with average *X* values of -0.30 and -0.64 in the pre-lid and the lid regions, respectively.

One of the simplest models to explain both the enzymatic and the NMR data in Figs. 1L and 4, respectively, is a three-state equilibrium mechanism involving an inactive, an active, and an intermediate state (Fig. 5A). The inactive state is similar to the *apo Pf*D structure, where both the pre-lid and the lid are disengaged. The active state is similar to the cGMP-bound structure, where both the pre-lid and the lid are engaged. The intermediate state exhibits a mixed character, as the pre-lid is engaged similarly to the active state, but the lid is disengaged, similarly to the inactive state (Fig. 5A). Next, we checked if it is possible to utilize this three-state model to back calculate the relative kinase activities.

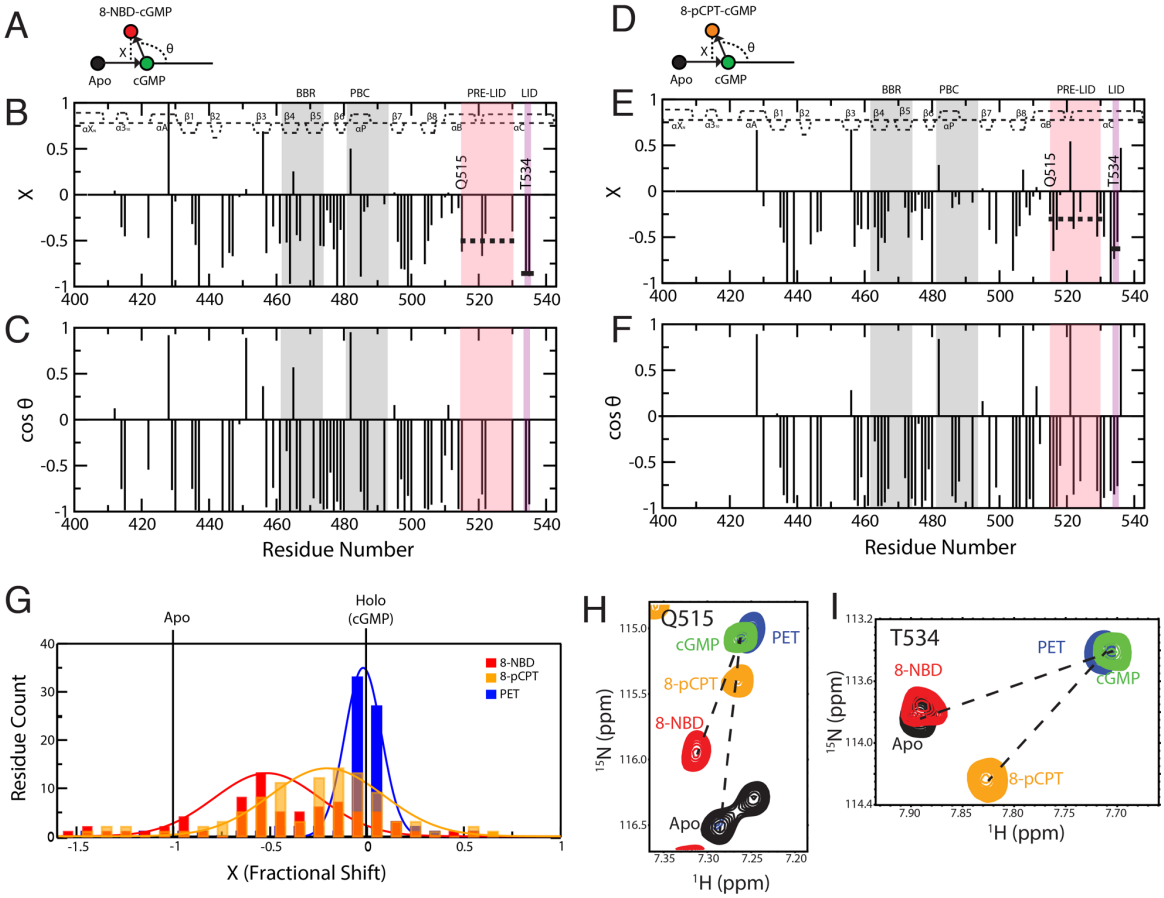

Figure 4. *CHemical Shift Projection Analysis (CHESPA) of cGMP-analog bound states reveals a third conformer with a disengaged lid.* CHESPA vector scheme, fractional shift (*X*) and *cos(Θ)* values plotted against residue number for 8-NBD-cGMP **(A-C)** and for 8-pCPT-cGMP **(D-F)**. The secondary structure of cGMP-bound *Pf*D is depicted on the top of each plot. Pre-Lid and Lid motifs are highlighted in pink and purple background, respectively. The PBC and BBR are highlighted in grey background. The average <*X*> values for residues common in both 8-NBD-cGMP bound and 8-pCPT-cGMP bound sample are indicated with a dashed and a solid line for the Pre-Lid and the Lid motifs, respectively. **(G)** Distribution of *X* values for 8-NBD-, 8-pCPT-, and PET-cGMP bound samples. **(H, I)** HSQC overlay expansions for representative residues in the pre-lid and lid regions of the *apo* (black) and the 8-NBD-cGMP (red), 8-pCPT-cGMP (orange), PET-cGMP (blue) and cGMP (green) bound samples.

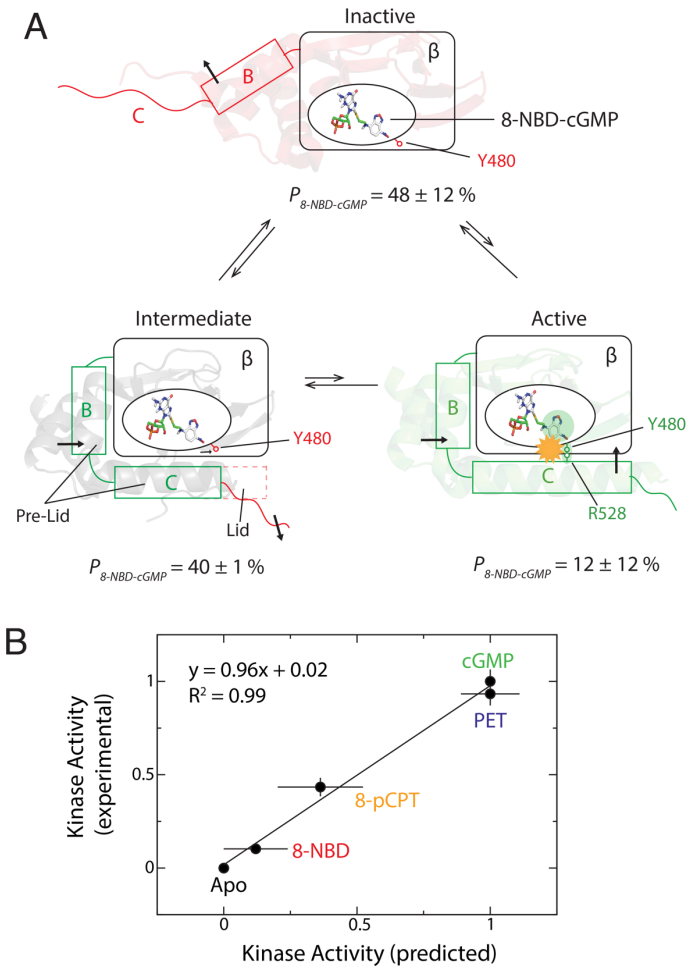

Figure 5. *Proposed model for PfD inhibition by 8-NBD-cGMP and comparison of calculated vs. measured kinase activities.* **(A)** Inhibition occurs through a three-state equilibrium, sampling a distinct holo-inactive intermediate state, where the pre-lid and PBC are engaged, similarly to the active state, but the lid is disengaged, similarly to the inactive state. The population of each state (*P*) is indicated. The structural shifts of the αB and αC helices are indicated with black arrows. The β-barrel is indicated with a rectangular box. The yellow starburst indicates the steric clash between the 8-NBD substituent and the R528 side chain. **(B)** Correlation plot of experimental *vs.* predicted relative kinase activities. The kinase activity prediction is based on the populations of inactive, intermediate, and active states (Table S1).

5.4.4 The CHESPA-based three-state model of *Pf*D inhibition explains the experimental kinase activities

Using the average *X* values for the pre-lid and the lid regions (Fig. 4B, E; Fig. S2A), the populations of the inactive, intermediate, and active states were estimated. Since the pre-lid is disengaged only in the inactive state, the average *X* of the pre-lid represents the population of

the inactive state. Similarly, the lid is engaged only in the active state. Hence, the population of the active state is estimated as 1 - $\langle X \rangle_{lid}$. The population of the intermediate is the percentage not accounted by the other two states. Using this approach, the populations of the inactive, intermediate, and active states for the *Pf*D:8-NBD-cGMP complex are 48 ± 12 %, 40 ± 12 %, and 12 ± 1 %**,** respectively (Fig. 5A; Table S1). Similarly, the three state-populations can be calculated for the 8-pCPT-cGMP and PET-cGMP-bound *Pf*D complexes based on the respective CHESPA data (Fig. 4E; Fig. S2; Table S1). Using these populations and assuming that the inactive and intermediate states are fully inhibitory, given the lid disengagement (14), while the active state is non-inhibitory, the relative kinase activity at ligand saturation induced by these cGMP-analogs was predicted. The predicted activation values correlate well with the experimental kinase activity values (Fig. 5B).

The ability of our three-state model to recapitulate the enzymatic data has three key implications. First, the measurements on the *Pf*D construct are relevant for the longer *Pf*PKG construct used in the kinase assays to probe the *Pf*PKG function. Second, the NMR chemical shift projection analysis and the resulting fractional shift values are suitable for predicting the populations of different functional states. Third, the mixed intermediate state, where only the lid region is disengaged, is inhibitory to an extent similar to the inactive state, further corroborating the pivotal role of the lid region in activation. Hence, we further probed the inhibitory mixed intermediate stabilized by the 8-NBD-cGMP analog.

5.4.5 8-NBD-cGMP binds to *Pf*D in a syn conformation and perturbs interactions critical for activation

As a first step towards investigating the mixed intermediate, we examined the base orientation of 8-NBD-cGMP as bound to *Pf*D. Typically, the base of cyclic nucleotides is oriented either in *syn vs. anti* relative to the ribose ring (34–38). To determine whether the guanine base of 8-NBD-cGMP is *syn* or *anti*, we could not rely on NOE based assessments, as this cGMP analogs lacks non-exchangeable protons in the base. Hence, we focused on the chemical shifts of the $C\gamma^2$ methyl of I465, which in the *Pf*D:cGMP complex is in direct contact with the guanine base, and of the $C\gamma$ methyl of T493, whose hydroxyl interacts with the amino group of cGMP (Fig. 1C). The chemical shifts of both I465 $C\gamma^2$ and T493 $C\gamma$ show only marginal changes when cGMP is replaced by 8-NBD-cGMP (Fig. 6A, B), suggesting that the 8-NBD-cGMP guanine base binds in a

syn conformation, similar to cGMP. This conclusion was confirmed also by the 3D map of 8-NBD-cGMP *vs.* cGMP NH CCS changes for residues in the β-barrel (Fig. 6C, red surface). Since residues in the β-barrel do not undergo significant structural changes upon cNMP binding, the perturbations sensed by the ΔCCS report mainly on direct binding contacts (33, 39–41). The ΔCCS map is fully consistent with 8-NBD-cGMP binding in *syn* rather than *anti* guanine orientation (Fig. 6C, residues within the red surface). Similarly, we confirmed through the β-barrel ΔCCS map that a *syn* orientation is preserved also for the guanine base of PET-cGMP (Fig. 6D, blue surface). For this analog, the substitution is at the 1 and 2 rather than the 8 position (Fig. 1I, K), causing the most significant CCS changes to cluster at the opposite side of the β-barrel for PET-cGMP compared to 8-NBD-cGMP, when both analogs maintain a *syn* guanine orientation (Fig. 6C,D; blue *vs.* red surfaces).

Although 8-NBD-cGMP preserves a *syn* guanine orientation when bound to *Pf*D, similar to cGMP, the introduction of the 8-NBD- moiety has a profound effect on the conformational ensemble accessed by *Pf*D, as shown by the NMR-based three-state model of Fig. 5A. Out of the three *Pf*D conformers in Fig. 5A, the mixed intermediate is the least characterized. Hence, we utilized MD simulation to further investigate this intermediate. For this purpose, we built an hybrid structure to resemble the intermediate state proposed based on the CHESPA data (Fig. 5A), relying on the cGMP-bound coordinates (PDB code: 4OGF) (14) for residues 401-532 and on the *apo* coordinates (PDB code: 5DYK) (24) for residues 534-542, which span the lid region. The hybrid model provided the initial coordinates for a 1 μs MD trajectory and Fig. 6E-F show representative structures selected based on the cluster analysis of such trajectory (Table S2).

In agreement with the data of Fig. 6A-C, Fig. 6E shows that the *Pf*D-bound 8-NBD-cGMP preserves a *syn* guanine orientation. Fig. 6F illustrates that the lid region of the intermediate state is disengaged, while the pre-lid is engaged. Fig. 6G shows that when the intermediate conformation is overlaid with the cGMP-bound structure (PDB code: 4OFG), the R528 side chain of 4OFG clashes with the NBD moiety of 8-NBD-cGMP (Fig. 6G; grey sticks). The steric clash explains why in the simulated intermediate structure, the R528 side chain moves away from the 8-NBD-cGMP and rotates outward, breaking the interaction with Y480 (Fig. 6G; red sticks). Considering that the Y480-R528 interaction is critical for activation (14, 21), the perturbation of R528 caused by 8-NBD is consistent with the lack of kinase activity observed upon replacement of cGMP with 8-NBD-cGMP.

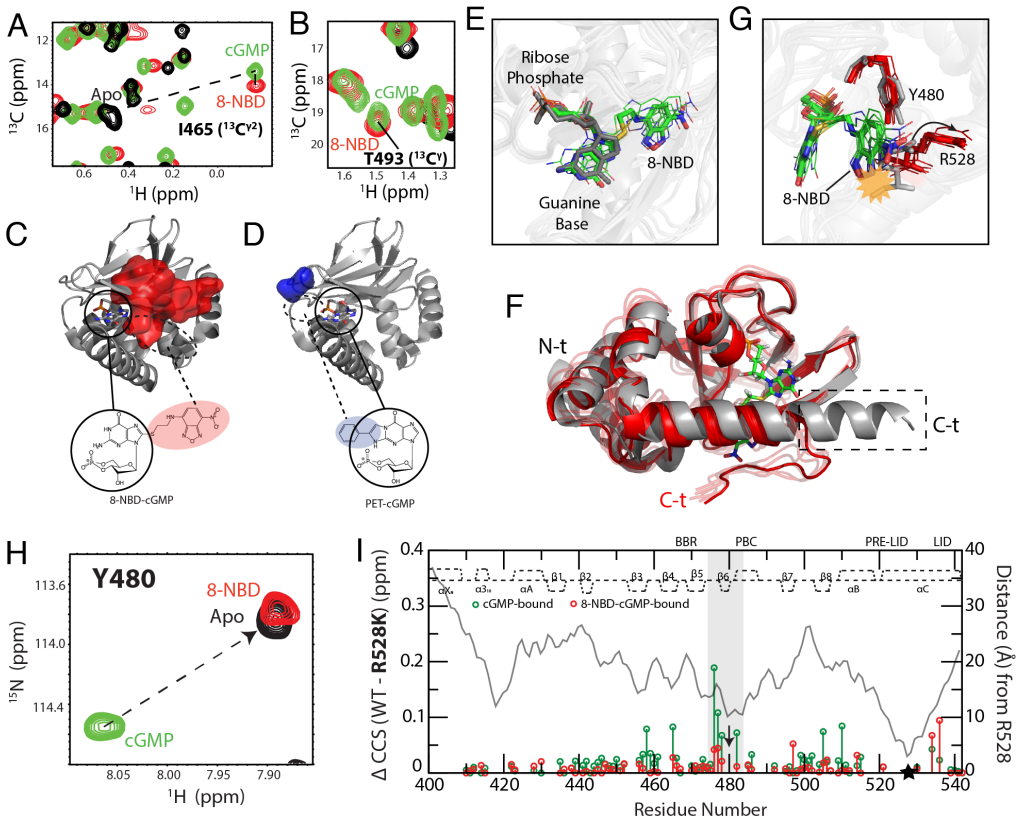

Figure 6. *Syn conformation of 8-NBD-cGMP bound to PfD and effect of 8-NBD on the Y480-R528 interaction.* **(A, B)** Overlaid ^{13}C-^{1}H HSQC spectral expansions of *apo* (black), cGMP bound (green) and 8-NBD-cGMP bound (red) *Pf*D, zoomed into (A) I465 ($^{13}C^{\gamma 2}$) and (B) T493 ($^{13}C^{\gamma}$), which interact with the guanine base of cGMP. The *apo* peak for T493 ($^{13}C^{\gamma}$) could not be assigned. **(C, D)** Map of residues in the β-barrel that exhibit ΔCCS relative to cGMP-bound *Pf*D greater than the average ΔCCS + 2 S.D. of the PET-cGMP *vs.* cGMP ΔCCS for the (C) 8-NBD-cGMP- and (D) PET-cGMP-bound *Pf*D. Circles indicate the cGMP portion of the analog in its *syn* orientation (PDB: 4OFG). The dashed circles represent the region where the base substituents (*i.e.* 8-NBD or PET) are expected to be located when the cGMP portion of the analogs is in the *syn* orientation. **(E)** Overlay of the structure of cGMP:*Pf*D (PDB code: 4OFG) and representative structures of 8-NBD-cGMP:*Pf*D generated from MD simulations (Table S2). The cGMP (dark grey) aligns with the cGMP portion of the 8-NBD-cGMP (green:C, white:H, blue:N, red:O, yellow:S, orange:P). **(F)** Aligned representative structures of 4OFG (grey) and 8-NBD-cGMP:*Pf*D (red) generated from MD simulations. The dashed box indicates the portion of the C-terminal αC helix that becomes disordered in the 8-NBD-cGMP:*Pf*D intermediate. **(G)** Similar to (F), but zoomed into the Y480-R528 region. The yellow starburst indicates the steric clash of 8-NBD moiety with the R528 side chain in the 4OFG structure. The arrow indicates the structural shift of the R528 side chain upon binding of 8-NBD-cGMP. **(H)** ^{1}H-^{15}N HSQC spectra of *apo* (black), cGMP-bound (green) and 8-NBD-cGMP-bound (red) samples overlaid and zoomed in on Y480. **(I)** WT *vs.* R528K CCS differences for cGMP- (green) and 8-NBD-cGMP- (red) bound samples. Residues assigned in both the cGMP-bound and the 8-NBD-cGMP bound samples are plotted. The distance (Å) measured from R528 using the cGMP-bound structure (PDB code: 4OFG) is shown in grey line. The secondary structure of cGMP-bound *Pf*D is depicted on the top of each plot. The highlighted region indicates residues near Y480, where the perturbation induced by the R528K mutation in the cGMP-bound complex is lost when cGMP is replaced by 8-NBD-cGMP. The black arrow indicates Y480, while the black star denotes R528.

This perturbation revealed by the MD simulations is consistent with the significant 8-NBD-cGMP *vs.* cGMP chemical shift changes occurring at or near Y480 (Fig. 3A). The Y480 NH HSQC cross-peak of the cGMP:*Pf*D complex moves completely towards the *apo* position when cGMP is replaced by 8-NBD-cGMP (Fig. 6H), confirming that the 8-NBD moiety perturbs the Y480-R528 interaction. To further corroborate this result, we generated the R528K mutant and compared the R528K *vs.* WT chemical shifts for both cGMP- and 8-NBD-cGMP-bound samples (Fig. 6I). For the cGMP:*Pf*D complex the largest R528K *vs.* WT ΔCCS values cluster primarily close to Y480 (Fig. 6I), as expected based on the R528-Y480 interaction observed in the cGMP:*Pf*D structure (14). However, when cGMP is replaced by 8-NBD-cGMP, the R528K *vs.* WT CCS changes in the vicinity of Y480 are markedly suppressed (Fig. 6I), confirming that in the 8-NBD-cGMP:*Pf*D complex the R528-Y480 interaction is significantly weakened compared to the cGMP:*Pf*D structure.

Similar analyses were carried out to probe the effect of 8-NBD-cGMP on the capping triad interactions between R484, Q532, and D533, which are also critical for activation (14). We found that the R484-D533 interaction is perturbed in the simulated intermediate structure of the 8-NBD-cGMP:*Pf*D complex (Fig. S3A). To confirm such perturbation, we measured the CCS changes between WT and the R484A mutant for both the cGMP- and 8-NBD-cGMP-bound samples (Fig. S3B). Fig. S3B reveals that the R484A *vs.* WT CCS changes in the C-terminal helices, especially in the vicinity of Q532-D533, are suppressed when cGMP is replaced with 8-NBD-cGMP, confirming that 8-NBD-cGMP perturbs the capping interaction between R484 and the C-terminal helices. These results are in full agreement with the MD simulations, suggesting that the 8-NBD substituent destabilizes also the capping triad.

Hence, we conclude that upon introduction of the NBD group at the 8-guanine position, the *syn* base orientation is preserved but the Y480-R528 contact and the capping triad interactions are significantly perturbed, thus compromising the full engagement of the C-helix and explaining why 8-NBD-cGMP functions as an effective allosteric antagonist of the *Pf*PKG kinase.

5.4.6 Sampling a mixed intermediate state is beneficial for maximizing kinase inhibition while minimizing affinity losses

The three-state model with the mixed intermediate state featuring an engaged pre-lid and a disengaged lid (Fig. 5A) provides an excellent strategy for *Pf*PKG kinase inhibition without significantly compromising affinity. Reconciling high inhibitory efficacy and potency would be more challenging for a simple two-state model. In this case, the disengagement of the lid necessary for inhibition also implies the concurrent disengagement of other *Pf*D elements necessary for high-affinity binding, such as the PBC in its entirety. On the contrary, in the mixed intermediate state (Fig. 5A), which exhibits a similar inhibitory effect as the inactive state, maintains the pre-lid and the adjacent PBC engaged. For example, while the capping carboxylate of D533 is displaced away from R484 in the PBC, the side chain of this arginine in the mixed intermediate remains in an orientation similar to the active conformation (Fig. S3A), thus minimizing perturbations of the interactions with the cyclic nucleotide. Hence, based on the three-state model of Fig. 5A, we hypothesize that the 8-NBD-cGMP preserves an affinity comparable to the endogenous allosteric effector, cGMP.

Our hypothesis is confirmed through surface-plasmon resonance (SPR) measurements (Fig. 7) showing that the affinities of 8-NBD-cGMP and cGMP are comparable (*i.e.* $K_d = 59 \pm 4$ *vs.* 51 ± 7 nM; Table S3), despite their markedly different efficacies in terms of kinase activation (Fig. 1L; Fig. S1A). This conservation of affinity is especially important, since 8-NBD-cGMP acts as a competitive antagonist (Fig. S1B). Hence, 8-NBD-cGMP serves as an excellent example for how sampling a mixed intermediate state enables significant inhibition without major affinity losses by selectively disengaging only structural units strictly necessary for kinase activation. Similar inhibition strategies are anticipated to inform the design of future *Pf*PKG allosteric inhibitors, which may serve as anti-malaria drug leads.

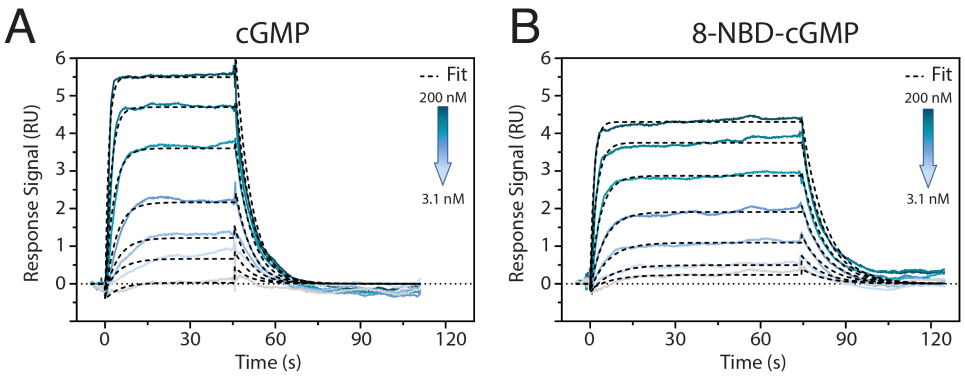

Figure 7. *Surface plasmon resonance binding studies of cGMP and 8-NBD-cGMP to PfPKG 401-853 (PfD – catalytic domain) demonstrate similar binding kinetics*. Direct binding assays were performed by capturing poly-histidine tagged *Pf*PKG 401-853 on a Ni-NTA sensor chip and injecting a dilution series of **(A)** cGMP for 45 s and **(B)** 8-NBD-cGMP for 70 s, respectively. Rate and equilibrium binding constants are reported in Table S3. A Langmuir 1:1 model was applied for fitting.

5.5. Experimental Procedures

Expression and Purification

The *Pf*PKG CBD-D construct (401-542) (*i.e. Pf*D) within a His-tagged expression vector pQTEV (14) was expressed in the *E. coli* strain BL21 (DE3). The transformed *E. coli* was grown in a minimal media enriched with $^{15}NH_4Cl$ and ^{13}C-glucose and supplemented with D-biotin, thiamine HCl, $MgSO_4$, and $CaCl_2$. The cells were grown at 37 °C to an optical density of 0.7 (at λ = 600nm), induced with 0.5 mM IPTG and then incubated for an additional 18 h at 18 °C. Cells were harvested, resuspended in the lysis buffer (50mM Tris, pH 7.4, 500mM NaCl, 1mM BME) and lysed using a cell disruptor. The cell debris was removed through centrifugation and then the supernatant was loaded onto a Ni^{2+} Sepharose resin. The cell lysate was allowed to flow through and the column was rinsed with 50 mM Tris, pH 7.4, 500 mM NaCl, 1 mM BME, and 20 mM imidazole. After thorough rinsing, the protein was eluted with 50 mM Tris, pH 7.4, 500 mM NaCl, 1 mM BME, and 300 mM imidazole. The eluted protein was then dialyzed in 50 mM Tris, pH 7.4, 100 mM NaCl, 1mM BME with TEV protease for 24 h at 4 °C. The cleaved products were loaded on the Ni^{2+} Sepharose resin. The protein without the His-tag was obtained through collecting the flow-through and was further purified with a HiLoad 16/60 Superdex 75 gel filtration column (GE healthcare) equilibrated with NMR buffer (50 mM Tris, pH 7, 100 mM NaCl, 10 mM MgCl2,

1mM DTT). The His-tagged *Pf*PKG 401-853 construct including the catalytic domain was expressed in *E. coli* TP2000 and purified using Ni-NTA and size exclusion chromatography, as previously described (21).

NMR Spectroscopy

NMR experiments were performed on a Bruker Avance 700 MHz spectrometer equipped with a 5-mm TCI cryoprobe or a Bruker Avance 850 MHz spectrometer equipped with a triple resonance TXI probe. All experiments were acquired at 306 K in NMR buffer (50 mM Tris, pH 7, 100 mM NaCl, 10 mM MgCl2, 1 mM DTT) with 5% D_2O. All NMR spectra were processed with NMRPipe (42) and analyzed using Sparky (43). Three-dimensional triple-resonance NMR experiments (*i.e.* HNCACB, CBCA(CO)NH, HNCA, HN(CO)CA, HNCO, HCCH-TOCSY, and (H)CC(CO)NH) were acquired and used to assign the two-dimensional ^{1}H-^{15}N HSQC and ^{1}H-^{13}C HSQC NMR spectra of cGMP-bound *Pf*D. Since the *apo* sample was prone to precipitation, 2D-N_z-exchange, 2D-Difference N_z-exchange, and 2D-C_z-exchange experiments with mixing time of 250 ms were used to transfer the chemical shift assignments from the cGMP-bound *Pf*D to the *apo Pf*D spectra. The cGMP-analog bound spectra were assigned through spectral comparison with cGMP-bound spectra, if no ambiguities were present, and through 2D-N_z-exchange and 2D-Difference N_z-exchange with the *apo* state. Chemical shift assignments of R528K:cGMP and R528K:8-NBD-cGMP were obtained through spectral comparison with WT spectra, if no ambiguities were present.

Chemical Shift Analyses

All spectra utilized for chemical shift analyses were acquired with 100 µM *Pf*D and saturating amounts of cGMP or cGMP-analogs (2 mM) or without any cNMP addition for *apo* spectra. For accurate chemical shift comparisons, an internal reference (*i.e.* ^{15}N-labeled N-acetylglycine) was used to align the spectra in Sparky and the resulting chemical shift values were used to compute the compounded chemical shift differences and perform the Chemical Shift Projection Analysis (CHESPA) following previously described protocols (29, 30, 34, 44, 45). The fractional shift (*X*) values and $cos(\Theta)$ values were computed for residues with cGMP-analog bound *vs.* cGMP-bound CCS difference > 0.05 ppm. The average $\langle X \rangle$ values for the pre-lid and the lid were calculated using residues that were assigned in all five samples (*i.e. apo,* cGMP-

bound, 8-NBD-cGMP-bound, 8-pCPT-cGMP-bound, and PET-cGMP-bound *Pf*D), had *X* values between 0 and -1 and ΔCCS (cGMP-analog bound *vs.* cGMP-bound) values greater than 0.05 ppm, ensuring reliable *X* and $cos(\theta)$ values. The distribution of *X* values for cGMP-analogs were computed using the residues that exhibited $|cos(\theta)| > 0.75$ to minimize biases from nearest-neighbour effects.

Site-Directed Mutagenesis

The R528K mutation was created through site-directed mutagenesis using a KOD Hot Start Master mix (Novagen) and primer pairs (synthesized by IDT), forward – CTGGCCCACTTGGAAGAGAAGATTAAGATGCAGGATAC and reverse – GTATCCTGCATCTTAATCTTCTCTTCCAAGTGGGCCAG. The reaction protocol provided by the KOD Hot Start kit was followed. Template DNA was degraded with DpnI for 2 h at 37 °C and the reaction product was used for transformation of *E. coli* top10 cells. The transformed colony was grown in LB media for 18 h at 37 °C. Plasmids were isolated from the *E. coli* using the GeneJET Plasmid Miniprep Kit (Thermo Fisher Scientific). The purified plasmids were sequenced to verify the mutation. The expression and purification of *Pf*D R528K were carried out using the same protocol as for the WT *Pf*D.

Kinase Assays

Specific kinase activities were determined using an enzyme coupled spectrophotometric assay (46). In a quartz cuvette, purified *Pf*PKG 401-853 was mixed with the reaction buffer (100 mM MOPS pH 7.0, 10 mM $MgCl_2$, 5 mM β-mercaptoethanol 1 mM ATP, 1 mM phosphoenolpyruvate, 230 µM NADH, 15 U/ml lactate dehydrogenase, 8.4 U/ml pyruvate kinase). The reactions were started by adding 1 mM PKStide (GRTGRRNSI; GeneCust, Luxembourg) and monitored in the absence and presence of 100 µM of each cyclic nucleotide (cGMP, 8-*p*CPT- and PET-cGMP) for at least 1 minute. Specific kinase activity was calculated according to the Lambert Beer law.

Kinase activity induced by 8-NBD-cGMP was measured by microfluidic mobility shift assay using a Caliper DeskTop Profiler (PerkinElmer, Waltham, MA, USA). Here, 100 µM of cGMP or 8-NBD-cGMP were mixed with assay buffer (20 mM MOPS (pH 7), 300 mM NaCl, 10 mM $MgCl_2$, 1 mM ATP, 1 mM DTT, 990 µM PKStide, 10 µM FITC-PKStide (FITC-GRTGRRNSI; GeneCust,

Luxembourg, 0.05% L-31) and a fixed protein concentration and continued as previously described (21). The assay was also conducted with multiple concentrations of 8-NBD-cGMP or cGMP, ranging from 0.1 nM to 300 µM. For the competition assay, the protein was pre-incubated with 350 nM cGMP and varying concentration of 8-NBD-cGMP was added to the reaction and substrate conversion was monitored over 2 hr.

The combined kinase inhibition data were further analysed and normalized using GraphPad Prism 8.3.0 (GraphPad Software).

Surface Plasmon Resonance (SPR)

Direct binding data was obtained via SPR using a Biacore T200 (GE Healthcare Life Sciences). Briefly, 200-300 RU of Ni^{2+} (5 mM $NiCl_2$ in running buffer) were immobilized on a poly NTA derivatized sensor chip (NIHC 1000M; XanTec bioanalytics GmbH). Subsequently, His-tagged *Pf*PKG 401-853 in running buffer (20 mM HEPES, 150 mM NaCl, 50 µM EDTA, 0.01% P20, pH 7.3) was captured at a flow rate of 10 µL/min to an immobilization level of 500-2500 RU. Next, association was measured by injection of a dilution series of the respective cyclic nucleotide for 45-75 s. Then running buffer was injected for 60-180 s to initiate dissociation. Regeneration of the sensor chip surface was achieved by consecutively injecting 0.5 M EDTA (pH 8) for 600 s, followed by injections of 3 M guanidinium HCl, 0.5 % SDS and 3 M guanidinium HCl for 240 s each. Unless stated otherwise, all kinetic measurements were performed at 25 °C in running buffer and a flow rate of 50 µL/min. Data was evaluated with the Biacore T200 Evaluation Software 3.0 using a global fit and assuming a 1:1 Langmuir binding model. Further data processing was performed using GraphPad Prism 8.3.0 (GraphPad Software).

Molecular Dynamic Simulations

Initial Model Preparation. The structure of 8-NBD-cGMP in a *syn* conformation was generated using RDKit (47). A model of the mixed intermediate state sampled by the *Pf*D:8-NBD-cGMP complex was then built using residues 401-533 from the active *Pf*D:cGMP crystal structure (PDB code: 4OFG) (14), and lid region residues 534-542 from the inactive *apo Pf*D crystal structure (PDB code: 5DYK) (24). The 8-NBD-cGMP ligand was docked into the resulting mixed structure of *Pf*D using AutoDock4 with default parameters generated by AutoDockTools (48). Residues 463-494, where the PBC and BBR regions are located, were assigned as the binding

pocket for AutoDock. The structure in which the ribose-phosphate and guanine moieties of the docked ligand were best aligned with the position of cGMP in the cGMP-bound active structure (PDB code: 4OFG) (14) was selected as initial coordinates for MD simulations.

Molecular Dynamic Simulation Protocol. All simulations were performed using the AMBER 16 software PMEMD.CUDA (49) on the Shared Hierarchical Academic Research Computing Network (SHARCNET). The Amber ff99SBnmr force field was employed for the protein, while RESP charge and the general Amber force field were applied to generate the parameters for 8-NBD-cGMP using the Gaussian09 program (50) and the antechamber module implemented in AMBER 16, as previously described (51). The TIP3P water model was applied in the form of a rectangular MD solvent box surrounding the *Pf*D:8-NBD-cGMP structure, with a minimum distance of 12 Å between the *Pf*D:8-NBD-cGMP structure and the box edge. To mimic the experimental conditions, the charged residues and N-/C-termini were set to the protonation states expected at pH 7, following a protocol similar to that implemented in (52), and Na+ and Cl- ions were added to mimic a 100 mM salt concentration.

The simulations started with an energy minimization performed with harmonic restraints on the protein backbone (with a force constant of 5 kcal/mol-Å^2). The system was then gradually heated from 0 K to 100 K at constant volume and then heated from 100 K to 306 K in the NPT ensemble, and all the heating process employed harmonic restraints on protein backbone (with a force constant of 3 kcal/mol-Å^2) for a total of 1 ns followed by an equilibration period of 1.2 ns with main chain atoms restrained with a force constant of 1 kcal/mol-Å^2. Then a 1 μs production MD trajectory was generated in the NPT ensemble at 306 K and 1 atm with weak-coupling algorithm, saving structures every 10 ps for subsequent analysis. A cluster analysis for 20000 frames recorded from the MD trajectory (*i.e.* the structures recorded at 50 ps intervals) was performed, with β-core alignment, using the CPPTRAJ protocol (53).

Data availability

The NMR chemical shift assignment for cGMP-bound *Pf*D has been deposited in Biological Magnetic Resonance Data Bank (BMRB) with the code 50203. All remaining data are contained within the article.

5.6 Acknowledgements

We thank Dr. B. VanSchouwen, Dr. S. Boulton, H. Shao, R. Ahmed, N. Jafari and Dr. S.S. Taylor for helpful discussions. Furthermore, we thank A. Morell and K. Zupfer for help with protein purification and kinase activity assays.

5.7 References

1. WHO (2019) *World Malaria Report 2019*
2. Cowman, A. F., Healer, J., Marapana, D., and Marsh, K. (2016) Malaria: Biology and Disease. *Cell*. **167**, 610–624
3. Doerig, C., Billker, O., Pratt, D., and Endicott, J. (2005) Protein kinases as targets for antimalarial intervention: Kinomics, structure-based design, transmission-blockade, and targeting host cell enzymes. *Biochim. Biophys. Acta - Proteins Proteomics*. **1754**, 132–150
4. Brochet, M., and Billker, O. (2016) Calcium signalling in malaria parasites. *Mol. Microbiol.* **100**, 397–408
5. Hopp, C. S., Bowyer, P. W., and Baker, D. A. (2012) The role of cGMP signalling in regulating life cycle progression of Plasmodium. *Microbes Infect.* **14**, 831–837
6. Taylor, H. M., McRobert, L., Grainger, M., Sicard, A., Dluzewski, A. R., Hopp, C. S., Holder, A. A., and Baker, D. A. (2010) The Malaria Parasite Cyclic GMP-Dependent Protein Kinase Plays a Central Role in Blood-Stage Schizogony. *Eukaryot. Cell*. **9**, 37–45
7. Moon, R. W., Taylor, C. J., Bex, C., Schepers, R., Goulding, D., Janse, C. J., Waters, A. P., Baker, D. A., and Billker, O. (2009) A Cyclic GMP Signalling Module That Regulates Gliding Motility in a Malaria Parasite. *PLoS Pathog.* **5**, e1000599
8. McRobert, L., Taylor, C. J., Deng, W., Fivelman, Q. L., Cummings, R. M., Polley, S. D., Billker, O., and Baker, D. A. (2008) Gametogenesis in Malaria Parasites Is Mediated by the cGMP-Dependent Protein Kinase. *PLoS Biol.* **6**, e139
9. Govindasamy, K., Jebiwott, S., Jaijyan, D. K., Davidow, A., Ojo, K. K., Van Voorhis, W. C., Brochet, M., Billker, O., and Bhanot, P. (2016) Invasion of hepatocytes by Plasmodium sporozoites requires cGMP-dependent protein kinase and calcium dependent protein kinase 4. *Mol. Microbiol.* **102**, 349–363
10. Miller, L. H., Ackerman, H. C., Su, X., and Wellems, T. E. (2013) Malaria biology and disease pathogenesis: insights for new treatments. *Nat. Med.* **19**, 156–167
11. Fairhurst, R. M. (2015) Understanding artemisinin-resistant malaria. *Curr. Opin. Infect. Dis.* **28**, 417–425
12. Alam, M. M., Solyakov, L., Bottrill, A. R., Flueck, C., Siddiqui, F. A., Singh, S., Mistry, S., Viskaduraki, M., Lee, K., Hopp, C. S., Chitnis, C. E., Doerig, C., Moon, R. W., Green, J. L., Holder, A. A., Baker, D. A., and Tobin, A. B. (2015) Phosphoproteomics reveals malaria parasite Protein Kinase G as a signalling hub regulating egress and invasion. *Nat. Commun.* **6**, 7285
13. Diaz, C. A., Allocco, J., Powles, M. A., Yeung, L., Donald, R. G. K., Anderson, J. W., and Liberator, P. A. (2006) Characterization of Plasmodium falciparum cGMP-dependent protein kinase (PfPKG): Antiparasitic activity of a PKG inhibitor. *Mol. Biochem. Parasitol.* **146**, 78–88
14. Kim, J. J., Flueck, C., Franz, E., Sanabria-Figueroa, E., Thompson, E., Lorenz, R., Bertinetti, D., Baker, D. A., Herberg, F. W., and Kim, C. (2015) Crystal Structures of the Carboxyl cGMP Binding Domain of the Plasmodium falciparum cGMP-dependent Protein Kinase Reveal a Novel Capping Triad Crucial for Merozoite Egress. *PLOS Pathog.* **11**, e1004639
15. Collins, C. R., Hackett, F., Strath, M., Penzo, M., Withers-Martinez, C., Baker, D. A., and Blackman, M. J. (2013) Malaria Parasite cGMP-dependent Protein Kinase Regulates Blood Stage Merozoite Secretory Organelle Discharge and Egress. *PLoS Pathog.* **9**,

e1003344
16. Cohen, P. (2002) Protein kinases — the major drug targets of the twenty-first century? *Nat. Rev. Drug Discov.* **1**, 309–315
17. Baker, D. A., and Deng, W. (2005) Cyclic GMP-dependent protein kinases in protozoa. *Front. Biosci.* **10**, 1229
18. Kim, J. J., Lorenz, R., Arold, S. T., Reger, A. S., Sankaran, B., Casteel, D. E., Herberg, F. W., and Kim, C. (2016) Crystal Structure of PKG I:cGMP Complex Reveals a cGMP-Mediated Dimeric Interface that Facilitates cGMP-Induced Activation. *Structure*. **24**, 710–720
19. Moon, T. M., Sheehe, J. L., Nukareddy, P., Nausch, L. W., Wohlfahrt, J., Matthews, D. E., Blumenthal, D. K., and Dostmann, W. R. (2018) An N-terminally truncated form of cyclic GMP–dependent protein kinase Iα (PKG Iα) is monomeric and autoinhibited and provides a model for activation. *J. Biol. Chem.* **293**, 7916–7929
20. Deng, W., Parbhu-Patel, A., Meyer, D. J., and Baker, D. A. (2003) The role of two novel regulatory sites in the activation of the cGMP-dependent protein kinase from Plasmodium falciparum. *Biochem. J.* **374**, 559–565
21. Franz, E., Knape, M. J., and Herberg, F. W. (2018) cGMP Binding Domain D Mediates a Unique Activation Mechanism in Plasmodium falciparum PKG. *ACS Infect. Dis.* **4**, 415–423
22. Berman, H. M., Ten Eyck, L. F., Goodsell, D. S., Haste, N. M., Kornev, A., and Taylor, S. S. (2005) The cAMP binding domain: An ancient signaling module. *Proc. Natl. Acad. Sci.* **102**, 45–50
23. Huang, G. Y., Kim, J. J., Reger, A. S., Lorenz, R., Moon, E. W., Zhao, C., Casteel, D. E., Bertinetti, D., Vanschouwen, B., Selvaratnam, R., Pflugrath, J. W., Sankaran, B., Melacini, G., Herberg, F. W., and Kim, C. (2014) Structural basis for cyclic-nucleotide selectivity and cGMP-selective activation of PKG i. *Structure*. **22**, 116–124
24. El Bakkouri, M., Kouidmi, I., Wernimont, A. K., Amani, M., Hutchinson, A., Loppnau, P., Kim, J. J., Flueck, C., Walker, J. R., Seitova, A., Senisterra, G., Kakihara, Y., Kim, C., Blackman, M. J., Calmettes, C., Baker, D. A., and Hui, R. (2019) Structures of the cGMP-dependent protein kinase in malaria parasites reveal a unique structural relay mechanism for activation. *Proc. Natl. Acad. Sci.* **116**, 14164–14173
25. Monod, J., Wyman, J., and Changeux, J.-P. (1965) On the nature of allosteric transitions: A plausible model. *J. Mol. Biol.* **12**, 88–118
26. Akimoto, M., Moleschi, K., Boulton, S., VanSchouwen, B., Selvaratnam, R., Taylor, S. S., and Melacini, G. (2014) Allosteric linkers in cAMP signalling. *Biochem. Soc. Trans.* **42**, 139–144
27. Akimoto, M., Selvaratnam, R., McNicholl, E. T., Verma, G., Taylor, S. S., and Melacini, G. (2013) Signaling through dynamic linkers as revealed by PKA. *Proc. Natl. Acad. Sci. U. S. A.* **110**, 14231–6
28. VanSchouwen, B., Selvaratnam, R., Giri, R., Lorenz, R., Herberg, F. W., Kim, C., and Melacini, G. (2015) Mechanism of cAMP Partial Agonism in Protein Kinase G (PKG). *J. Biol. Chem.* 10.1074/jbc.M115.685305
29. Selvaratnam, R., VanSchouwen, B., Fogolari, F., Mazhab-Jafari, M. T., Das, R., and Melacini, G. (2012) The projection analysis of NMR chemical shifts reveals extended EPAC autoinhibition determinants. *Biophys. J.* **102**, 630–9
30. Selvaratnam, R., Chowdhury, S., VanSchouwen, B., and Melacini, G. (2011) Mapping allostery through the covariance analysis of NMR chemical shifts. *Proc. Natl. Acad. Sci. U.*

S. A. **108**, 6133–8
31. Akimoto, M., McNicholl, E. T., Ramkissoon, A., Moleschi, K., Taylor, S. S., and Melacini, G. (2015) Mapping the Free Energy Landscape of PKA Inhibition and Activation: A Double-Conformational Selection Model for the Tandem cAMP-Binding Domains of PKA RIα. *PLoS Biol.* **13**, e1002305
32. Boulton, S., Akimoto, M., Akbarizadeh, S., and Melacini, G. (2017) Free energy landscape remodeling of the cardiac pacemaker channel explains the molecular basis of familial sinus bradycardia. *J. Biol. Chem.* **292**, 6414–6428
33. Boulton, S., Selvaratnam, R., Blondeau, J.-P., Lezoualc'h, F., and Melacini, G. (2018) Mechanism of Selective Enzyme Inhibition through Uncompetitive Regulation of an Allosteric Agonist. *J. Am. Chem. Soc.* **140**, 9624–9637
34. Das, R., Chowdhury, S., Mazhab-Jafari, M. T., SilDas, S., Selvaratnam, R., and Melacini, G. (2009) Dynamically Driven Ligand Selectivity in Cyclic Nucleotide Binding Domains. *J. Biol. Chem.* **284**, 23682–23696
35. Rehmann, H., Arias-Palomo, E., Hadders, M. A., Schwede, F., Llorca, O., and Bos, J. L. (2008) Structure of Epac2 in complex with a cyclic AMP analogue and RAP1B. *Nature*. **455**, 124–127
36. Zagotta, W. N., Olivier, N. B., Black, K. D., Young, E. C., Olson, R., and Gouaux, E. (2003) Structural basis for modulation and agonist specificity of HCN pacemaker channels. *Nature*. **425**, 200–205
37. Su, Y., Dostmann, W. R., Herberg, F. W., Durick, K., Xuong, N. H., Ten Eyck, L., Taylor, S. S., and Varughese, K. I. (1995) Regulatory subunit of protein kinase A: structure of deletion mutant with cAMP binding domains. *Science*. **269**, 807–13
38. Clayton, G. M., Silverman, W. R., Heginbotham, L., and Morais-Cabral, J. H. (2004) Structural Basis of Ligand Activation in a Cyclic Nucleotide Regulated Potassium Channel. *Cell*. **119**, 615–627
39. Dolgova, N. V., Yu, C., Cvitkovic, J. P., Hodak, M., Nienaber, K. H., Summers, K. L., Cotelesage, J. J. H., Bernholc, J., Kaminski, G. A., Pickering, I. J., George, G. N., and Dmitriev, O. Y. (2017) Binding of Copper and Cisplatin to Atox1 Is Mediated by Glutathione through the Formation of Metal–Sulfur Clusters. *Biochemistry*. **56**, 3129–3141
40. McNicholl, E. T., Das, R., SilDas, S., Taylor, S. S., and Melacini, G. (2010) Communication between Tandem cAMP Binding Domains in the Regulatory Subunit of Protein Kinase A-Iα as Revealed by Domain-silencing Mutations. *J. Biol. Chem.* **285**, 15523–15537
41. Fayos, R., Melacini, G., Newlon, M. G., Burns, L., Scott, J. D., and Jennings, P. A. (2003) Induction of Flexibility through Protein-Protein Interactions. *J. Biol. Chem.* **278**, 18581–18587
42. Delaglio, F., Grzesiek, S., Vuister, G., Zhu, G., Pfeifer, J., and Bax, A. (1995) NMRPipe: A multidimensional spectral processing system based on UNIX pipes. *J. Biomol. NMR* **6**, 277-293
43. Goddard, T. D., and Kneller, D. G. (2006) *SPARKY, NMR Assignment and Integration Software,* Version 3. University of California at San Francisco
44. Boulton, S., Akimoto, M., Selvaratnam, R., Bashiri, A., and Melacini, G. (2015) A Tool Set to Map Allosteric Networks through the NMR Chemical Shift Covariance Analysis. *Sci. Rep.* **4**, 7306
45. Selvaratnam, R., Mazhab-Jafari, M. T., Das, R., and Melacini, G. (2012) The auto-inhibitory

role of the EPAC hinge helix as mapped by NMR. *PLoS One*. **7**, e48707
46. Cook, P. F., Neville, M. E., Vrana, K. E., Hartl, F. T., and Roskoski, R. (1982) Adenosine cyclic 3',5'-monophosphate dependent protein kinase: kinetic mechanism for the bovine skeletal muscle catalytic subunit. *Biochemistry*. **21**, 5794–5799
47. Riniker, S., and Landrum, G. A. (2015) Better Informed Distance Geometry: Using What We Know To Improve Conformation Generation. *J. Chem. Inf. Model.* **55**, 2562–2574
48. Morris, G. M., Huey, R., Lindstrom, W., Sanner, M. F., Belew, R. K., Goodsell, D. S., and Olson, A. J. (2009) AutoDock4 and AutoDockTools4: Automated docking with selective receptor flexibility. *J. Comput. Chem.* **30**, 2785–2791
49. Case, D. A., Betz, R. M., Cerutti, D. S., Cheatham, T. E., Darden, T., and Duke, R. E. (2016) AMBER16, University of California at San Francisco
50. Frisch, M. J., Trucks, G. W., Schlegel, H. B., Scuseria, G. E., Robb, M. A., Cheeseman, J. R., Scalmani, G., Barone, V., Mennucci, B., Petersson, G. A., Nakatsuji, H., Caricato, M., Li, X., Hratchian, H. P., Izmaylov, A. F., Bloino, J., Zheng, G., Sonnenberg, J. L., Hada, M., Ehara, M., Toyota, K., Fukuda, R., Hasegawa, J., Ishida, M., Nakajima, T., Honda, Y., Kitao, O., Nakai, H., Vreven, T., Montgomery, J. A., Peralta, J. E., Ogliaro, F., Bearpark, M., Heyd, J. J., Brothers, E., Kudin, K. N., Staroverov, V. N., Kobayashi, R., Normand, J., Raghavachari, K., Rendell, A., Burant, J. C., Iyengar, S. S., Tomasi, J., Cossi, M., Rega, N., Millam, N. J., Klene, M., Knox, J. E., Cross, J. B., Bakken, V., Adamo, C., Jaramillo, J., Gomperts, R., Stratmann, R. E., Yazyev, O., Austin, A. J., Cammi, R., Pomelli, C., Ochterski, J. W., Martin, R. L., Morokuma, K., Zakrzewski, V. G., Voth, G. A., Salvador, P., Dannenberg, J. J., Dapprich, S., Daniels, A. D., Farkas, Ö., Foresman, J. B., Ortiz, J. V., Cioslowski, J., and Fox, D. J. (2016) Gaussian 09, Revision E01, Wallingford CT
51. Huang, J., Sun, B., Yao, Y., and Liu, J. (2017) Fast and Reliable Thermodynamic Approach for Determining the Protonation State of the Asp Dyad. *J. Chem. Inf. Model.* **57**, 2273–2280
52. VanSchouwen, B., Selvaratnam, R., Fogolari, F., and Melacini, G. (2011) Role of Dynamics in the Autoinhibition and Activation of the Exchange Protein Directly Activated by Cyclic AMP (EPAC). *J. Biol. Chem.* **286**, 42655–42669
53. Roe, D. R., and Cheatham, T. E. (2013) PTRAJ and CPPTRAJ: Software for Processing and Analysis of Molecular Dynamics Trajectory Data. *J. Chem. Theory Comput.* **9**, 3084–3095
54. Han, B., Liu, Y., Ginzinger, S. W., and Wishart, D. S. (2011) SHIFTX2: significantly improved protein chemical shift prediction. *J. Biomol. NMR*. **50**, 43–57

5.8 Supplementary Information

Table S1. *Population of inactive, intermediate and active states sampled by the complexes of PfD and 8-NBD-cGMP, 8-pCPT-cGMP, or PET-cGMP**

	8-NBD-cGMP	8-pCPT-cGMP	PET-cGMP
Inactive	48 ± 12%	30 ± 9%	0 ± 1%
Intermediate	40 ± 12%	34 ± 16%	0 ± 11%
Active	12 ± 1%	36 ± 13%	103 ± 11%

*The populations were estimated from the average fractional shift (*X*) values of the pre-lid and the lid region obtained from the CHESPA analysis (Fig. 4 and S2).

Table S2. *Cluster distribution from a 1 μs MD trajectory of PfD:8-NBD-cGMP**

Cluster	Frames	Fraction
1	19086	0.954
2	610	0.03
3	81	0.004
4	70	0.004
5	36	0.002
6	34	0.002
7	33	0.002
8	27	0.001
9	19	0.001
10	4	0

* Representative structures from the most populated cluster (*i.e.* cluster 1) were used in Fig. 6.

Table S3. *Direct binding measurements of cGMP and cGMP-analogs to PfPKG 401-853 (CBD-D – Catalytic domain)**

	cGMP	8-NBD-cGMP	8-pCPT-cGMP	PET-cGMP
k_{ass} [10^6 $M^{-1}s^{-1}$]	2.76 ± 0.53	1.94 ± 0.20	42.0 ± 32.7	6.52 ± 1.29
k_{diss} [s^{-1}]	0.14 ± 0.03	0.11 ± 0.01	0.06 ± 0.03	0.02 ± 0.01
K_d [nM]	51 ± 7	59 ± 4	1.7 ± 0.7	2.6 ± 0.3

* Association and dissociation rate constants were obtained employing SPR (Fig. 7). SD was determined using at least triplicates.

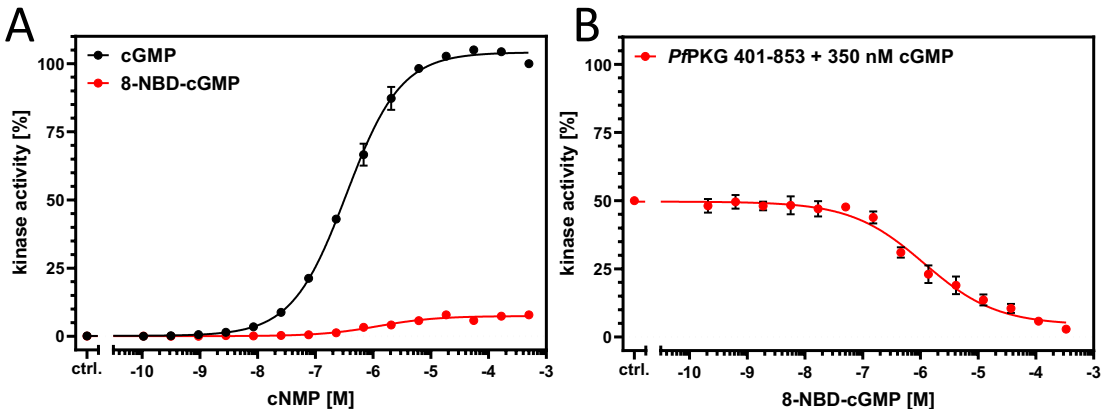

Figure S1. *Partial agonistic and antagonistic properties of 8-NBD-cGMP on PfPKG activation.* (A) Kinase activation with cGMP (black) and 8-NBD-cGMP (red). *Pf*PKG (401-853) was incubated with different concentrations of cGMP and 8-NBD-cGMP, respectively, and the kinase activity was measured using microfluidic mobility shift assays. Activity refers to conversion of the substrate peptide PKStide. (B) *Pf*PKG (401-853) was pre-activated to about 50% of the maximum kinase activity with 350 nM cGMP. The influence of 8-NBD-cGMP on kinase activity was tested by adding a dilution series of 8-NBD-cGMP to the reaction. Subsequently, substrate conversion was monitored over 2 h.

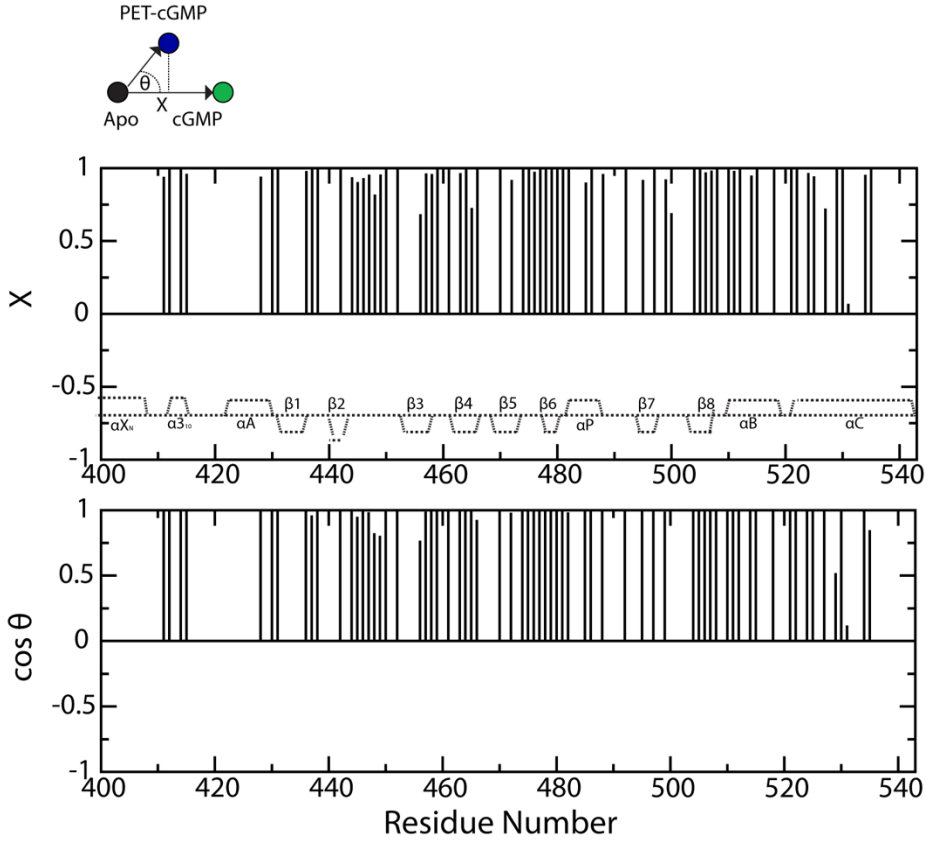

Figure S2. *CHemical Shift Projection Analysis (CHESPA) of PfD:PET-cGMP*. **(A)** CHESPA vector scheme, fractional shift (*X*) and **(B)** *cos(Θ)* values plotted against residue. The secondary structure of cGMP-bound *Pf*D is depicted on the bottom of the *X* plot.

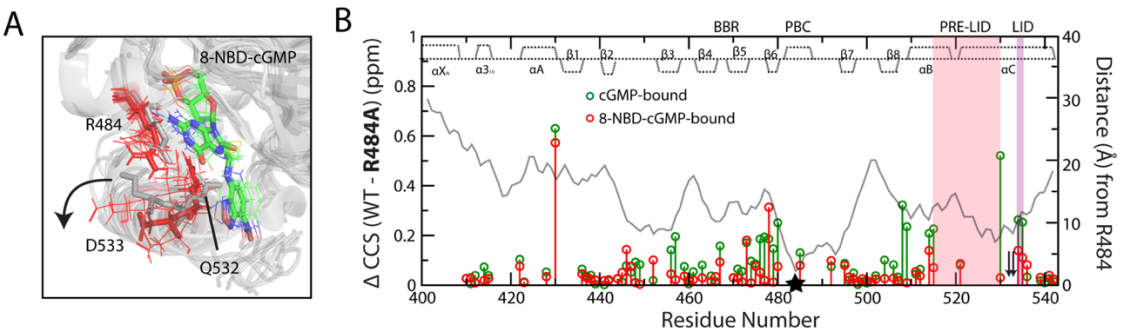

Figure S3. *Effect of the 8-NBD Substituent on the Capping Triad Interactions.* 8-NBD-cGMP binding to *Pf*D perturbs the interaction of R484 with the C-terminal helices and the capping triad. **(A)** Aligned representative structures of cGMP:*Pf*D (grey; PDB code: 4OFG) and 8-NBD-cGMP:*Pf*D (red) generated from MD simulations and zoomed into the capping triad region (R484, Q532, D533). The arrow indicates the shift of the D533 side chain upon binding of 8-NBD-cGMP. **(B)** WT *vs.* R484A CCS differences for the cGMP- (green) and 8-NBD-cGMP- (red) bound PfD samples. Only residues assigned in both samples are plotted. The distance (Å) measured from R484 using the cGMP-bound structure (PDB code: 4OFG) is shown in grey line. The secondary structure of cGMP-bound *Pf*D is depicted at the top of the plot. Pre-Lid and Lid motifs are highlighted in pink and purple background, respectively. The black arrows indicate residues Q532 and D533, which are part of the capping triad, while the black star denotes R484.

Chapter 6

Conclusion and Future Perspectives:

Inhibition Explained through Conformational Ensembles Sampling Distinct "Mixed" States

6.1 Author's Preface:

The work presented in this chapter has previously been published and is reproduced here with permission from the Computational and Structural Biotechnology Journal, Elsevier. Full citation is as follows:

Byun, J. A., VanSchouwen, B., Akimoto, M., and Melacini, G. (2020) Allosteric Inhibition Explained through Conformational Ensembles Sampling Distinct "Mixed" States. *Comput. Struct. Biotechnol. J.* In press.

This review article encompasses the summaries of all the findings from the previous chapters and puts them in the context of current literature. It discusses the common emerging theme of "mixed" state playing an essential role in explaining the mechanisms of observed allosteric inhibition. Hence, I have decided to include this review as the concluding chapter.

6.2 Abstract

Allosteric modulation provides an effective avenue for selective and potent enzyme inhibition. Here, we summarize and critically discuss recent advances on the mechanisms of allosteric partial agonists for three representative signalling enzymes activated by cyclic nucleotides: the cAMP-dependent protein kinase (PKA), the cGMP-dependent protein kinase (PKG), and the exchange protein activated by cAMP (EPAC). The comparative analysis of partial agonism in PKA, PKG and EPAC reveals a common emerging theme, *i.e.* the sampling of distinct "mixed" conformational states, either within a single domain or between distinct domains. Here, we show how such "mixed" states play a crucial role in explaining the observed functional response, *i.e.* partial agonism and allosteric pluripotency, as well as in maximizing inhibition while minimizing potency losses. In addition, by combining Nuclear Magnetic Resonance (NMR), Molecular Dynamics (MD) simulations and Ensemble Allosteric Modeling (EAM), we also show how to map the free-energy landscape of conformational ensembles including "mixed" states. By discussing selected case studies, we illustrate how MD simulations and EAM complement NMR to quantitatively relate protein dynamics to function. The resulting NMR- and MD-based EAMs are anticipated to inform not only the design of new generations of highly selective allosteric inhibitors, but also the choice of multidrug combinations.

6.3 Introduction

Allostery is a ubiquitous mechanism adopted by macromolecules to respond to external stimuli. An allosteric perturbation typically induces structural and/or dynamical changes that regulate function. Allosteric stimuli include not only binding of small ligands or partner proteins, but also mutations and post-translational modifications. Allosteric sites are usually distant from the orthosteric sites, such as the enzyme substrate binding site, and are less conserved relative to the orthosteric sites due to lower evolutionary pressure (1, 2). Hence, allosteric modulation is a promising approach for eliciting selective and potent enzyme inhibition. This realization has prompted a plethora of studies for understanding allosteric communication and networks (3–5), allosteric drug design (6–9), as well as the mechanisms of allosteric inhibitors and partial agonists. The latter typically target the allosteric domains of enzymes such as kinases (10–12), guanine nucleotide exchange factors (13, 14), tyrosine kinases (15, 16), and proteases (17, 18), or protein-protein interfaces such as molecular chaperone-client interactions (19).

Considering that allosteric mechanisms are fundamentally dynamic in nature, nuclear magnetic resonance (NMR) spectroscopic methods serve as an excellent tool to map at atomic resolution the free energy landscape sampled by the conformational ensemble of dynamic allosteric domains. However, it is advisable to complement experimental methods with computational approaches to identify potential allosteric sites and refine hypotheses on rational design of allosteric drugs (20, 21). For example, molecular dynamics (MD) simulations combined with coordination propensity (CP) analysis, which permits an assessment of the intrinsic flexibility of proteins and the changes associated with ligand binding, were used to identify residues that are distant from the catalytic site, yet highly correlated (21). Another computational method known as the structure-based statistical mechanical model of allostery (SBSMMA), which quantifies energetics and cooperativity of allosteric communication, provides predictions on novel allosteric sites (5, 20).

Allosteric modelling is also crucial in providing insights on observable allosteric phenomena. In the EAM, the populations of each microstate are modeled through normalized Boltzmann factors, which are in turn dictated by the free energies of conformational change within each (sub)domain and of inter-(sub)domain interactions (10, 22–25). Knowledge of such populations enables the prediction of key observables, such as affinities and degrees of

activation/inhibition. Here, we provide examples to illustrate how complementing NMR with Molecular Dynamics (MD) simulations and Ensemble Allosteric Modeling (EAM) provides unique insight on protein dynamics and their relation to function and allosteric regulation.

In the first part of the review, we will summarize and analyze recent findings on the mechanisms of partial agonists for representative allosteric signalling enzymes: the cAMP-dependent protein kinase (PKA), the cGMP-dependent protein kinase (PKG), and the exchange protein activated by cAMP (EPAC) (10–14, 26–30). The goal of this initial section is to reveal emerging trends, such as stabilization of novel "mixed" states that play essential roles in explaining the observed functional response. In the second part of the review, we will discuss how MD simulations and EAM play critical roles in complementing the NMR data and leading to allosteric models that quantitatively and verifiably predict protein function.

This review does not claim to be exhaustive and we will focus primarily on illustrative cases from our own work on cyclic nucleotide monophosphate (cNMP)-binding domains (CBDs) (10–14). CBDs share a conserved fold architecture with a non-continuous -subdomain and a continuous -subdomain (Fig. 1A, B of Ch. 5). The N-terminal helices are collectively referred to as the N3A, while the cNMP-phosphate binding cassette (PBC) is located within the -subdomain (Fig. 1B of Ch. 5). CBDs are prototypical conformational switches, and we will focus on CBDs that serve as the central controlling unit for closed-to-open transitions, which are common in the regulation of signaling pathways. Nevertheless, we refer the reader to other excellent reviews and articles for a more comprehensive assessment of the field (22, 31–39).

6.4 Partial agonism in isolated allosteric domains reveals a common inhibitory mechanism where sampling of 'mixed' intermediate states maximizes inhibition while minimizing potency losses

Although allosteric signaling systems are often multi-domain proteins, here we will initially focus on a single allosteric domain, as this is the simplest case to start with, and it offers an essential 'building block' to understand more complex systems. In addition, it is often possible to identify a single domain that functions as the main 'central controlling unit' for the

whole multi-domain protein, such as CBD-D of *P. falciparum* PKG in Fig. 1A. When a partial agonist binds and induces changes in a single domain, functional modulations arise from at least two possible scenarios: (1) a simple shift of a two-state inactive-active conformational equilibrium to the inactive state (Fig. 1F of Ch. 5); or (2) a multi-state equilibrium sampling a distinct intermediate 'mixed' state that displays different degrees of resemblance to the inactive and active states in different regions of the domain (Fig. 1G of Ch. 5).

Recent studies on the mechanisms of partial agonists that target the CBDs of allosterically regulated enzymes show an emerging trend, where partial agonism is best accounted for in terms of sampling multi-state equilibria with mixed intermediate states (11–14). A common feature shared by these mixed intermediate states is the differential allosteric response of the C-terminal helix and the PBC (Fig. 1B of Ch. 5). The PBC directly interacts with the phosphate of the cNMP, while the C-terminal helix of the allosteric domain serves as a capping lid for the cNMP (Fig. 1B of Ch. 5). In PKG and EPAC, the C-terminal helix also directly links the CBD to the catalytic domain or region. The mixed states (Fig. 1G of Ch. 5) offer a simple but effective explanation for the mechanism of inhibition of these enzymes.

***h*PKG.** One of the first cases in which mixed intermediates were reported to explain partial agonism in a CBD pertains to human cGMP-dependent protein kinase (*h*PKG) and cAMP (12). *h*PKG includes two tandem CBDs (CBD-A and CBD-B) preceding the kinase domain (26, 40). Although the CBD-B of *h*PKG preferentially binds cGMP relative to cAMP, the higher intracellular concentration of cAMP suggests that additional mechanisms promote selective cGMP-dependent activation of *h*PKG in conjunction with the cGMP-*versus*-cAMP affinity differential (26, 40–42). For example, another difference that contributes to cGMP-*versus*-cAMP selective activation is that cAMP acts as a partial agonist for *h*PKG. To determine the mechanism of such partial agonism, NMR chemical shift projection analyses (CHESPA) and ^{15}N relaxation measurements aimed at characterizing internal dynamics were utilized (12).

CHESPA revealed a non-uniform distribution of fractional activations indicative of cAMP-bound CBD-B sampling a three-state equilibrium among the inactive state, the active state, and a mixed intermediate state (Fig. 1A). In the inactive state, the N-terminal helices (N3A) are in the 'in' conformation, and the PBC and C-terminal helices are in the 'out' conformation and flexible, as confirmed by ^{15}N relaxation measurements. The opposite is true

for the active state. In the mixed intermediate state, the orientation of both the N3A and PBC resembles that of the active state, but the C-terminal helices are disengaged and more dynamic, similar to the inactive state (Fig. 1A; dashed box). This disengagement of the C-terminal helices, which directly link CBD-B to the catalytic domain, alters the relative positioning of the catalytic domain to CBD-B, and thus, the accessibility of the kinase substrates to the catalytic binding pocket. This allows the mixed state to preserve at least partial kinase inhibition and provides a viable explanation as to why even if cAMP binds *h*PKG due to its high intracellular concentration, it leads to only minimal cross-activation of cGMP- and cAMP-dependent signalling pathways.

***pf*PKG**. PKG is also involved in proliferation of the *Plasmodium falciparum* parasite, one of the primary pathogens responsible for malaria (43–48). Elucidating the mechanism of allosteric inhibition through targeting the cGMP-binding domain of *P. falciparum* PKG (*pf*PKG) may potentially help in designing new drugs to combat malaria, as is needed due to an increasing resistance to current treatments. For this purpose, a cGMP-analog which activates *pf*PKG only partially, known as 8-NBD-cGMP, was investigated in complex with CBD-D of *pf*PKG (11). *pf*PKG contains four tandem CBDs (Fig. 1A of Ch. 5), but CBD-D is the domain primarily responsible for the autoinhibition and the cGMP-dependent activation of *pf*PKG (49, 50).

The CHESPA analysis of the CBD-D of *pf*PKG shows that the 8-NBD-cGMP-bound CBD-D samples a conformational ensemble that includes its native inactive and active states, as well as a mixed intermediate state. In this mixed state, the pre-lid region, which includes a helix that rotates in conjunction with the PBC, resembles the active state, whereas the lid in the C-terminal helix is disengaged, similar to the inactive state (Fig. 1B; dashed box) (11). MD simulations were performed starting from a model of the mixed intermediate built based on the structural information gathered from NMR. The MD trajectories corroborated the hypotheses on the conformation of the bound 8-NBD-cGMP, and the overall structure of the otherwise elusive mixed intermediate state (*vide infra*).

The combined CHESPA and MD results show that sampling a mixed intermediate state allows the inhibitor to preserve high affinity to the allosteric domain through the engagement of essential elements of the binding site, such as the PBC that stabilizes the interaction with

the phosphate of the analog. On the other hand, the lid disengagement makes the domain inhibition-competent by failing to form interactions critical for activation. Hence, we hypothesized that inhibitors which stabilize the mixed intermediate state relative to the native inactive or active states are more potent than those that simply target purely inactive or active states. Targeting the fully inactive state alone is likely to lead to affinity losses and poor potency, while targeting the fully active state compromises the efficacy of the inhibitor. Targeting the mixed intermediate, however, provides an opportunity to enhance the inhibition without excessively compromising the potency.

EPAC. The guanine Exchange Protein directly Activated by cAMP (EPAC) is another cyclic nucleotide-regulated enzyme that serves as a potential drug target for the treatment of a wide range of diseases, from pancreatic (51, 52) to breast cancer (53), diabetes (54) and viral infections such as SARS and MERS (55). Recent mechanistic studies have focused on elucidating the mechanisms of two different EPAC allosteric partial agonists discovered through screening: I942 (13) and CE3F4R (14). Both I942 and CE3F4R are non-cNMP ligands acting on the CBD of EPAC isoform 1 (EPAC1), and both stabilize mixed intermediate states, yet through very distinct mechanisms (13, 14).

I942 is a competitive partial agonist with respect to cAMP (13, 27), and its mechanism of action conforms to the pattern observed in the previously discussed mechanisms based on an ensemble of three states, including a purely inactive, a purely active, and a mixed intermediate state (Fig.1C) (13). The distinguishing feature of this mixed intermediate state is that the PBC adopts the 'in' conformation, similar to the active state, while the C-terminal hinge helix, which is responsible for orienting the catalytic region relative to the regulatory region, is in the 'out' conformation, similar to the inactive state (Fig. 1C; dashed box). Hence, the I942 partial agonism arises through stabilization of both inactive and intermediate states (Fig. 1C).

Sampling of a mixed EPAC1 CBD state is also central to the mechanism of CE3F4R, which is an unconventional partial agonist since it is uncompetitive with respect to cAMP (14, 29). CE3F4R binding to EPAC1 is conditional on cAMP binding, and partial agonism arises *via* formation of a ternary complex involving the EPAC1 CBD, cAMP and CE3F4R (29). CE3F4R binding occurs at the α/β subdomain interface, as opposed to the cAMP binding site (Fig. 1D).

This binding mechanism allows CE3F4R to act as a wedge that stabilizes a cAMP-bound mixed intermediate state where the PBC is engaged by cAMP (*i.e.* active PBC conformation), but the hinge helix is in the inactive conformation.

Due to the inactive orientation of the hinge in the presence of CE3F4R, EPAC1 adopts a closed topology where the catalytic domain is inaccessible to its Rap substrate (Fig. 1D). This mechanism of stabilization of the mixed intermediate state not only explains why CE3F4R is selective for EPAC1 *vs.* the EPAC2 isoform, but also provides critical insight into the use of allosteric inhibitor combinations. In EPAC2 a glutamine residue in the EPAC1 PBC is replaced by a lysine, which forms a salt bridge with a glutamate in the hinge helix, thus stabilizing its active conformation and destabilizing the mixed intermediate preferred by CE3F4R. The mixed state also provides a basis to understand why CE3F4R cannot be used in combination with the phosphorothioate cAMP analog Rp-cAMPS, which is a well-known allosteric antagonist of EPAC1 (56). Rp-cAMPS binds to the cAMP binding site and stabilizes the PBC in the 'out' conformation due to the presence of the bulky sulfur atom, thus destabilizing the mixed state to which CE3F4R selectively binds.

The CE3F4R/Rp-cAMPS example highlights the importance of elucidating the mechanism of allosteric inhibition to guide the choice of inhibitor mixtures. In principle, ideal multidrug combinations could be identified solely based on 'blind' screening campaigns (57). However, inherent combinatorial complexity is a notorious bottleneck in combination therapies, as it limits the feasibility of exhaustively searching all possible drug-pairs from conventional libraries (58, 59). Hence, knowledge of allosteric mechanisms is anticipated to be valuable for filtering ligand libraries into more targeted subsets to enable more efficient combinatorial screening.

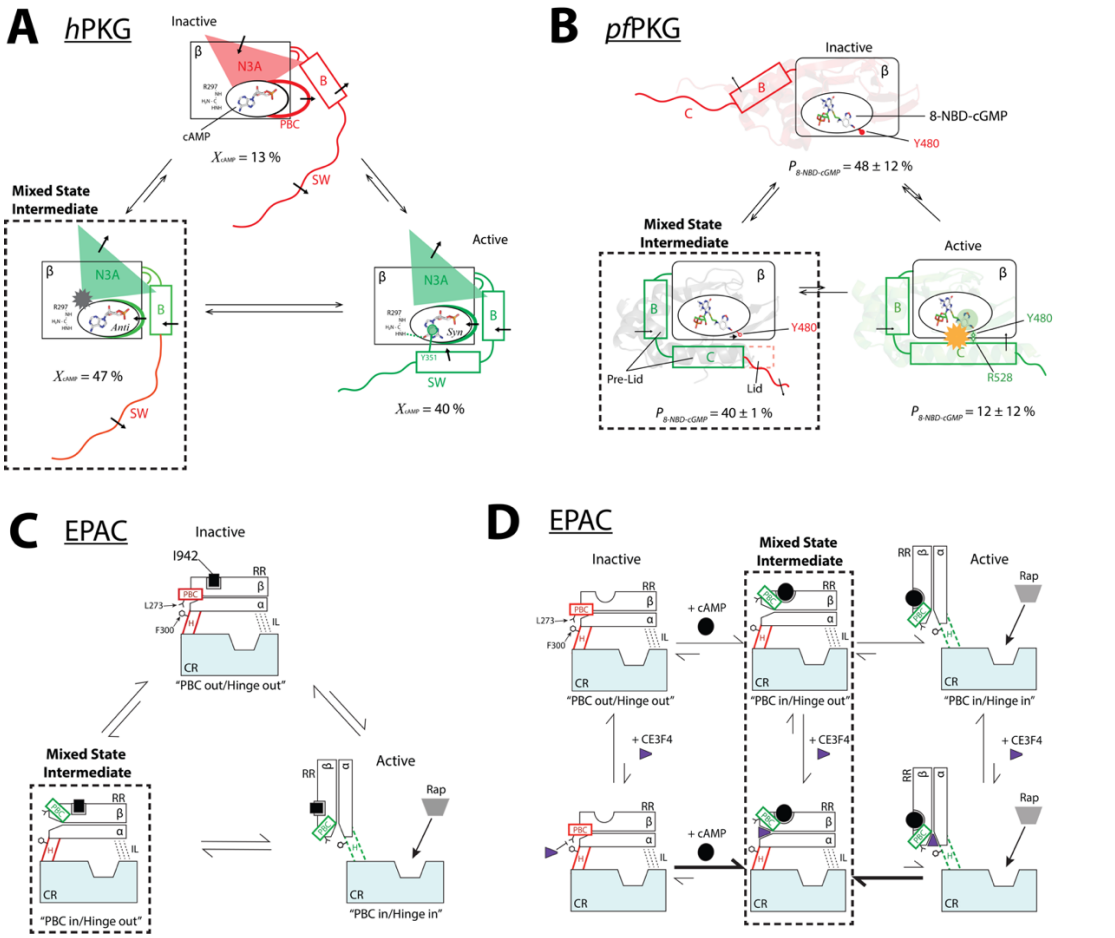

Figure 1. *Sampling mixed intermediate states of isolated CBDs enables partial agonists to maximize inhibition without significantly compromising affinities*. **(A)** CBD-B of human PKG bound to cAMP samples inactive and active conformers as well as an intermediate state (dashed box), where only its C-terminal switch helix (SW) is disengaged and dynamic (12). The figure was reproduced with permission and was originally published in the Journal of Biological Chemistry. VanSchouwen B, Selvaratnam R, Giri R, Lorenz R, Herberg FW, Kim C, et al. Mechanism of cAMP Partial Agonism in Protein Kinase G (PKG). J. Biol. Chem. 2015; 290:28631-38641. © the American Society for Biochemistry and Molecular Biology. **(B)** *Plasmodium falciparum* PKG bound to 8-NBD-cGMP. The mixed intermediate state (dashed box) features an engaged pre-lid region to promote inhibitor binding, but the C-terminal lid remains disengaged to ensure inhibition (11). The figure was reproduced with permission and was originally published in the Journal of Biological Chemistry. Byun JA, Van K, Huang J, Henning P, Franz E, Akimoto M, et al. Mechanism of allosteric inhibition in the Plasmodium falciparum cGMP-dependent protein kinase. J. Biol. Chem. 2020;295:8480–91. © the American Society for Biochemistry and Molecular Biology. **(C)** EPAC1 bound to I942. The mixed intermediate (dashed box) includes a PBC "in" and C-terminal hinge helix (H) "out" conformation (13). The out conformation of the hinge helix leads to inhibition of the catalytic region (CR) as it obstructs access to its Rap1 substrate. **(D)** EPAC1 bound to cAMP and CE3F4R, which uncompetitively binds to EPAC1 and stabilizes the mixed intermediate state (dashed box), where the PBC is "in" and the C-terminal hinge (H) is "out" (14). The figures are adapted with permission from Boulton S, Selvaratnam R, Blondeau J-P, Lezoualc'h F, Melacini G. Mechanism of Selective Enzyme Inhibition through Uncompetitive Regulation of an Allosteric Agonist. J Am Chem Soc 2018;140:9624–37. Copyright 2018 American Chemical Society.

In general, the examples discussed above illustrate how diverse partial agonists enhance their effectiveness to bind and inhibit target enzymes through sampling mixed intermediate states. The mixed intermediates are ideally suited for maintaining stable binding interactions with the ligands through the engaged PBC, while retaining the ability to inhibit enzymatic function by disengaging the C-terminal helix that links the regulatory and catalytic domains or regions, thus perturbing interactions required for activation. However, the partial agonism mechanisms discussed so far are based on the effect of the allosteric modulator on single isolated domains. Considering that signaling proteins are often multi-domain, it is critical to explore whether mixed states also play a central role in longer constructs that better recapitulate multi-domain complexity.

6.5 Sampling of 'mixed' intermediate states by an allosteric multi-domain system explains allosteric pluripotency

Mixed intermediate states are relevant also for multi-domain proteins, especially when different domains bind the same allosteric ligand, but with different allosteric responses. An example of this type of mixed state for a multi-domain system was observed in the cAMP-dependent protein kinase (PKA) bound to Rp-cAMPS (Rp). Rp (Fig. 1A of Ch. 2) is the primary allosteric inhibitor for PKA known to date, despite extensive screening efforts aimed at inhibiting the cancer-driver function of PKA (60–64). Interestingly, in the presence of MgATP, Rp acts as an antagonist for PKA, but in the absence of MgATP, it acts as an agonist (65). This phenomenon is referred to as allosteric pluripotency. Understanding allosteric pluripotency is essential to translate allosteric modulators into effective therapeutics, because when the effect of an allosteric ligand depends on the environmental conditions, undesired side effects may arise (66).

PKA. A distinct difference between PKA and the allosteric enzymes discussed above (PKG and EPAC) is that the PKA regulatory subunit (R) and catalytic subunit (C) belong to separate polypeptide chains (Fig. 1E and 3F, G of Ch. 2) (67–69). In the absence of cAMP, the R-subunit binds and inhibits the C-subunit (Fig. 3F of Ch. 2) (67). The R-subunit of PKA includes two tandem CBDs (CBD-A and B). When cAMP binds to each of the CBDs (A and B),

conformational changes occur within the R-subunit (Fig. 3G of Ch. 2) that allow the release of the C-subunit (67). The main R:C interaction is through CBD-A, especially though the inhibitory linker in CBD-A that docks into the active site of the C-subunit (68). This interaction is further stabilized through binding of MgATP (Fig. 3F of Ch. 2) (70).

When both CBDs adopt an 'on' state similar to the cAMP-bound state (Fig. 3G of Ch. 2), the R-subunit is inhibition-incompetent and the kinase function of PKA is turned on. When CBD-A shifts to the 'off' state, similar to the C-subunit-bound structure, the R-subunit is inhibition-competent and has the potential to turn off the kinase function of PKA. CHESPA shows that when Rp binds to the R-subunit in the absence of C-subunit and of inter-CBD interactions, Rp turns off CBD-A and turns on CBD-B (10). However, the inter-CBD interaction, which relies on the capping of the cNMP base moiety in CBD-A by residue W260 of CBD-B (71, 72), facilitates the conversion of CBD-A to the on state, as confirmed through NMR and independent MD simulations (*vide infra*) (10). This conversion leads Rp-bound R-subunit to sample a complex conformational ensemble that includes a ground state, where both CBDs are in the on state and interacting with each other, and multiple excited states in which the inter-CBD interaction is absent (Fig. 5A of Ch. 2). One of the excited states of the $R:Rp_2$ complex is inhibition-competent as CBD-A is in the 'off' state (Fig. 5A of Ch. 2). The relative population of each state in the ensemble was computed through EAM, resulting in a map of the free energy landscape for the R-subunit (Fig. 3E).

The free energy landscape of PKA R rationalizes the allosteric pluripotency observed for Rp. In the presence of MgATP, the R:C interaction is favoured, and the mixed inhibition-competent state becomes the ground state upon C-subunit binding, forming a stable $C:R:Rp_2$ complex and leading to PKA inhibition (Fig. 5B of Ch. 2). In the absence of MgATP, the R:C interaction is less stable, and thus, the mixed state remains at a high free energy level and the kinase is active, as the ground state of $R:Rp_2$ does not bind PKA C (Fig. 5C of Ch. 2). Hence, the main driver of the allosteric pluripotency is the mixed excited state where CBD-A is off and CBD-B is on (Fig. 5A of Ch. 2).

Overall, the comparative analysis of partial agonism in *h*PKG, *pf*PKG, EPAC (Fig. 1) and PKA (Fig. 5A of Ch. 2) reveals that mixed conformational states, either within or between domains, provide critical explanations of allosteric modulation and meaningful insights into potential drug design strategies. The mixed intermediate states were primarily identified by

NMR spectroscopy. NMR enables Chemical Shift Projection and Covariance Analyses (CHESPA and CHESCA), which have proven instrumental in determining the mechanism of partial agonism and allosteric pluripotency (10–14). Further insight is obtained when NMR is complemented with additional structural and dynamical information from MD simulations and related to function through an EAM. In the second half of this review, we will discuss how MD simulations and EAM can be implemented to complement NMR and bridge the gap between protein dynamics and function.

6.6 MD simulations provide a glimpse of the otherwise elusive 'mixed' inhibitory intermediate states, and means to generate targeted and testable hypotheses

In conjunction with experimental analyses, MD simulations can be used to assess or confirm allosteric features that are not easily accessible by experimentally, as well as to formulate hypotheses for further experimental work. An example is illustrated by the recent study of the mechanism of inhibition of *Pf*PKG by the cGMP analogue 8-NBD-cGMP (11). As discussed in the previous section of the review, through functional and NMR-based analyses it was determined that upon binding 8-NBD-cGMP, the critical CBD of *Pf*PKG (*i.e.* CBD-D) samples an inhibition-competent intermediate structure in which the pre-lid region is in an active-like arrangement, while the C-terminal lid remains disengaged as in the inactive state (Fig. 2B). To further investigate the molecular details of the intermediate structure, MD simulations were performed on the cGMP-bound active structure of *Pf*PKG CBD-D, and on an 8-NBD-cGMP-bound hybrid structure of *Pf*PKG CBD-D, which represents the intermediate state. The latter consists of the N-terminal α-helices, β-core and pre-lid region of the active structure, and the C-terminal lid of the inactive structure grafted onto the end of the pre-lid region, with 8-NBD-cGMP docked into the cGMP binding pocket (Fig. 6E, F of Ch. 5).

Representative structures were selected from each simulation *via* cluster analysis and overlaid to compare the structural tendencies in each simulation (Fig. 6E-G, S3A of Ch. 5). In agreement with the NMR data, the overlaid structures suggested that the guanine base and ribose-phosphate moieties of 8-NBD-cGMP preserve a binding pose similar to that of cGMP

(Fig. 6E of Ch. 5). More notably, the structures suggested that the side chain of lid residue R528 would sterically clash with the 8-NBD moiety of 8-NBD-cGMP in the active structure, but not in the intermediate structure, thus favoring disengagement of the lid *via* disruption of the key Y480/R528 interaction that forms in the active-state arrangement of the lid (Fig. 6F, G of Ch. 5) (50). The intermediate structure also perturbs the capping triad, leading to disengagement of the R484/D533 lid interaction (Fig. S3A of Ch. 5). Indeed, subsequent NMR-based comparisons of the R528K and R484A mutants with wild-type *Pf*PKG CBD-D revealed that the mutations produced visible perturbations within cGMP-bound *Pf*PKG CBD-D, while the perturbations were largely suppressed within 8-NBD-cGMP-bound *Pf*PKG CBD-D (Fig. 6I, S3B of Ch. 5), suggesting that the Y480/R528 and R484/D533 interactions are disrupted in 8-NBD-cGMP-bound wild-type *Pf*PKG CBD-D, and thus confirming the conclusions drawn from the MD simulations. This example illustrates the synergy between MD simulations and NMR analyses of regulatory conformational equilibria.

Another example of the use of MD simulations is illustrated by the recent study of allosteric pluripotency that occurs upon binding of the cAMP analogue R_p-cAMPS (Rp) to the tandem CBDs of the PKA regulatory subunit (10). In particular, NMR-based analyses of the PKA R-subunit both with and without bound PKA C-subunit suggested that coupling between the conformational equilibria within the CBD-A and CBD-B domains of the R-subunit, and the previously-reported inter-domain interaction between CBD-A and CBD-B, is a key contributor to the allosteric pluripotency observed upon Rp binding. To refine this hypothesis, MD simulations were performed on Rp-bound structures of the R-subunit, and the R-subunit in complex with the C-subunit (Fig. S4 of Ch. 3). The simulations were started from available structures with the R-subunit in its fully-inactive (*i.e.* with both CBD-A and CBD-B in their 'off' conformations, and not interacting with one another; Fig. S4A, B of Ch. 3) or fully-active conformation (*i.e.* with both CBD-A and CBD-B in their 'on' conformations, and interacting with one another; Fig. S4C of Ch. 3), as well as from a series of hybrid structures with CBD-A in its 'off' conformation and CBD-B in its 'on' conformation (Fig. S4D-I of Ch. 3). The latter structures were generated by grafting the CBD-B from the active structure onto the CBD-A from the inactive structure. Specifically, the structures of the tandem CBDs were joined at points along the intervening α-helix where kinks are present in the active structure but not in the inactive structure, resulting in hybrid structures with varying distances between the CBD-A and CBD-B

domains (Fig. S4D-I of Ch. 3 and Fig. 4A of Ch. 2). The structures generated from each simulation were then analyzed by computing RMSDs from the inactive and active structures, and distances between the centers-of-mass (CMs) of the constituent domains, to assess the structural tendencies during each simulation (Fig. 4A, D, F of Ch. 2).

In agreement with the original NMR-based hypothesis, the simulation results suggested a coupling between the conformational equilibria within the CBD-A and CBD-B domains, and the inter-domain interaction between the CBD-A and CBD-B domains. Specifically, while CBD-B remained close to its 'on' conformation for all hybrid structures (Fig. 4F of Ch. 2 and S5G, S6I-J of Ch. 3), CBD-A consistently exhibited a shift to its 'on' conformation in the hybrid structures where CBD-A and CBD-B were closer together (*i.e.* the "225" hybrid structures shown in Fig. S4D, G of Ch. 3), but remained closer to its 'off' conformation in the hybrid structures where CBD-A and CBD-B were further apart (*i.e.* the "231" and "242" hybrid structures shown in Fig. S4E, F, H, I of Ch. 3; Fig. S5F and S6E, G of Ch. 3; Fig. 4D of Ch.2). These results corroborated that formation of the inter-domain interaction between CBD-A and CBD-B promotes a shift of CBD-A to its 'on' conformation. In addition, the CBD-A domain and C-subunit moved apart from one another in the "225" hybrid structure, but remained close to one another in the "231" and "242" hybrid structures (Fig. S5B of Ch. 3), highlighting a coupling between intra-R-subunit conformational shifts and C-subunit binding. Finally, it was predicted based on the simulation results that the distance between the CBD-A and CBD-B domains should vary among the different types of R-subunit complexes in the order C-subunit:R-subunit > C-subunit:R-subunit:$(Rp)_2$ > R-subunit:$(Rp)_2$ > R-subunit:$(cAMP)_2$. This MD-based prediction was then tested, and confirmed, through paramagnetic relaxation enhancement (PRE) NMR experiments. This example on PKA, together with the previous example on *Pf*PKG, illustrates how comparative analyses of MD simulations are an effective tool to refine hypotheses on the conformational ensembles accessed by dynamic systems. These hypotheses can then be tested through targeted *ad hoc* NMR experiments. However, MD simulations and NMR data alone are not always sufficient to enable the formulation of allosteric models that quantitatively predict function. To address this limitation and enable quantitative predictions, it is advantageous to complement MD and NMR with ensemble allosteric modeling, as explained in the next section.

6.7 Ensemble Allosteric Models (EAMs) bridges dynamics to function

It is often challenging to bridge the gap between dynamics and function by relying solely on NMR data, especially when dealing with a complex system. Thus, ensemble allosteric models (EAMs) are valuable for bridging the state dynamics mapped at atomic resolution by NMR to functional predictions testable through low-resolution assays such as enzymatic assays and electrophysiology (10). EAMs are a statistical mechanical description of the free energy landscape, in which free energy levels are translated into specific state populations through normalized Boltzmann factors. As a result, EAMs enable the prediction of macroscopic averaged observables, such as binding affinities and degrees of activation/inhibition (10, 23).

To build an EAM, the first step is to define all of the microstates that are sampled by the system. To this end it is convenient to start from the simplest system, *i.e.* the apo form of the macromolecule, which typically samples 'on/off' conformational states. Further states can then be added to the EAM by including inter-domain interactions (*e.g.* closed *vs.* open states) and binding events (*e.g.* apo *vs.* bound states). For example, in the case of PKA and Rp (Fig. 3E), these states arise by considering combinations of (a) the 'off' and 'on' states of each domain; (b) the apo and Rp-bound states; and (c) the presence and absence of CBD-A:CBD-B interaction. The Boltzmann statistical weights of these states can then be estimated based on input parameters that include (i) the free energy difference of 'off' vs. 'on' states, (ii) the state-specific association constant of the ligand for each domain, (iii) the free energy of inter-domain interaction, and (iv) the state-specific association constant of the C-subunit to the R-subunit. Most of these input parameters can be measured through NMR, as discussed in the following section.

6.8 Measuring EAM input parameters by NMR

The input parameters of EAM can be effectively determined based on NMR data, such as chemical shifts and H/D exchange rates (10). For example, in the case of the PKA/Rp system, the first parameter to determine is the free energy difference of 'off' *vs*. 'on' states in the apo form of each domain, *i.e.* input (i) for CBD-A and B, defined as ΔG_A and ΔG_B, respectively. The

ΔG_A and ΔG_B free energies are determined considering that the exchange between the 'on' *vs.* 'off' states of each domain is fast in the NMR chemical shift time scale for both apo CBDs (Fig. 2A). This allowed us to measure the fraction of 'on' and 'off' states of the apo CBD-A and CBD-B based on the NMR chemical shifts (Fig. 2B). Such fractions were then converted into the ΔG_A and ΔG_B parameters assuming a two-state 'on'/'off' Boltzmann equilibrium for each domain (Fig. 5A of Ch. 2).

To see how the ensemble of states sampled by the apo R-subunit is remodelled by Rp binding (Fig. 5A of Ch. 2), it is necessary to measure input parameter (ii), which refers to the state-specific association constants of the ligand to each domain. To simplify the measurement, we first measured for each CBD the ratio of state-specific association constants (ρ_A and ρ_B) based on the relative fractions of 'off' states in the apo and Rp-saturated CBDs, which are simply measured through NMR chemical shift analyses (Fig. 2C, D). We then measured the association constant of Rp for the 'off' state by titrating Rp into the R:C complex, which locks the R-subunit in the 'off' state, and monitoring the resulting NMR chemical shift changes. Based on the ρ_A and ρ_B values, and the respective association constants of Rp to the 'off' state, we then obtained also the association constant of Rp for the 'on' state of each domain.

Next, we measured input parameter (iii), which is the free energy of inter-domain interaction (ΔG_{AB}). ΔG_{AB} was measured through two independent approaches. The first method relies on the intensity of the cross-peak arising from the open topology (*i.e.* absence of inter-domain interaction) and on comparing that intensity to that of the cross-peak arising from the closed topology (*i.e.* presence of inter-domain interaction; Fig. 2E, F). This method can be used when the open and closed topologies are in slow exchange in the NMR chemical shift time scale. However, since the open and closed topologies exhibit different relaxation properties, the intensity measurements need to be corrected for the differential relaxation in the open *vs.* closed topologies. This can be done by utilizing mutations or ligands that lock the system in the open topology or the closed topology.

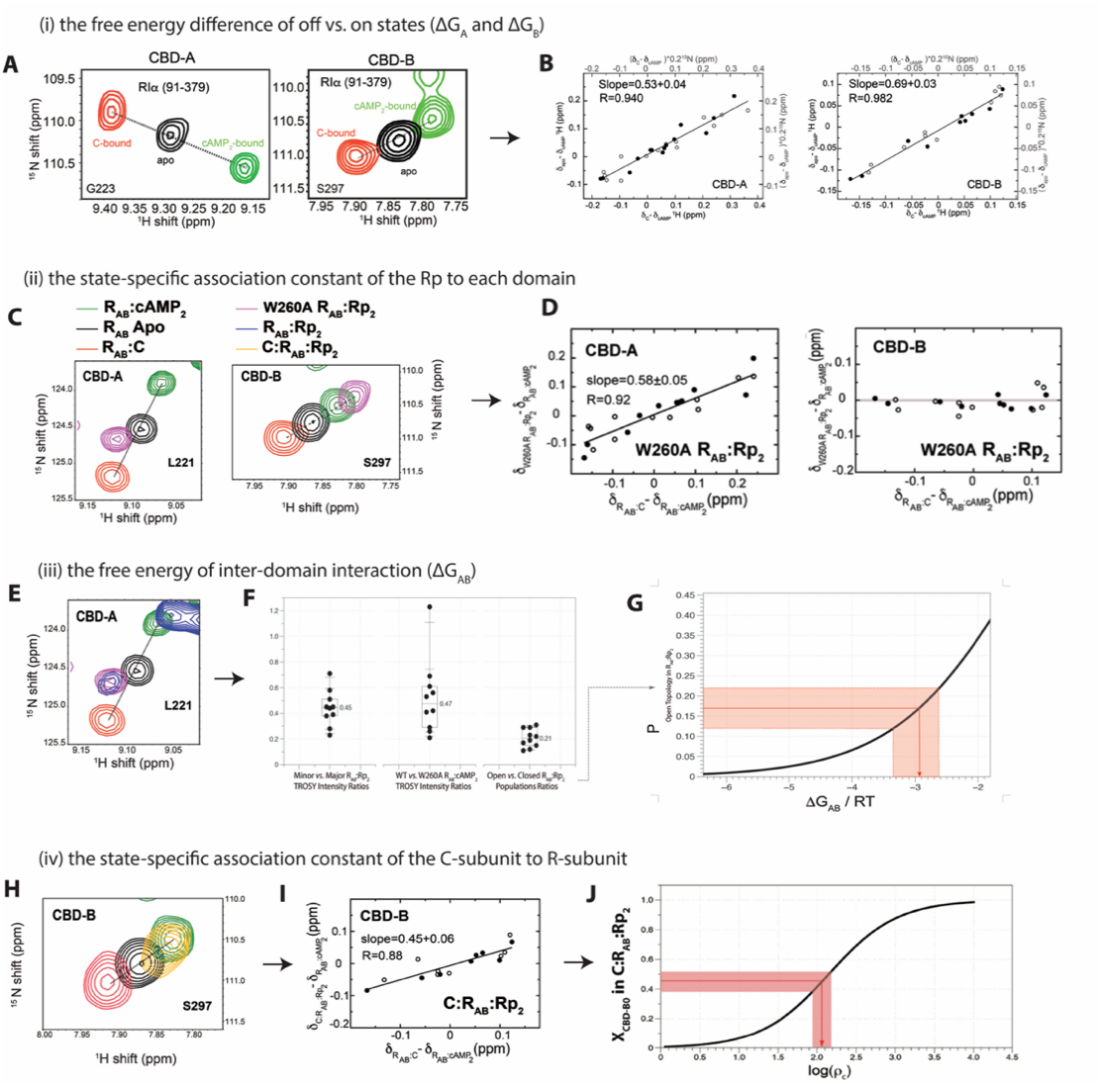

Figure 2. *Measuring EAM input parameters by NMR.* **(A)** Representative NMR TROSY cross-peaks of apo R-subunit (CBD-A and CBD-B) and the reference cAMP-bound and C-bound R-subunits. **(B)** Chemical shift correlation plots of CBD-A and CBD-B for the apo sample, where the slope represents the fraction of 'off' states in each domain. The closed and open circles represent ^{1}H and ^{15}N chemical shifts, respectively. Figures are adapted from Akimoto M, McNicholl ET, Ramkissoon A, Moleschi K, Taylor SS, Melacini G. Mapping the Free Energy Landscape of PKA Inhibition and Activation: A Double-Conformational Selection Model for the Tandem cAMP-Binding Domains of PKA RIα. PLoS Biol. 2015;13:e1002305. **(C)** Similar to panel (A), but with the addition of the W260A:Rp_2 TROSY spectrum. **(D)** Similar to panel (B), but for the W260A:Rp_2 sample. **(E)** Similar to panel (C), but with the addition of the WT:Rp_2 TROSY spectrum. **(F)** Based on the TROSY cross-peaks in panel (E), the intensities of the minor and major peaks are measured, allowing for the calculation of the open *vs.* closed population ratios. This population is used to estimate the $\Delta G_{AB,}$ as shown in panel **(G)**. **(H)** Similar to panel A (right), but with the addition of the C:R:Rp_2 TROSY spectrum. **(I)** Similar to panel (D), but for CBD-B of the C:R:Rp_2 complex. **(J)** The fraction of 'off' state of CBD-B in the C:R:Rp_2 sample can be used to estimate the ratio of state-specific association constants of C-subunit for R-subunit (ρ_C). Figures were adapted from Byun JA, Akimoto M, VanSchouwen B, Lazarou TS, Taylor SS, Melacini G. Allosteric pluripotency as revealed by protein kinase A. Sci Adv 2020;6:eabb1250. Reprinted with permission from AAAS.

Once the population of the open topology of the Rp-bound state is estimated, the free-energy of inter-domain interaction can be obtained by calculating through the EAM how the open topology population depends on ΔG_{AB} (Fig. 2G). The second approach we adopted to independently cross-check the ΔG_{AB} value obtained from the first method relies on H/D exchange rates. By measuring the difference in the maximal protection factors (PFs) of the amide hydrogens in CBD-A of the WT *vs.* the W260A mutant (which silences the inter-domain interaction), it is possible to estimate the free energy of inter-domain interaction ΔG_{AB}. The two approaches provided comparable values for ΔG_{AB}.

Using similar approaches (Fig. 2H-J), we measured the last set of input parameters (iv), *i.e.* the state-specific affinities of the C-subunit for the R-subunit. To take into account how these affinities depend on the concentration of MgATP (70), we introduced a scaling factor (γ), with $\gamma = 1$ in the presence of MgATP and $\gamma << 1$ in the absence of MgATP. These R:C affinities are important for determining the average fraction of R-subunit bound to C-subunit in the absence and presence of cNMP, which in turn lead to the fractional change of kinase activity upon cNMP addition.

After the EAM parameters were determined by NMR, it was possible to compute the statistical weights of each state in the conformational ensemble, and to quantitatively predict kinase activities upon addition of ligands such as cyclic nucleotides. Specifically, the average effective R:C association constants in the absence and presence of excess cNMP, such as Rp, were calculated as averages of state-specific association constants weighed by the populations in the apo or cNMP-bound forms (both in the absence of C-subunit). With these effective R:C association constants, the concentration of R-subunit not bound to the C-subunit ([R]) in the absence and presence of excess cNMP was computed through a classical quadratic equation (Eq. (1-4)).

$$[R]_{no\ cNMP} = [R]_{Tot.} - 0.5(b_{no\ cNMP} - \sqrt{b^2_{no\ cNMP} - 4[R]_{Tot.}[C]_{Tot.}}) \quad (1)$$

with: $$b_{no\ cNMP} = [R]_{Tot.} + [C]_{Tot.} + (\frac{\mathbf{1}}{\langle \boldsymbol{K_{C,no\ cNMP}} \rangle}) \quad (2)$$

$$[R]_{cNMP} = [R]_{Tot.} - 0.5(b_{cNMP} - \sqrt{b^2_{cNMP} - 4[R]_{Tot.}[C]_{Tot.}}) \quad (3)$$

with: $$b_{cNMP} = [R]_{Tot.} + [C]_{Tot.} + (\frac{\mathbf{1}}{\langle \boldsymbol{K_{C,cNMP}} \rangle}) \quad (4)$$

where the K_C values refer to the average effective R:C association constants either in the absence or presence of excess cNMP. With these [R] values and the effective R:C association constants, the fractional change of kinase activity (ϕ) caused by the addition of cNMP was then computed based on classical Michaelis-Menten kinetics, in which the R-subunit serves as a competitive inhibitor of the C-subunit. Reference (10) includes detailed explanations on the derivations of relevant equations, and the construction of the EAM for PKA allosteric pluripotency.

6.9 The EAM enables dissection of key allosteric drivers

With a fully parametrized EAM, it is possible to predict the kinase activity under different conditions, such as high or low concentrations of MgATP, varying substrate affinities (*i.e.* K_m constants) and concentrations, and different R:C concentration ratios. As shown in Fig. 6A of Ch. 2, the kinase activities predicted through the EAM with high and low γ values are in good agreement with the kinase activities measured experimentally for PKA:Rp in the presence and absence of MgATP (65). Similar to the effect of MgATP, the affinity of the kinase substrate also affects the R:C affinity and therefore contributes to varying responses of PKA to Rp, as is confirmed through both the EAM and enzymatic assays (Fig. 6E of Ch. 2). These results illustrate how the EAM bridges the dynamical information revealed through NMR experiments to the functional activity measured through enzymatic assays.

Another distinct feature of the EAM is that it can also be used to dissect which factors within the system contribute to the agonism-to-antagonism switch (*i.e.* allosteric pluripotency). For example, we can estimate what the effect on kinase function would be if the inter-domain interactions were absent. By setting the ΔG_{AB} parameter to 0, the kinase activity was predicted, which still exhibited significant activation (Fig. 6A of Ch. 2). This allowed us to propose that the agonism observed with Rp arises not only from the inter-domain interaction that stabilizes CBD-A in the 'on' state, but also from the CBD-B shifting to the 'on' state upon binding of Rp.

Another relevant prediction of the EAM is that if the 'mixed' state is not sampled by the multi-domain protein, *i.e.* if both domains respond similarly to an allosteric effector, then full allosteric pluripotency will not be observed. For instance, using the PKA and Rp example, when

Rp acts as an agonist for both CBD-A and CBD-B, the EAM predicts that Rp agonistically activates the kinase function of PKA in both the absence and presence of MgATP. On the other hand, when both CBDs are turned 'off' by binding to Rp, only antagonism or partial agonism is anticipated for Rp in the presence and absence of MgATP. These scenarios show how the 'mixed' state plays an essential role in driving allosteric pluripotency in a multi-domain system and provide a compelling example of the added allosteric insight offered by the EAM.

Overall, the MD/EAM combination has played an important role as a predictive tool, and for developing critical hypotheses. MD simulations have provided insights on the conformational transition of CBD-A that were otherwise elusive. Such insight on the selective interaction of CBD-B with the 'on' state of CBD-A was critical for setting up the EAM. For example, when determining the statistical weight of the $A_{on}B_{on}$ state, it allowed for an important correction of the state-specific association constant of Rp to the 'on' state of CBD-A based on the free-energy of inter-domain interaction. EAM then further predicted the functional outcome under different environmental conditions or properties of the system, such as the state-specific association constants or the free-energy of inter-domain interaction. This is a valuable resource to propose and examine hypotheses on the mechanisms underlying the observed function of a mutant or an analog-bound system.

6.10 Concluding remarks

In this review, we have shown how the combination of NMR, MD and EAM has revealed a plethora of partial agonism mechanisms. An emerging feature common to several mechanisms of partial agonism is a deviation from the classical two-state model of allostery (*i.e.* the active-inactive equilibrium). Such deviation arises primarily from the sampling of a 'mixed' state, in which different structural moieties within the same protein molecule exhibit different degrees of similarity to the active *vs.* inactive conformers. The mixed state may already be transiently sampled as a binding intermediate for the endogenous unmodified allosteric effectors, such as cAMP or cGMP.

Here, we have discussed a few examples of systems that sample such mixed states upon binding of allosteric partial agonists, specifically the cNMP-binding domains of different

enzymes. However, mechanisms based on mixed states are not limited only to the systems discussed here, suggesting that such mechanisms represent a potentially more generic phenomenon. For example, when imatinib, a clinically approved allosteric cancer therapeutic, binds to its target Abl kinase, the complex exhibits a 'mixed' state, where parts of the structure (*i.e.* the αC and P-loop) resemble the active state and other parts of the structure (*i.e.* the catalytic DFG motif) resemble the inactive state (Fig. 3) (73). The DFG motif in the 'out' conformation, similar to the inactive state, allows the imatinib to inhibit the kinase (73).

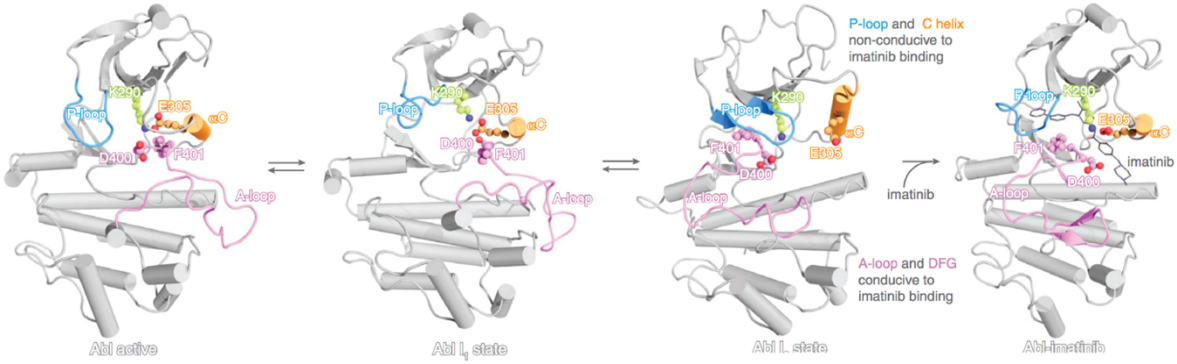

Figure 3. *Abl kinase bound to imatinib adopts a 'mixed' conformation.* The structures of Abl in the active state (left), the two inactive states (I_1 and I_2; middle), and the imatinib-bound state (right) are shown. The imatinib-bound state exhibits DFG and A-loop conformations resembling the I_2 inactive state, and αC and P-loop conformations resembling the active state (73). The figure was adapted from Xie T, Saleh T, Rossi P, Kalodimos CG. Conformational states dynamically populated by a kinase determine its function. Science 2020;370:eabc2754. Reprinted with permission from AAAS.

In general, the ability of modified ligands to stabilize and at least partially 'trap' a mixed intermediate reflects the presence of 'mixed' allosteric drivers within the same partial agonist (Fig. 4). For example, in the case of 8-NBD-cGMP, the unmodified cyclic phosphate moiety stabilizes the PBC of *pf*PKG in the 'on' conformation, similar to cGMP, while the modified base moiety stabilizes the C-terminal lid in the 'off' conformation. The opposite is true for Rp-cAMPS, where the modified cyclic phosphate stabilizes the PBC in the 'off' state, while the unmodified base favors native lid interactions in PKA, similar to cAMP, allowing

'on'/'on' inter-domain interactions to occur. It is the balance between these diverging allosteric drivers within the same ligand (Fig. 4) that dictates whether a mixed state is stabilized by a given partial agonist.

When a partial agonist stabilizes a mixed state, such mixed conformations often play a key role in the mechanism of partial agonism. For example, the mixed intermediate state stabilized by a partial agonist in an isolated domain may serve as an effective means to enhance the affinity of a partial agonist, as loss of activation is achieved with minimal disengagement of key binding elements, as in the case of 8-NBD-cGMP binding to *pf*PKG. Mixed states also rationalize the isoform selectivity of allosteric modulators, as in the case of the CE3F4R and EPAC. Furthermore, we anticipate that mixed states play a key role in dictating the non-additivity of functional group contributions to the free energy of ligand binding, as recently reported (74). In addition, the mixed conformational state in a multi-domain system, where domains respond differently to the same allosteric ligand, is an essential driver of allosteric pluripotency.

Overall, mixed conformational states within or between domains not only provide essential explanations for the observed functional responses, such as enzyme inhibition or allosteric pluripotency, but also offer new opportunities for drug design and therapeutic strategies, including synergistic multidrug combinations. For example, the allosteric pluripotency model proposed for PKA predicts that Rp-cAMPS is more likely to function as an antagonist than an agonist if administered together with an 'adjuvant' that weakens inter-domain interactions. In the case of EPAC, a mixed inhibitory intermediate explains why CE3F4R is an effective inhibitor in the presence of the cAMP agonist but not of the Rp-cAMPS reverse agonist.

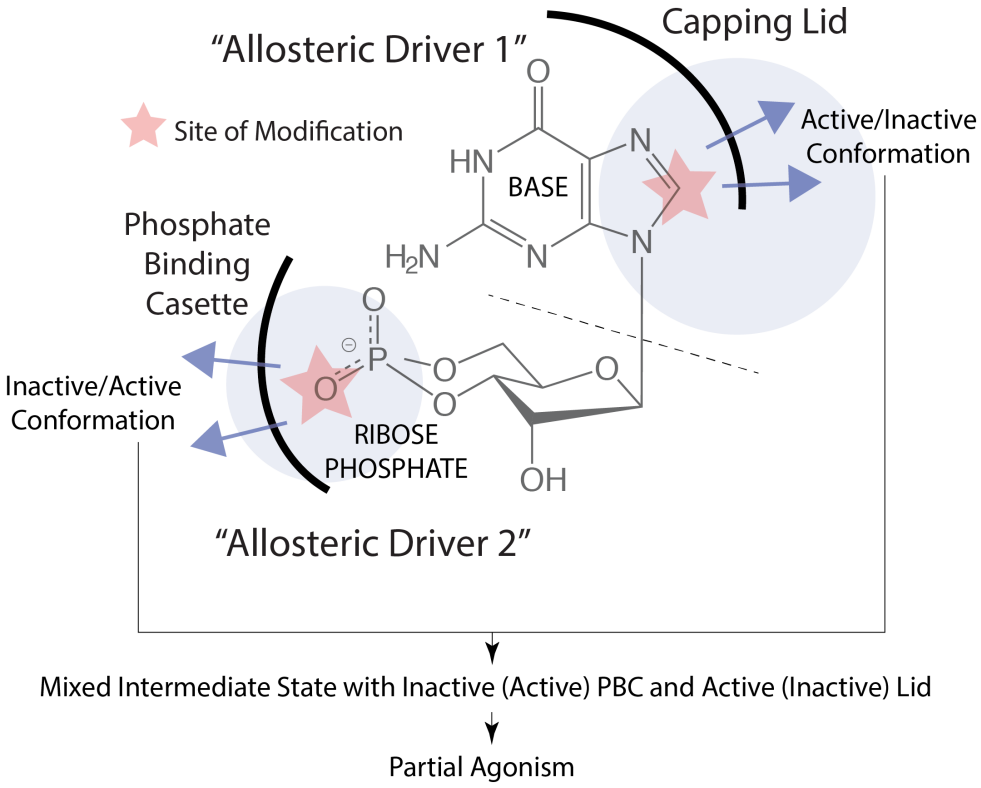

Figure 4. *Different allosteric drivers within the same partial agonist can lead to 'mixed' conformational states.* The cyclic nucleotide cGMP, which forms interactions with a CBD mainly through its base moiety (allosteric driver 1) and its ribose-phosphate moiety (allosteric driver 2), is shown as an example. The base is stabilized in the binding pocket through interactions with the base-binding region and capping lid of the CBD, whereas the phosphate binding cassette (PBC) of the CBD interacts with the ribose-phosphate of the cyclic nucleotide. When the ribose-phosphate is modified, for example, by replacing the equatorial oxygen with a bulkier sulfur, steric clashes with the PBC lead to the PBC sampling the "out" orientation, typical of the inactive conformation. On the other hand, when the base is modified, for example, by introducing additional aromatic motifs, engagement of the capping lid interaction, typical of the active conformation, may be perturbed. If two distinct allosteric drivers within the same ligand preferentially bind different conformations (*e.g.* active *vs.* inactive), mixed intermediate states are stabilized.

Considering that the cNMP binding domain is quite ubiquitous and serves as a prototype for conformational switches, the mixed conformational states we detected are also likely to be observed in other allosterically regulated proteins. Since the main determinant for the mixed conformational states lies in the mixed nature of the ligand, which includes drivers of inhibition and activation, and in how tightly these different drivers are coupled to different protein sections (*i.e.* domains or subdomains), we anticipate that any protein:ligand complex

with such properties may sample mixed conformational states. The functional implications of sampling mixed states are best appreciated through quantitative allosteric models.

Quantitative models can be assembled by exploiting the synergies between NMR spectroscopy, MD simulations and EAM calculations. NMR is critical to identify the key states in the conformational ensemble. Starting from these states, MD enables the formulation of specific targeted hypotheses that can often be further tested by NMR, thus providing a higher-resolution picture of the ensemble. Based on the identified ensemble, an EAM model is built and parameterized by NMR to quantitively relate dynamics to function as measured by low-resolution assays (*e.g.* enzyme assays, electrophysiology, *etc.*) (Fig. 5). The ability to implement quantitative dynamics-function relationships is a first critical step towards tapping the translational potential of protein dynamics by facilitating the design of new allosteric modulators.

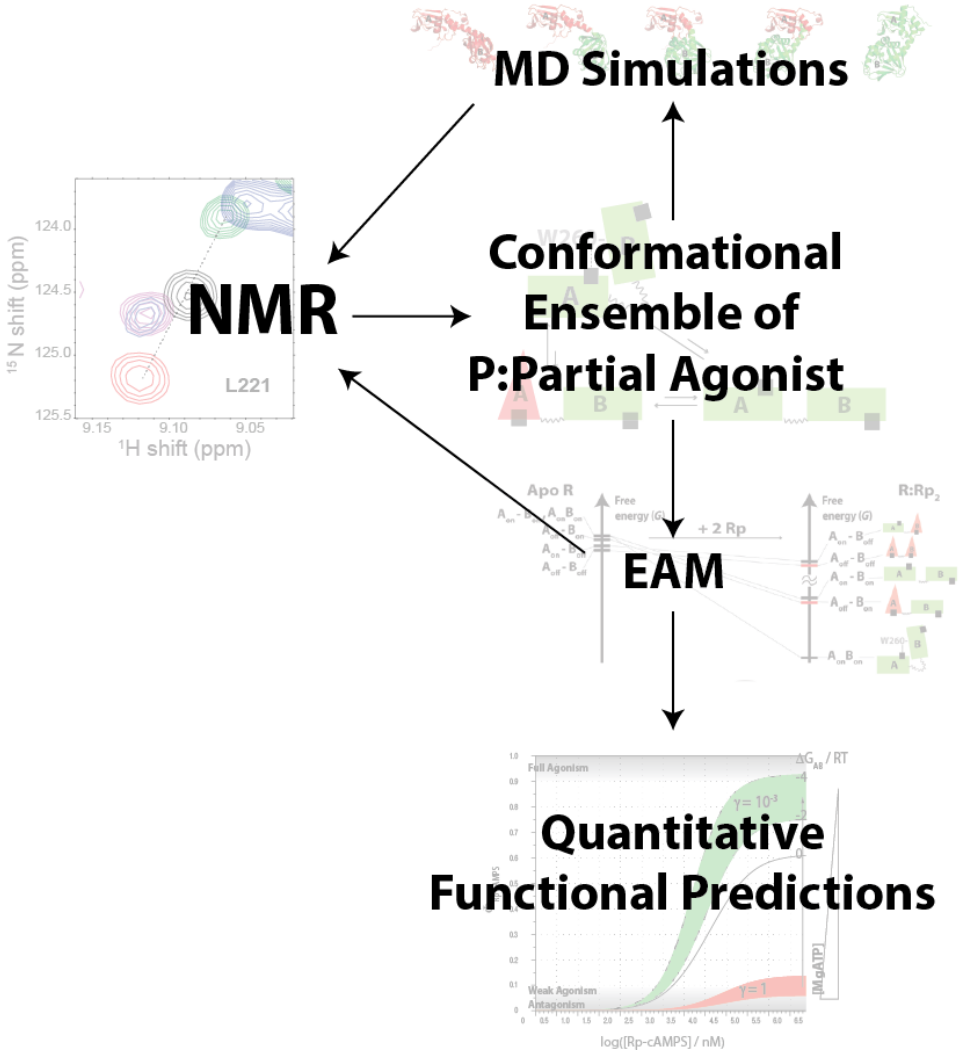

Figure 5. *Synergies between NMR, MD and EAM enable quantitative modeling of enzyme function.* NMR provides an initial map of the states within the conformational ensemble of a protein:partial-agonist complex, which serves as a basis to build initial structures for MD simulations and an EAM. The MD simulations serve as an effective means to generate refined targeted hypothesis to be tested by NMR. The EAM input parameters can often be measured by NMR. The fully parametrized EAM model enables to bridge from protein dynamics to quantitative predictions of enzymatic function (*e.g.* kinase activity). Figures are adapted from Byun JA, Akimoto M, VanSchouwen B, Lazarou TS, Taylor SS, Melacini G. Allosteric pluripotency as revealed by protein kinase A. Sci Adv 2020;6:eabb1250. Reprinted with permission from AAAS.

6.11 References

1. Yang, J.-S., Seo, S. W., Jang, S., Jung, G. Y., and Kim, S. (2012) Rational Engineering of Enzyme Allosteric Regulation through Sequence Evolution Analysis. *PLoS Comput. Biol.* **8**, e1002612
2. Nussinov, R., and Tsai, C.-J. (2015) The Design of Covalent Allosteric Drugs. *Annu. Rev. Pharmacol. Toxicol.* **55**, 249–267
3. Wodak, S. J., Paci, E., Dokholyan, N. V., Berezovsky, I. N., Horovitz, A., Li, J., Hilser, V. J., Bahar, I., Karanicolas, J., Stock, G., Hamm, P., Stote, R. H., Eberhardt, J., Chebaro, Y., Dejaegere, A., Cecchini, M., Changeux, J.-P., Bolhuis, P. G., Vreede, J., Faccioli, P., Orioli, S., Ravasio, R., Yan, L., Brito, C., Wyart, M., Gkeka, P., Rivalta, I., Palermo, G., McCammon, J. A., Panecka-Hofman, J., Wade, R. C., Di Pizio, A., Niv, M. Y., Nussinov, R., Tsai, C.-J., Jang, H., Padhorny, D., Kozakov, D., and McLeish, T. (2019) Allostery in Its Many Disguises: From Theory to Applications. *Structure*. **27**, 566–578
4. Liu, J., and Nussinov, R. (2016) Allostery: An Overview of Its History, Concepts, Methods, and Applications. *PLOS Comput. Biol.* **12**, e1004966
5. Guarnera, E., and Berezovsky, I. N. (2019) On the perturbation nature of allostery: sites, mutations, and signal modulation. *Curr. Opin. Struct. Biol.* **56**, 18–27
6. Nussinov, R., and Tsai, C.-J. (2013) Allostery in Disease and in Drug Discovery. *Cell*. **153**, 293–305
7. Lu, S., Shen, Q., and Zhang, J. (2019) Allosteric Methods and Their Applications: Facilitating the Discovery of Allosteric Drugs and the Investigation of Allosteric Mechanisms. *Acc. Chem. Res.* **52**, 492–500
8. Sheik Amamuddy, O., Veldman, W., Manyumwa, C., Khairallah, A., Agajanian, S., Oluyemi, O., Verkhivker, G. M., and Tastan Bishop, Ö. (2020) Integrated Computational Approaches and Tools for Allosteric Drug Discovery. *Int. J. Mol. Sci.* **21**, 847
9. Guarnera, E., and Berezovsky, I. N. (2020) Allosteric drugs and mutations: chances, challenges, and necessity. *Curr. Opin. Struct. Biol.* **62**, 149–157
10. Byun, J. A., Akimoto, M., VanSchouwen, B., Lazarou, T. S., Taylor, S. S., and Melacini, G. (2020) Allosteric pluripotency as revealed by protein kinase A. *Sci. Adv.* **6**, eabb1250
11. Byun, J. A., Van, K., Huang, J., Henning, P., Franz, E., Akimoto, M., Herberg, F. W., Kim, C., and Melacini, G. (2020) Mechanism of allosteric inhibition in the Plasmodium falciparum cGMP-dependent protein kinase. *J. Biol. Chem.* **295**, 8480–8491
12. VanSchouwen, B., Selvaratnam, R., Giri, R., Lorenz, R., Herberg, F. W., Kim, C., and Melacini, G. (2015) Mechanism of cAMP Partial Agonism in Protein Kinase G (PKG). *J. Biol. Chem.* 10.1074/jbc.M115.685305
13. Shao, H., Mohamed, H., Boulton, S., Huang, J., Wang, P., Chen, H., Zhou, J., Luchowska-Stańska, U., Jentsch, N. G., Armstrong, A. L., Magolan, J., Yarwood, S., and Melacini, G. (2020) Mechanism of Action of an EPAC1-Selective Competitive Partial Agonist. *J. Med. Chem.* **63**, 4762–4775
14. Boulton, S., Selvaratnam, R., Blondeau, J.-P., Lezoualc'h, F., and Melacini, G. (2018) Mechanism of Selective Enzyme Inhibition through Uncompetitive Regulation of an Allosteric Agonist. *J. Am. Chem. Soc.* **140**, 9624–9637
15. Schoepfer, J., Jahnke, W., Berellini, G., Buonamici, S., Cotesta, S., Cowan-Jacob, S. W., Dodd, S., Drueckes, P., Fabbro, D., Gabriel, T., Groell, J.-M., Grotzfeld, R. M., Hassan, A. Q., Henry, C., Iyer, V., Jones, D., Lombardo, F., Loo, A., Manley, P. W., Pellé, X., Rummel, G., Salem, B., Warmuth, M., Wylie, A. A., Zoller, T., Marzinzik, A. L., and Furet, P. (2018) Discovery of Asciminib (ABL001), an Allosteric Inhibitor of the Tyrosine Kinase Activity of BCR-ABL1. *J. Med. Chem.* **61**, 8120–8135
16. Skora, L., Mestan, J., Fabbro, D., Jahnke, W., and Grzesiek, S. (2013) NMR reveals the allosteric opening and closing of Abelson tyrosine kinase by ATP-site and myristoyl pocket inhibitors. *Proc. Natl. Acad. Sci.* **110**, E4437–E4445
17. Vahidi, S., Ripstein, Z. A., Juravsky, J. B., Rennella, E., Goldberg, A. L., Mittermaier, A. K., Rubinstein, J. L., and Kay, L. E. (2020) An allosteric switch regulates Mycobacterium tuberculosis ClpP1P2 protease function as established by cryo-EM and methyl-TROSY NMR. *Proc. Natl. Acad. Sci.* **117**, 5895–5906

18. Li, Y., Zhang, Z., Phoo, W. W., Loh, Y. R., Li, R., Yang, H. Y., Jansson, A. E., Hill, J., Keller, T. H., Nacro, K., Luo, D., and Kang, C. (2018) Structural Insights into the Inhibition of Zika Virus NS2B-NS3 Protease by a Small-Molecule Inhibitor. *Structure*. **26**, 555-564.e3
19. Paladino, A., Woodford, M. R., Backe, S. J., Sager, R. A., Kancherla, P., Daneshvar, M. A., Chen, V. Z., Bourboulia, D., Ahanin, E. F., Prodromou, C., Bergamaschi, G., Strada, A., Cretich, M., Gori, A., Veronesi, M., Bandiera, T., Vanna, R., Bratslavsky, G., Serapian, S. A., Mollapour, M., and Colombo, G. (2020) Chemical Perturbation of Oncogenic Protein Folding: from the Prediction of Locally Unstable Structures to the Design of Disruptors of Hsp90–Client Interactions. *Chem. – A Eur. J.* **26**, 9459–9465
20. Guarnera, E., and Berezovsky, I. N. (2019) Toward Comprehensive Allosteric Control over Protein Activity. *Structure*. **27**, 866-878.e1
21. Sanchez-Martin, C., Moroni, E., Ferraro, M., Laquatra, C., Cannino, G., Masgras, I., Negro, A., Quadrelli, P., Rasola, A., and Colombo, G. (2020) Rational Design of Allosteric and Selective Inhibitors of the Molecular Chaperone TRAP1. *Cell Rep.* **31**, 107531
22. Hilser, V. J., Wrabl, J. O., and Motlagh, H. N. (2012) Structural and Energetic Basis of Allostery. *Annu. Rev. Biophys.* **41**, 585–609
23. Motlagh, H. N., and Hilser, V. J. (2012) Agonism/antagonism switching in allosteric ensembles. *Proc. Natl. Acad. Sci.* **109**, 4134–4139
24. Motlagh, H. N., Wrabl, J. O., Li, J., and Hilser, V. J. (2014) The ensemble nature of allostery. *Nature*. **508**, 331–339
25. White, J. T., Li, J., Grasso, E., Wrabl, J. O., and Hilser, V. J. (2018) Ensemble allosteric model: energetic frustration within the intrinsically disordered glucocorticoid receptor. *Philos. Trans. R. Soc. B Biol. Sci.* **373**, 20170175
26. Huang, G. Y., Kim, J. J., Reger, A. S., Lorenz, R., Moon, E. W., Zhao, C., Casteel, D. E., Bertinetti, D., Vanschouwen, B., Selvaratnam, R., Pflugrath, J. W., Sankaran, B., Melacini, G., Herberg, F. W., and Kim, C. (2014) Structural basis for cyclic-nucleotide selectivity and cGMP-selective activation of PKG i. *Structure*. **22**, 116–124
27. Parnell, E., McElroy, S. P., Wiejak, J., Baillie, G. L., Porter, A., Adams, D. R., Rehmann, H., Smith, B. O., and Yarwood, S. J. (2017) Identification of a Novel, Small Molecule Partial Agonist for the Cyclic AMP Sensor, EPAC1. *Sci. Rep.* **7**, 294
28. Anand, G. S., Krishnamurthy, S., Bishnoi, T., Kornev, A., Taylor, S. S., and Johnson, D. A. (2010) Cyclic AMP- and (Rp)-cAMPS-induced conformational changes in a complex of the catalytic and regulatory (RI{alpha}) subunits of cyclic AMP-dependent protein kinase. *Mol. Cell. Proteomics*. **9**, 2225–37
29. Courilleau, D., Bisserier, M., Jullian, J.-C., Lucas, A., Bouyssou, P., Fischmeister, R., Blondeau, J.-P., and Lezoualc'h, F. (2012) Identification of a Tetrahydroquinoline Analog as a Pharmacological Inhibitor of the cAMP-binding Protein Epac. *J. Biol. Chem.* **287**, 44192–44202
30. Wu, J., Jones, J. M., Nguyen-Huu, X., Ten Eyck, L. F., and Taylor, S. S. (2004) Crystal structures of RIalpha subunit of cyclic adenosine 5'-monophosphate (cAMP)-dependent protein kinase complexed with (Rp)-adenosine 3',5'-cyclic monophosphothioate and (Sp)-adenosine 3',5'-cyclic monophosphothioate, the phosphothioate analogues of cA. *Biochemistry*. **43**, 6620–9
31. East, K. W., Skeens, E., Cui, J. Y., Belato, H. B., Mitchell, B., Hsu, R., Batista, V. S., Palermo, G., and Lisi, G. P. (2020) NMR and computational methods for molecular resolution of allosteric pathways in enzyme complexes. *Biophys. Rev.* **12**, 155–174
32. Boulton, S., and Melacini, G. (2016) Advances in NMR Methods To Map Allosteric Sites: From Models to Translation. *Chem. Rev.* **116**, 6267–6304
33. Lisi, G. P., and Loria, J. P. (2016) Solution NMR Spectroscopy for the Study of Enzyme Allostery. *Chem. Rev.* **116**, 6323–6369
34. Grutsch, S., Brüschweiler, S., and Tollinger, M. (2016) NMR Methods to Study Dynamic Allostery. *PLOS Comput. Biol.* **12**, e1004620
35. Wodak, S. J., Paci, E., Dokholyan, N. V, Berezovsky, I. N., Horovitz, A., Li, J., Hilser, V. J., Bahar, I.,

Karanicolas, J., Stock, G., Hamm, P., Stote, R. H., Eberhardt, J., Chebaro, Y., Dejaegere, A., Cecchini, M., Changeux, J.-P., Bolhuis, P. G., Vreede, J., Faccioli, P., Orioli, S., Ravasio, R., Yan, L., Brito, C., Wyart, M., Gkeka, P., Rivalta, I., Palermo, G., McCammon, J. A., Panecka-Hofman, J., Wade, R. C., Di Pizio, A., Niv, M. Y., Nussinov, R., Tsai, C.-J., Jang, H., Padhorny, D., Kozakov, D., and McLeish, T. (2019) Allostery in Its Many Disguises: From Theory to Applications. *Structure*. **27**, 566–578

36. Masterson, L. R., Cembran, A., Shi, L., and Veglia, G. (2012) Allostery and Binding Cooperativity of the Catalytic Subunit of Protein Kinase A by NMR Spectroscopy and Molecular Dynamics Simulations, pp. 363–389, 10.1016/B978-0-12-398312-1.00012-3
37. Novello, M. J., Zhu, J., Feng, Q., Ikura, M., and Stathopulos, P. B. (2018) Structural elements of stromal interaction molecule function. *Cell Calcium*. **73**, 88–94
38. Moroni, E., Paladino, A., and Colombo, G. (2015) The Dynamics of Drug Discovery. *Curr. Top. Med. Chem.* **15**, 2043–2055
39. Rosenman, D. J., Connors, C. R., Chen, W., Wang, C., and García, A. E. (2013) Aβ Monomers Transiently Sample Oligomer and Fibril-Like Configurations: Ensemble Characterization Using a Combined MD/NMR Approach. *J. Mol. Biol.* **425**, 3338–3359
40. Huang, G. Y., Gerlits, O. O., Blakeley, M. P., Sankaran, B., Kovalevsky, A. Y., and Kim, C. (2014) Neutron Diffraction Reveals Hydrogen Bonds Critical for cGMP-Selective Activation: Insights for cGMP-Dependent Protein Kinase Agonist Design. *Biochemistry*. **53**, 6725–6727
41. Wolter, S., Golombek, M., and Seifert, R. (2011) Differential activation of cAMP- and cGMP-dependent protein kinases by cyclic purine and pyrimidine nucleotides. *Biochem. Biophys. Res. Commun.* **415**, 563–566
42. Börner, S., Schwede, F., Schlipp, A., Berisha, F., Calebiro, D., Lohse, M. J., and Nikolaev, V. O. (2011) FRET measurements of intracellular cAMP concentrations and cAMP analog permeability in intact cells. *Nat. Protoc.* **6**, 427–438
43. Cowman, A. F., Healer, J., Marapana, D., and Marsh, K. (2016) Malaria: Biology and Disease. *Cell*. **167**, 610–624
44. Hopp, C. S., Bowyer, P. W., and Baker, D. A. (2012) The role of cGMP signalling in regulating life cycle progression of Plasmodium. *Microbes Infect.* **14**, 831–837
45. Taylor, H. M., McRobert, L., Grainger, M., Sicard, A., Dluzewski, A. R., Hopp, C. S., Holder, A. A., and Baker, D. A. (2010) The Malaria Parasite Cyclic GMP-Dependent Protein Kinase Plays a Central Role in Blood-Stage Schizogony. *Eukaryot. Cell*. **9**, 37–45
46. Moon, R. W., Taylor, C. J., Bex, C., Schepers, R., Goulding, D., Janse, C. J., Waters, A. P., Baker, D. A., and Billker, O. (2009) A Cyclic GMP Signalling Module That Regulates Gliding Motility in a Malaria Parasite. *PLoS Pathog.* **5**, e1000599
47. McRobert, L., Taylor, C. J., Deng, W., Fivelman, Q. L., Cummings, R. M., Polley, S. D., Billker, O., and Baker, D. A. (2008) Gametogenesis in Malaria Parasites Is Mediated by the cGMP-Dependent Protein Kinase. *PLoS Biol.* **6**, e139
48. Govindasamy, K., Jebiwott, S., Jaijyan, D. K., Davidow, A., Ojo, K. K., Van Voorhis, W. C., Brochet, M., Billker, O., and Bhanot, P. (2016) Invasion of hepatocytes by Plasmodium sporozoites requires cGMP-dependent protein kinase and calcium dependent protein kinase 4. *Mol. Microbiol.* **102**, 349–363
49. Kim, J. J., Flueck, C., Franz, E., Sanabria-Figueroa, E., Thompson, E., Lorenz, R., Bertinetti, D., Baker, D. A., Herberg, F. W., and Kim, C. (2015) Crystal Structures of the Carboxyl cGMP Binding Domain of the Plasmodium falciparum cGMP-dependent Protein Kinase Reveal a Novel Capping Triad Crucial for Merozoite Egress. *PLOS Pathog.* **11**, e1004639
50. Franz, E., Knape, M. J., and Herberg, F. W. (2018) cGMP Binding Domain D Mediates a Unique Activation Mechanism in Plasmodium falciparum PKG. *ACS Infect. Dis.* **4**, 415–423
51. Almahariq, M., Tsalkova, T., Mei, F. C., Chen, H., Zhou, J., Sastry, S. K., Schwede, F., and Cheng, X. (2013) A Novel EPAC-Specific Inhibitor Suppresses Pancreatic Cancer Cell Migration and Invasion. *Mol. Pharmacol.* **83**, 122–128
52. Wang, X., Luo, C., Cheng, X., and Lu, M. (2017) Lithium and an EPAC-specific inhibitor ESI-09

synergistically suppress pancreatic cancer cell proliferation and survival. *Acta Biochim. Biophys. Sin. (Shanghai)*. **49**, 573–580
53. Kumar, N., Gupta, S., Dabral, S., Singh, S., and Sehrawat, S. (2017) Role of exchange protein directly activated by cAMP (EPAC1) in breast cancer cell migration and apoptosis. *Mol. Cell. Biochem.* **430**, 115–125
54. Yan, J., Mei, F. C., Cheng, H., Lao, D. H., Hu, Y., Wei, J., Patrikeev, I., Hao, D., Stutz, S. J., Dineley, K. T., Motamedi, M., Hommel, J. D., Cunningham, K. A., Chen, J., and Cheng, X. (2013) Enhanced Leptin Sensitivity, Reduced Adiposity, and Improved Glucose Homeostasis in Mice Lacking Exchange Protein Directly Activated by Cyclic AMP Isoform 1. *Mol. Cell. Biol.* **33**, 918–926
55. Tao, X., Mei, F., Agrawal, A., Peters, C. J., Ksiazek, T. G., Cheng, X., and Tseng, C.-T. K. (2014) Blocking of Exchange Proteins Directly Activated by cAMP Leads to Reduced Replication of Middle East Respiratory Syndrome Coronavirus. *J. Virol.* **88**, 3902–3910
56. Badireddy, S., Yunfeng, G., Ritchie, M., Akamine, P., Wu, J., Kim, C. W., Taylor, S. S., Qingsong, L., Swaminathan, K., and Anand, G. S. (2011) Cyclic AMP Analog Blocks Kinase Activation by Stabilizing Inactive Conformation: Conformational Selection Highlights a New Concept in Allosteric Inhibitor Design. *Mol. Cell. Proteomics*. **10**, M110.004390
57. He, L., Kulesskiy, E., Saarela, J., Turunen, L., Wennerberg, K., Aittokallio, T., and Tang, J. (2018) Methods for High-throughput Drug Combination Screening and Synergy Scoring, pp. 351–398, 10.1007/978-1-4939-7493-1_17
58. Zimmer, A., Katzir, I., Dekel, E., Mayo, A. E., and Alon, U. (2016) Prediction of multidimensional drug dose responses based on measurements of drug pairs. *Proc. Natl. Acad. Sci.* **113**, 10442–10447
59. Wood, K. B. (2016) Pairwise interactions and the battle against combinatorics in multidrug therapies. *Proc. Natl. Acad. Sci.* **113**, 10231–10233
60. Saloustros, E., Salpea, P., Starost, M., Liu, S., Faucz, F. R., London, E., Szarek, E., Song, W.-J., Hussain, M., and Stratakis, C. A. (2017) Prkar1a gene knockout in the pancreas leads to neuroendocrine tumorigenesis. *Endocr. Relat. Cancer*. **24**, 31–40
61. Veugelers, M., Wilkes, D., Burton, K., McDermott, D. A., Song, Y., Goldstein, M. M., La Perle, K., Vaughan, C. J., O'Hagan, A., Bennett, K. R., Meyer, B. J., Legius, E., Karttunen, M., Norio, R., Kaariainen, H., Lavyne, M., Neau, J.-P., Richter, G., Kirali, K., Farnsworth, A., Stapleton, K., Morelli, P., Takanashi, Y., Bamforth, J.-S., Eitelberger, F., Noszian, I., Manfroi, W., Powers, J., Mochizuki, Y., Imai, T., Ko, G. T. C., Driscoll, D. A., Goldmuntz, E., Edelberg, J. M., Collins, A., Eccles, D., Irvine, A. D., McKnight, G. S., and Basson, C. T. (2004) Comparative PRKAR1A genotype-phenotype analyses in humans with Carney complex and prkar1a haploinsufficient mice. *Proc. Natl. Acad. Sci.* **101**, 14222–14227
62. Boikos, S. A., and Stratakis, C. A. (2007) Carney complex: the first 20 years. *Curr. Opin. Oncol.* **19**, 24–29
63. WIT, R. J. W., HOPPE, J., STEC, W. J., BARANIAK, J., and JASTORFF, B. (1982) Interaction of cAMP Derivatives with the "Stable" CAMP-Binding Site in the CAMP-Dependent Protein Kinase Type I. *Eur. J. Biochem.* **122**, 95–99
64. Poppe, H., Rybalkin, S. D., Rehmann, H., Hinds, T. R., Tang, X.-B., Christensen, A. E., Schwede, F., Genieser, H.-G., Bos, J. L., Doskeland, S. O., Beavo, J. A., and Butt, E. (2008) Cyclic nucleotide analogs as probes of signaling pathways. *Nat. Methods*. **5**, 277–278
65. Dostmann, W. R., and Taylor, S. S. (1991) Identifying the molecular switches that determine whether (Rp)-cAMPS functions as an antagonist or an agonist in the activation of cAMP-dependent protein kinase I. *Biochemistry*. **30**, 8710–6
66. Gielen, S. C. J. P., Burger, C. W., Kühne, L. C. M., Hanifi-Moghaddam, P., and Blok, L. J. (2005) Analysis off Estrogen Agonism and Antagonism of Tamoxifen, Raloxifene, and ICI182780 in Endometrial Cancer Cells: A Putative Role for the Epidermal Growth Factor Receptor Ligand Amphiregulin. *J. Soc. Gynecol. Investig.* **12**, e55–e66
67. Taylor, S. S., Ilouz, R., Zhang, P., and Kornev, A. P. (2012) Assembly of allosteric macromolecular

switches: lessons from PKA. *Nat. Rev. Mol. Cell Biol.* **13**, 646–658
68. Kim, C., Cheng, C. Y., Saldanha, S. A., and Taylor, S. S. (2007) PKA-I holoenzyme structure reveals a mechanism for cAMP-dependent activation. *Cell.* **130**, 1032–43
69. Huang, L. J., and Taylor, S. S. (1998) Dissecting cAMP Binding Domain A in the R I α Subunit of cAMP-dependent Protein Kinase. *J. Biol. Chem.* **273**, 26739–26746
70. Herberg, F. W., Dostmann, W. R. G., Zorn, M., Davis, S. J., and Taylor, S. S. (1994) Crosstalk between Domains in the Regulatory Subunit of cAMP-Dependent Protein Kinase: Influence of Amino Terminus on cAMP Binding and Holoenzyme Formation. *Biochemistry*. **33**, 7485–7494
71. Su, Y., Dostmann, W. R., Herberg, F. W., Durick, K., Xuong, N. H., Ten Eyck, L., Taylor, S. S., and Varughese, K. I. (1995) Regulatory subunit of protein kinase A: structure of deletion mutant with cAMP binding domains. *Science*. **269**, 807–13
72. Akimoto, M., McNicholl, E. T., Ramkissoon, A., Moleschi, K., Taylor, S. S., and Melacini, G. (2015) Mapping the Free Energy Landscape of PKA Inhibition and Activation: A Double-Conformational Selection Model for the Tandem cAMP-Binding Domains of PKA RIα. *PLoS Biol.* **13**, e1002305
73. Xie, T., Saleh, T., Rossi, P., and Kalodimos, C. G. (2020) Conformational states dynamically populated by a kinase determine its function. *Science (80-.).* 10.1126/science.abc2754
74. Boulton, S., Van, K., VanSchouwen, B., Augustine, J., Akimoto, M., and Melacini, G. (2020) Allosteric Mechanisms of Nonadditive Substituent Contributions to Protein-Ligand Binding. *Biophys. J.* **119**, 1135–1146